HEAT-ASSISTED INCREMENTAL SHEET FORMING OF TI-6AL-4V SHEETS

By

WEINING LI

A thesis submitted to the University of Birmingham for the degree of

DOCTOR OF PHILOSOPHY

Department of Mechanical Engineering
School of Engineering
College of Engineering and Physical Sciences
University of Birmingham
September 2022

UNIVERSITY OF BIRMINGHAM

University of Birmingham Research Archive
e-theses repository

This unpublished thesis/dissertation is under a Creative Commons Attribution 4.0 International (CC BY 4.0) licence.

You are free to:

Share — copy and redistribute the material in any medium or format

Adapt — remix, transform, and build upon the material for any purpose, even commercially.

The licensor cannot revoke these freedoms as long as you follow the license terms.

Under the following terms:

Attribution — You must give appropriate credit, provide a link to the license, and indicate if changes were made. You may do so in any reasonable manner, but not in any way that suggests the licensor endorses you or your use.

No additional restrictions — You may not apply legal terms or technological measures that legally restrict others from doing anything the license permits.

Notices:

You do not have to comply with the license for elements of the material in the public domain or where your use is permitted by an applicable exception or limitation.

No warranties are given. The license may not give you all of the permissions necessary for your intended use. For example, other rights such as publicity, privacy, or moral rights may limit how you use the material.

Unless otherwise stated, any material in this thesis/dissertation that is cited to a third-party source is not included in the terms of this licence. Please refer to the original source(s) for licencing conditions of any quotes, images or other material cited to a third party.

ABSTRACT

Single point incremental forming (SPIF) is a sheet forming technique that deforms sheet materials incrementally to a designated shape. The process has shown high ability to deform low-strength materials for good geometrical accuracy and formability at room temperature. Deforming high-temperature alloys, such as Ti-6AI-4V, requires integrated heat sources to increase the ductility of the metal sheets for deformation. However, the integration of heating results in unpredictable thermomechanical behaviours on the formability, geometric accuracy, thickness distribution and surface quality. Considerable research efforts have been in developing in different heating methods and designing novel tools and analytical modelling to resolve the limitations. The current challenge remains to improve the localised and stable heating and functional tool design to reduce the thermal expansion and friction at the tool-surface contact area and the analysis of relationship between thermal and mechanical effects. This PhD research aims to develop and improve the induction heating-assisted SPIF system for Ti-6AI-4V sheets in tool design, lubrication, tool path optimisation and numerical analysis. Total four research methods include the study of microstructural and mechanical properties for low temperature (600 ℃ and 700 ℃) deformation using Zener-Hollomon parameter (Z-parameter). A novel tool design with water-cooling lubricant system to assist lubricant service. A combination of crystal plasticity finite element simulation method (CPFEM), representative volume element (RVE) and cellular automata (CA) to predict the grain orientation, crystal texture and grain size evolution in experimental scale and microstructure. A radial basis function (RBF) artificial neural network to optimise the tool path for improvements of geometric accuracy and surface quality above beta-transus (950 ℃) temperature.

ACKNOWLEDGMENTS

I would like to dedicate to my family, supervisors and university safety and technical staff who assisted me to make the thesis possible. A sincere appreciation to my first supervisor, Professor **Khamis Essa**, without whom none of this would have come to be. His tremendous support and guidance during my PhD research both as supervisor and mentor were indispensable for my main research and the cost of essential work. I would like to thank my second supervisor Professor **Moataz M Attallah** who supervised and guided my research papers and provided the essential laboratory works for my research. Further, I would like to thank Raya Al-Dadah who orientated the commencing of my PhD work; Dr Ludwig Schneider, Theresa Morris, Dr Yu Lung Chiu and Dr Manmath Dash provided the training for Electron Microscopes; safety officers Donna M Johnson and Katie Tyler who helped me to orientate my lab works; Stephen Brookes and Benjamin Fox who helped me developed my physics theory and initiated my physics experimental tools. A special thanks to the mates in my research group, Dr Prveen Bidare, Dr Sheng Li, Dr Nikolina Kovacev, Dr Ahmed Binobaid, Dr Michele de Lisi, Dr Abdullah Alqahtani, Dr Mohammad Almadani, Dr Abdullah Mohammed and Dr Chang Shu who cooperated and helped me throughout my PhD study.

I will not be able to accomplish this feat without the encouragement and love of my family. I am grateful for my supportive and loving family, my mother **Min Wu** and my father **Wanpeng Li**, who always stood by me through thick and thin. No words can express what you mean to me. This thesis is dedicated to you.

Table of Contents

Page

List of Figures

List of Tables

Abbreviations

ALLIE	Internal Energy
ALLKE	Kinetic Energy
ALLAE	Artificial Strain Energy
AC	Alternative Current
AI	Artificial Intelligence
ANN	Artificial Neural Network
CAD	Computer Aided Design
CAM	Computer Aided Manufacture
CPFEM	Crystal Plasticity Finite Element Simulation Method
DRX	Dynamic recrystallisation
DRV	Dynamic recovery
EBSD	Electron Backscatter Diffraction
EDX	Energy-dispersive X-ray spectroscopy
FE	Finite Element
GND	Geometrically Necessary Dislocations
ISF	Incremental Sheet Forming

IFCT	Incremental Forming with a Counter Tool
MARS	Multivariate Adaptive Regression Spline
PSO	Particle Swarm Optimization
RSM	Response Surface Methodology
RVE	Representative Volume Element
RBF	Radial Basis Function
RMSE	Root Mean Squared Error
RT	Room Temperature
SEM	Scanning Electron Microscope
SPIF	Single Point Incremental Forming
TPIF	Two Points Incremental Forming
UVSPIF	Ultrasonic Vibration Single Point Incremental Forming
Z-parameter	Zener-hollomon Parameter

Nomenclature

θ	contact angle
L	die hole distance
R_b	ball radius
R_d	die hole shoulder radius
h	shell bulging height
x_b	ball centre location
l_2	extended rule of contact arc
ε_x	uniform strain in x-direction
ε_y	uniform strain in y-direction
ε_t	uniform strain in thickness-direction
Y	predicted response
D	ball-roller diameter
ΔZ	step size
F	feed rate
C_0	mean value of the response
C_1	linear coefficient

C_3	linear coefficient
C_{11}	quadratic coefficient
C_{13}	quadratic coefficient
C_{12}	double interaction coefficient
C_{23}	double interaction coefficient
ε	deviation between the observation and calculation
σ	yield stress
$\bar{\varepsilon}^{pl}$	equivalent plastic strain
$\dot{\bar{\varepsilon}}^{pl}$	equivalent plastic strain rate
$\dot{\varepsilon}_0$	reference strain rate
T	working temperature
T_r	room temperature
T_m	melting temperature
A	yield stress at reference strain rate and temperature
B	coefficient of strain hardening
C	coefficient of strain rate strengthening
m	thermal softening coefficient

n	strain hardening exponent
t	sheet thickness
x_1	nodes at top surface x-direction
y_1	nodes at top surface y-direction
z_1	nodes at top surface z-direction
x_2	nodes at lower surface x-direction
y_2	nodes at lower surface y-direction
z_2	nodes at lower surface z-direction
t_f	final thickness of the workpiece
t_0	initial thickness of the workpiece
θ	wall angle
S_a	average surface roughness
S_q	the root-mean-square height
S_p	maximum peak height
S_v	maximum valley depth
S_z	maximum height
A	material constant

σ	flow stress
Q	apparent activation energy
R	gas constant
T	experimental temperature
α	material constant
β	material constant
n_1	material constant
n	material constant
F	deformation gradient tensor
F^P	plastic deformation gradient
F^e	non-plastic component
J	ratio of the deformed to the undeformed volume
L	macroscopic velocity gradient
L^e	velocity gradient
L^p	velocity gradient for the plastic part
$\dot{\gamma}^\alpha$	α slip system shear rate
s^α	unit vector for slip direction

m^{α}	unit vector for slip plane for α^{th} slip system
$\tilde{s}^{\alpha}$	normal vector to the α^{th} slip system
$\tilde{m}^{\alpha}$	normal vector to the α^{th} slip system
m_0^{α}	vectors of slip direction
n_0^{α}	Vectors of the slip plane normal
S_0^{α}	slip resistance in unit of Schmid tensor
E^*	elastic strain
I	2nd order tensor of identity
T^*	crystalline Cauchy stress
C	fourth-order elasticity tensor
T	grain level symmetrical Cauchy stress tensor
F^*	non-plastic deformation gradient
R^*	lattice rigid rotation
U^*	stretch tensor
Q	grain orientation
$\dot{\gamma}^{\alpha}$	shear rate

$\dot{\gamma}_0$	reference shear rate
χ	coefficient of material rate sensitivity
τ^{α}	α slip system acting resolved shear stress
s^{α}	dislocation acted deformation resistance
μ	shear modulus
b	Burger's vector
ρ^{α}	density of dislocation for α^{th} slip system
N	number of slip systems
u_1	constant for fitting
T	working temperature
T_0	reference temperature
u_2	coefficient of Hall–Petch
d	average grain size
$d\dot{\rho}^{+}$	density of dislocation in the increasing order
k_1	work hardening constant
ρ	dislocation density
$\dot{\varepsilon}$	strain rate

$d\dot{\rho}^{-}$	dislocation density in decreasing order
k_2	function depends on the working strain rate and temperature.
k_{20}	constant
ω	constant
$\dot{n}(T)$	nucleation rate
$\dot{n}(T_{\mathrm{m}})$	nucleation rate at melting temperature
C	constant
η	DRX fraction
ε	true strain
r_{d}	mean radius of DRXed grain
σ_{s}	steady-state flow stress
μ	shear modulus
b	Burger's vector
ρ_c	dislocation density at critical level
λ	grain boundary energy
l	average free path for dislocation
M	mobility at the grain boundary

C_1	constant
φ	constant
Q_{deform}	stored energy under deformation
ψ	material molar volume
ρ_{GND}	geometrically necessary dislocations
P	driving force
dE_i^{vol}	evolution in the volume energy
dE_i^{sur}	energy of grain boundary
ρ_m	matrix grain of dislocation densities
ρ_r	matrix grain of DRXed grains
r	grain radius
λ_m	boundary energy above 15°
θ_m	critical misorientation angle at 15°
v	Poisson ratio
δ	characteristic grain boundary thickness
D_{0b}	coefficient of diffusion at ideal 0 K
Q_{diffu}	activation energy for self-diffusion activation energy

v	migration rate
σ	isothermal macroscopic flow stress under hot deformation
$\bar{\rho}$	average dislocation density
ρ_i	dislocation density
V_i	volume at i^{th} grain
V_{total}	volume in total
ϕ_i	radial basis activation function
$\|\cdot\|$	Euclidean distance
c_j	centre of the hidden neuron
σ_j	width of the hidden neuron
k	output of the node
R^2	squared multiple correlation coefficient
β	bias or distortion
I_{w}	Wilmott index
N	number of data in each group
X_c	predicted data
X_m	measured experimental data

ε	error function
P_i	best fitness
P_g	global best fitness
X_i	ith particle position
V_i	ith particle velocity
w	weight inertia
λ	constriction factor
c_1	constant variables in acceleration
c_2	constant variables in acceleration
$w_{\max}$	maximum coefficient
$w_{\min}$	minimum coefficient
$k_{\max}$	maximum value of iterations
θ_{ik}	thresholds for connection of RBF neural network
θ_{kl}	thresholds for connection of RBF neural network
w_{ik}	connection weights between the RBF network input and hidden layers
w_{kl}	connection weights between the RBF network hidden and the output layers
$f(X)$	fitness value corresponding to x_i

$E(X)$	error level after each RBF training by individual X
$d_j(k)$	weight update objective function output
m	number of nodes for output layers
$f\left(x_i^{(k)}\right)$	obtained fitness value based on each particle
$f\left(p_i^{(k-1)}\right)$	value of individual extreme
a	number of output layers
b	number of input layers
c	constant in range of 1 to 10
η	learning rate
α	momentum factor
m	initial population size
ω	inertia weight
$v_{\max}$	maximum speed
ΔW_{ij}	deviation of RBF network particle
$k-1$	time

List of publications

First author journal article publications:

Li, W., M.M. Attallah, and K. Essa, *Experimental and numerical investigations on the process quality and microstructure during induction heating assisted incremental forming of Ti-6Al-4V sheet*. Journal of Materials Processing Technology, 2022. 299: p. 117323. DOI: 10.1016/j.jmatprotec.2021.117323.

Li, W., K. Essa, and S. Li, *A novel tool to enhance the lubricant efficiency on induction heat-assisted incremental sheet forming of Ti-6Al-4 V sheets.* The International Journal of Advanced Manufacturing Technology, 2022. DOI: 10.1007/s00170-022-09284-z.

Crystal plasticity model of induction heating assisted incremental sheet forming with recrystallisation simulation in cellular automata. Accepted by The International Journal of Advanced Manufacturing Technology.

Application of machine learning on tool path optimisation and cooling lubricant in induction heating-assisted single point incremental sheet forming of Ti-6Al-4V sheets. Accepted by International Journal of Advanced Manufacturing Technology.

Heat-assisted incremental sheet forming for high strength materials - A review. Under review by International Journal of Advanced Manufacturing Technology.

Co-author journal article publications:

Kovacev, N.; Li, S.; Li, W.; Zeraati-Rezaei, S.; Tsolakis, A.; Essa, K. *Additive Manufacturing of Novel Hybrid Monolithic Ceramic Substrates*. Aerospace, 2022. **9**(5). DOI: 10.3390/aerospace9050255.

1. Introduction

1.1. Background

Conventional sheet-forming processes are normally established in complex and expensive tool system designs fixed for limited designated geometry and only economically feasible for mass production. The global challenge in the manufacturing industry includes developing flexible and economical forming processes to produce sheet materials in complicated geometry for rapid prototyping. Incremental sheet forming (ISF) is a new class forming process which can complete the objectives. SPIF has undergone development in decades and refers to a die-less sheet forming process, as shown in **Figure 1-1**[1]. The process excels in forming complex shapes or rapid prototypes using die-less and simple tools.

The process has received increasing attention due to its high flexibility and low cost. Previous studies by Honarpisheh et al. [2] and Al-Ghamdi and Hussain [3] revealed that SPIF has shown high performance in deforming relative low-strength materials, such as aluminium and magnesium alloy sheets, at room temperature. However, the product's geometrical accuracy suffers from a large elastic springback resulting from the die-less nature of the process and the formability is significantly reduced. For high-temperature alloy sheets, such as Ti-6Al-4V, steel and Nickel-based superalloys, the room temperature SPIF process did not achieve high product quality. Ambrogio et al. [4], Formisano et al. [5], Fan et al. [6] and Göttmann et al. [7] investigated the integration of heating sources to reduce the material flow stress, which able to provide heating temperature to the sheet materials to increase its ductility and improve the formability and reduce the forming force to achieve better surface quality.

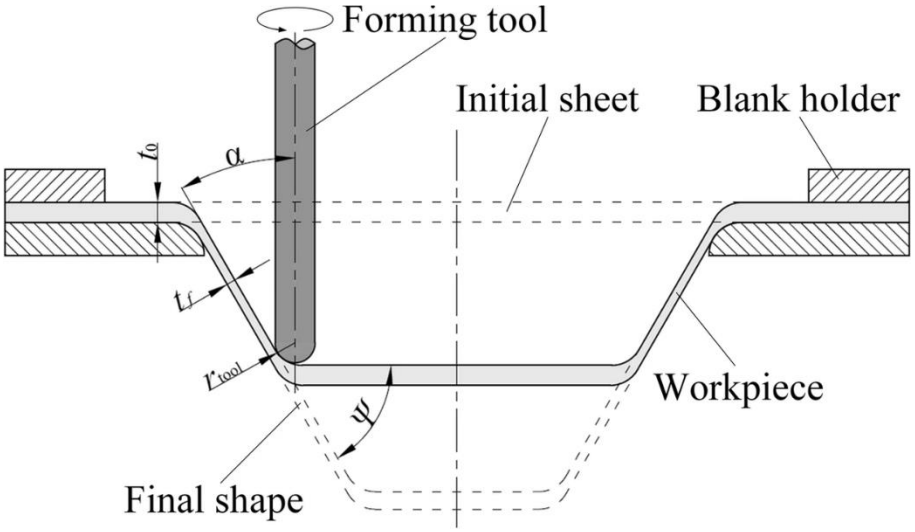

Figure 1-1. The illustration of SPIF [1].

1.2. Motivation

There have been several attempts to utilise SPIF for deforming materials at elevated temperatures. However, the obtained surface quality from high-temperature experiments has produced high wear track and adherence of lubricant from the tool-surface contact area, electric sparks in electric heating and oxide layer on workpiece surface during the high-temperature deformation process. The heat-assisted SPIF has substantial potential if various aspects, such as formability, geometric accuracy and surface quality, can be improved by collating those aspects with the forming tool design, tool path plan and correlate the mechanical properties and microstructural evolution during the process.

1.3. Aims and Objectives

This PhD project aims to study the mechanical and microstructural properties under dynamic localised heat input SPIF system to deform Ti-6Al-4V thin sheets and improve the process quality. The following objectives will be approached to achieve the aim;

1. Study the history of metal forming works and propose the main objectives of this

project.

2. A literature review on recent research for current development of SPIF process.

3. Correlate the mechanical and microstructural properties for induction heating assisted SPIF of Ti-6Al-4V at relatively low temperatures.

4. A tool design to enhance the lubrication and improve the surface and process quality.

5. Develop a microstructural numerical modelling to predict the evolution in crystal structure and correlate the outputs with the process parameters.
6. Develop an artificial neural network to optimise the tool path to improve the geometric accuracy.
7. A conclusion of this PhD project and future improvements to optimise the current technology.

1.4. Thesis organisation

Chapter 1 (objective 1) presents brief background about the SPIF process and outlines the motivation of this PhD project. The aims and objectives of this thesis as well as the thesis structure are presented in this chapter.

Chapter 2 (objective 2) reports the state of the art in this research field as well as the current limitations and challenges. The types and improvements of tool design, numerical methods for tool path planning, improvements of lubrication, different numerical modelling for typical features, and microstructural analysis under various process parameters are discussed and summarised.

Chapter 3 (objective 3) reports the experimental, numerical and microstructural investigation of induction heating assisted SPIF of Ti-6Al-4V sheets at 600 ℃ and 700 ℃. This chapter aims

to relate mechanical properties (forming force, geometric accuracy and thickness) with microstructural evolution (grain size, orientation and micro-hardness).

Chapter 4 (objective 4) reports a new designed tool with water-cooling lubricant to enhance the lubricating efficiency and surface quality for induction heating assisted SPIF of Ti-6Al-4V sheets at 700 ℃. The chapter investigates the lubricating methods and subsequent effects on geometric and surface characteristics.

Chapter 5 (objective 5) reports the FE modelling at the microstructure level to present the crystal plasticity and microstructural evolution during the induction heating assisted SPIF of Ti-6Al-4V sheets at 700 ℃. In this chapter, the CPFEM, RVE and CA models were combined to predict microstructural properties.

Chapter 6 (objective 6) reports an artificial neural network optimisation of the tool path. The chapter also presents the integration of new tool design and water-cooling lubricant system in induction heating assisted SPIF of Ti-6Al-4V sheets at the range of beta-transus temperature (950 – 1080 ℃). In this chapter, RBF networks, FE modelling and experimental works have been correlated to present mechanical and microstructural properties for Ti-6Al-4V sheets at temperatures above phase transition.

Chapter 7 (objective 7) presents the conclusion and future research of this project.

2. Literature review

Weining Li [a], Moataz M. Attallah [b], Khamis Essa [a]

[a] *Mechanical Engineering, University of Birmingham, Edgbaston, Birmingham, B15 2TT, UK*

[b] *School of Metallurgy and Materials, University of Birmingham, Edgbaston, Birmingham, B15 2TT, UK*

This chapter is under review as a review article in *International Journal of Advanced Manufacturing Technology* entitled "Heat-assisted incremental sheet forming for high strength materials - A review".

Credit authorship contribution statement

Weining Li: Conceptualization, Investigation, Writing - original draft.

Moataz M. Attallah: Management of SEM booking, Writing - review & editing.

Khamis Essa: Writing - review & editing, Supervision.

Review contributions:

- Review of recent research in heat-assisted incremental sheet forming for high-strength materials of heating methods, tools design, tool path design, lubricant and coating, numerical analysis and microstructure analysis.
- The future improvements and open research questions.

2.1. Introduction

This chapter discusses the previous studies on different ISF processes and current improvements in deforming high-strength materials. The first section is based on classifications of ISF processes and the advantages and limitations of the forming processes. The second section compares the different heating approaches in the SPIF process for high-strength materials and the advantages and limitations of each approach. The chapter will then show the state-of-the-art development in tool design, tool path optimisation and improvements in lubrication in the heat-assisted SPIF process. The following section will outline the existing numerical modelling approaches used to simulate SPIF processes at macro and microscale levels. The final section will compare the current analytical methods used to analyse the heat-assisted SPIF process.

2.2. Development and classifications of incremental sheet forming

The ISF process is a metal forming process developed from the conventional sheet forming process with the application of a computer numerical control (CNC) system to attempt a progressive deformation of the sheet materials [8]. The typical ISF is classifiable into three different types: incremental forming with a counter tool (IFCT), two points incremental forming (TPIF) and single point incremental forming (SPIF).

2.2.1. Incremental forming with a counter tool

Figure 2-1(a) illustrates the working mechanism of incremental forming with a counter tool. The figure show that the deforming tool is assisted by a movable counter-support tool to maintain the geometric formation and accuracy. The counter tool is supported by a CNC machine with movement syncretised with the forming tool to produce complex forming shapes. Behera et al. [9] studied the IFCT with robotic forming arms, which can provide flexible

movement to deform the sheet materials to complex forming shapes. Such driving mechanisms significantly improved the formability and geometric accuracy.

The IFCT process is currently under development by the manufacturing industry to induce elevated temperature [10] to deform high-temperature materials, such as high-strength steel, and a path planning optimisation process [11, 12] to improve geometric accuracy. However, the integration of robotic forming arms represents a complicated process with high equipment costs. To avoid affecting the working mechanism of two robotic arms, the temperature is supported by high-frequency converter and the electric flux is flowed between forming tool and workpiece. Due to the safety measures, the forming tool and workpiece must be insulated. Further, the provided temperature is supported to the whole workpiece and unstable for high temperature. According to study by Möllensiep et al. [10], the achieved temperature can be maintained at 300 ℃ for constant support and a maximum temperature reach of 600 ℃, where the heating temperature is able to perform on higher temperature materials, such as titanium and nickel alloy sheets.

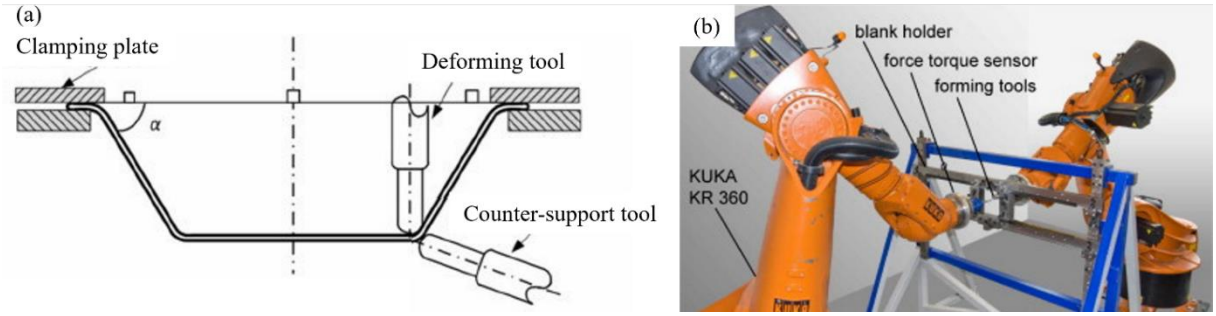

Figure 2-1. Working mechanism of IFCT, (a) working mechanism, [9] (b) IFCT with robotic forming arms [10].

2.2.2. Two points incremental forming

In the TPIF process, the sheet materials are clamped with a fixture. The forming tool deforms

on the outer surface of the workpiece from the top to bottom, according to the tool path with a full or partial die underneath the workpiece to assist the forming process. **Figure 2-2**(a) illustrates the TPIF with full die, where the full die has the same geometry as the forming shape placed under the workpiece; the forming tool deforms the workpiece according to the tool path and the error from tool movements is reduced by the full die. The partial die can act as a backing plate underneath the workpiece to support the forming tool as assistance for critical parts during the forming process, as shown in **Figure 2-2**(b). Compared with the full die, the partial die can be made to assist the forming tool to achieve higher formability but relative lower geometric accuracy.

The TPIF process has advantages in providing high geometric accuracy products, and the die can be made of wood or foam, according to the nature of the process, to reduce the cost [13]. According to the studies by Mostafanezhad et al. [14] and Attanasio et al. [15], tool path optimisation can improve the geometric accuracy, and the surface quality can be enhanced by optimising the wall angle and forming force. Studies show that the future improvement of TPIF is limited as the addition of die supports has constrained the flexibility of the ISF process where the die limits the formability; heating sources can only be applied to the whole workpiece to avoid affecting the die support. The process is applicable for low-strength alloys, such as aluminium, magnesium and polymers, which able to provide high geometric accuracy forming with relative low formability.

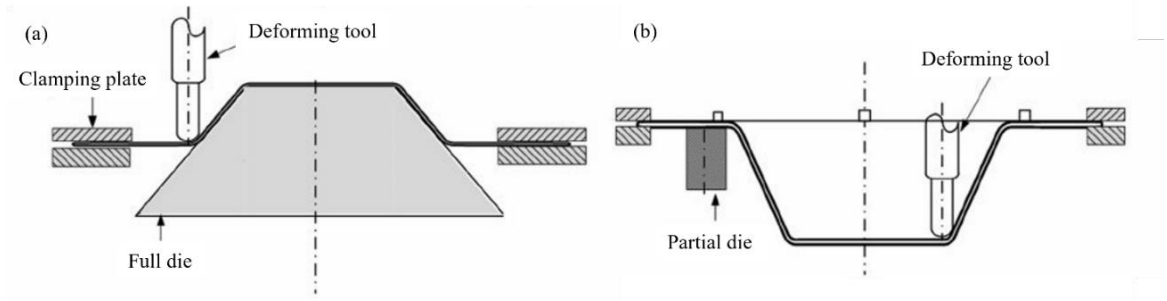

Figure 2-2. Working mechanism of TPIF, (a) TPIF with full die, (b) TPIF with partial die [9].

2.2.3. Single point incremental forming

SPIF is a die-less ISF process which provides maximum flexibility in the sheet metal forming category. As shown in **Figure 2-3**, the workpiece is clamped by the edges rigidly without any supporting dies underneath and only has one applicable deforming tool for complex forming shapes.

Compared with IFCT and TPIF processes, SPIF shows a significant improvement in formability as the nature of the die-less forming process provides maximum flexibility for the forming tool movements. The process is applicable for metal alloy and polymer sheets and the tool path can be generated from the computer-aided design (CAD), which shows its suitability for the majority of complex forming shapes. For instance, the studies [16, 17] investigated the improvement in formability and geometric accuracy for low-strength alloy sheets (aluminium, magnesium, copper). Other studies [18-21] also applied the forming process on polymers (polyvinyl chloride (PVC), polypropylene (PP), polyoxymethylene, polyethylene (PE), polyamide (PA), polycarbonate (PC) and polyethylene terephthalate (PET)) by modifying the tool path and tool design to achieve high formability with reduced fracture risk. The common SPIF forming shapes have been presented in **Figure 2-4** [22]. According to Panjwani et al. [23] and Sousa [24], the formability of SPIF is expandable to both axisymmetric and non-axisymmetric forming shapes with high geometric accuracy.

Although SPIF can successfully deform low-strength materials since low forming force is needed, the current challenge revolves around integrating the heating source on high-temperature materials, such as titanium, nickel or steel, to increase the ductility of material sheets. The previous study by Lu et al. [25] investigated tool-rotation induced vibration heating to the AZ31magnesium sheets, the tool-surface friction induced localised heating successfully generated localised heating to the workpiece and increased the ductility of material. Another

study by Al-Obaidi et al. [26] investigated the electric-assisted SPIF on high-strength steel sheets which presented localised heating to the workpiece which successfully reduced the forming force and achieved better formability. Göttmann et al. [27] investigated the laser heating-assisted SPIF on Ti-6Al-4V which revealed high-precision localised heating to the workpiece and relatively constant heating temperature to provide high geometric accuracy. However, the findings also indicate incredible springback, pronounced wear tracks on the surface and uneven thickness distribution. To overcome the limitations, previous research [28, 29] proposed ball-roller tools and multi-axis fixtures to produce a pronounced friction reduction during the process and enable a significant increase in wall angle to improve the formability. The studies [30-33] proposed mathematical methods to compensate the tool path and studies [34-37] applied artificial neural networks to study and improve the tool path plan to reduce the error from springback and prediction of temperature distribution during the process.

Although significant improvements have achieved in these studies, the equipment for heating sources is expensive and requires external safety measurements. The pronounced wear tracks and springback caused by the heating source are not fully solved. Thus, future improvements are required in this field to improve the geometric accuracy, surface quality, formability and a reduction in production cost.

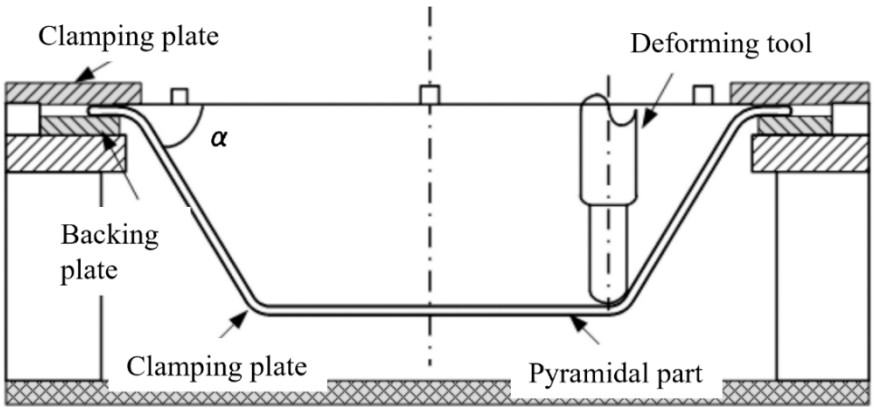

Figure 2-3. Working mechanism of SPIF process [9].

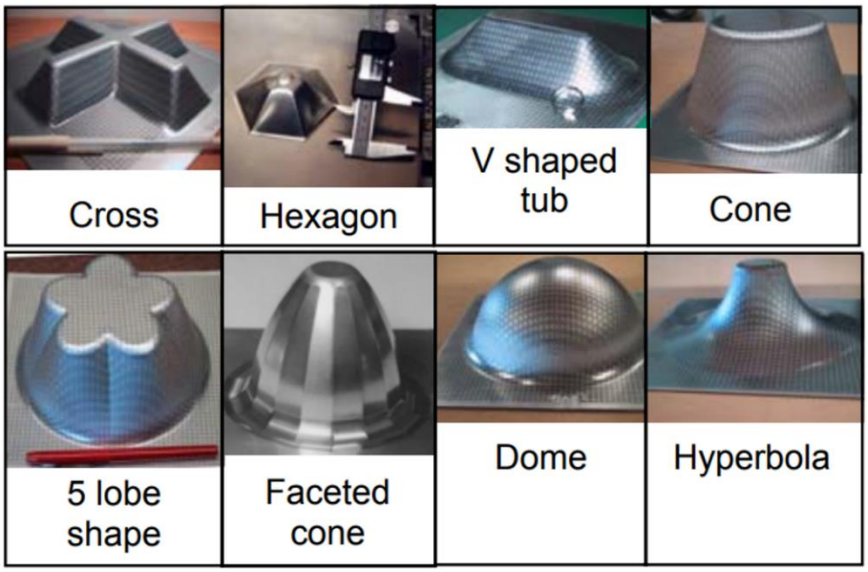

Figure 2-4. SPIF forming shapes [22].

2.3. Heat-assisted single point incremental forming

To increase the formability and geometric accuracy of conventional SPIF process for high-strength materials, heating sources represents a critical step to reduce the high forming force during the process. The commonly used heating sources in SPIF processes can be divided into five categories: friction stir, ultrasonic vibration, electric heating, laser heating and induction heating methods. Each heating method indicates advantages and limitations in the forming process and considerable future improvements.

2.3.1. Friction stir assisted single point incremental forming

Friction stir-assisted single point incremental forming (FSSPIF) constitutes a simple heat-assisted SPIF process where the localised temperature can be applied to the workpiece at the deformation zone between the rapid tool movement and contact workpiece. Giuseppina et al. [38] experimentally and numerically studied the temperature by friction during the FSSPIF and the parameter effects on the temperature distribution on the sheet material, which proved that the generated temperature is able to deform Titanium alloys. However, a pronounced wear was

detected on the deformed surface. Liu [39] applied FSSPIF to perform on 1.5 mm AA7075-O sheets with different rotation tool speeds from 3000 rpm to 7000 rpm, which results in a temperature up to 140 ℃ to increase the ductility of materials and achieve a reduction in forming force to improve the formability.

However, this heating-assisted SPIF lacks stability and proves insufficient for high-strength materials. As shown in **Figure 2-5** [40], on the investigation of friction stir SPIF on 1 mm Ti-6Al-4V sheets, which resulted in pronounced geometric inaccuracy, cracks, wear marks and significant tool wear have been reported as a rotation of 2000 rpm – 3000 rpm with a temperature range from 400 ℃ – 460 ℃. Ambrogio and Gagliardi [41] applied a rotation speed of 5000 rpm to Ti-6Al-4V sheets, which achieved a temperature up to 600 ℃. However, the generated temperature cannot be maintained constantly, resulting in unpredictable springback and reduced surface quality. This result indicates that FSSPIF is not reliable to produce high accuracy and surface quality products for high-strength materials due to its non-constant temperature increase.

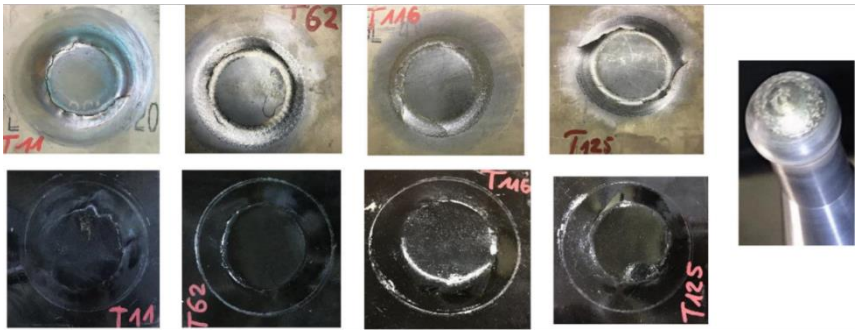

Figure 2-5. Results obtained from the friction stir SPIF of Ti-6Al-4V sheets [40].

2.3.2. Ultrasonic vibration single point incremental forming

Ultrasonic vibration single point incremental forming (UVSPIF) has developed from the UV stamping, drawing, drilling, extrusion and hydroforming operations of metal alloys and

polymers [42-47] to enhance the forming limits by applying vibrated-localised deformation to the forming tool. The standard UVSPIF process is illustrated in **Figure 2-6**(a) [48] and the measured forming force reduction is illustrated in **Figure 2-6**(b) [48]. It can be noticed that the average forming force was reduced around 500 N during UVSPIF of pure titanium bimetal sheet. Baghlani et al. [44] successfully applied a high-frequency vibration feed rate in the drilling process to increase the rotational speed of the tool and the temperature can be transferred to the workpiece by contacting, the results indicated a strong reduction in forming force during the process of Inconel 738LC superalloy. Cheng et al. [49] applied UV to deform Al 7075 alloy sheets in the SPIF and TPIF processes at 20 kHz oscillating frequency. The study commented that a significant reduction of applied forming forces during both processes which successfully increased the ductility of the materials and improved the formability accordingly. Due to the energy transfer to membrane vibration, the magnitude of force reduction in SPIF proves relatively lower than TPIF. Bai et al. [50] applied static pressure support in UVSPIF to study the forming force's relevance to the static pressure. By increasing the frequency to approximately 30 kHz, the pressure produces a sufficient grain size reduction of the 1 mm AL1060 sheets to increase the material ductility. The study by Sun et al. [51] proposed that the UVSPIF process could reduce the springback and waviness feature to improve the geometric accuracy and surface quality to improve 2 mm AA-5052 sheets compared with the conventional SPIF process. Cheng et al. [52] commented that the forming force of UVSPIF of AA1050-O alloy sheets can be reduced by 66.7% using a 10μm vibration amplitude.

Recently, Sakhtemanian et al. [48] studied UVSPIF on low carbon steel/commercially pure titanium bimetal alloy sheets. The findings show that the localised temperature reached approximately 250 ℃ and a reduction of forming force from 500 to 1000 N. Further, the study detected a DRX process and followed flow stress decrease. The phenomenon indicates further improvements in formability if higher temperature can be applied. However, the study also

proposed that the temperature induced by UV is unstable which results in uncontrollable forming force. The unstable temperature induced insufficient microstructure evolution and unpredictable straining effects which may results in high risk of crack especially for high-strength materials.

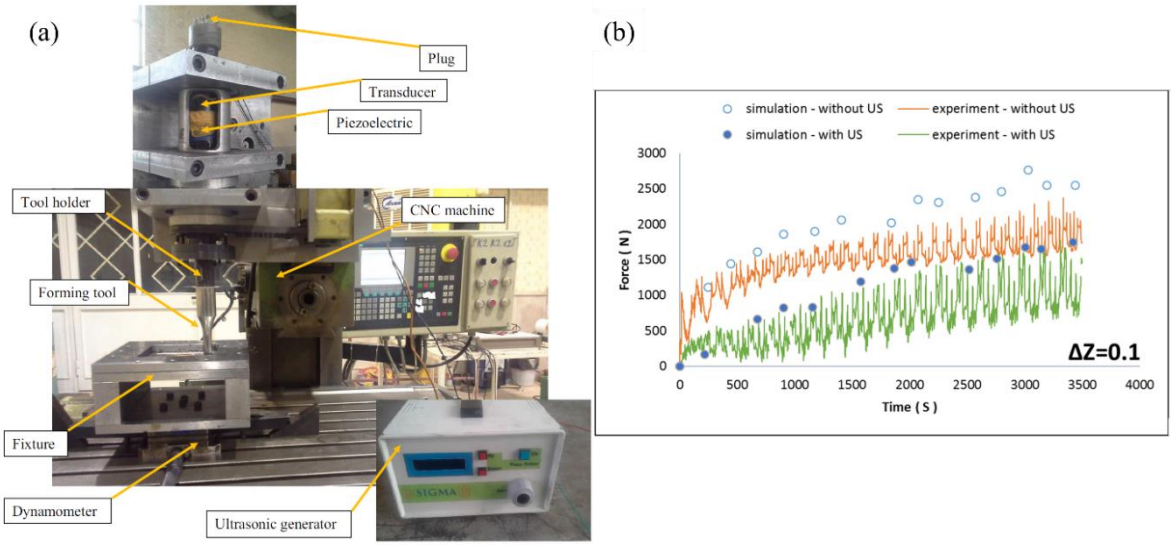

Figure 2-6. UVSPIF process, (a) illustration of UVSPIF, (b) measured forming force from the UVSPIF process [48].

2.3.3. Electric heating assisted single point forming

To further increase the temperature for heat-assisted SPIF systems for high-strength materials, the studies [54-56] established analytical models to investigate the heating and deformation mechanism for the electric heating-assisted SPIF process. Meier and Magnus [57] and Möllensiep et al. [10] developed direct current (DC) to the robotic arm-controlled tools to direct a temperature of 600 ℃ to the steel metal sheets. The study reported a significant reduction in the forming force to approximately 2000 N to produce the flexible and accurate forming shape for 1mm DC04 steel. Other studies [53, 58, 59] investigated the electric-heating SPIF of Ti-6Al-4V sheets by introducing a DC power to the interface of the Ti-6Al-4V sheet and tool to form a simple DC closed circuit, as shown in **Figure 2-7**. According to Joule's law, a flowing

DC current from tool to workpiece generates heat and raises temperature and flux through the area. To ensure the safety, tool and workpiece are insulated to allow a restricted are for flux flow. The electric heating of Ti-6Al-4V sheets for various target temperatures produces different results. For instance, Fan et al. [6] achieved a relatively stable temperature distribution at 500 ℃. The obtained surface quality result, shown in **Figure 2-8**(a), reveals a significant Joule heat effect on the inner surface of the workpiece. Another study by Ao et al. [60] increased the temperature to 820 ℃ using a high-power generator to provide large energy to Ti-6Al-4V sheets. However, the formed shapes were not optimal, as shown in **Figure 2-8**(b), large cracks, pronounced springback and burning holes were detected. This result can be attributed to the unstable temperature distribution and friction along the process, which produced electric sparks at tool-workpiece contact area and induced unpredictable deformation along the tool path of the workpiece. Vahdani et al. [59] maintained the forming temperature at 690 ℃, which successfully achieved a wall angle of 60° and reached a base depth of 58 mm, as shown in **Figure 2-8**(c). Vahdani et al. [61] induced a temperature of 750 ℃ to Ti-6Al-4V, AA6061 aluminium, and DC01 steel sheets, which also revealed a pronounced Joule heating effect on the formed shapes and large cracks appeared, which indicated such an effect's proportionality to the temperature: the higher temperature induces greater Joule heating effect.

In summary, electric heating-assisted SPIF represents an acceptable method to process high-temperature alloy sheets, which can produce high formability. However, the flux of current induces the temperature on the whole workpiece and temperature is not maintained constantly between the contact area under the forming tool and other areas of the workpiece. Further, the flux of current also induces a significant Joule heating effect according to the temperature, resulting in noticeable springback, cracks, wear tracks and oxidations. Thus, a constant high-temperature localised heating method is required to heat the contact area between the forming

tool and workpiece.

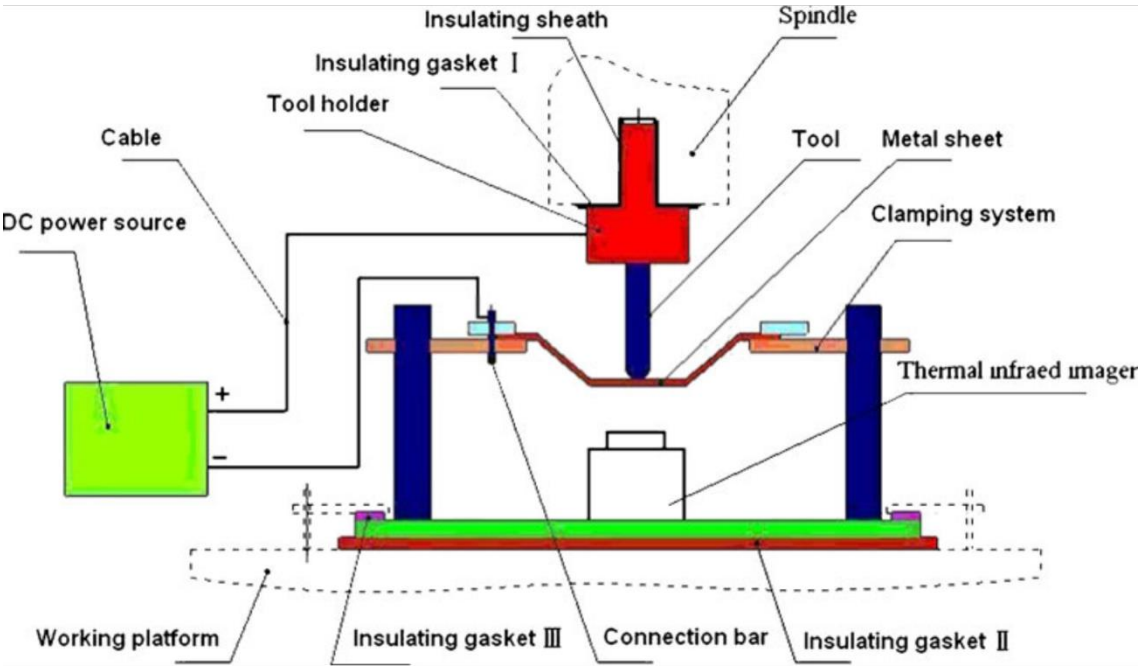

Figure 2-7. Working mechanism of electric-heating SPIF system [53].

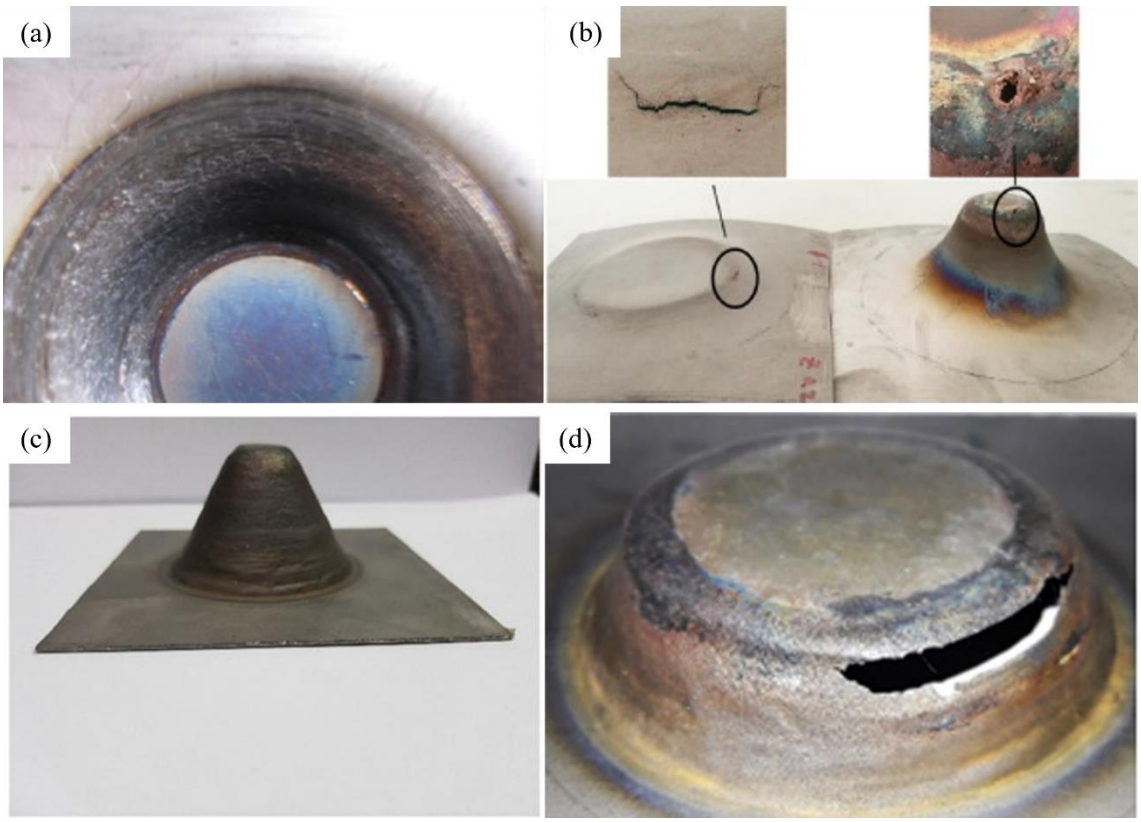

Figure 2-8. Obtained surface quality results, (a) Joule heating effect on inter-surface [6], (b) cracks on outer-surface [60], (c) outer-surface [59], (d) cracks on outer-surface [61].

2.3.4. Laser heating assisted single point incremental forming

In order to provide precise and localised elevated temperature to the predefined tool path in hot SPIF operations. Duflou et al. [62] proposed laser heating to provide accurate and localised elevated temperature to the predefined tool path in hot SPIF operations and deform 1.25 mm Al 5182 sheet metals. By adjusting the power of the beam to 500 W, the temperature can remain constant up to 350 ℃. Compared with the room temperature SPIF, the forming force was reduced from 1400 N to 700 N, and the forming angle increased from 32° to 56°. However, the relative lower temperature did not reduce the springback during the process, and heating on the surface reduced the surface quality. Lehtinen et al. [63] studied laser heating SPIF on 0.75 mm DC04 steel using a 1 kW fibre laser. Although the study investigated laser heating on high-strength sheet metal, the surface quality could not compare with that produced under room temperature, as shown in **Figure 2-9**(a-b), where pronounced heating wear and minor-cracks appeared on the surface with heating **Figure 2-9**(b) and the room temperature product **Figure 2-9**(a) provided a smooth surface without noticeable wear and cracks.

Göttmann et al. [7] proposed a high-power (10 kW) fibre laser heating-assisted SPIF system and developed in the study by Göttmann et al. [27] for 1.5 mm Ti-6Al-4V sheets, as shown in **Figure 2-10**(a, b) where the laser spot system has been attached to the tool to allow a sync movement. The laser heating system uses beam shaping optics and displacement to direct the laser beam to the advanced area of the tool to provide rapid heating. The temperature can be maintained at 400 ℃ to provide localised heating on the workpiece surface. However, the obtained surface quality does not reach the required levels. The laser beam heating dissipates the lubricant rapidly in advance of the tool, thus resulting in a large area of scratches between

the surface and tool. Findings also show that the material's particles have produced from the surface and left a large volume of the wear debris on the surface, as shown in **Figure 2-11**(a). Removing the coating from the tool due to the high-temperature results in a high adhesion of lubricant and wear debris to the tool, which may affect the geometric accuracy and surface quality.

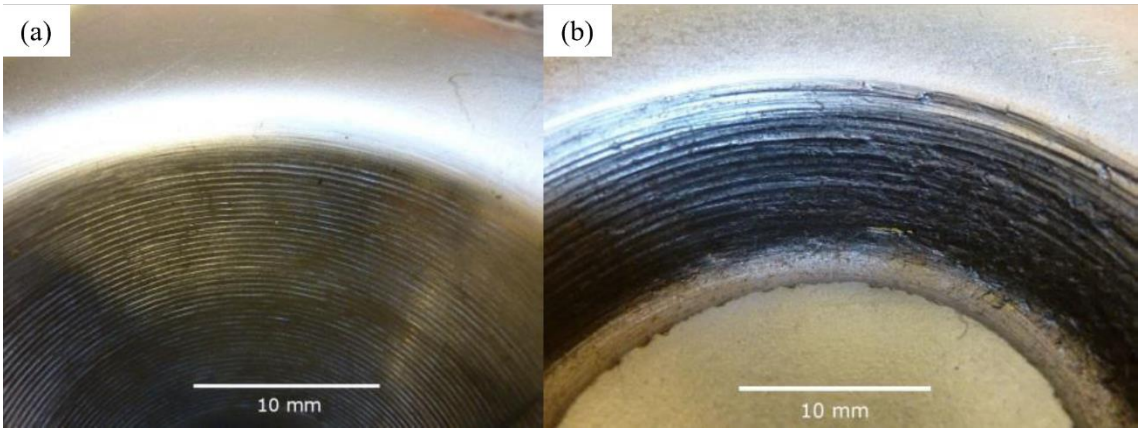

Figure 2-9. Surface quality of final formed workpiece, (a) without heating, (b) with heating [63].

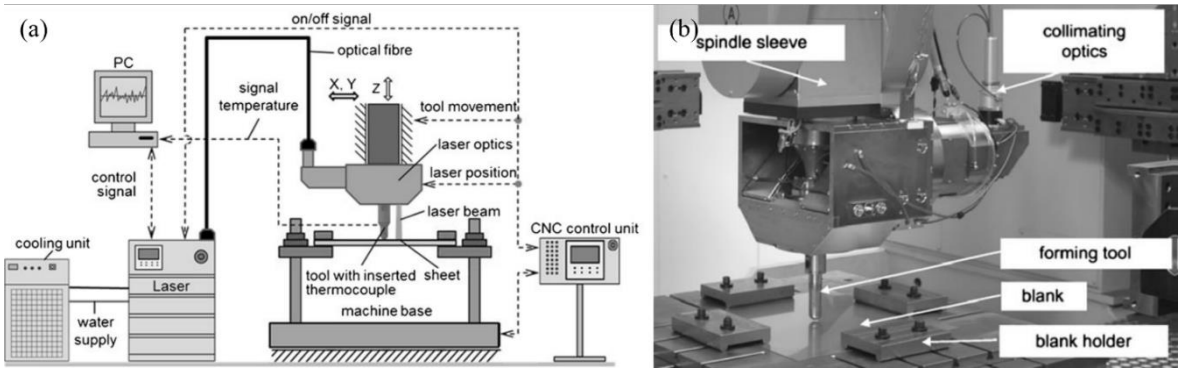

Figure 2-10. Laser heating SPIF system, (a) working mechanism, [7] (b) experimental setup. [27]

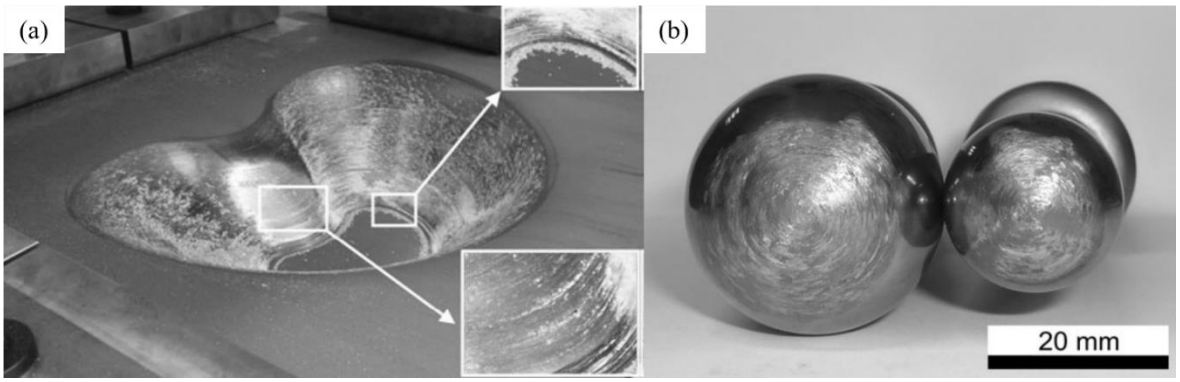

Figure 2-11. Surface quality and tool wear (a) wear debris on formed workpiece, (b) tool wear on different tool tip diameter [27].

2.3.5. Induction heating assisted single point incremental forming

Compared with the discussed heating methods in previous sections, induction heating-assisted SPIF can provide high temperatures and localised heating to the workpiece with relatively low-cost equipment and higher surface quality. Al-Obaidi et al. [26] proposed a tool-heater synchronised induction heating-assisted SPIF system, as shown in **Figure 2-12**. The induction heating coil is positioned underneath the workpiece and connected to the mounting of as the forming tool to synchronise movements. The study investigated the forming process for 1.6 mm DP 980 steel dual-phase metal sheets. Wall angles of 45°, 55° and 60° underwent testing at temperatures of 785 ℃, 790 ℃ and 800 ℃ with a tolerance of 30 ℃. The obtained results indicate a dramatic improvement in geometric accuracy compared with that achieved under the room temperature, which cannot produce a complete forming shape. The study also observed the improved geometric accuracy at the region with constant induction power, where higher power indicated a higher reduction in springback. Such a situation means higher temperature reduces more forming forces and results in better ductility to achieve higher geometric accuracy. Al-Obaidi et al. [64] further investigated the induction heating-assisted SPIF on 1.2 mm HCT 980C steel to achieve a wall angle of 70°. The results reveal that the forming forces

can decrease by 66.63% using 5 kW power to provide localised heating at 750 ℃ to the workpiece.

Ambrogio et al. [4] proposed an induction heating SPIF process on 1 mm Ti-6Al-4V sheets for 600 ℃ and 700 ℃ with an additional cooling system. A tank of liquid nitrogen had been prepared to spray the tool-surface contact area at different phases of the process. According to the results, the cooling process significantly improved the geometric accuracy**.** Compared with friction and electric heating-assisted SPIF, induction heating reserves less safety measurements and applicable to integrate with external features to improve the process quality. Such heating method able to provide a localised heating to the tool-workpiece contact area to increase the geometric accuracy and reduce the lubricant dissipation on the surface, as shown in **Figure 2-13**.

The induction heater has a relatively lower cost and simple setup compared with the previously discussed heating-assisted SPIF systems and the product quality is better achieved. The localised and accurate heating results in improved geometric accuracy and formability. However, the surface quality can be further improved. As shown in **Figure 2-14**, by applying same MoS_2 lubricant and closed heating temperature on Ti-6Al-4V sheets, the electric-heating assisted SPIF product [61] revealed pronounced wear and cracks on the formed surface, and the induction-heating SPIF product [65] produced better surface quality. The study by induction heating commented that the lubricant dissipation is according to the temperature, while higher temperature (around 700 ℃) significantly increased dissipation from early stage of the process. To reduce such effects, Li et al. [66] applied a water-cooling channel tool to assist a flow of liquid lubricant to reduce the temperature at tool-surface contact area. Such an approach is adjustable and able to produce stable heating temperature throughout the process to induce equiaxed microstructural evolution and maintain a constant DRX process.

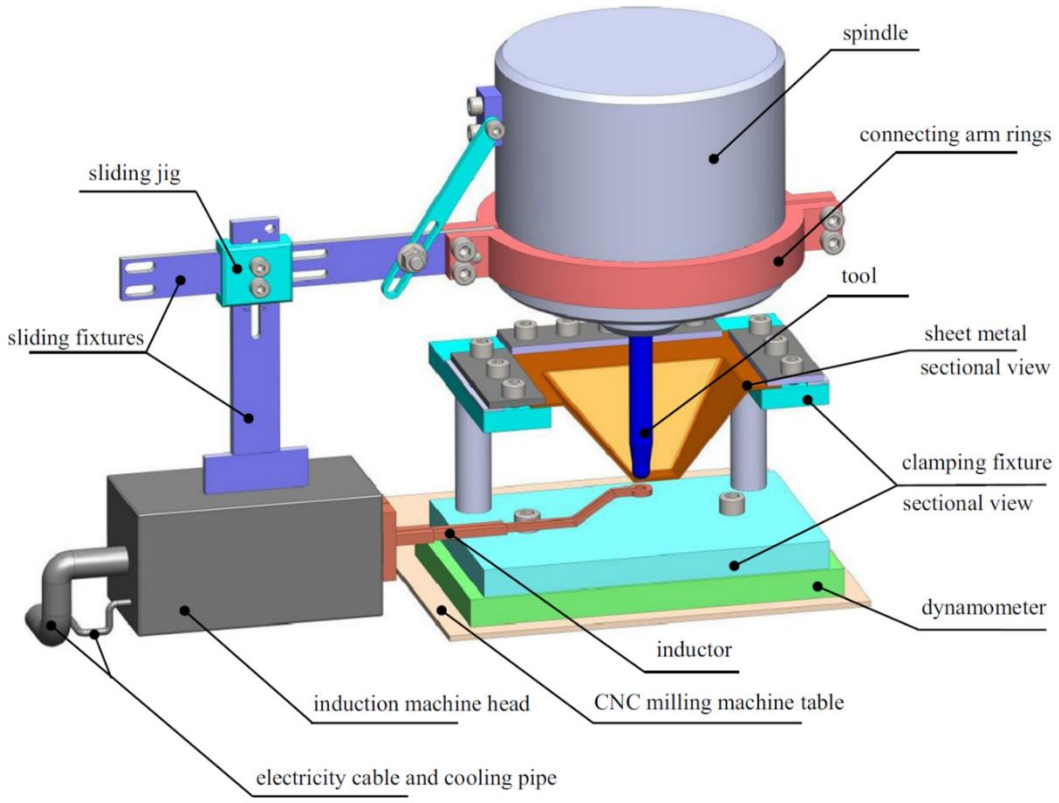

Figure 2-12. Working mechanism of induction heating assisted SPIF system [67].

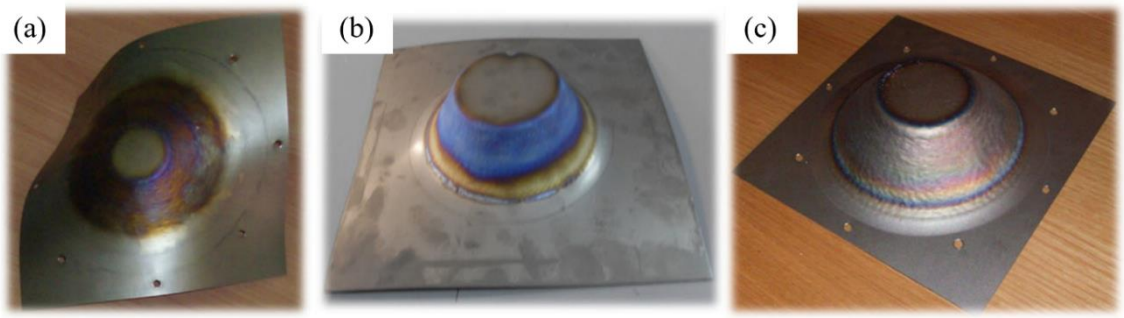

Figure 2-13. Geometric accuracy analysis, (a) room temperature, (b) electric heating, (c) induction heating with cooling [4].

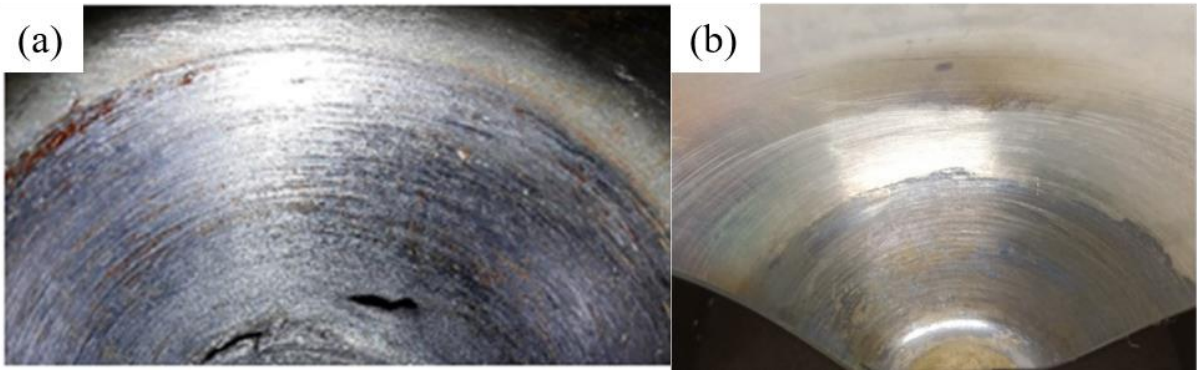

Figure 2-14. Comparison of surface quality, (a) electric-heating assisted SPIF [61], (b) induction-heating assisted SPIF [65].

2.3.6. Summary of heat-assisted single point incremental sheet process

Heat-assisted SPIF processes have significantly improved the deformation of high-strength materials. However, due to the regional or localised heating methods, numerous issues require addressing, including temperature dominant stress-strain effects on the formability and geometric accuracy, wear debris and lubricant dissipation effects on the surface quality, constant and accurate heating temperature to the workpiece and the need to design efficient tools to reduce the friction at the contacting area. **Table 2-1** presents the details of heating methods and relevant findings from each heat-assisted SPIF process.

Table 2-1. Summary and details of different heat-assisted SPIF processes

Heating Methods	**Materials**	**Advantages**	**Limitations**	**Refs.**
Friction stir	AA7075-O, Ti-6AL-4V	-Low cost. -Localised heating by friction. -Efficient for low-strength materials. -Temperature up to 600 ℃.	- Passive heating method. - Temperature is uncontrollable. - Not efficient for high-strength materials. - Not efficient enough to sufficiently reduce forming force. - Significant springback and unfavourable surface quality for high-strength materials.	Liu [39], Grün et al. [40], Ambrogio and Gagliardi [41]
Ultrasonic vibration	INCONEL 738LC, AL 7075,	- Low cost.	- Passive heating method. - Temperature is uncontrollable.	Baghlani et al. [44], Cheng et

	AL1060, AA-5052, AA1050-O, low carbon steel/commercially pure titanium bimetal alloy.	- Localised heating by ultrasonic vibration. - Efficient for low-strength materials. - Temperature can be reached at 250 ℃.	- Not efficient for high-strength materials. - Not sufficiently efficient to reduce forming force. - Significant springback and unfavourable surface quality for high-strength materials. - Low formability for high-strength materials.	al. [49], Bai et al. [50], Sun et al. [51], Cheng et al. [52], Sakhtemanian et al. [48]
Electric heating	DC 04 steel, Ti-6Al-4V	- Medium cost. - Active heating method. - Regional heating to the workpiece. - Temperature is controllable from 400 ℃ – 750 ℃.	- Temperature is uncontrollable above 800 ℃. - Large Joule heating effects. - Detectable springback and unfavourable surface quality. - High percentage of product failures.	Meier and Magnus [57], Fan et al. [6], Vahdani et al. [61], Ao et al. [60], Vahdani

		- Efficient for high-strength materials.		et al. [61], Möllensiep et al. [10]
Laser heating	Al 5182, DC 04 steel, Ti-6Al-4V	- Active heating method. - Localised heating. - Temperature is controllable from 350℃ – 400℃. - Sustainable and constant heating support. - High formability. - Efficient for high-strength materials.	- High cost. - Laser heating is not available for temperatures higher than 400℃. -Laser heating burns the surface and damages the surface quality. - Rapid dissipation of lubricant. - Complex experimental setup and safety measurements.	Duflou et al. [62], Lehtinen et al. [63], Göttmann et al. [27], Göttmann et al. [7]

		- Sufficient reduction in forming force.		
Induction heating	DC 04 steel, DP 980 steel, HCT 980C steel, Ti-6Al-4V	- Low cost. - Active heating method. - Localised heating. - Rapid and constant heat transfer. - No limitation of temperature. - Efficient for high-strength materials. - Sufficient reduction in forming force. - High formability.	- Uneven localised temperature support to the workpiece. - Rapid dissipation of lubricant. - Significant wear. - Detectable springback.	Al-Obaidi et al. [67], , Ambrogio et al. [4], Li et al. [65]

2.4. Tool design

The forming tool has critical effects on forming shapes, geometric accuracy and surface quality. The conventional tools have stable and sufficient performance for the SPIF process of low-strength materials. However, conventional tools unable to provide sufficient performance for high-strength materials, especially in the heat-assisted SPIF process. This section compares the conventional tools with ball-roller tools' performance in formability, geometric accuracy and surface quality.

2.4.1. Conventional tools

In the heat-assisted SPIF process for high-strength materials, the tools must take the pronounced thermomechanical deformation from the process, preventing the thermo-expansion from the temperature and adhesion of lubricant during the incremental steps. The conventional tools in SPIF have a hemisphere shape with a diameter from 5 mm to 20 mm, according to the experimental designs. **Figure 2-15** presents a series of tools designed in the hemisphere and flat shapes with different tooltip diameters according to the wall angle and step size. For heat-assisted SPIF operations, conventional tools did not provide high performance levels in terms of surface quality and geometric accuracy. **Figure 2-16** illustrates the investigation by Vahdani et al. [61] of the electric-heating assisted SPIF on Ti-6Al-4V sheets at 750 ℃. The outer shape presented an uneven geometry in forming thickness and pronounced wear, and abrasive adhesion of lubricant appeared on the inner workpiece and tool, which indicated the low functioning endurance of conventional tools during the heat-assisted SPIF. Kumar et al. [68] investigated the forming limits of conventional tools (hemisphere and flat), as shown in **Figure 2-17**(a, b), where R_1 has a tool diameter of 3.76 mm and R_2 has a tool diameter of 7.52 mm with a side diameter (tool corner) of 1.4 mm. The study found that the hemisphere tool achieved higher formability than flat tools as it increased the rounded surface reduces the contact to the

workpiece. The flat tool surface able to produce more accurate geometric, however, the tool corner is increased to reduce the formability. The size of tool is relevant to the geometric accuracy and formability, smaller tool size is applicable to take smaller step size which is essential to produce more accurate geometry and complicated shapes. However, the lower contact area increased the forming force which increased the risk of cracking in forming of high in-depth shapes.

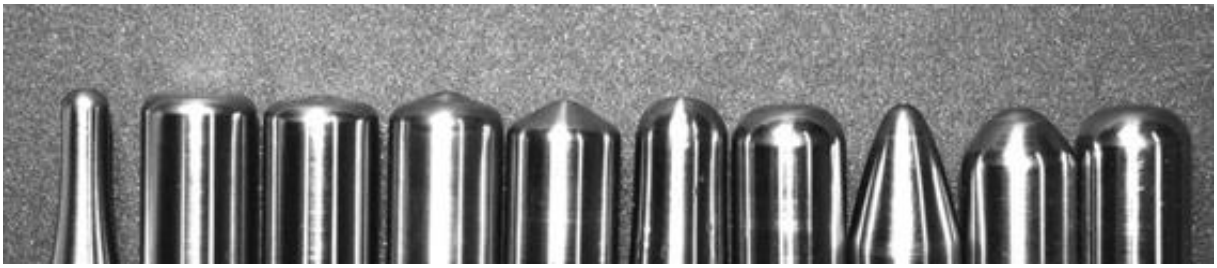

Figure 2-15. Different tool shapes and dimensions [69].

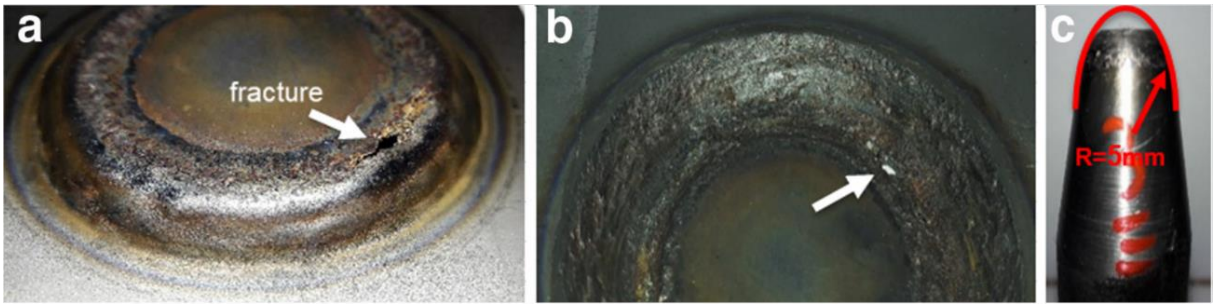

Figure 2-16. Electric-heating SPIF of Ti-6Al-4V, (a) outer surface, (b) inner surface, (c) tool tip wear [61].

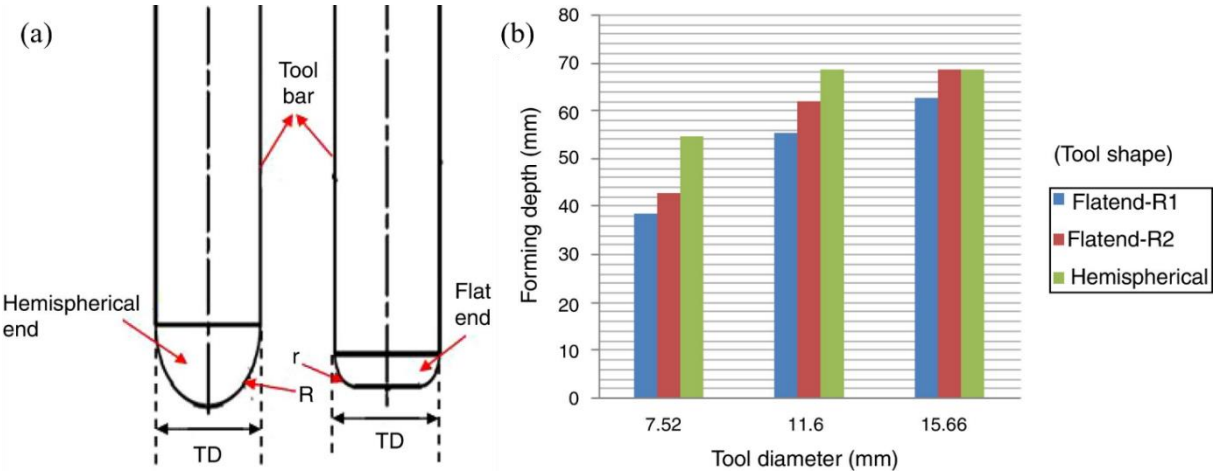

Figure 2-17. Conventional tool and effects, (a) tool shape and diameter, (b) Effect of tool diameter on forming depth [68].

2.4.2. Ball-roller tools

Recently, ball-rolling tools have been designed to reduce the friction between the tool and workpiece, as shown in **Figure 2-18**(a), produced by Iseki [70]. The plane-strain deformation model in **Figure 2-18**(b) reveals the approximation of strain distribution between the ball-roller tool and workpiece. The study proposed a relationship between the strain distribution by rolling-tool and the forming geometry according to the ball roller radius, wall angle and working depth. The proposed equations have been further validated in a study by Iseki and Naganawa [71]. The relationship can be expressed as:

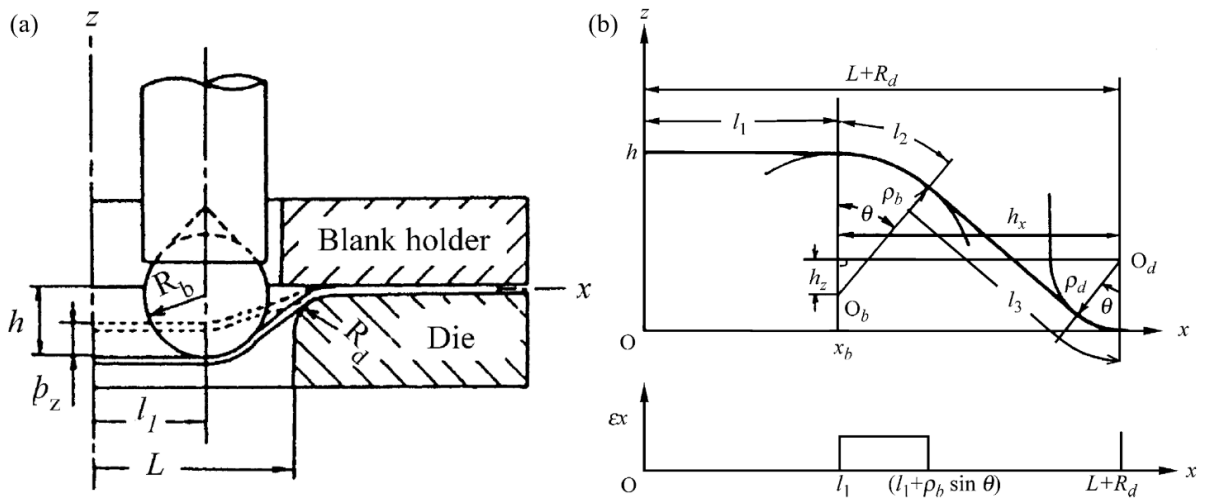

Figure 2-18. Ball-roller tool and working mechanism, (a) section view of the ball-roller tool, (b) plane-strain deformation of the ball-roller tool [70].

$$\theta = \sin^{-1}\left[\frac{\rho_\mathrm{b}+\rho_\mathrm{d}}{(h_x^2+h_z^2)^{1/2}}\right] - \tan^{-1}\left(\frac{h_z}{h_x}\right) \tag{2-1}$$

$$\rho_\mathrm{b} = R_\mathrm{b} + \frac{1}{2}t_0,\ \rho_\mathrm{d} = R_\mathrm{d} + \frac{1}{2}t_0 \tag{2-2}$$

$$h_x = L + R_\mathrm{d} - x_\mathrm{b},\ h_z = \rho_\mathrm{b} + \rho_\mathrm{d} - h \tag{2-3}$$

$$\ell_1 = x_\mathrm{b},\ \ell_2 = \rho_\mathrm{b}\theta \tag{2-4}$$

$$\ell_3 = h_x\cos\,\theta - h_z\sin\,\theta + \rho_\mathrm{d}\theta \tag{2-5}$$

where R_b denotes the ball radius, R_d denotes the die hole shoulder radius, θ denotes the contact angle, L denotes the die hole distance, h denotes the shell bulging height and x_b denotes the ball centre location. By applying the following contact rule, arc l_2, uniform strains: ε_x, ε_y, ε_t on the x-direction can be expressed as:

$$\varepsilon_x = -\varepsilon_t = \ln\left[\frac{\ell_2}{L + R_{\mathrm{d}} - \ell_1 - \ell_3}\right],\ \varepsilon_y = 0 \tag{2-6}$$

Kilani et al. [72] studied the ball-roller tools and proposed a response surface methodology (RSM) to predict the process parameters, including forming force, thinning thickness and surface roughness. The relationship can be expressed as:

$$\begin{aligned} Y = \quad & C_0 + C_1 D + C_2 \Delta Z + C_3 F + C_{11} D^2 + C_{22} \Delta Z^2 \\ & + C_{33} F^2 + C_{12} D \cdot \Delta Z + C_{13} D \cdot F + C_{23} \Delta Z . F + \varepsilon \end{aligned} \tag{2-7}$$

where Y denotes the predicted response, D denotes the ball-roller diameter, ΔZ denotes the step size, F denotes the feed rate, C_0 denotes the mean value of the response, C_1 to C_3 represent the linear coefficient, C_{11} to C_{13} represent the quadratic coefficient and C_{12} to C_{23} represent the double interaction coefficient. ε denotes the deviation between the observation and calculation.

Lu et al. [73] proposed a novel ball-roller tool design, as shown in **Figure 2-19**(a). The ball-roller was attached to the tool body and controlled by a 3-axis CNC machine with the roller always facing the workpiece. According to the study, a maximum 80° wall angle can be

achieved, and the designed tool able to apply the tool tip to the forming wall to reduce the friction on the forming surface and achieved excellent geometric accuracy.

Naranjo et al. [74] investigated the tribological characterisation for oven-heated SPIF of Ti-6Al-4V sheets at 200 ℃, 300 ℃ and 400 ℃ . The ball-roller is 10 mm in diameter, and all experiments were implemented without lubricant. The findings indicate that the adhesion of material increases with the rising temperature, which means a more pronounced rate of material adhesion at higher temperatures. The study also proposed that a tribo-layer can be observed as temperature increases due to heat diffusion.

To eliminate the adherence of material contamination and lubricant, Liu et al. [29] designed ball-rolling and wheel-rolling tool with inner water-cooling channel, as shown in **Figure 2-20**(a-b) where the hollow tool with a water hole can be connected to the water tap, which induces water to cool down the steel ball-roller. According to the study, the tool provided high performance levels in the electric heating-assisted SPIF process for Ti-6Al-4V at 500 ℃ .

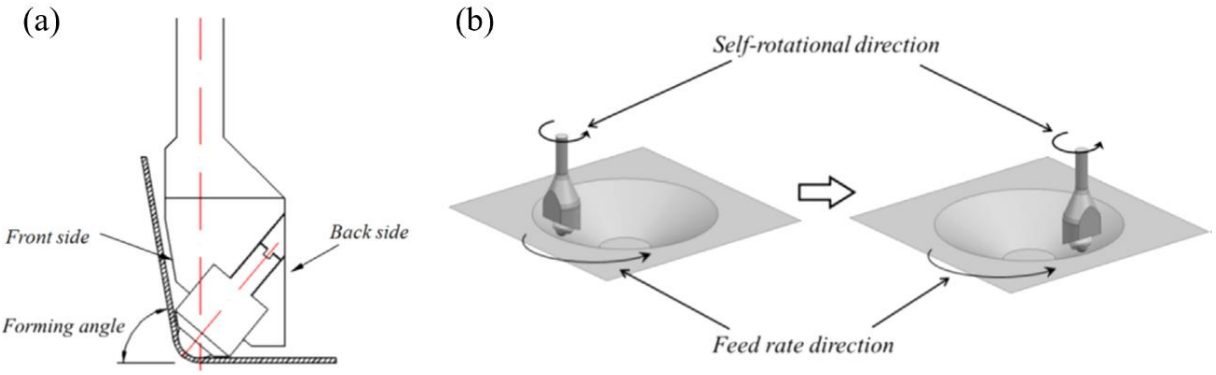

Figure 2-19. Ball-roller tool and working mechanism, (a) section view of ball-roller tool, (b) working mechanism in tool path [73].

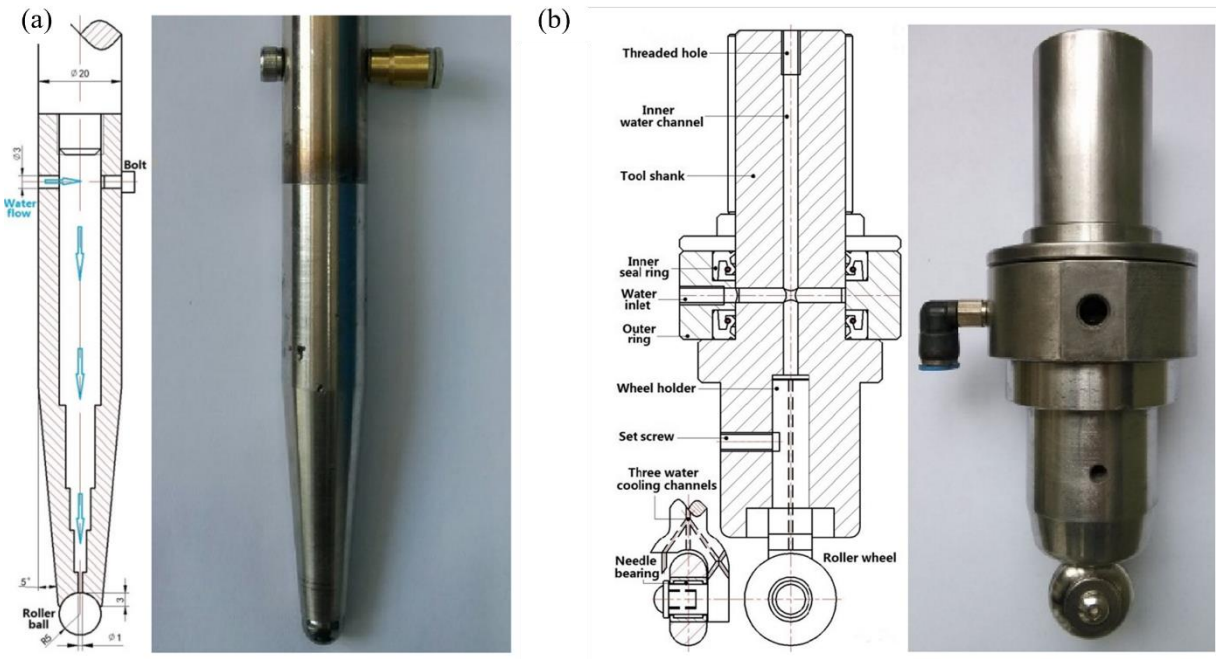

Figure 2-20. Water-cooling ball-roller tool design, (a) rolling-ball with water-cooling channel, (b) rolling-wheel tool with water-cooling channel [29].

2.4.3. Summary of tool design

The type, shape and tool diameter affect the formability, geometric accuracy and surface quality of forming shapes. The advantages and limitations of conventional tools and ball-roller tools for heat-assisted SPIF are presented in **Table 2-2**.

Table 2-2. Summary and details of different types of tools.

Tool type	Advantages	Limitations
Conventional tool	- Low cost. - Simple design.	- Extensive and significant adhesion of removal materials and lubricant. - Strong wear tracks.

	- Different cap shape and size can be made to match process parameters.	- Low formability. - High risk of cracking.
Ball-roller tool	- Low wear tracks. - Reduced contact area and rolling ball to reduce adhesion of materials and lubricants. - The water-cooling system can be integrated to reduce the thermo-expansion of the ball-roller. - Ball-rollers can be made of different materials to meet the thermomechanical strength for different sheet materials.	- Complex design. -High cost.

2.5. Tool path design

This section compares the effect of the contour and helical tool paths in the designs of forming shapes, geometric accuracy and surface quality. The tool path optimisation works, including compensation and machine learning models will be discussed.

2.5.1. Contour and helical tool path

The tool paths for ISF processes are predefined by CAD/CAM software and implemented by CNC machines. According to the product shape, the tool path can have axisymmetric or non-axisymmetric designs. The tool path can be designed as a contour (z-level) profile or helical

(spiral) profile, as shown in **Figure 2-21** [75]. The conventional tool path in **Figure 2-21**(a) is in a contour profile where an accumulated step change tool path to follow the tool motion to make steps according to the contour step. This tool path applies to any forming shapes, including axisymmetric or non-axisymmetric. However, the overlap of increment steps will leave a distinct mark on the deforming surface, as shown in **Figure 2-22**(a) [76]. The helical tool path in **Figure 2-21**(b) able to overcome the limitation. Such tool path was developed by Skjoedt et al. [77] and applied in the study by Attanasio et al. [15], the tool path uses an algorithm to produce a tool path to achieve the geometry without stopping for a step change. The algorithm can only produce an axisymmetric profile and the starting and ending positions cannot be fully completed as the algorithm unable to complete a full circle tool path. As the forming shape illustrated in **Figure 2-22**(b), the Helical tool path can provide high geometric accuracy and surface quality (no contour change); however, it is only limited to the axisymmetric forming shape due to its nature of mathematics calculation. The contour tool path is available for any shape, but the step change tool path affects the geometric accuracy and surface quality.

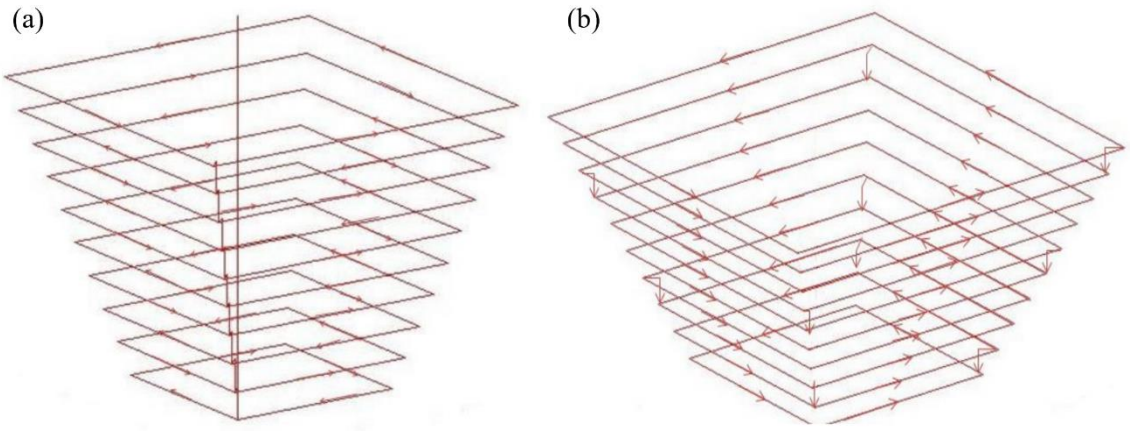

Figure 2-21. Tool path design, (a) contour (Z-level) profile, (b) helical (spiral) profile [75].

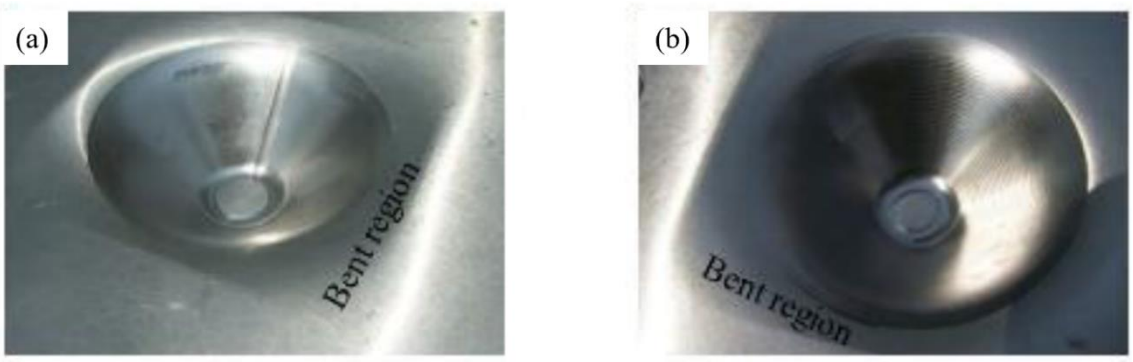

Figure 2-22. Products produced by different tool path profiles, (a) contour, (b) helical [76].

2.5.2. Compensation and RSM optimisation

The study by Azaouzi and Lebaal [78] created a response surface method (RSM) to optimise the tool path. According to the study, the original tool path was obtained from the FE modelling and optimised by combining the quadratic programming algorithm and surface response method, as shown in **Figure 2-23**. The parameter h and d represent the depth and diameter for the stage 1 tool path, and H and D represent the depth and diameter for the stage 2 tool path. H and D are constants to form designed forming shape, and h and d are design variables to optimise the tool path. The optimised tool path has been applied in simulation to predict the thickness distribution. The results show that the thickness at the maximum depth decreased by approximately 1 mm and the distribution approaches constant which reduced the tool motion fluctuations. The tool is more fit with low-fluctuated thickness distribution where the risk of crack is reduced and the surface quality is increased, the geometric accuracy is also improved according to optimised tool path. Behera et al. [79] investigated a multivariate adaptive regression spline (MARS) non-parametric regression analysis to compensate for the tool path inaccuracies of the SPIF process. The study commented that the obtained geometric issues can be captured by graphs, and the framework may study the topological conceptual graphs to predict the optimal tool path. Other studies by [30, 80-84] implemented algorithms to correct the tool path depending on the process parameters to improve the geometric accuracy.

Observations have revealed that the tool path correction and compensation is based on the number of parameters affecting the accuracy. The tool path optimisation is efficient in single parameter calculation and becomes less efficient in calculating the multi-parameters system.

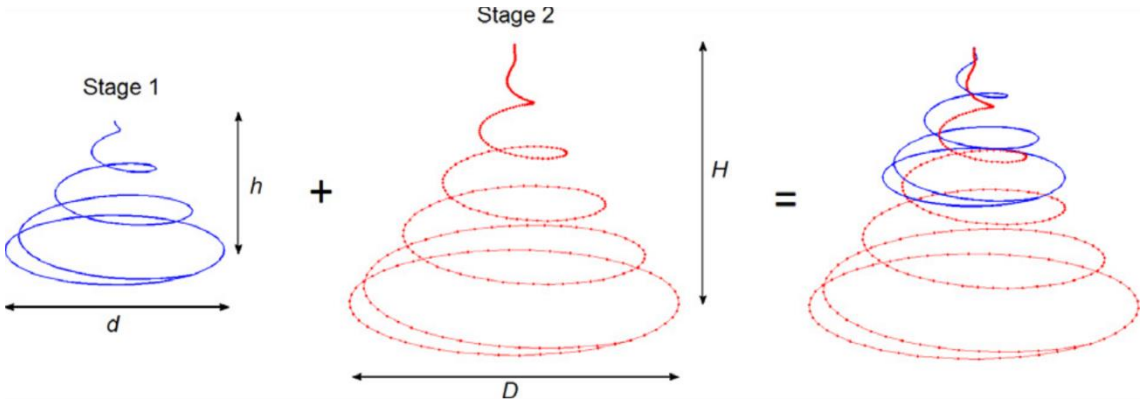

Figure 2-23. Tool path optimisation [78].

2.5.3. ANN optimisation and image network analysis

Due to improvements in computing technology, machine learning has been applied in optimising tool paths to improve geometric accuracy. For instance, Liu et al. [34] and Akrichi et al. [85] applied the deep learning artificial neural networks (ANN) model to predict the forming parameters, including the construction of tool path plan, calculation of roundness and positioning deviation for each increment step. The ANN tool path optimisation is shown in **Figure 2-24**. The promising results have shown the framework's suitability for complex sheet metal forming to optimise the tool path planning. Jiang et al. [37] proposed the ANN framework's use in electric heating SPIF systems to study the measured temperature and forming force and apply neurons and predict the outcome according to the process parameters. The predicted values can be further used in microstructural revolution, which provides clear evidence that machine learning is applicable in heat-assisted SPIF systems to enhance the process parameters. Further, Behera et al. [82] proposed an image network analysis with the integration of topological conceptual graphs on the critical stages during the process. The

outcomes will be studied and optimised by analysing algorithm to compensate the error from the tool path. Further, an optimised tool path will be created to improve the geometric accuracy at critical area during the SPIF process. Similarly, Bautista-Monsalve et al. [86] investigated an image database to make training of different classification algorithms as learning approach to study the wear and cracks on the forming surface to predict the surface quality for heat-assisted SPIF for Ti-6Al-4V sheets. The image network is efficient for all ISF systems in capturing the forming effects, including the geometric coordinates, thickness distribution and surface quality to optimise the tool path plan, compensate the error from tool motion, wear and cracks according to the process. However, the performance depends on the efficiency of algorithm in analysing the visual effects, which requires high resolution image and wide range of capturing. The error percentage is relatively higher than ANN networks on optimisation of obtained parameters.

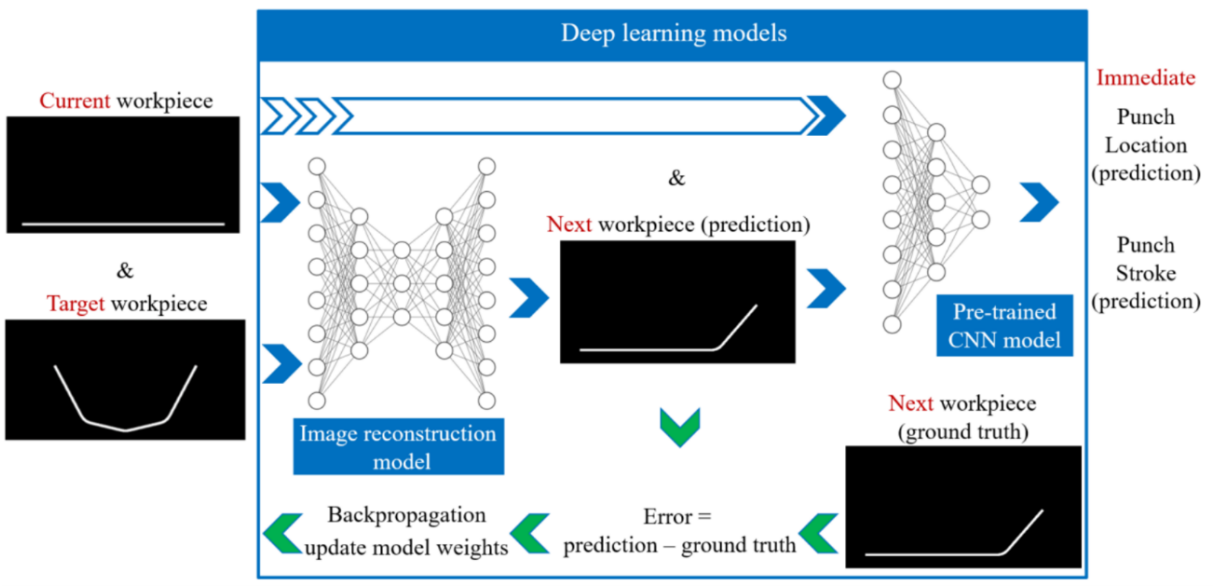

Figure 2-24. ANN optimisation process [34].

2.5.4. Summary of tool path design

The tool path for ISF operations is significant in producing accurate forming shapes. Process

parameters, including step size, feed rate, tool shape and diameter, will affect accuracy. To eliminate the limitations, the tool path can be optimised to compensate for the geometrical from the process parameters to improve the forming accuracy. **Table 2-3** shows the details of the tool design.

Table 2-3. Summary of tool path design

Tool path	**Advantages**	**Limitations**
Contour	- Applicable for all types of forming shapes. - High formability and complete finish of forming the design.	- The step change tool path will remain a distinct mark on the surface. - Relatively lower geometric accuracy and surface quality.
Helical	- High geometric accuracy and surface quality (non-contour steps).	- Only applicable for axisymmetric forming shapes. - Low formability and unable to complete the full forming shape (limited by algorithm).
Compensation and corrections	- Applicable for all types of tool paths. - High performance for single process parameters.	- Complex algorithm design. - Low efficiency for multi-process parameters.

RSM optimisation	- Aids study of explanatory and response variables to optimise the tool path.	- Requires proper design of experiments to achieve accurate results.
ANN optimisation	- Aids study of one or more response variables to optimise the process parameters. - User-friendly software control.	- Requires a high-performance computer to train multi-process parameters.
Image network analysis	- Using topological conceptual graphs to solve the critical issues. - All calculations are based on captured graphs, which reduces the computing time.	- Complex algorithm design. - Only applicable for specific captured issues.

2.6. Lubricants and coating

Graphite grease, machine oil and MoS_2 paste/spray are common lubricants used in SPIF systems. For the heat-assisted SPIF process, the common lubricants remain unsuitable in terms of achieving high surface quality and geometric accuracy. In this section, different types (paste, spray, liquid) of lubricants will be compared to assess their effect on surface quality and geometric accuracy.

2.6.1. Lubricants and coatings in ISF work

Lubricant and coating are significant factors in affecting surface quality for ISF processes. The selection of lubricant or coating depends on the materials, process parameters and temperature.

For room temperature SPIF processes, the sheet materials affect the performance of lubricant and coating as the materials have different surface roughness and yield strength significantly affects the forming forces. The tool motion will be affected by high forming force and the performance of lubricant or coating will be reduced, which further cause geometric inaccuracy and cracks. For instance, Sornsuwit and Sittisakuljaroen [87] investigated the performance of MoS_2 on SUS 304 and SUS 316L stainless steels and Grade 2 titanium (Ti Gr2). The lubricant MoS_2 is a self-mixed paste of MoS_2 powder with petroleum jelly in a ratio of 4:1. The tool diameter is 10 mm, and all workpieces are all 1 mm thickness and have a feed rate of 3140 mm/min for all experiments. The surface quality for each material is shown in **Figure 2-25**, which shows that the lubricant performance deteriorates according to the yield strength of the materials; Ti Gr2 revealed the worst surface quality on the deforming surface. **Figure 2-26** reveals the formability and surface roughness. It can be observed that Ti Gr2 also revealed the worst formability and surface roughness distribution. However, MoS_2 still represents the best lubricant for Ti Gr2 sheets compared with other lubricants. Hussain et al. [88] proposed different mixing methods for MoS_2 and graphite powders to make different types of lubricants for SPIF for pure titanium sheets. The study designed three types of lubricants where lubricant one is the liquid type that mixes different percentages of MoS_2 and graphite powders in water, lubricant two is paste type which mixes MoS_2 in grease and lubricant three is spray type which mixes MoS_2 in alcohol and ketone. According to the results, the spray lubricant indicated an excessive adherence on the surface. The medium paste represents less adherence, and liquid lubricant indicates the lowest adherence and surface roughness, indicating that liquid MoS_2 is more favourable for titanium alloys as there is a low chance of adherence to the deforming surface. Diabb et al. [89] investigated the mixing of SiO_2 nanoparticles in vegetable oil, which revealed the suitability of less viscous liquid lubricant for SPIF processes. Other than the lubricant, Hussain and Al-Ghamdi [90] studied a plasma electrolytic oxidation (PEO) coating

comprising MoS_2 powder with electrolyte on workpieces for SPIF processes. The results revealed that the coating on forming surface indicated better performance than the MoS_2 paste with grease, thus representing a better method to improve the surface quality.

For the heat-assisted SPIF process for high-strength materials, the coating unable to work under elevated temperatures. The conventional lubricants in spray, paste or liquid will dissipate during the process [65, 91]. To improve the lubricating service, Li et al. [92] developed a mixture lubricant consists of WS_2 powder mixed with high-temperature lubricating oil which successfully reduced the lubricant adherence during 500 ℃ electric heating-assisted SPIF of Ti-6Al-4V sheets. Further, Liu et al. [29] developed a water-cooling system on the tool to cool down the ball-roller tool tip and Li et al. [66] improved the design to enable a flow of liquid MoS_2 to lubricate the forming surface and cool down the ball-roller tool tip together. This method able to provide sufficient lubricating to prevent the dissipation and reduce the thermal expansion of tool and contact surface continuously.

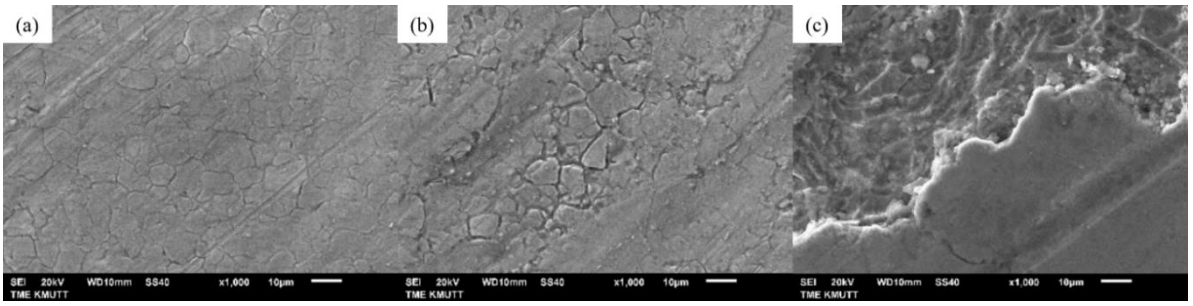

Figure 2-25. Surface quality on workpiece, (a) SUS 304, (b) SUS 316L, (c) Ti Gr2 [87].

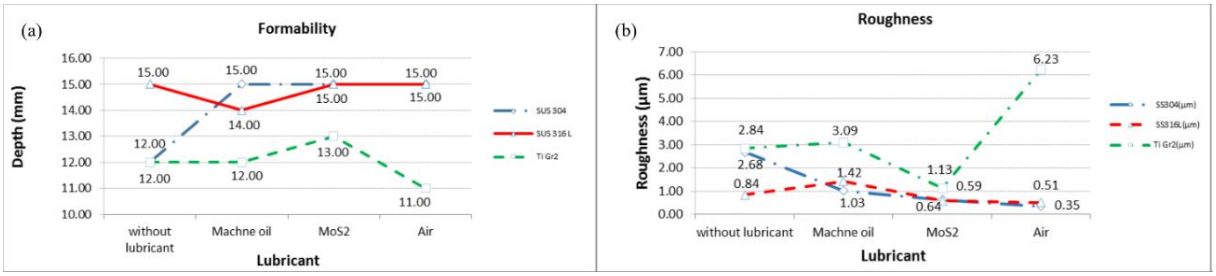

Figure 2-26. Formability and surface roughness, (a) formability, (b) surface roughness [87].

2.6.2. Summary of lubricants and coating

Among the series of lubricants, liquid MoS_2 performed well in ISF processes and this lubricant has been widely used in processing of high-strength alloys such as titanium and steel. The application of lubricant in heat-assisted SPIF process requires a constant existence throughout the process to prevent dissipation during the high-temperature process. The summary of lubricants and coatings are shown in **Table 2-4**.

Table 2-4. Details of lubricants and coating

Lubrication	**Advantages**	**Limitations**
Spray	- Easy application. - Efficient for low-strength materials. - Efficient for room temperature SPIF.	- Low efficiency for high-strength materials. - Not efficient for heat-assisted SPIF.
Paste	- Relatively low viscosity. - Fast dissipation in heat-assisted SPIF processes.	- Low efficiency for high-strength materials. - Not efficient for heat-assisted SPIF.
Liquid	- Lowest viscosity.	- Must work with a water-cooling system to provide sufficient and sustainable

	- High performance for high-strength materials. - High performance for heat-assisted SPIF with a water-cooling system.	lubrication to the heat-assisted SPIF process.
Coating	- High performance for high-strength materials.	- Burns-off and removal during heat-assisted SPIF.

2.7. Numerical analysis

This section compares different types of numerical analysis (implicit, explicit) in accurately predicting geometric accuracy, thickness distribution, forming force and temperature. Furthermore, the studies of microstructural FE analysis, including CPFEM, RVE and CA, undergo discussion in relation to accurately predicting the microstructure behaviour of SPIF or relevant metal forming processes.

2.7.1. FE modelling

To predict the mechanical behaviour during the SPIF process, numerical modelling has been established based on user-defined constitutive laws in literature to perform the FE simulation. Currently, commercial ABAQUS, LS-DYNA and ANSYS software provide user-defined processing and post-processing works.

For conventional FE modelling of SPIF works, the tool components are normally considered as a “rigid” body and the sheet materials are defined as “deformable”. The movement of the tool in the FE model aligns with the experimental SPIF process, which can be assigned to the path displacements and temperature conditions. The complex forming shape and step size may

increase a large number of discrete increments in the simulation. According to Silva and Martins [93], the tolerance setting in the CAM program determined the number of increment points. A tolerance of 0.01 mm resulted in approximately 400 increment points per metre for the hyperbolic cone and 8 points per metre (the sides are straight) for the pyramid in the FE simulation. Vertical step down was set equal to 0.5mm, and the coefficient of friction adopting Amonton–Coulomb's law was assumed to be zero ($\mu = 0$).

To solve a FE problem, certain calculating features and computation time require consideration before running the simulation. For instance, in ABAQUS standard simulation, two solver types, explicit and implicit, are provided to solve FE problems. In the explicit solver, the data output is calculated from the current state; calculation is straightforward and less computational time is needed for a single explicit increment. However, the solver type is not available for large time increments as the error will increase exponentially and destabilise the calculating method. In the implicit solver, the data output is calculated directly from the previous state, which is a coupled system requiring non-linear algorithms such as the Newton-Raphson method. The computational time and memory required to complete an implicit increment exceed that of an explicit solver because of the number of equations requiring a solution using this method.

In SPIF simulation, the explicit solver tends to consider material quasi-static behaviour to reduce the computational time rather than the implicit solver, which takes more computation time and has a higher risk of producing non-convergence results due to the complex behaviour on tool-workpiece contact. Durgun et al. [94] compared the explicit and implicit solvers in an ABAQUS simulation of SPIF processes. The workpiece has 7300 S4R shell elements and seven thickness elements. **Figure 2-27** shows the geometric and strain comparison between explicit, implicit and optical measurements. According to the findings, both solver types agree with the optical measurement and explicit solver, indicating a relatively better match than the implicit

solver. The study also found that the implicit solver has a larger computational time than the explicit solver. However, the explicit solver lacks efficiency for large time increments, as stated by Gupta and Jeswiet [95], which exponentially increased the computational time. The studies by [96-98] proposed that the kinetic energy (ALLKE) must be less than 10% of the maximum internal energy (ALLIE) in the explicit solver. Li et al. [65] investigated the explicit analysis of 600 ℃ and 700 ℃ induction heating-assisted SPIF processes for the Ti-6Al-4V using the C3D8T element. The study proposed a graph to indicate the error and the computational time difference between different mass scaling, as shown in **Figure 2-28**. Different mass scaling values revealed that lower mass scaling required more computational time, and the percentage of error decreased, as shown in **Figure 2-28**(b). Thus, the mass scaling requires controlling to provide higher accuracy and balance the computational time. Desalegn et al. [99] studied the SPIF on different dimensions of geometry and revealed that explicit analysis is more efficient for larger dimensions than small ones. Lora et al. [100] and Ambrogio et al. [101] proposed a combination method using explicit for SPIF operation and implicit for tool release (contact between tool and workpiece), which also saved computational time.

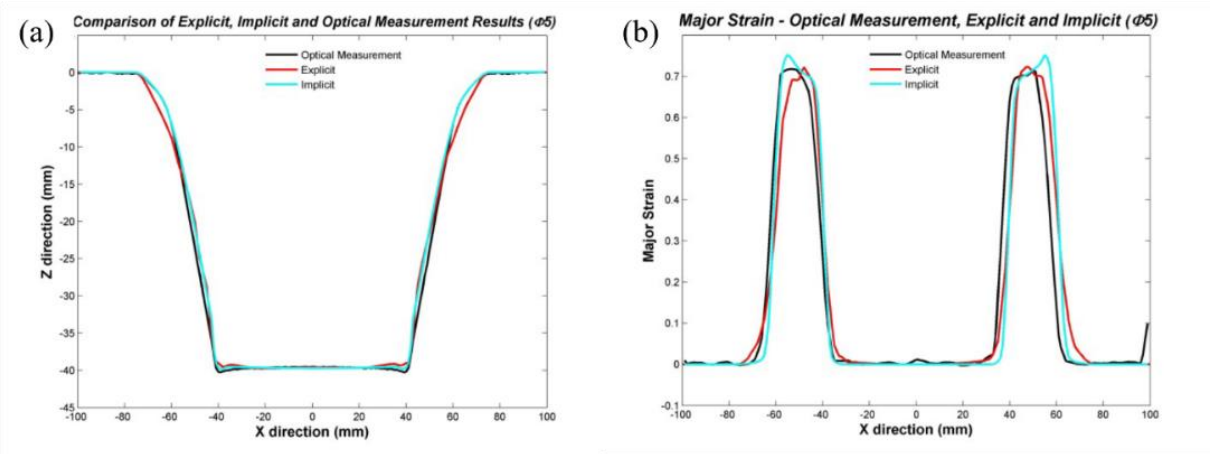

Figure 2-27. Geometric and strain comparison between explicit and implicit analysis, (a) geometric comparison, (b) strain comparison [94].

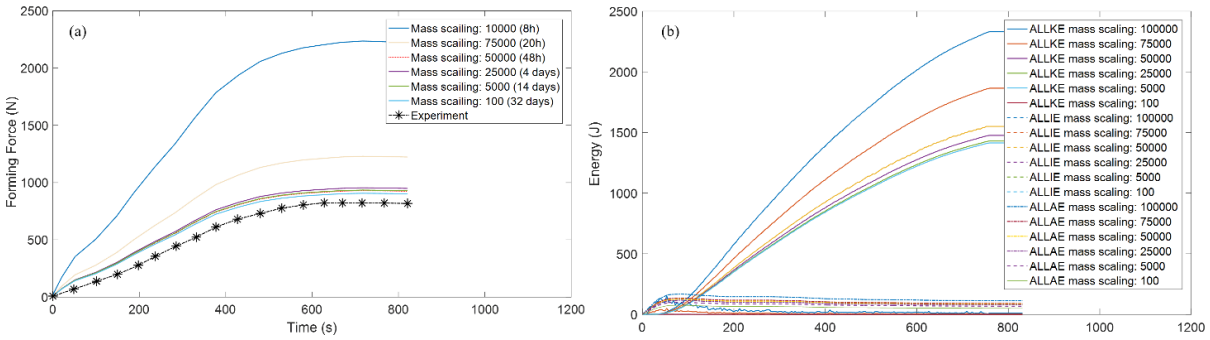

Figure 2-28. Effects from different mass scaling, (a) forming force, (b) energy history [65].

2.7.2. CPFEM, RVE and CA modelling

Rather than a macroscopic scale analysis of SPIF operations, mesoscopic and microscopic scale analysis can be presented by applying the crystal plasticity finite element method (CPFEM) to simulate the experimental scale or partial scale plasticity behaviour and representative volume element (RVE) to simulate the grain level strain-stress behaviour based on particular parts throughout the process. The studies [102, 103] combined CPFEM and RVE to simulate SPIF of 7075-O aluminium sheet by importing the plasticity properties from CPFEM and used the output results as inputs in the RVE model. Electron backscatter diffraction (EBSD) was used to obtain the grains orientation at critical parts of the workpiece and established RVE model using DREAM.3D software [104] to present the plasticity behaviour accurately. Han et al. [105] proposed two advanced anisotropic yield functions (Yld2000-2D, Yld2004-18p) to simulate the experimental deep drawing for 2090-T3 aluminium alloy sheets. The output results were compared with experiments and the best-fit output results were used in RVE model to predict yield surface evolution.

The studies by [106, 107] have applied the Linux coding software DAMASK [108] to establish the auto-generated tessellation to perform microscopic RVE simulation to calculate the grain level orientation, texture, and strain-stress behaviour. Based on DAMASK integrated spectral solvers, the calculations on single-crystal constitutive laws can be processed in user-friendly

way with less computational time. The studies on numerical framework for CPFEM and RVE [109-111] applied another Linux coding software NEPER [112] to generate auto-generated tessellation or EBSD obtained grains orientation to simulate the DRX and phase-field behaviour on metal processing works. Based on ABAQUS subroutine construction of single-crystal and polycrystal constitutive modelling. The findings indicate that the anisotropy coefficients of materials produced accurate results, and especially for heat-assisted mechanical deformation, anisotropy coefficients depending on temperature must be obtained before simulation. As the software is more flexible to establish and mesh experimental scale model, macroscopic, mesoscopic and microscopic CPFEM and RVE modelling can be formed easily. However, the software did not integrate any solver system, ABAQUS subroutine or other software solving systems have to be used to process the crystal plasticity calculation.

Further, Chuan et al. [113] integrated CPFEM with cellular automata (CA) to demonstrate the dynamic recrystallisation (DRX) for isothermal hot compression, which theoretically validated the combination of crystal plasticity and DRX behaviour to simulate the hot deformation process of steel alloys. Another research Li et al. [114] studied a combining CPFEM, RVE and CA methods to study the grain orientation, crystal texture and DRX for induction heating of SPIF for Ti-6Al-4V. As shown in **Figure 2-29**, the combination proposed a novel method to study mechanical properties (strain-stress behaviour) in macroscopic scale CPFEM and a transfer of obtained properties to RVE model corresponding to critical forming regions during the process and finally a CA modelling to predict the grains growth based on obtaining crystal plasticity results from CPFEM and RVE. The process, including extraction of the grain's orientation data from EBSD, applied the information in an experimental scale CPFEM, obtained the grain-level stress-strain data and input the data in RVE to create the crystal texture using the MATLAB toolbox MTEX [115] to produce the DRX behaviour. Single crystal constitutive models based on general elastic lattice distortion and plastic deformation without effects on

lattice geometry were used in the research and the results able to output the grain level stress and strain data to form DRX evolution, and misorientation angles to form crystal texture. The results were validated with experimental microstructure results. However, the modelling can be improved by inducing phase transition and twin grains calculations to predict the results for temperature up to beta-transus.

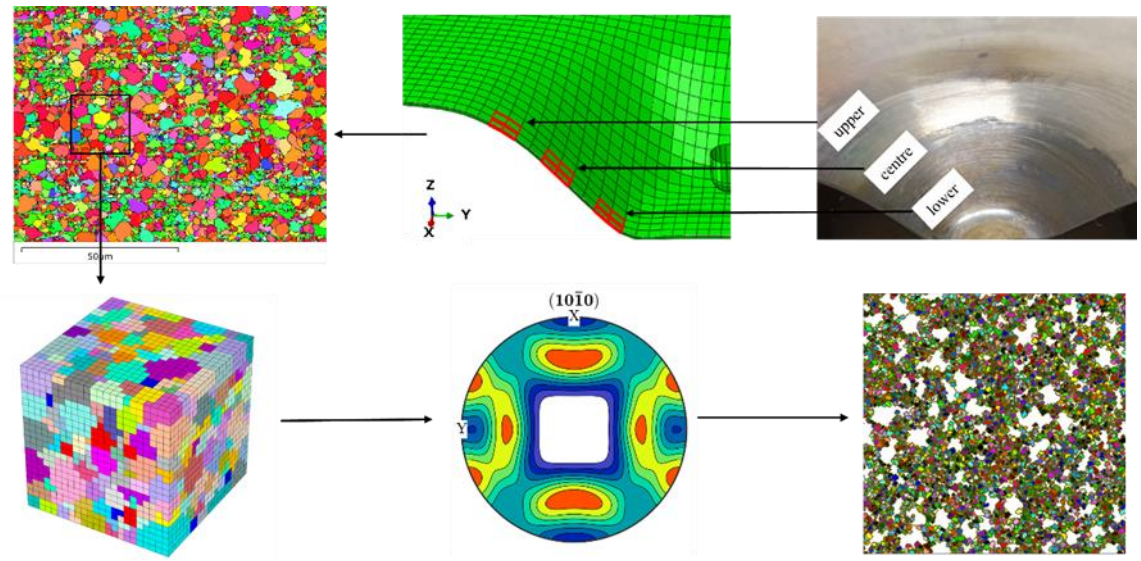

Figure 2-29. Process chart for microstructural evolution for heat-assisted SPIF.

2.7.3. Summary of numerical analysis

The numerical analysis can analyse the mechanical and thermal behaviour for experimental scale SPIF processes, and CPFEM, RVE and CA can estimate the material's microstructure evolution. The comparisons of solver types in FE modelling are presented in **Table 2-5**. The summary of FE microstructure analysis is shown in

Table 2-6.

Table 2-5. Comparisons of solver types in FE modelling

Solver type	Advantages	Limitations
Explicit	- Low computational time. - Efficient for small increment points. - Approximately constant increment size.	- Not efficient for large increment times. - Mass scaling affects the accuracy and computational time.
Implicit	- Linear to mildly non-linear. - Efficient for large increment times.	- Large computational time. - Not efficient for small increment times. - The accuracy varies for increment size.

Table 2-6. FE microstructure analysis

Solver type	Advantages	Limitations
CPFEM	- Applicable for multi-scale macroscopic, mesoscopic and microscopic scale analysis.	- Polycrystalline model needs more investigation to reduce the consumptions.
	- Efficient modelling of material's plasticity behaviour.	- Single crystal model is constraint for microstructure evolution without phase transition and twin grains.
RVE	- Applicable for microscopic scale analysis and mesoscopic scale.	- Not applicable for macroscopic scale analysis.
	- Efficient mechanics for heterogeneous materials and plasticity properties estimation.	- The accuracy varies for increment size.
	- Efficient production of grain's level stress, strain and crystal texture.	

CA	- Applicable for microscopic scale analysis. - Efficient for DRX and grain size evolution.	- Not applicable for macroscopic scale and mesoscopic scale analysis.

2.8. Microstructure analysis

This section discusses the effects of microstructural evolution in SPIF room temperature and elevated temperature in correlation with forming force, formability, geometric accuracy, thickness and temperature distribution.

2.8.1. Microstructure analysis for SPIF

In SPIF process, the tool follows the tool path to make incremental deformation to the sheet materials. The applied forming force and heating induce mechanical and thermal behaviour to the workpiece. The strain hardening work will increase the microstructural evolution and the domination of such evolution is a critical factor to study to control or optimise the process quality. As shown in **Figure 2-30**, the study by Shrivastava and Tandon [116] revealed the microstructural evolution and grain size distribution in SPIF of AA1050 sheet metals. According to the findings, a strong reduction of grain size can be observed (42.4 μm to 11.05 μm), which revealed grain refinement throughout the forming process. Further, numerous low angle grain boundaries (2 - 15°) have been transformed to high angle boundaries (above 15°), indicating that the work hardening increased.

For heat-assisted SPIF on Ti-6Al-4V, Li et al. [65] observed pronounced grain refinement for temperatures from as-received to 600 ℃ and 700 ℃ as shown in **Figure 2-31**. The study obtained that the increase in temperature successfully increased the ductility of workpiece

which reduced the forming force and achieved better geometric accuracy. The study also found that 700 ℃ induced more DRX initiation than 600 ℃ which produced finer grain and contributed to the grain boundary strengthening. The grain growth at higher temperature (above 700 ℃) is a key factor to produce constant straining work which approached sustainable forming force growth thus improved the geometric accuracy and remained a stable thickness distribution. Other studies by Zhang et al. [117] and Zhang et al. [118] investigated temperature's influence on the formability, microstructure and fracture morphology of SPIF of magnesium materials. The studies revealed that the higher temperature increased the DRX, which reduced the forming force, increased formability and further reduced the risk of fracture. Further, the reduction in grain size activated the grain's boundary dislocation, thus enabling the neighbouring deformation, which enhanced the straining process and achieved higher micro-hardness.

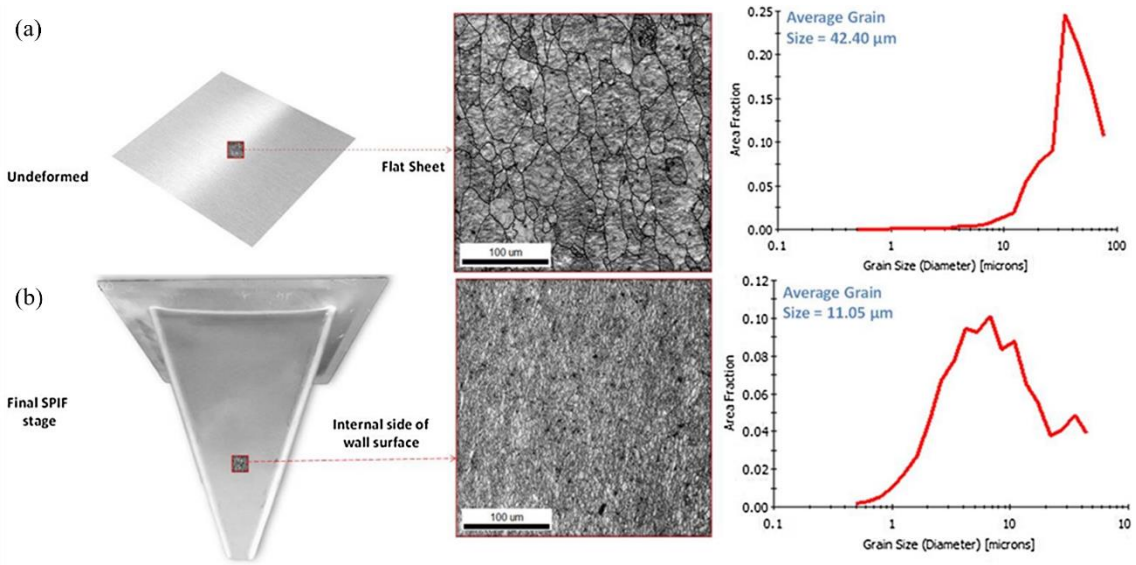

Figure 2-30. Microstructural evolution and grain size distribution histogram throughout the SPIF process of AA1050 sheets, (a) as-received sheets, (b) deformed sheets [116].

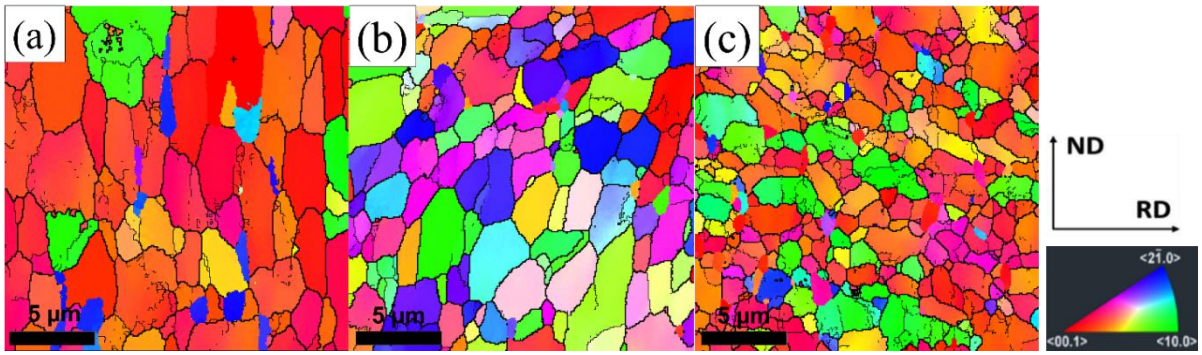

Figure 2-31. Microstructural evolution of as-received sample (a) IPF map of as-received sample (b), IPF map of 600 ℃ sample and (c) IPF map of 700 ℃ sample [65].

2.8.2. Summary of microstructure analysis

The microstructure analysis encounters limitations in establishing constitutive models to correlate thermal microstructure evolution and mechanical properties. Unlike measurable mechanical behaviours, the investigation of microstructure can only be obtained from microscopic characteristics on a specific area. For heat-assisted SPIF processes, the unstable forming force and temperature induce different microstructure from starting, centre and ending area. Further, different heating methods and experimental parameters, such as step size, feed rate and tool design produce a combination of effects to the microstructure evolution. Thus, experimental measured microstructure characteristics should correlate with numerical microstructure analysis by importing the experimental data to the microstructure models to predict the crystal texture, grain orientation and grain size evolution throughout the process. The microstructural analysis is significant to study to produce accurate results to correlate the relationship with mechanical properties.

2.9. Summary of open research question

- To apply SPIF on high-strength materials, heat sources can be improved to provide localised temperature to workpiece. The heating temperature should be rapid and moved

together with the tool motion to keep constant temperature distribution.

- Ball-roller tools indicate higher formability, surface quality and geometric accuracy than conventional tools. However, the ball-roller has a high risk of thermal expansion during high temperature deformation. Thus, water-cooling system is essential to integrate to the tool to provide cooling to the tool and reduce the lubricant dissipation.

- Conventional lubricants and coatings did not provide sufficient performance to the workpiece during heat-assisted SPIF process. High temperature cause rapid dissipation of lubricant and burn-off of coatings. It is essential to design high temperature lubricant to resist the thermomechanical behaviour during the SPIF process.

- The helical tool path is preferable for axisymmetric forming shapes, and the contour tool path is preferable for all types of forming shapes. To optimise the tool path plan, RSM, ANN and image analysis can correct and optimise the tool path to compensate for the error from the forming force and temperature. For the heat-assisted SPIF process, ANN has more potential to study the behaviours of temperature and tool path coordinates to produce the optimal tool path. However, the error percentage will increase for unstable temperature distribution.

- Numerical modelling can be correlated with CPFEM, RVE and CA modelling to provide macroscopic-mesoscopic-microstructure analysis throughout the heat-assisted SPIF process. The essential part is to determine accurate experiment and microstructure results and data transfer to the modelling, connection of each model should be studied.

Please note that certain reviews in the literature review will be provided in chapter 3 – 6 that covers the relevant works to the research publications.

3. Experimental and numerical investigations on the process quality and microstructure during induction heating assisted increment forming of Ti-6Al-4V sheet

Weining Li [a], Moataz M. Attallah [b], Khamis Essa [a]

[a] *Mechanical Engineering, University of Birmingham, Edgbaston, Birmingham, B15 2TT, UK*

[b] *School of Metallurgy and Materials, University of Birmingham, Edgbaston, Birmingham, B15 2TT, UK*

This research was published as a full-length research article in Journal of Materials Processing Technology:

Li, W., M.M. Attallah, and K. Essa, *Experimental and numerical investigations on the process quality and microstructure during induction heating assisted incremental forming of Ti-6Al-4V sheet*. Journal of Materials Processing Technology, 2022. 299: p. 117323. DOI: 10.1016/j.jmatprotec.2021.117323.

Credit authorship contribution statement

Weining Li: Conceptualization, Investigation, Methodology, Validation, Software, Formal analysis, Writing - original draft.

Moataz M. Attallah: Writing - review & editing, Resources of lab equipment, Supervision.

Khamis Essa: Writing - review & editing, Resources of lab equipment, Supervision, Project administration.

Research contributions:

This chapter aims to complete the objective 3 which covers the following insights:

- A rapid and constant induction heating SPIF system to provide localised heating to deform Ti-6AI-4V alloy sheet.
- The relation between mechanical and microstructural behaviours was investigated by analysing the straining and thermal behaviour with the microstructural evolution.
- The FE model has been established to provide strain and strain rate history at critical regions of the deformed workpiece and input the simulated results to Zener-Hollomon parameter (Z-parameter) to correlate the grain size and micro-hardness.

Abstract

The conventional single point incremental forming (SPIF) process is unable to produce high geometrical accuracy and formability for the Ti-6AI-4V alloy sheet. In response, this chapter has proposed a reliable high-frequency induction heating-assisted SPIF system. Rapid localised heating (600 ℃ and 700 ℃) was integrated with a synchronized Inconel 625 Nickel alloy ball-roller forming tool to achieve high geometric accuracy and surface quality. This chapter also produced new insights into correlating mechanical and microstructural properties in SPIF at 600 ℃ and 700 ℃. To investigate the mechanical properties (forming force, geometric accuracy, thickness profile), an explicit finite element (FE) simulation was established to predict the results. The output strain history from the FE simulations was used as input and integrated with electron backscatter diffraction (EBSD) and micro-hardness characterisations, to form a constitutive model (Arrhenius model) to calculate the Zener-Hollomon parameter (Z-parameter). The grain size and micro-hardness experimental results were correlated with Z-parameter calculation to predict the microstructural development at the initial, middle, and final stages of the deformation process. The mechanical results revealed that the 700℃ experiment produced enhanced geometric accuracy and thickness profile, with a reduced forming force. However, the surface quality is reduced as the lubricant dissipated rapidly, while the ball-roller tool effectively compensated for this behaviour by reducing the friction. At the microstructural level, 600 ℃ revealed strong strain hardening and grain deformation, and 700 ℃ revealed better grain refinement by dynamic recovery (DRV) and dynamic recrystallisation (DRX). A proportional relationship between Z parameters and grain size and a low-high-low micro-hardness profile was proposed.

Keywords: Hot Single Point Incremental Forming, Deformation behaviour, Finite Element analysis, Recrystallisation, Constitutive model, Zener-Hollomon parameter, Micro-hardness.

3.1. Introduction

Ti-6AI-4V alloy has been widely used in aviation, automotive and medical industries, on account of its advantageous properties such as high strength, service temperature, and corrosion resistance. However, the deformation of Ti-6Al-4V remains a challenge. SPIF is a highly flexible computer numerical control (CNC) controlled sheet metal forming process that is efficient for relatively low strength materials at room temperature. For instance, Kumar et al. [68] reported excellent forming quality of aluminium alloy sheets. Further, Duflou et al. [119] studied the state-of-the-art of current SPIF methods and stated that the heating source should be integrated with the system to deform high-strength materials. In recent years, heat-assisted SPIF systems have been developed to deform high-strength alloy sheets. Ambrogio et al. [4] have created an induction heating-assisted SPIF system that can deform the Ti-6Al-4V sheet at a temperature above 600 ℃. Using the same heating method, Al-Obaidi et al. [26] obtained excellent geometric accuracy when deforming 22MnB5 steel at 750 ℃. This study successfully applied thermomechanical behaviour on high-strength materials that induced material microstructural recrystallisation, which resulted in the reduction of material anisotropy. Thus, there are new challenges to study the heating method and subsequent microstructure characterisation to understand the mechanical behaviour of the materials in the SPIF process.

In previous work, laser heating assisted SPIF was reported by Göttmann et al. [27]. A high-power laser heating system was used to deform a 1.5 mm thickness Ti-6Al-4V sheet. The laser is well-positioned to provide precise localised heating on the workpiece. However, the laser heating produced a strong heating track on the workpiece surface, and the apparatus setup is complicated, incurring a high cost and requiring extra safety measures. Alternatively, Xu et al. [120] introduced the electric heating-assisted SPIF system, where a high-voltage direct current (DC) transformer generates the heat with the electric flux spread through the entire workpiece to make the material ductile. However, the spread of electric flux resulted in geometrical

inaccuracy and adverse surface quality. Recently, Ambrogio et al. [4] have developed an induction heating assisted SPIF system where the heating coil is positioned underneath the sheet; with a connection to the forming tool, accurately localised heating is generated in the material from the centre to the outer surface. Thus, both geometrical accuracy and surface quality can be achieved by such a heating method. In this chapter, an induction heating-assisted SPIF system has been developed to provide rapid and accurate localised heating to deform the Ti-6Al-4V workpiece.

To reveal the relation between mechanical and microstructure behaviours, Shrivastava and Tandon [116] studied the microstructural evolution of AA1050 aluminium sheet under SPIF. The study proposed a method that to combine the experimentally measured mechanical properties and FE simulation obtained strain history to correlate the microstructural development. However, no attention has been given to apply this to heat-assisted SPIF especially for high strength materials such as Ti-6Al-4V. Thus, this chapter aims to build a heat-assisted SPIF system to address the above challenge.

In summary, to develop an economical, efficient, and high-accuracy SPIF system for Ti-6Al-4V alloy, a featured induction heat-assisted SPIF system has been developed. The mechanical and microstructural behaviours of Ti-6Al-4V for 600˚C and 700˚C which are close and above Ti-6Al-4V recrystallisation temperature. To correlate the mechanical and microstructural behaviours, FE simulations were established to verify the experimental results and to develop a constitutive model to estimate the microstructural development and deformation behaviour.

3.2. Material and methods

3.2.1. Experimental setup

To deform the Ti-6Al-4V alloy sheet, a high forming force is required during the process. The conventional tool tip may cause fractures and wear tracks on the workpiece surface due to the

high friction force. A ball-roller tool tip forming tool was developed in this chapter, as shown in **Figure 3-1**. The tool shank was made of stainless steel with a 10 mm diameter IN 625 nickel alloy ball-roller as the tool tip. To cool down the forming tool, the tool shank has a hollow inner structure which provides a direction for heat flow from the tool tip that reduces the thermo-expansion. During the process, the rotation of ball-roller reduces the friction on the tool-surface contact area, the heat flow from the tool will be directed by the path and released from the air valves.

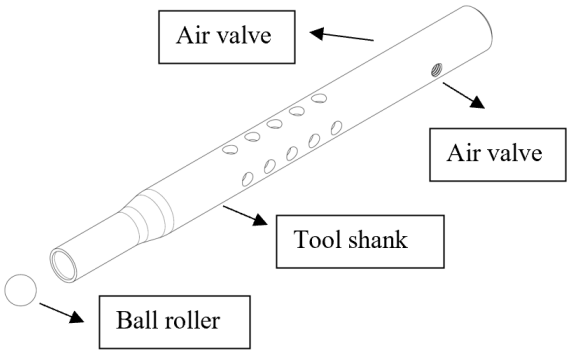

Figure 3-1. Design of ball-roller forming tool.

The induction heating SPIF system setup can be viewed in **Figure 3-2**(a-e). The main induction heater has a high frequency (900 kHz) alternating current (AC) inductor with a maximum power of 6.6 KW. The heat generation is obtained through the electromagnetic field that penetrates the workpiece to generate a rapid eddy current to heat the workpiece from inner to outer surfaces. The heating coil diameter is 10 mm with three turns, which can provide maximum and accurate localised heating. The temperature can be maintained constant, with an error of 2% for a minimum heating process of 20 hours. A flexible support fixture was designed to hold the heating head to allow the synchronized movement between the heating coil and the forming tool in XYZ directions (**Figure 3-2**(a)). A mini 50kN low profile diaphragm load cell (**Figure 3-2**(b)) was fixed on the top of the forming tool to measure the reaction force during the process. The heating coil and forming tool setup were shown in **Figure 3-2**(c). The instantaneous

temperature of the forming tool tip is measured by an infrared thermo-couple fixed on the forming tool holder by flexible support (**Figure 3-2**(d)), which has a measurement range from 400 ℃ to 1200 ℃.

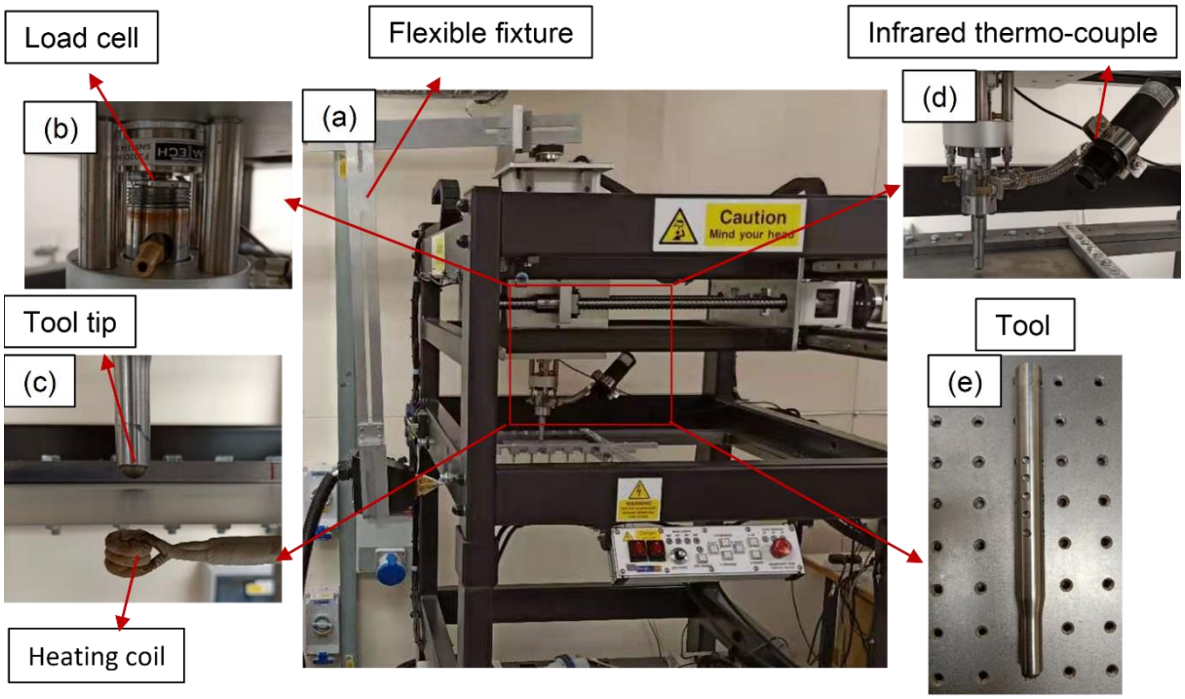

Figure 3-2. Overview of the induction heat-assisted SPIF system (a) flexible support fixture (b) load cell (c) forming tool-workpiece working scheme (d) infrared thermo-couple (e) forming tool.

3.2.2. Material and process parameters

3.2.2.1. Materials

A standard α-β class Ti-6Al-4V alloy sheet was chosen as the workpiece, with a size of 150 mm × 150 mm and a thickness of 0.8 mm. The chemical composition of the used Ti-6Al-4V alloy is shown in **Table 3-1**.

A heat-resistant liquid MoS_2 lubricant spray was used in this project to penetrate the specimen surface for even fits. According to the product datasheet, this lubricant is functional up to 600 ℃.

Table 3-1. Chemical composition of Ti-6Al-4V

Ti	Al	V	C	O	N	H	Fe
Balanced	5.3	3.8	0.1	0.2	0.05	0.01	0.3

3.2.2.2. CAD model and process parameters

The final shape is a truncated cone that has a 100 mm major diameter, 30 mm height, and 45^{o} wall angle as shown in **Figure 3-3**. The tool path was generated by Matlab, and a G-code was obtained from the MATLAB coordinates output file to control the CNC machine. The detailed parameters and working temperatures are listed in **Table 3-2**. From the initial testing of 600 ℃ and 700 ℃ induction heating assisted SPIF, it can be seen in **Figure 3-4** that the temperature rise at the initial stage is usually lower (around 30℃) than the set temperature, since time is taken (around 30 s) for heat generation to acquire steady-state. The steady-state temperature has a variation of $\pm$ 2 ℃. When the process progresses to the last stage (final 40-60 s), the recorded temperature is slightly higher (around 30 ℃) than the set as the whole workpiece has been subject to consecutive hot deformation. As the shape design is getting smaller at the ending stage, the high-frequency heat transfer and rapid tool movement result in re-heating behaviour at small areas that increases higher readings.

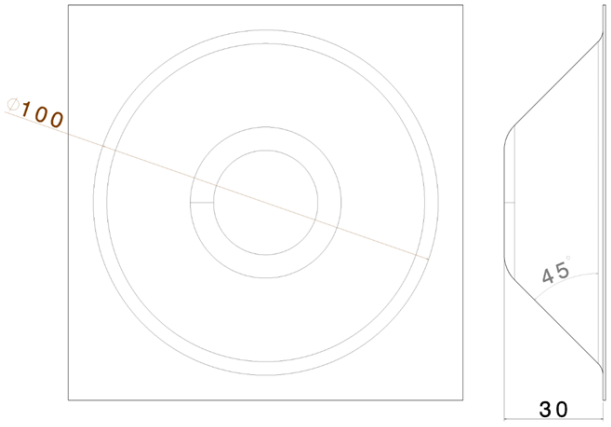

Figure 3-3. The dimensions of truncated cone to be made by induction heating assisted SPIF.

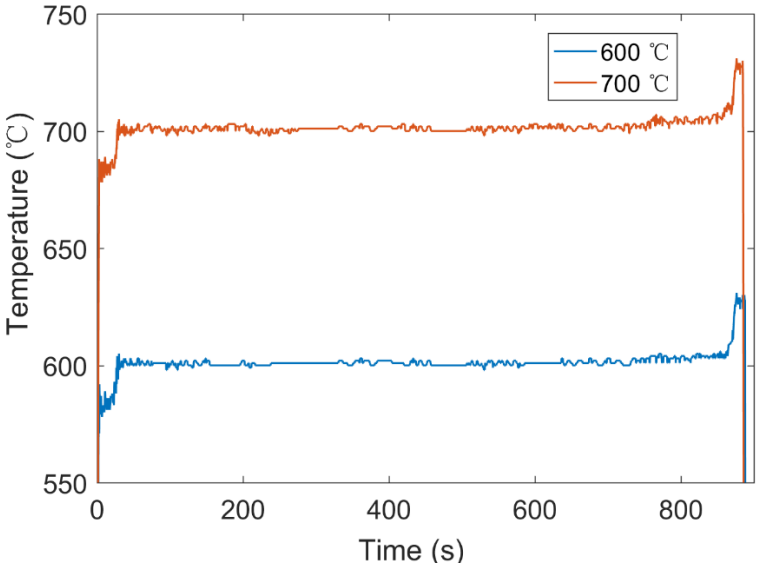

Figure 3-4. Measured temperature history for SPIF at 600 ℃ and 700 ℃.

Table 3-2. Experimental parameters

EXPERIMENTAL PARAMETERS	TARGET TEMPERATURE (700 ℃)	TARGET TEMPERATURE (600 ℃)
Feed rate (mm/min)	1000	1000
Step size	0.5	0.5
Power (kW)	5.5	5.0
Frequency (kHz)	650	650

3.3. Finite Element Modelling

Abaqus CAE was used in this project for FE modelling of the induction heating-assisted SPIF process. The forming tool is considered an analytical rigid body with a pitch diameter of 10

mm. The dimension of the workpiece is 150 mm × 150 mm, with a thickness of 0.8 mm. The mechanical and thermal properties are provided by the Ti-6Al-4V alloy supplier. The details are represented in **Table 3-4** and **Table 3-4**.

Table 3-3. Mechanical properties of Ti-6Al-4V

Temperature (℃)	**Young's modulus (GPA)**	**Poisson's ratio**	**Density (kg/m^3)**
25	113	0.33	4420
600	65.5	0.33	4336
700	55.5	0.33	4324

Table 3-4. Thermal properties of Ti-6Al-4V

Temperature (℃)	**CONDUCTIVITY (W/M℃)**	**EXPANSION**	**HEAT CAPACITY (J/KG℃)**
25	7	8.9×10^{-6}	546
600	14.2	1.03×10^{-5}	673
700	15.5	1.05×10^{-5}	694

3.3.1. Johnson-Cook (J–C) model

A J-C model [121] was established to achieve a valid FE model using experimental data and assumptions from the literature. The model is under multiplicative law which able to provide a function of von mises tensile flow stress according with strain, strain rate and temperature-dependent viscoelastic variables. A flow stress prediction was produced with the application of the J-C model final equation and later compared with the literature for validation purposes. The constitutive equation of J–C model can be presented using the following equation:

$$\sigma = \left[A + B\left(\bar{\varepsilon}^{pl}\right)^{n}\right]\left(1 + C\ln\frac{\dot{\bar{\varepsilon}}^{pl}}{\dot{\varepsilon}_0}\right)\left[1 - \left(\frac{T - T_r}{T_m - T_r}\right)^{m}\right] \quad (3\text{-}1)$$

Where σ is the yield stress, $\bar{\varepsilon}^{pl}$ is the equivalent plastic strain, $\dot{\bar{\varepsilon}}^{pl}$ is the equivalent plastic strain rate, $\dot{\varepsilon}_0$ is the reference strain rate, T is the working temperature, T_r is the room temperature, T_m is the melting temperature, A is the yield stress at reference strain rate and temperature, B is the coefficient of strain hardening, C is the coefficient of strain rate strengthening, m is the thermal softening coefficient, and n is the strain hardening exponent.

3.3.2. Determination of material constants

By assuming that the reference temperature and strain rate is equivalent to the working temperature and plastic strain rate, the J-C can be simplified as:

$$\sigma = A + B\left(\bar{\varepsilon}^{pl}\right)^{n} \quad (3\text{-}2)$$

By applying natural logarithm on both sides, **Eq. (3-2)** can be expressed as:

$$\ln(\sigma - A) = \ln B + n\ln\bar{\varepsilon}^{pl} \quad (3\text{-}3)$$

Substituting the value of A in **Eq. (3-3)** and plotting graph between $\ln(\sigma - A)$ and $\ln B + n\ln\bar{\varepsilon}^{pl}$

and obtain the material constant B which is the intercept of the plot, n is the gradient.

To validate the J-C model predicted, specific constant values were obtained from the literature and set as input values in the J-C model calculation. By referencing the study by Xu et al. [122] on DRX of Ti-6Al-4V, the reference temperature T_r can be considered as 293 K and the melting temperature T_m can be considered as 1660 K. Since the working mechanism of the ISF process is governed by the complex stress and strain distribution in the forming area, common materials processing maps are not representative of the process. However, it is useful to obtain a strain rate from the literature that is close to the experiments in this chapter and to use it to validate the J-C model formation. The study by Gatea et al. [123] investigated the effect of forming parameters on the pure titanium ISF process, wherein the experiments indicate that the strain rate varies from 0.01 s^{-1} to 0.08 s^{-1}depends on the feed rate and wall angle. Another study by Desalegn et al. [99] has commented that the strain rate increases according to the increase of temperature in warm SPIF of aluminium alloy, where the range of strain rate varies 0.01 s^{-1} to 0.1 s^{-1}. In this chapter, the strain rate is set as $\dot{\varepsilon}_0$ = 0.01 s^{-1} which agrees with previous studies on ISF processes. The results can be validated with a processing map provided by the literature by Nemat-Nasser et al. [124], who studied the deformation behaviour of Ti-6Al-4V for a wide range of temperatures and strain rates. Other J-C model constants are obtained from the study Kotkunde et al. [125]. These constants values were verified in the study by Lee and Lin [126] on hot deformation of Ti-6Al-4V and Wang et al. [127] on J-C modelling of Ti-6Al-4V alloy.

Assuming a constant reference strain rate and temperature, **Eq. (3-3)** can be expressed as:

$$\sigma = \left[A + B\left(\bar{\varepsilon}^{pl}\right)^{n}\right]\left(1 + C\ln\frac{\dot{\bar{\varepsilon}}^{pl}}{\dot{\varepsilon}_0}\right) \tag{3-4}$$

The constant C can be obtained from the gradient from the plotting of $\ln\left[1-\sigma/\left(A+B\left(\bar{\varepsilon}^{pl}\right)^{n}\right]\right.$ and $\ln\frac{\dot{\bar{\varepsilon}}^{pl}}{\dot{\varepsilon}_0}$.

Assuming a constant working temperature and reference strain rate, hence **Eq. (3-4)** can be expressed as:

$$\ln\left[1-\sigma/\left(A+B\left(\bar{\varepsilon}^{pl}\right)^{n}\right]\right. = m\ln\left(1-\frac{T-T_r}{T_m-T_r}\right) \tag{3-5}$$

From the flow stress data for every fixed plastic strain at different temperatures, the constant m can be obtained from the gradient from the plotting of $\ln\left[1-\sigma/\left(A+B\left(\bar{\varepsilon}^{pl}\right)^{n}\right]\right.$ and $\ln\left(1-\frac{T-T_r}{T_m-T_r}\right)$. Thus, material constants C and m were determined using the least-square method.

The J-C model can be expressed as:

$$\sigma = \left[880.5+689.2\left(\bar{\varepsilon}^{pl}\right)^{0.35}\right]\left(1+0.009\ln\frac{\dot{\bar{\varepsilon}}^{pl}}{\dot{\varepsilon}_0}\right)\left[1-\left(\frac{T-T_r}{T_m-T_r}\right)^{0.85}\right] \tag{3-6}$$

The determined material constants are represented in **Table 3-5**.

Table 3-5. Material constants for Ti-6Al-4V

A (MPa)	**B (MPa)**	**C**	**n**	**m**	**$\dot{\varepsilon}_0$ (s^{-1})**
880.5	689.2	0.009	0.35	0.85	0.01

3.3.3. Flow stress behaviour validation and characterisation

To validate the J-C model, the predicted flow stress behaviours were compared with experimental flow curves obtained by Nemat-Nasser et al. [124] (at room temperature (RT),

526.85 ℃, and 726.85 ℃). In the present investigation, a similar range of temperatures and strain rates were used. As shown in **Figure 3-5**, the J-C model predicted flow behaviours agreed with the previous study.

It can be seen from **Figure 3-5** that the flow stress is sensitive to temperature when the strain rate is constant. Additionally, the flow stress at RT is increasing rapidly according to the increase of strain at the initial stage (strain: 0 - 0.05), which indicates that rapid work hardening takes place. The behaviour is less pronounced for 526.85 and 726.85 ℃. The previous study by Xia et al. [128] on the isothermal hot deformation of Ti-6Al-4VRu reported that the rapid increase of DRV at the initial stage is the main reason that causes the sharp increase in flow stress at low temperatures. During the DRV process, the rearrangement and removal of dislocations in the deformed grains' crystal structure led to their stored energy reduction and a sharp increase in the yield strength. The sharp increase is reduced as the temperature increases due to the DRX. The temperature increases the energy at grain boundaries until a critical value is reached. The recrystallisation takes place and induces a dynamic softening on the materials, thus healing the DRV. By observing **Figure 3-5**, a clear peak is present at 700 ℃ that indicates an occurrence of DRX, which softens the sharp increase by DRV.

Please note that the comparison of flow stress behaviour is used to validate the J-C model to prove its accuracy to simulate the induction heating SPIF process.

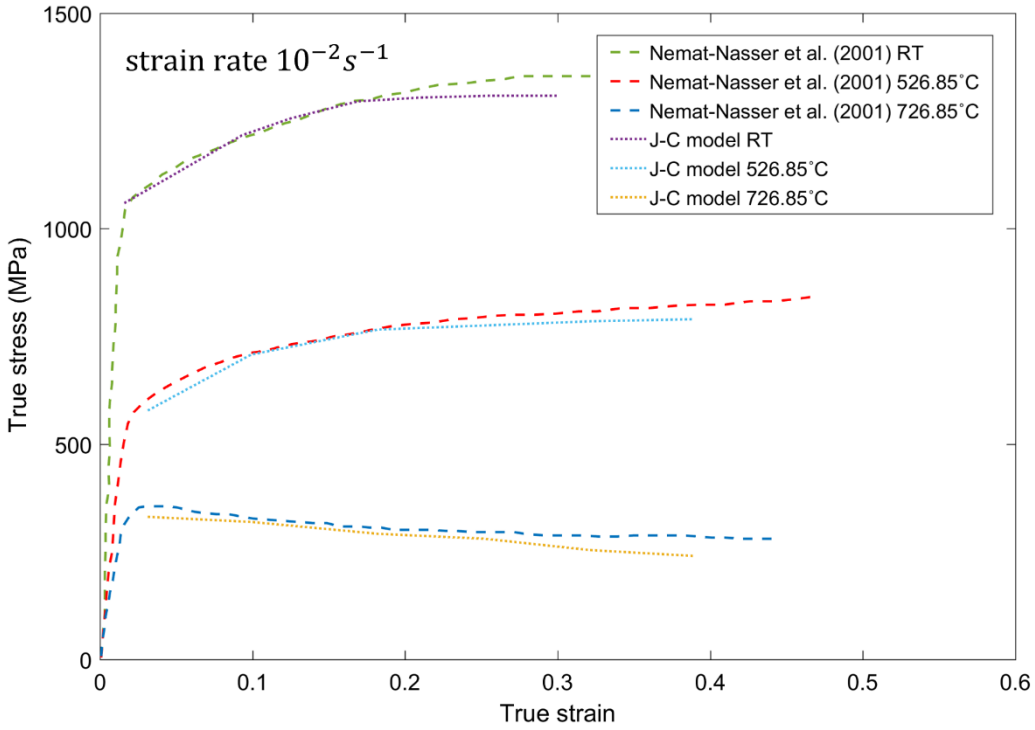

Figure 3-5. True stress-strain curves comparison between the literature and J-C models.

3.3.4. FEM processing

The induction heating SPIF can be expressed as a dynamic and temperature-displacement simulation in ABAQUS CAE. Coupled temperature - displacement explicit regime is used for process simulation. Since explicit analysis requires a large number of elements, mass scaling has been used to reduce the computational time. In this chapter, several mass scaling factors ranging from 100-100000 were used to test the reliability of the FE model. A workstation equipped with 20 Intel® Xeon® CPUs of 3 GHz and 120 GB ram was used to run the FE simulations. To ensure that the model is close to quasi-static and reduce the effect of mass scaling on the prediction accuracy, the kinetic energy should not exceed 10% of the maximum internal energy, as reported in the literature by Essa and Hartley [129] and Huang et al. [130]. **Figure 3-6**(a) shows the distributions of internal energy (ALLIE), kinetic energy (ALLKE), and artificial strain energy (ALLAE) at different mass scaling factors. Please note the simulations results are represented at 600 ℃ as an example. From **Figure 3-6**(b), it can be

noticed the ALLKE and ALLAE for all mass scaling factors did not exceed 10% of ALLIE which proves the reliability of the FE model. The effects of mass scaling on forming force and computational time are shown in **Figure 3-6**(b). It can be seen that mass scaling factors of 100000 and 75000 show less computational time (8 h and 20 h), but poor prediction accuracy of the forming force. When the mass scaling factor is reduced to 50000 or less, the prediction accuracy is close to the experimental result, with a reasonable computational time of 48 h. Please note that the data in **Figure 3-6**(b) were smoothed using the Savitzky-Golay filter method in the MATLAB plot toolbox.

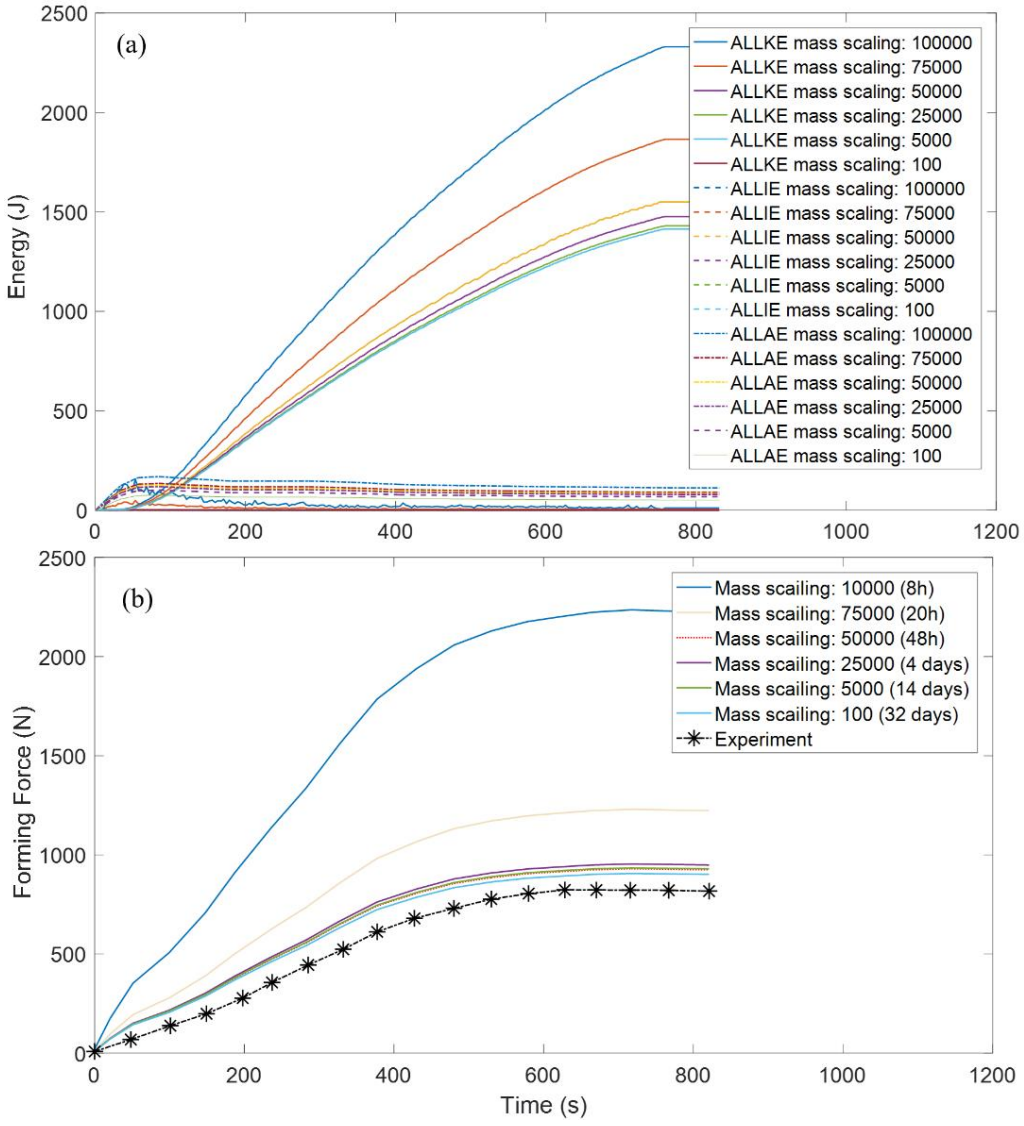

Figure 3-6. FE modelling of SPIF at 600 ℃ using different mass scaling factors (a) energy history (b) forming force.

The interaction between workpiece and tool was defined as a surface-to-surface contact with Tangential behaviour. A friction value of 0.1 was set in the model; this value was obtained from the previous study by Gatea et al. [131] on the modelling of ductile fracture in SPIF, based on Coulomb's friction law calculation. The friction model and value have been further verified with the study by Honarpisheh et al. [133] on hot SPIF simulation. The four edges of the workpiece were constrained using displacement boundary conditions where $U_x = U_y = U_z = 0$, and the tool was defined as a rigid body. The boundary conditions setting followed the general SPIF modelling conditions reported by Essa and Hartley [134]. The same FE conditions setting and experimental setup has been verified in another previous study by Moser et al. [135] on the FE modelling of double-side ISF. Two temperature boundary conditions (600 ℃ and 700 ℃) are set for the forming tool to simulate different experimental environments. Since the experiments recorded a temperature variation at the initial and final stages, a 30 ℃ temperature variation has been applied to the first 30 s (-30 ℃) and final 50s (+30 ℃) of tool path movement amplitude to compensate for the error in temperature history. The element selected for the FE analysis is 8-node thermally coupled brick, trilinear displacement, and temperature (C3D8T) which is most applicable for this analysis. A total of 7200 elements are applied to the workpiece with an approximate global size of 0.0025 and a maximum deviation factor of 0.1.

3.4. Geometrical, surface, and material characterisation

3.4.1. 3D geometric scanning

Geometric accuracy is a significant factor that reveals the overall performance and quality characteristics of parts made by the SPIF process. The FARO Edge-scan 8-Axis laser 3D Scanning Arm was used in this study to obtain the 3D cloud of points of deformed parts. The resolution of this system is 40 μm, with a measurement error of ± 0.2 μm. Geomagic was then used to process the cloud of points and obtain a highly accurate measurement of the final profile

and thickness distribution.

3.4.2. Surface roughness

Surface roughness is the most common measure to represent the surface quality of the forming parts. Alicona Infinite Focus is a highly accurate optical 3D surface measurement system to measure the surface roughness of the as-received and deformed samples. This machine is equipped with various optical microscopes which enables it to provide precise 3D surface data with a vertical resolution of 50 nm, minimum measurable roughness of 0.03 µm and measurement error of 2%. 401MVD Vickers micro-hardness tester is used in this chapter to provide high accurate micro-hardness results of the as-received and deformed samples with a measurement error of 0.5%.

3.4.3. SEM

A benchtop SEM JOEL 6000 was used in this project to analyse the microstructure of the as-received and deformed samples. The images can be taken at magnifications from 20x to 50,000x with an accelerating voltage of 15 kV. All SEM samples were mounted, and chemical-mechanical polishing with 0.04 µm Colloidal Silica (OP-S) suspension was used. Etching was performed on each sample using Kroll's reagent (2 ml HF, 10 ml HCl, 88 ml H_2O) to provide a more pronounced microstructure.

3.4.4. EBSD

Philips XL-30 was used in this chapter for grain growth analysis. This instrument was fitted with an Oxford Instruments INCA EDS system and an HKL EBSD system with a Nordlys camera. The camera utilized 100% 1344 × 1024 pixels resolution and a rapid 8 × 8 pixels binning. The obtained data were analysed with HKL CHANNEL 5 software to perform microstructural characterisation.

The EBSD data were collected with the following information: every slice at a step size of 0.07 μm, the pixel binning mode was set as 2 × 2, and the accelerating voltage was 30 kV with an electron beam current of 5 nA.

3.4.5. Micro-hardness

Wilson® hardness tester was used in this project to provide high accurate hardness results of the as-received and deformed samples. The measurements follow GB/T 4340.1-2009 HV 0.1 metal hardness testing standard with a testing load of 100 gm. The machine reading error is 0.5%.

3.5. Results and discussion

3.5.1. Forming force

A comparison between simulation and experimental forming force at 600 ℃ and 700 ℃ is shown in **Figure 3-7**(a-b). The tool motion on the tool path induced pronounced noise to the load cell, thus, Savitzky-Golay method was used to filter the data and produce clear trend of forming force. For the experimental results, there is a surface-to-surface contact between the workpiece and forming tool at the initial experimental setup, with a variation of 50 N - 80 N is applied on the workpiece. For the simulation results, an ideal initial situation was assumed wherein the forming force is 0 N at the starting point of the process.

As illustrated in **Figure 3-7**(a-b), experimental and simulation forming forces are agreed upon from the beginning to the steady-state region. Since the strain rate for these two experiments remains almost constant, the temperature dominates the forming force trendline. At 600 ℃, the temperature is relatively low to induce pronounced DRV and DRX, and the strain hardening and grain deformation form a strong micro-texture which induces the high forming force. At 700 ℃, the pronounced grains slip and dislocation results in better DRV and DRX to form an

enhanced grain refinement, which leads to a relatively isotropic microstructure that reduces the forming force. This agrees with the study by Davarpanah et al. [18] on microstructural properties of SPIF on polymers. The study reported that at room temperature strain-induced deformation and recrystallisation lead to anisotropic microstructure, while cycle heating results in enhanced recrystallisation that leads to isotropic properties. Another study by Bantounas et al. [136] on the investigation of grain orientation of Ti–6Al–4V shows that a better grain refinement can be achieved by increasing the temperature at a constant strain rate, which proves that both temperature and strain rate have effects on recrystallisation results. Additionally, the study by Guan et al. [137] on FE simulation of high-speed machining of magnesium reported that common hexagonal close packed (HCP) crystal materials favour the shear band induced local-strain recrystallisation that occurs at heat treatment. High forming force is required for strain hardening induced deformation texture at low temperature. Conversely, the heat treatment on Ti–6Al–4V induces shear band strain to HCP crystals that form an enhanced recrystallised texture.

By comparing the experimental and simulation results, it can be demonstrated that an excellent agreement has been achieved. The collected raw data shows strong fluctuation towards the end of the deformation process. Data filtering may result in little deviation at the regions with high fluctuation, which explains the negligible difference between simulation and experimental results at the end of the forming process. Besides, lubricant dissipation towards the end of the process may lead to a change in the friction coefficient which affects the forming force. Hussain et al. [138] has investigated the malfunction of lubricant in SPIF of Titanium alloy. The study reported that adherence of the workpiece material on the tool may lead to unpredictable failures on the workpiece, thus affecting the deformation process Further, a study by Fan et al. [139] revealed that the temperature variation during the SPIF process could lead to local springback which could significantly affect to the deformation process.

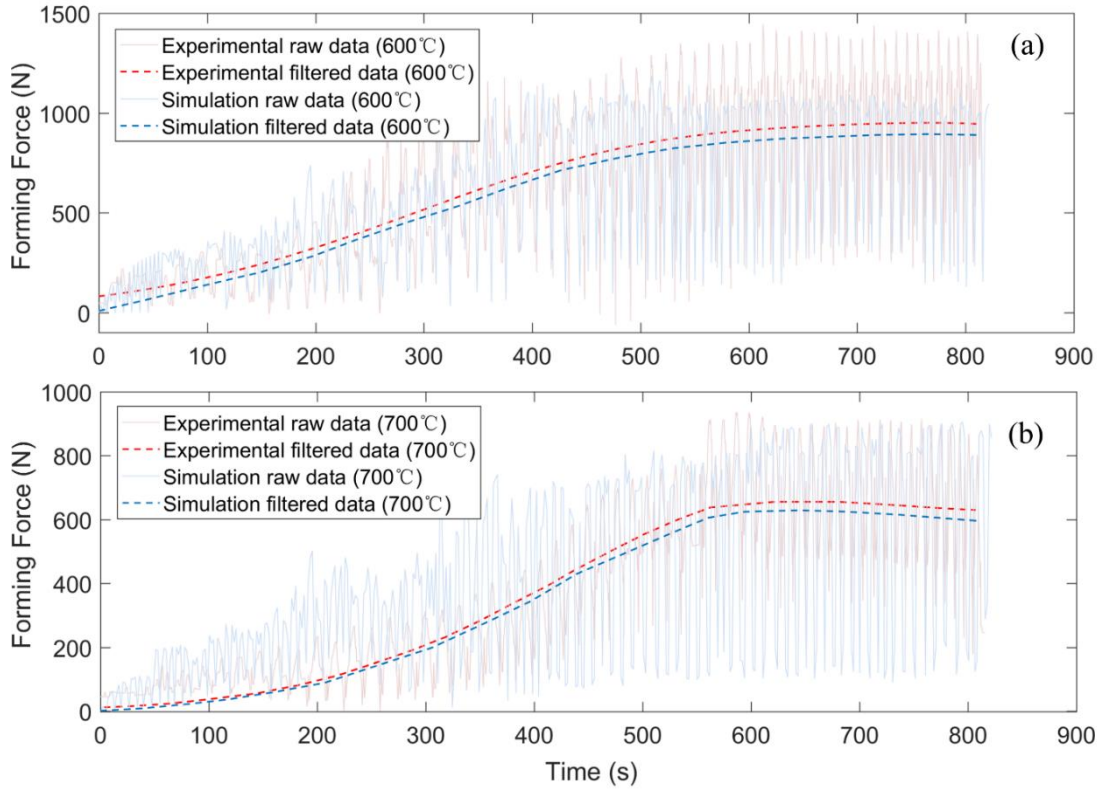

Figure 3-7. Comparison of forming forces between experimental and FE simulation at (a) 600 ℃ (b) 700 ℃.

3.5.2. Geometric profile

The FE profile of the workpiece formed at 600 ℃, and 700 ℃ as well as the experimentally measured profile are shown in **Figure 3-8**(a-b). A path from the workpiece edge to the centre was obtained from the FE model to demonstrate the FE profile data. It is important to note that the experimentally measured profiles were obtained using FARO 3D scanning on the clamped workpiece to match the displacement boundary conditions applied in the FE simulation. This prevents any errors from unclamping and cooling to reveal the impact of introducing the induction system. If rapid localised heating is transferred to the workpiece precisely, the experimentally measured profile should agree with the FE simulation.

As illustrated in **Figure 3-8**(a-b), only slight springback at the cone base and pillow effect at the cone centre were measured before unclamping. Still noticeable, the successful application

of rapid localised heating has enhanced the deformation process. Hence, it can be concluded that induction heating assisted SPIF can deform Ti–6Al–4V with high geometric accuracy. The measured profile at 700 ℃ shows excellent agreement with the FE profile compared with that at 600 ℃. This can be attributed to the enhanced recrystallisation-induced microstructure that results in a reduction in springback and pillow effects. This is a typical phenomenon that occurs in hot SPIF as the thermomechanical behaviour may induce high residual stress and stress relaxation in the material which results in springback and pillow effects. Similar observations were also reported in a previous study by Ortiz et al. [140] on the geometric accuracy of the hot SPIF process.

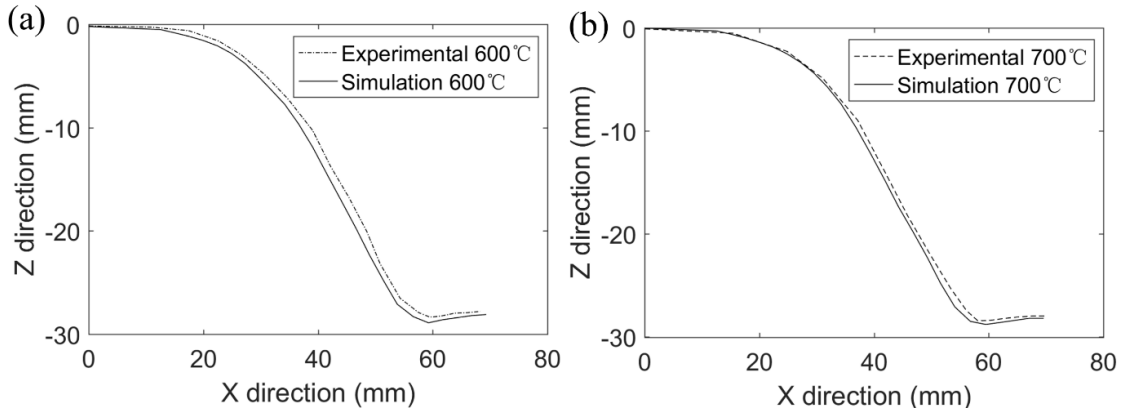

Figure 3-8. Comparison between FE and experimental profile at (a) 600 ℃ and (b) 700 ℃.

3.5.3. Thickness distribution

Figure 3-9 and **Figure 3-10** illustrate the thickness distributions measured from the sheet edge to its centre at 600 ℃ and 700 ℃, respectively. The sheet thickness of FE simulation can be obtained using **Eq. (3-7)**, and the theoretical thickness distribution can be obtained from the sine law as shown in **Eq. (3-8)**. Cao et al. [141] studied the ISF process and reported that the sine law is efficient to predict the thickness distribution of deformed parts. The experimental thickness (X, Y, Z displacement) was obtained using the FARO 3D scanner for two paths, with one path on the upper surface and the other one on the lower surface of the deformed workpiece.

The sheet thickness can be calculated by the following equation:

$$t = \sqrt{(x_1 - x_2)^2 + (y_1 - y_2)^2 + (z_1 - z_2)^2} \quad (3\text{-}7)$$

Where t is the sheet thickness, x_1, y_1, z_1 are the coordinates of nodes on the top surface path, x_2, y_2, z_2 are the coordinates of nodes on the lower surface path.

The theoretical thickness distribution can be obtained by applying cosine law as the following equation:

$$t_f = t_0 \sin\theta \quad (3\text{-}8)$$

Where t_f is the final thickness of the workpiece, t_0 is the initial thickness of the workpiece, θ is the wall angle. This equation was proposed in the previous study by Hussain and Gao [142] to estimate the thickness distribution in SPIF. Lu et al. [143] applied the same principle to predict the theoretical thickness of double-side ISF. Another study by Tolipov et al. [144] on multi-point forming also verified its efficiency to estimate the thickness distribution in sheet metal forming.

From **Figure 3-9**(a-b), it can be seen that the sheet thinning is proportional to the cone depth. The theoretical thickness produced a distribution without uneven thickness approach on X-direction to achieve the perfect sine law sheet thinning of 0.565 mm for a 45^o wall angle. The simulation matched with the measured results, however, the heating temperature and forming force still produced disturb thickness distribution. As illustrated, the maximum sheet thinning remains constant from 30 mm to 50 mm at X-direction along the cone wall. At 600 ℃, the experimentally measured thickness distribution slightly outfits the one obtained from the FE simulation (from 0 mm to 20 mm at X-direction). This can be attributed to insufficient heat generation at the initial stage of the process. The rapid tool movements and insufficient temperature at this region (around 570 ℃) initiated a strong DRV process that induced high

strain hardening, thus resulting in strong springback. Once the temperature acquired steady-state at 600 ℃ (from 20 mm onwards at X-direction), the experimentally measured thickness shows good agreement with the FE simulation. This phenomenon reveals good evidence of grains deformation that assists the material softening which leads to better agreement.

As shown in **Figure 3-9**(b), the experimentally measured thickness at 700 ℃ shows very good agreement with the FE simulation. At the initial stage (from 0 mm to 20 mm at X-direction), a slight outfit can be observed. This outfit is eliminated as the process progresses to the steady-state temperature region (from 20 mm onwards). This phenomenon reveals the presence of DRX initiated at the initial stage and then becoming more pronounced at the steady-state stage.

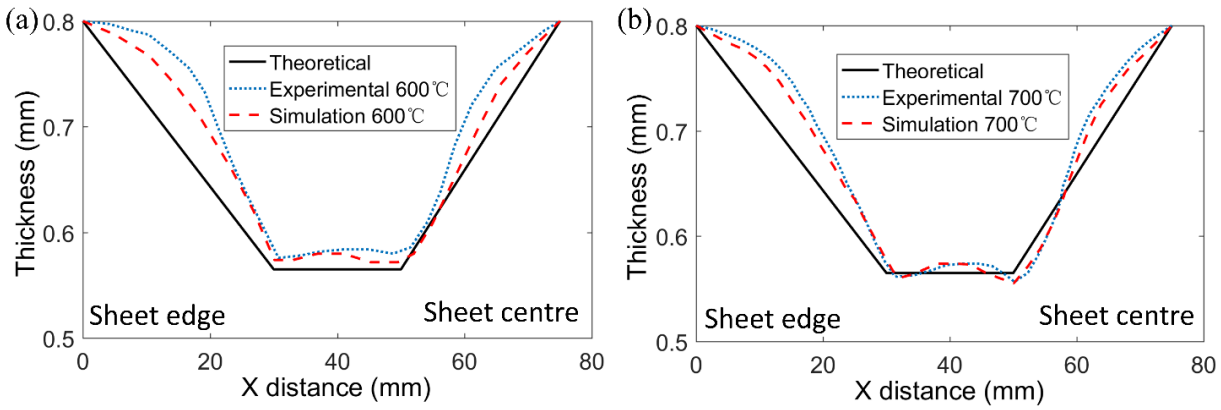

Figure 3-9. Comparison of thickness distribution obtained by the theoretical sine law, experiment and FE simulation (a) 600 ℃, (b) 700 ℃.

3.5.4. Surface roughness

For each formed workpiece (600 ℃ and 700 ℃), 3 sections (5 mm^2) were cut off from the upper, centre, and lower parts for surface roughness measurement as shown in **Figure 3-10**(a-b). The 3D surface topography of each sample is represented in **Figure 3-11**(a-g). **Figure 3-12** illustrates the average surface roughness (S_a) of all samples, and **Table 3-6** represents the root-mean-square height (S_q), maximum peak height (S_p), maximum valley depth (S_v), maximum

height (S_z) of each sample.

From the visual observation of results in **Figure 3-10**(a) and **Figure 3-10**(b), it can be seen that the surface quality at 600 ℃ is better than that at 700 ℃. Only a limited number of wear tracks are observed on the 600 ℃ samples. The dark colour from the centre to the lower region can be attributed to the adherence of dried lubricant. Conversely, the 700 ℃ sample reveals obvious wear tracks from the upper until the lower region. Such a phenomenon can be attributed to the exorbitant temperature and rapid lubricant dissipation during the process. The lubricant service temperature is 600 ℃; the exceeding working temperature may therefore cause lubricant malfunction. For effective operating condition, as in **Figure 3-10**(a), the upper region shows a smooth surface with limited wear tracks, which indicates functional lubricant. As the process progressed to the centre region, observable wear tracks occurred, and the material colour becomes darker incrementally. The phenomenon indicates a slow dissipation of the lubricant; the liquid lubricant transforms to a viscous state as the temperature increases. The rapid movement of the forming tool results in the formation of contaminated layers that adheres to the workpiece surface. By observing the surface of the 700 ℃ sample in **Figure 3-10**(b), it is worth noting that slight contamination (dark colour) can be observed at the centre region as the lubricant dissipation is more rapid even without any contamination being formed. The colour change of the 700 ℃ sample can also support the presence of recrystallisation. According to a previous study by Ortiz et al. [145] on hot SPIF of Ti-6Al-4V, the colour change appears when samples are heat-treated at 900 ℃ for 2h and indicates pronounced grains dislocation in the crystal, which is enhanced in the process. Another study by Satko et al. [146] on oxygen layer evolution in titanium microstructure reveals that an oxidation α-case layer can be formed at long exposures (420 h) at a relatively low temperature (650 ℃). Since the working temperature for this study is 700 ℃, the colour change only reveals a sudden variation of temperature when the tool leaves its position to the new path (ending and starting point of each path) throughout

the process. The movement of forming tool in this region may result in limited oxidation as the temperature fluctuates around the set temperature.

From the 3D surface topography profile shown in **Figure 3-11**(a-g), it can be seen that the measurements of S_a between 600 ℃ and 700 ℃ SPIF process is in similar distribution. By comparing the details, S_a for SPIF at 700 ℃ is higher than 600 ℃, this is evident that the dissipation of lubricant has an observed effect on the distribution of S_a along the SPIF process, however, there is no strong effect on the shape forming.

As illustrated in **Figure 3-12**. It is noticed that the values of S_a is increasing with the progressing of the SPIF process while lower values of S_a at 600 ℃ as compared with that at 700 ℃. The previous study by Ambrogio et al. [147] on induction heating SPIF of Ti-6Al-4V using MoS_2 (the same lubricant used in this investigation), reported that the induction heating SPIF has better performance than electric heating and friction heating SPIF. In this chapter, the ball-roller tool tip has shown higher surface quality than the previous work. Please note that all data in this figure are filtered by the Gaussian filter for inclined planar surfaces to reduce the noise.

By investigating the measured amplitude parameters of each sample in **Table 3-6**, it can be observed that the S_q is following the same trend as S_a. This is evident that the friction is increasing while the lubricant dissipates. However, it is still noted that the S_z (difference between S_p and S_v) of 600 ℃ and 700 ℃ samples are in converse trend. The upper region of 600 ℃ indicates higher values and the centre regions reveal relatively lower values, and the values are maintained in the lower regions. However, the opposite trend can be observed at 700 ℃. This is clear evidence that the 600 ℃ at the upper region is insufficient and unstable to soften the material thus leads to a higher forming force that increases the S_z between each step. As the forming tool is progressing to the centre and lower region, the workpiece becomes soft enough which leads to a reduction in S_z. While this phenomenon is insignificant at 700 ℃ since

the temperature is sufficient to increase the ductility of the workpiece at the upper region, the measured S_z in the deformed samples is very small. As the forming tool is progressing to the centre and lower region of the workpiece, the dissipation of lubricant results in an increase of S_z, however, results are still lower than that at 600 ℃. This phenomenon proves that the lower forming force at 700 ℃ improves the geometric accuracy while surface roughness can be improved if proper lubricant is used.

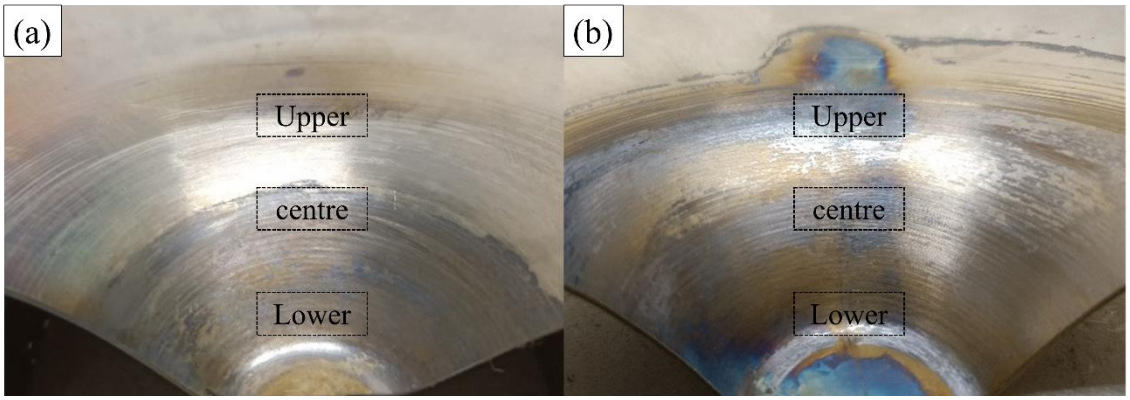

Figure 3-10. locations of collected samples for surface roughness measurements (a) 600 ℃ (b) 700 ℃.

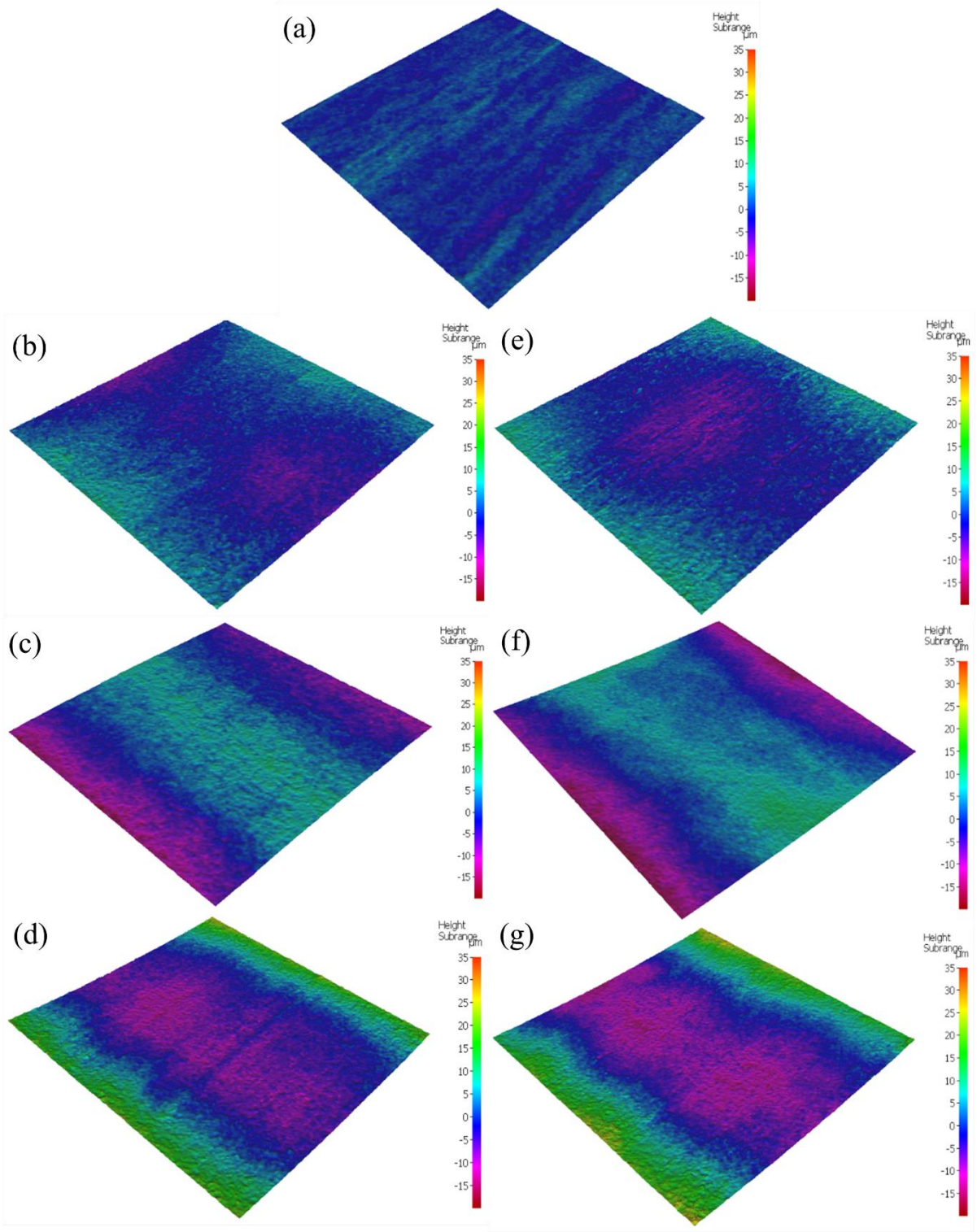

Figure 3-11. Surface roughness for (a) as-received (b) 600 ℃ upper region (c) 600 ℃ centre region (d) 600 ℃ lower region (e) 700 ℃ upper region (f) 700 ℃ centre part (g) 700 ℃ lower region.

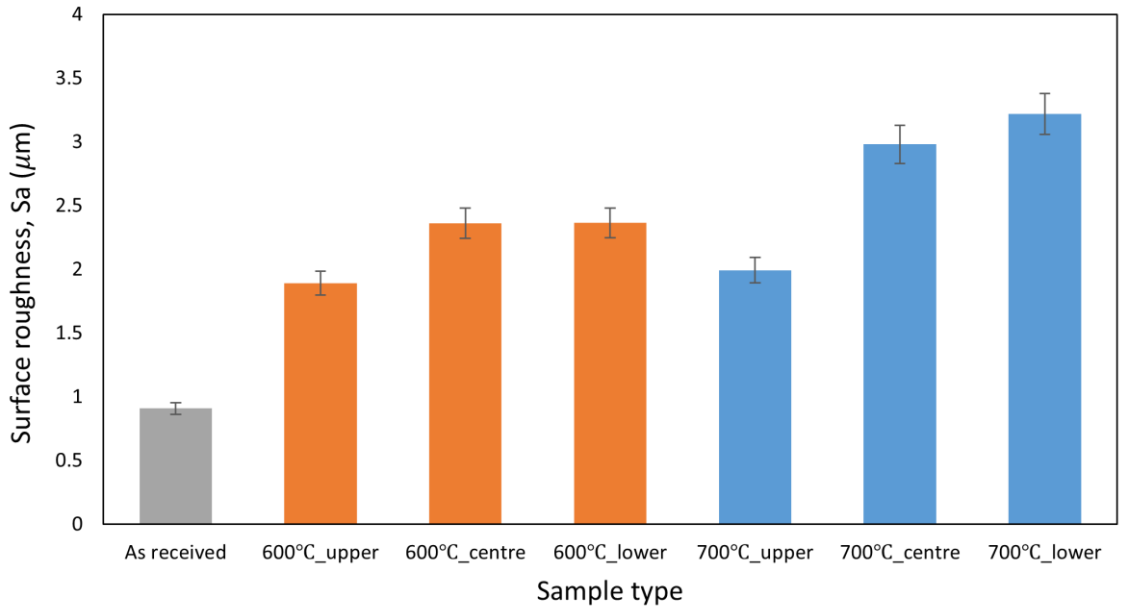

Figure 3-12. Filtered surface roughness histogram for different samples.

Table 3-6. Measured amplitude parameters of each sample

	S_q (μm)	S_p (μm)	S_v (μm)	S_z (μm)
As received	1.143	2.490	3.710	6.20
600 ℃ upper region	1.842	7.545	7.441	14.986
600 ℃ centre region	2.116	6.998	5.751	12.748
600 ℃ lower region	2.261	6.185	6.913	13.098
700 ℃ upper region	2.608	5.358	5.403	10.761
700 ℃ centre region	3.651	5.570	5.977	11.548
700 ℃ lower region	3.673	6.185	6.913	13.098

3.6. Microstructure analysis

3.6.1. SEM analysis

The microstructures of the lower region in the as-received, 600 ℃ and 700 ℃ samples are shown in **Figure 3-13**. As illustrated, the microstructure is mainly α phase, the average α grain size in the as-received SEM image (**Figure 3-13**(a)) is estimated to be 5 µm – 10 µm with random equiaxed grain shape. The intergranular β phase grains are detected at α phase boundaries. A noticeable increase in finer α grains is observed in **Figure 3-13**(b), and a pronounced increase of finer α grains can be seen in **Figure 3-13**(c). As illustrated, the grain size of fine α grains for 600 ℃ and 700 ℃ samples is reduced to 5µm. This can be considered as strong evidence that the grain refinement level increases as the temperature increases.

The previous study, reported by Qu et al. [148] on microstructural evolution and oxidation mechanisms of titanium alloy, reveals that titanium alloy exhibits excellent oxidation resistance at 700 ℃. However, clear recrystallisation can be observed at this temperature. In the present study, it is worth noticing that the induction heating system successfully dominates the level of grain refinement at 600 ℃ and 700 ℃, which supports the forming tool with a sufficient thermomechanical force to deform the workpiece.

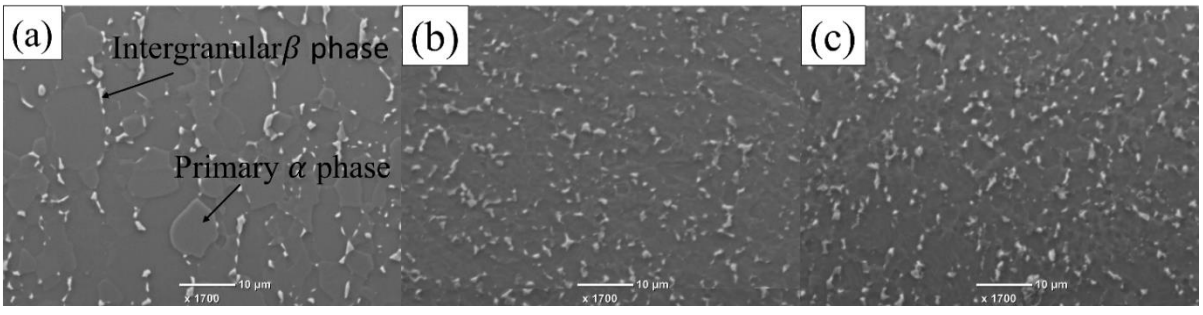

Figure 3-13. SEM images of (a) as-received sample (b) 600 ℃ sample (c) 700 ℃ sample.

3.6.2. EBSD analysis

To study the fraction of Ti-6Al-4V grain size changes and orientation after the hot SPIF process, EBSD was performed on each of the upper, centre, and lower region samples. Please note that only the lower region samples data were presented in this study since they have revealed the required information under the peak temperature and strain throughout the process. The EBSD scanning direction is the perspective of transverse direction (TD), which represents the in-depth (thickness direction) microstructure changes of the sample without the effects from the rolling manufacture process.

The lower region samples at 600 ℃ and 700 ℃ were obtained from EBSD examined inverse pole figure (IPF) maps, and are illustrated in **Figure 3-14**(a-c). The average grain size for all samples was calculated by EBSD post-processing software HKL Channel 5 and represented in **Figure 3-15**. Grain area (μm^2) is selected to represent the average grain size as the scan area is relatively small with limited grain numbers. The average grain area is more representable than the average length (μm) to distinguish the grain size difference.

As shown in **Figure 3-14**(a), the as-received sample exhibits a structure of coarse equiaxed grains of 4.62 μm^2 (**Figure 3-15**); no noticeable recrystallized grains can be observed from the figure. Conversely, the 600 ℃ revealed a significant difference as shown in **Figure 3-14**(b), notably, a pronounced increase of recrystallised finer grains is generated, and the average grain size is reduced to 3.39 μm^2 (**Figure 3-15**). However, the temperature is relatively low to induce significant DRV and DRX, which only results in a texture with the initiation of grains deformation. When the temperature increases to 700 ℃, as in **Figure 3-14**(c), a pronounced growth of recrystallised finer grains can be observed at coarser grain boundaries, and the average grain size is reduced to 1.44 μm^2 (**Figure 3-15**). This is strong evidence that grain deformation and DRV can be initiated at low temperatures (600 ℃) with high strain hardening, and a more completed DRV and DRX be achieved by increasing the temperature to 700 ℃.

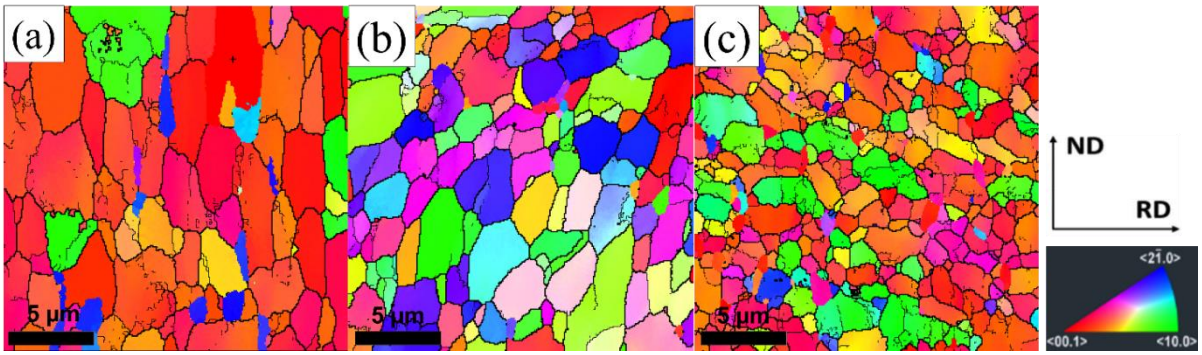

Figure 3-14. Microstructural evolution of as-received sample (a) IPF map with grain boundary distribution of as-received sample (b), IPF map with grain boundary distribution of 600 ℃ sample and (c) IPF map with grain boundary distribution of 700 ℃ sample.

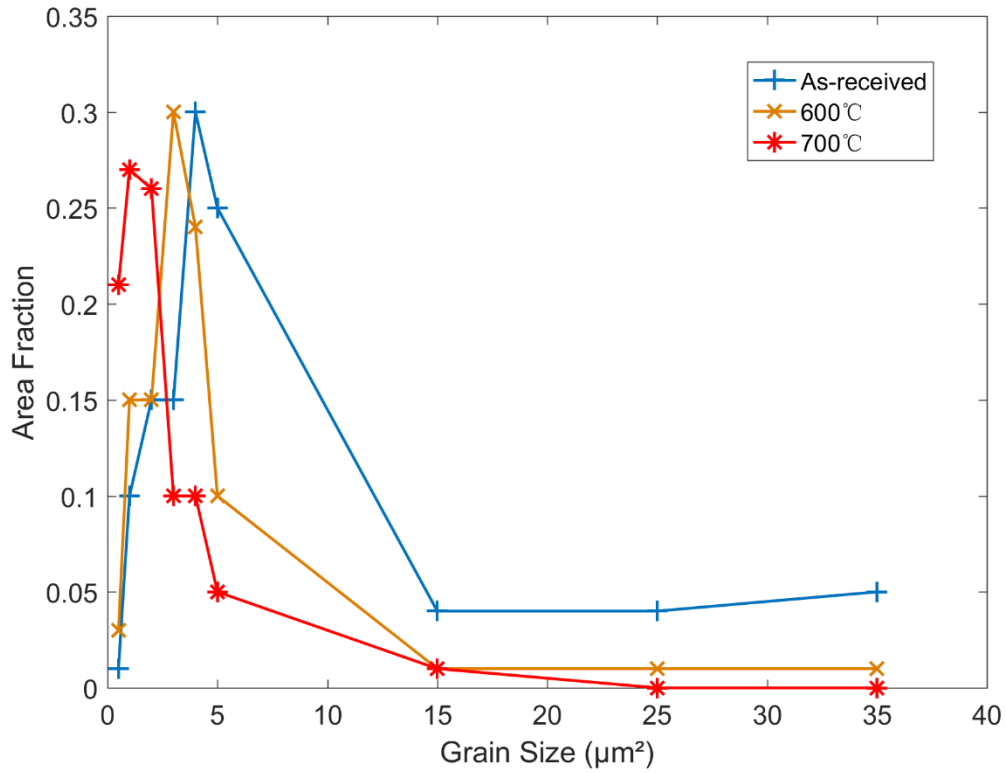

Figure 3-15. Grain size evolution (a) as-received sample, (b) 600 ℃ SPIF sample and (c) 700 ℃ SPIF sample.

The details of the misorientation angle distribution of IPF maps (**Figure 3-14**) are collected from HKL Channel 5 and statistically re-arranged using the MATLB MTEX toolbox which is created by Niessen et al. [149] on the study of grain reconstruction from transformed

microstructures, as shown in **Figure 3-16**. Notably, the as-received sample reveals a high percentage of low-angle grains (< 15°), while the percentage of high-angle grains (> 15°) is increased incrementally, with further temperature increasing and strain hardening. According to a study on SPIF of AA1050 aluminium sheets by Shrivastava and Tandon [116], the low-angle grains (< 15°) commonly appear on the as-received sample and are transferred to high-angle grains (> 15°) on the deforming sample. Such a phenomenon is also a typical feature that reveals the presence of DRX on hot deformation of Ti–6Al–4V alloy, which is also observed in previous study by Orozco-Caballero et al. [150] on the ductility of α-Ti under different temperatures. The study reported that the low-angle grains subject to deforming grains at low temperatures, the majority of them slip to recrystallised high-angle grains in high-temperature deformation, which provides a microstructure that makes the material ductile. Zherebtsov et al. [151] have investigated the microstructure evolution of Ti–6Al–4V during low-temperature superplastic deformation, supported the previous conclusion and reported that the behaviour is more pronounced above 650 ℃ as the temperature could initiate a better DRX process. In this chapter, the thermomechanical straining behaviour at 700 ℃ accelerates the grain slip and dislocation that results in enhanced DRV and DRX. Thus, the misorientation angle increase is much higher than 600 ℃, where 600 ℃ only represents a misorientation texture due to insufficient temperature. The study by Wang et al. [152], on grain refinement mechanism in Ti-6Al-4V alloy, states that the crystal texture of α-Ti induces transformation if the grains slip from stable slip modes to active slip modes during hot deformation works. Therefore, 700 ℃ in the present work provides sufficient temperature to support a constant incremental straining behaviour to the sample for full grains slip initiation.

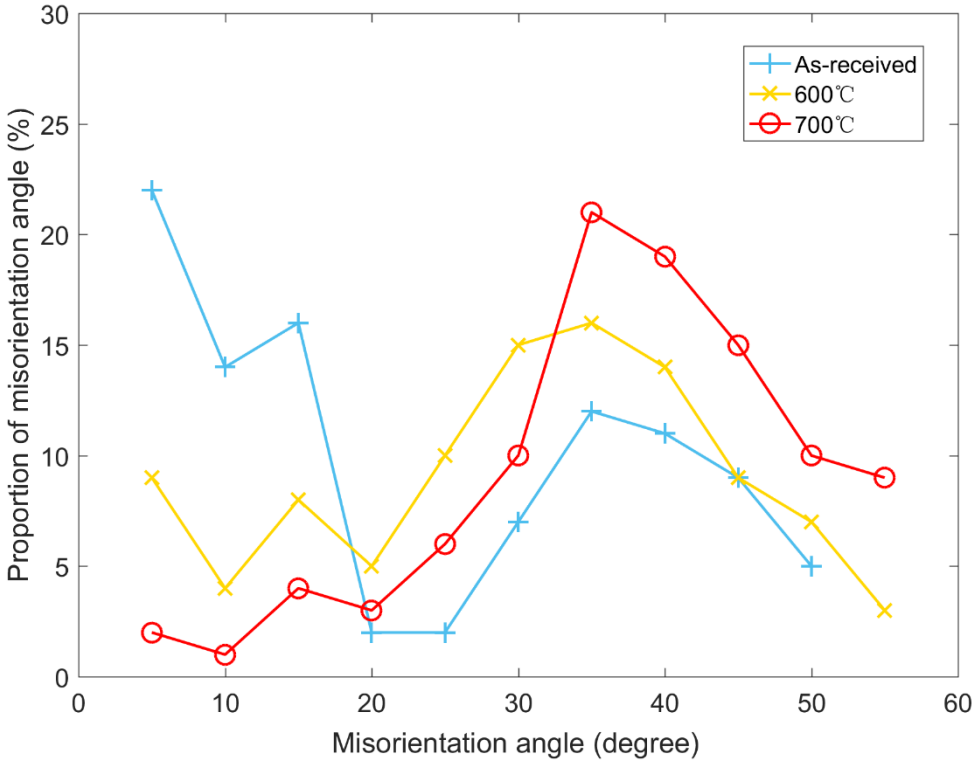

Figure 3-16. Misorientation angle distribution histogram of as-received, 600℃, 700℃ samples.

3.6.3. Micro-hardness

The micro-hardness measurements are applied to the TD surface of each sample. The orientation of the indents was in a step-down arrangement which covers the measurements from the upper sample edge to the lower edge. Due to the sheet thinning in the experiment, only 5 indents can be applied to the deformed samples, where 9 indents were applied to the as-received sample.

As illustrated in **Figure 3-17**, the as-received sample indicates a high-low-high hardness distribution. Since the Ti-6Al-4V sheets being used in this chapter are manufactured by hot rolling, the surface has been heat-treated before manufacturing. Thus, it may result in slight oxidation on the surface. The previous study by Dai et al. [153] on microstructure and hardness of Ti–6Al–4V sheet surface under heat-treatment work, has reported that the average hardness readings on the as-received sample surface are slightly higher than the centre region, which is

due to the surface finishing process that induces thermal-strain. Such behaviour may results in limited oxidation that enhances the α-stabilising of Ti-6Al-4V, thus increasing the hardness at the surface.

Conversely, the micro-hardness profile of all deformed samples (at 600 ℃ and 700 ℃) illustrates a low-high-low distribution profile. Such behaviour can be attributed to the working mechanism of induction heating. In such a system, the magnetic field penetrates the workpiece that generates a rapid alternating eddy current at the centre material which is then spreading to the outer region. Thus, the highest thermomechanical strain will occur in the centre region. Such a phenomenon is a crucial factor that enhances the strain-hardening work from centre to edge. The previous study by Najafabady and Ghaei [154] on the investigation of effects on the hardness of Ti-6Al-4V alloy by hot incremental forming, has reported that the strain hardening is pronounced at 600 ℃, and it is effective in increasing the micro-hardness. Another study by Sabat et al. [155] on the texture and microstructure evolution of Ti-6Al-4V revealed that the strain hardening and grain deformation induce higher micro-hardness readings at 600 ℃. However, the temperature is insufficient to generate the full DRV and DRX process. Thus, it results in the creation of a deforming microstructure, which is demonstrated by the presence of a strong deformation texture. Using a higher temperature of 700 ℃ accelerates the dislocation mobility and results in full DRV and DRX, which can be manifested in grain refinement, as shown in the EBSD measurements (**Figure 3-15** and **Figure 3-16**).

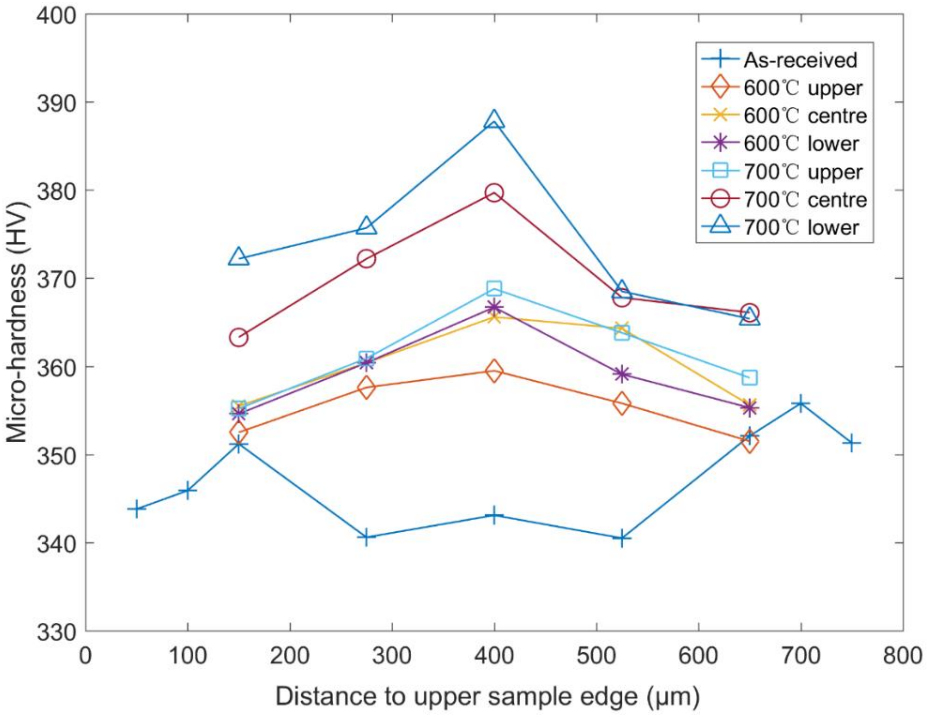

Figure 3-17. Micro-hardness profile distribution of all samples.

3.6.4. Calibration of Zener-Hollomon parameter

To relate the mechanical properties (strain, strain rate) with microstructure evolution (grain refinement, hardness distribution), an Arrhenius type constitutive model has been established to demonstrate the relationship.

In this chapter, the samples are obtained from different positions (upper, centre, lower) of the deformed workpieces at different temperatures (600 ℃, 700 ℃). Three unique nodes from the FE model transverse direction (thickness direction) are selected to extract the raw data for these three positions as shown in **Figure 3-18**. The Savitzky-Golay filter method is used to reduce the frequency noise of the raw data.

Figure 3-19(a) represents the equivalent plastic strain for transverse direction and **Figure 3-19**(b) represents the strain rate for the 600 ℃ samples. The 700 ℃ samples are not illustrated as its data closely resembles that at 600 ℃, with an increase in values. It is worth noting that the equivalent strain distribution can be correlated with strain rate distribution through-

thickness. As the forming tool passes through the unique node, the strain rate climbs the peak and induces an increase in equivalent strain. As stated in the previous study by Smith et al. [156] on the anisotropic yield criterion for pressure-dependent materials, hardening behaviour is sensitive to the equivalent plastic strain distribution, especially dependent on the rigid indenter displacement. In the SPIF process, each step-down increment stretches the surface of the workpiece and induces uniform thickness distribution. As the maximum thickness (between the centre and lower part) is achieved, the strain distribution tends to maintain its value.

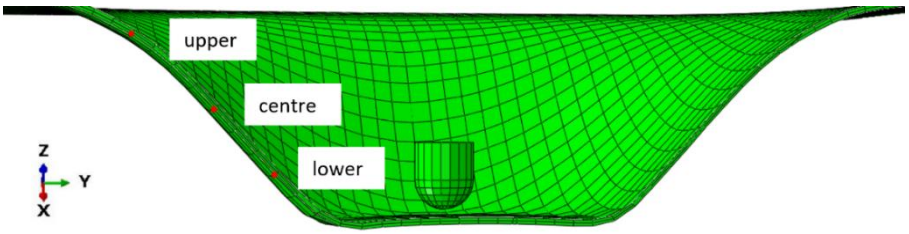

Figure 3-18. Positions of the upper, centre, and lower nodes from the FE model.

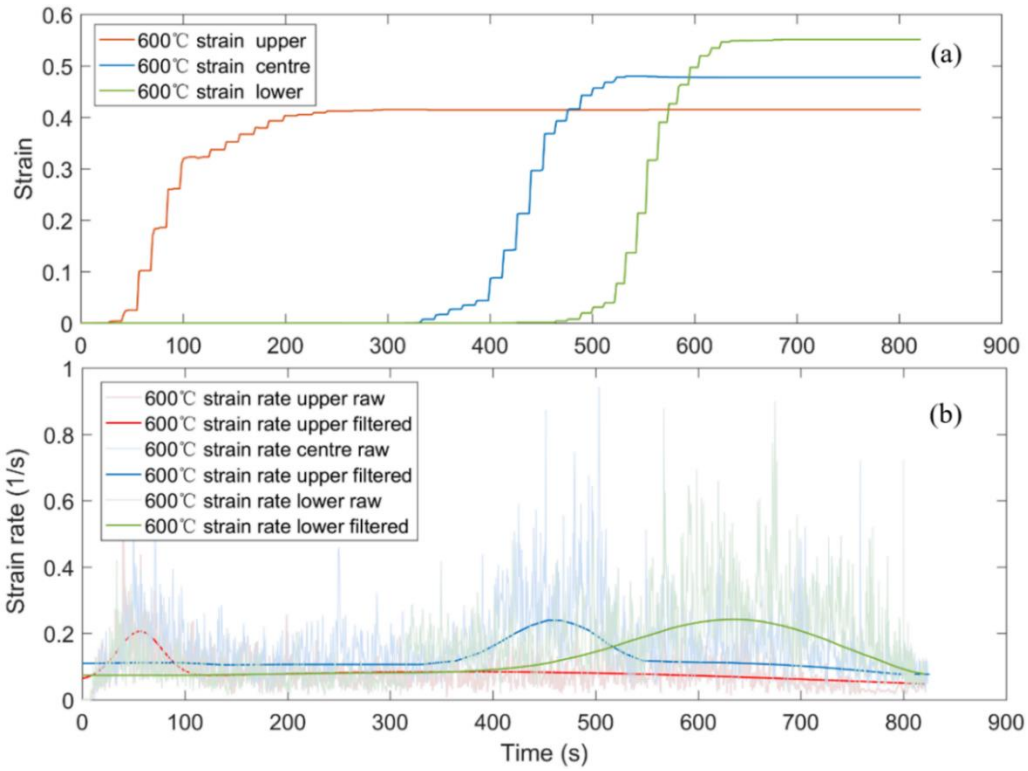

Figure 3-19. FE history output for upper, centre, lower region (a) equivalent strain for SPIF at 600 ℃ (b) strain rate for SPIF at 600 ℃.

To establish the Arrhenius model, the peak strain rate value and its corresponding equivalent strain value for the unique nodes are used for calculation. The 600 ℃ upper samples are used as an example, equivalent strain ≈ 0.4 and strain rate ≈ 0.2 s^{-1}.

The Arrhenius equation can be expressed as:

$$\dot{\varepsilon} = AF(\sigma)\exp\left(-\frac{Q}{RT}\right) \tag{3-9}$$

Where $\dot{\varepsilon}$ is the strain rate, A is the material constant, σ is the flow stress, Q is the apparent activation energy, R is the gas constant (8.314 J/K mol), T is the experimental temperature (K).

The flow stress σ can be expressed as three conditions:

$$F(\sigma) = \begin{cases} \sigma^{n_1}, \alpha\sigma < 0.8 & \text{condition 1} \\ \exp(\beta\sigma), \alpha\sigma < 1.2 & \text{condition 2} \\ \sinh(\alpha\sigma)^n, \text{for all } \sigma & \text{condition 3} \end{cases} \tag{3-10}$$

Where α, β, n_1, n are material constants. Condition 1 represents the low-stress level; condition 2 represents the high-stress level; condition 3 includes all stress and strain level.

The strain rate for deformation can be produced by using the Zener-Hollomon parameter (Z-parameter). The equation can be expressed as:

$$Z = \dot{\varepsilon}\exp\left(\frac{Q}{RT}\right) \tag{3-11}$$

Where Z is the Zener-Hollomon parameter, $\dot{\varepsilon}$ is the strain rate, Q is the apparent activation energy, R is gas constant (8.314 J/K mol), and T is the experimental temperature (K).

The material constants can be calculated by obtaining the gradients from the fitting equations by transforming **Eq. (3-9)** and considering condition 3 from **Eq. (3-10)**. Where the constant n_1 can be obtained from the gradient of plotting $ln\sigma - ln(\dot{\varepsilon})$. The constant β can be obtained reciprocal of gradient from the plotting of $ln\sigma - ln(\dot{\varepsilon})$. By substituting the calculated constants β and n_1 into the equation $\alpha = \beta/n_1$, α can be calculated accordingly. The details of

calculations and fitting graphs are not represented in this chapter to avoid distraction from the main objective here. The calculated material constants are represented in **Table 3-7**.

Table 3-7. Identification of material constants

Constants	**α, MPa^{-1}**	**β**	**n_1**	**n**
600 ℃	0.045	0.0012823	0.0281	29.128
700 ℃	0.036	0.0012465	0.0350	35.831

Substituting the calculated constants to the fitting equations, $Q_{600℃}$ = 261.30 KJ/mol and $Q_{700℃}$ = 321.43 KJ/mol. The results of Q have been validated with studies Tabei et al. [157] on constitutive modelling of Ti-6Al-4V under hot deformation, Weiss and Semiatin [158] on alpha titanium alloys under thermomechanical processing, and Xiao et al. [159] on constitutive modelling and microstructure changes of Ti-6Al-4V under hot tension.

Substituting $Q_{600℃}$ = 261.30 KJ/mol and $Q_{700℃}$ = 321.43 KJ/mol into **Eq. (3-11)**, the equation can be expressed as:

$$Z = \begin{cases} Z_{600℃} = \dot{\varepsilon}\exp\left(\frac{261.30}{RT}\right) \\ Z_{700℃} = \dot{\varepsilon}\exp\left(\frac{321.43}{RT}\right) \end{cases} \quad (3\text{-}12)$$

3.6.5. Grain size vs. Z-parameter

To demonstrate the relation between grain size and Z-parameter, the grain size of the upper, centre, and lower samples was obtained from EBSD. By obtaining the strain rate values from the corresponding FE nodes from **Figure 3-18**, the Z parameter can be calculated using **Eq.**

(3-12). By applying a natural logarithm on both sides of grain size (d) and Z-parameter (Z), the relationship is represented in **Figure 3-20**. It is important to note that labels 1,2,3 in the figure represent the upper, centre, and lower regions of the sample, respectively. Since the temperature supply at the upper region is insufficient, that leads to weak strain hardening and results in higher grain size. Once the temperature acquires a steady-state at the centre and lower region, the grain size is then reduced as better grains refinement is achieved.

It is worth noting that temperature and strain rate are key factors that motivate the grains dislocation microstructurally. An increase in temperature leads to accelerate dislocation process that results in the development of stress relaxation between the grains that enhance the DRX process. Thus, the grain refinement at 700 ℃ is more pronounced than that at 600 ℃. A study by Ammouri et al. [160] has investigated the grain size and Z-parameter relations of AZ31B alloy and reported a similar observation that the grain size is inverse-proportional to Z-parameter. This is attributed to the thermal activation in the material microstructure. The process increases the crystal dislocation which induces grain growth and refinement, results in low angle to high-angle grains transformation in the low Z-parameters zone.

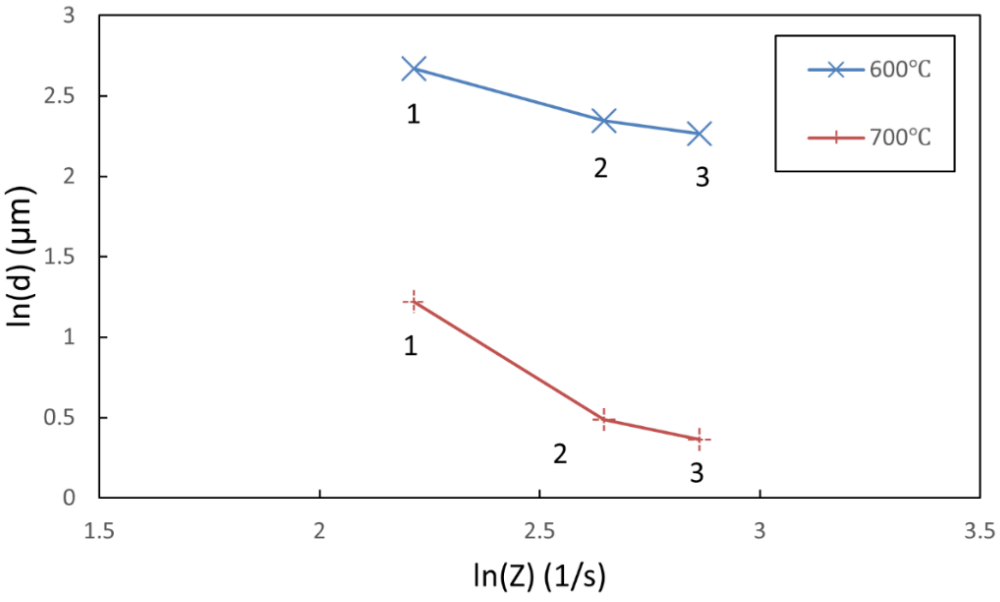

Figure 3-20. Relationship between $\ln(Z) - \ln(d)$.

3.6.6. Micro-hardness vs. Z-parameter

The micro-hardness values were collected from the upper, centre, and lower region samples, with positions from the upper edge to the lower edge to demonstrate the relation between micro-hardness and Z-parameter. The strain rate values were obtained from step-down nodes on the element thickness surface to correspond to each micro-hardness value. Z-parameter values were calculated based using **Eq. (3-12)**. Hence, applying the natural logarithm on Z-parameter, the relationship between them is shown in **Figure 3-21**.

As indicated, the increase of the Z-parameter leads to an increase in micro-hardness. It is observed that the Z-parameter distribution for all samples is in a low-high-low profile which agrees with the micro-hardness profile, as shown in

Figure 3-19. The nodes at the upper and lower edge reveal lower micro-hardness and Z values, and the centre nodes reveal higher values. The strain hardening is relatively higher at centre regions than surface edges since the heat is generated from the material centre to the outer surface. Due to the heat loss, the temperature at the surface edges is slightly lower than that at the centre. This is clear evidence that the temperature affects the Z-parameters distribution, and slight variance of temperature (± 30 ℃) throughout the thickness may induce a noticeable change. By comparing the temperatures, it is noted that 700℃ shows higher micro-hardness readings with close Z-parameter values to 600 ℃. This demonstrates that the DRX at 700 ℃ is more pronounced than at 600 ℃, wherein the strong dislocation mobility of grains enhances the micro-hardness of the workpiece. Similar results were reported by Valoppi et al. [161] on electric heating SPIF, which concluded that the higher temperature initiates higher strain hardening that enhances the stretching mechanism. The temperature releasing strong internal stresses that induces an annealing phenomenon on the workpiece thus induces higher micro-hardness readings.

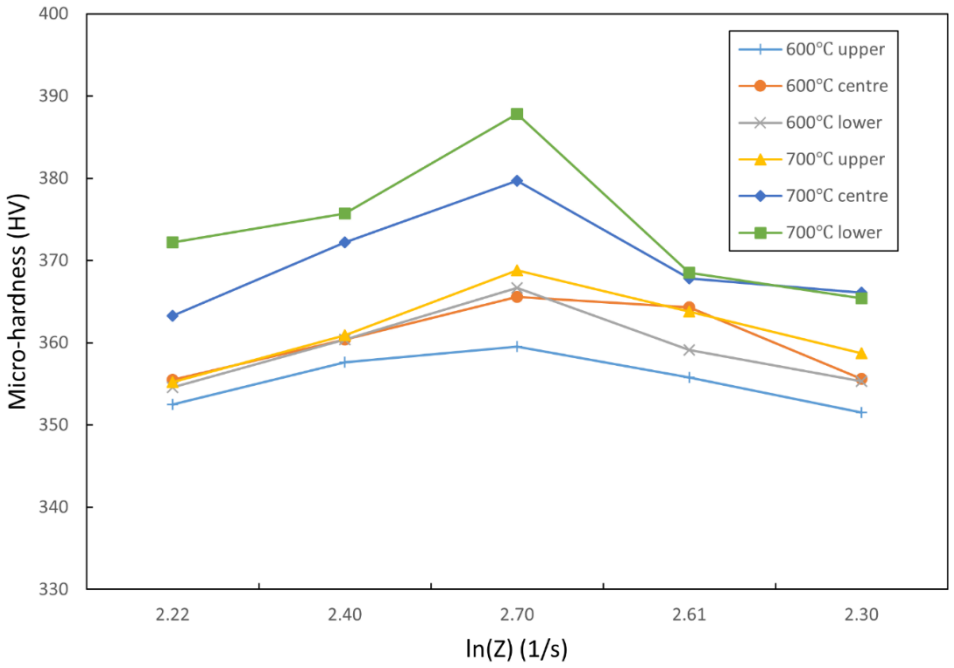

Figure 3-21. Relationship between $\ln(Z)$ – Microhardness(HV)

3.7. Conclusion

This chapter has determined the thermal, mechanical, and microstructure properties of the induction heating assisted SPIF process of the Ti-6Al-4V alloy sheet. The performance is significantly affected by temperature and its relevant strain rate distribution:

- The Nickel alloy ball-roller tool exhibits high performance to reduce friction and improves geometric accuracy and surface quality.
- Temperature is a key factor that affects geometrical accuracy. 700 ℃ produced more efficient DRX than 600 ℃ which enable a more ductile workpiece and induced stable forming force to deform the material hence achieve better geometrical accuracy.
- The lubricant is dissipating as the forming tool passing through the centre and lower region of the workpiece. Therefore, the surface roughness parameter S_a is increased. This phenomenon is more pronounced at 700 ℃ samples.

- The S_z at 600 ℃ has a peak value at the upper region and is reduced for the centre and lower regions. The opposite trend can be observed at 700 ℃ due to the dissipation of lubricant.
- The FE model predicts the mechanical properties with a high degree of accuracy. The temperature variations during the experiments as well as the data filtering affect the prediction accuracy.
- SEM and EBSD results reveal an increment of grain refinement for as-received, 600℃ and 700 ℃ samples. The grains slip is more sufficient at 700 ℃, which leads to pronounced DRX that generates more isotropic microstructure than at 600℃.
- Z-parameter calculations estimate an inverse proportion between the grain size and Z-parameter. This phenomenon is more pronounced at 700℃, which proves that the higher temperature is more effective in activating strong grains slip and re-orientation.
- The relation between micro-hardness and Z-parameter reveals that the micro-hardness is very sensitive to the temperature, as a slight variation of thermal-straining between the material centre and surface will induce a noticeable change in micro-hardness. The induction heating is more efficient at the material centre, thus resulting in a low-high-low micro-hardness profile.

In the future, lubricants should be improved to reduce the dissipation in the heat-assisted SPIF process. Uniform heating temperature and constant strain rate are interesting factors to investigate as they affect the homogeneity of Ti-6Al-4V, resulting in different thermal, mechanical, and microstructural properties.

Acknowledgement

This work was funded by the Department of Mechanical Engineering, University of Birmingham.

4. Lubricant evaluation and improvements in induction heat-assisted incremental sheet forming of Ti-6Al-4V sheets

Weining Li [a], Khamis Essa [a] , Sheng Li [a]

[a] *Mechanical Engineering, University of Birmingham, Edgbaston, Birmingham, B15 2TT, UK*

This research was published as a full-length research article in *International Journal of Advanced Manufacturing Technology*

Li, W., K. Essa, and S. Li, *A novel tool to enhance the lubricant efficiency on induction heat-assisted incremental sheet forming of Ti-6Al-4 V sheets.* The International Journal of Advanced Manufacturing Technology, 2022. DOI: 10.1007/s00170-022-09284-z.

Credit authorship contribution statement

Weining Li: Conceptualization, Investigation, Methodology, Validation, Software, Formal analysis, Writing - original draft.

Khamis Essa: Writing - review & editing, Resources of lab equipment, Supervision, Project administration.

Sheng Li: Management of SEM booking, Writing - review & editing.

Research contributions:

This chapter aims to complete the objective 4 which covers the following insights:

- A new design of Molybdenum disulphide (MoS_2) lubricant to improve its endurance in heat-assisted SPIF.

- A design of controllable water-cooling system to direct liquid lubricant throughout the ball-roller tool to reduce the thermo-expansion and apply the lubricant to the workpiece in accordance with tool motion.

Abstract

For heat-assisted single point incremental sheet forming (SPIF) works of Ti-6Al-4V sheets, the use of lubricant has shown significant effects on surface quality and geometric accuracy at higher temperatures. Molybdenum disulphide (MoS_2) is a common lubricant widely used in SPIF works, however, it usually indicates ineffective performance at high temperatures. This chapter has studied different lubricants and proposed a novel mixture of MoS_2 to provide better surface quality and improve geometric accuracy. A forming tool with a ball-roller and water channel was designed to enable the MoS_2 mixture to pass through the tool tip, allowing easy application of the lubricant on the localised area and reduce the thermal expansion on the ball-roller. Surface roughness analysis has revealed that the water-cooling MoS_2 mixture performed well in reducing friction effects during process and produced better surface quality. Forming forces measurements, scanning electron microscope (SEM), energy dispersive X-ray Analysis (EDX) and micro-hardness tests also indicated that a higher strain hardening behaviour was detected for the water-cooling MoS_2 mixture.

Keywords: hot incremental sheet forming, lubricant, wear, surface roughness, micro-hardness, microstructural analysis, geometric accuracy, thickness profile.

4.1. Introduction

Single-point incremental forming (SPIF) is a flexible sheet forming process which has been investigated over decades to deform sheet metal to produce complicated prototypes. However, the deformation of high strength materials, such as Ti-6AI-4V alloy, remains a challenge. In recent years, the heat-assisted SPIF process has been thoroughly researched to produce a heat source to soften and deform the materials to the designated shape. However, the surface quality suffered and had declined at the end of the process. In the heat-assisted SPIF systems, it can be seen that surface roughness is a serious challenge that occurred in all hot SPIF processes.

MoS_2 is the most common lubricant used in the majority of hot SPIF works. By researching electric heat-assisted SPIF of Ti-6Al-4V studies [147, 162], it could be seen that the common MoS_2 was insufficient at temperatures above 450 °C, with electric sparks having a significant effect on the removal of the water-solubility of the lubricant. As the tool passed through the lubricant ash, the remaining lubricant adhered to the surface increasing the wear, which affected the surface quality. Cheng et al. [52] and Li et al. [163] have studied the ultrasonic vibration-assisted (UV) SPIF process and proposed positive effects in enhancing the geometric accuracy and surface quality using liquid lubricant (Shell M68) to improve the contact condition. Another study by Liu et al. [29] proposed a novel ball-roller for electric heat-assisted SPIF of Ti-6Al-4V sheets, which provided a better surface quality by reducing friction between the tool and the workpiece with common machine grease. The studies of induction heat-assisted SPIF works of Ti-6Al-4V have revealed a slightly better outcome as shown in the study by Ambrogio et al. [4]. Results revealed that without the effects of electric sparks, the common MoS_2 paste is more functional than when used with electric heat-assisted SPIF with the assistance of cryogenic cooling. However, the rapid change of temperature on the upper and lower surface of the workpiece still resulted in the ineffectiveness of the lubricant and an unsustainable performance. Another study by Ortiz et al. [33] revealed that high-temperature lubricant oil in

induction heat-assisted SPIF of Ti-6Al-4V sheets produced more favourable results showed that on surface quality than the common low-temperature lubricants. However, the endurance of lubricant was still insufficient at the end of the process, with a large amount of adhered wear observed.

In summary, it can be noticed that the endurance of lubricants during the heat-assisted SPIF process is a key factor affects the surface quality. The majority of common lubricants are ineffective at the higher temperature (above 400°C) deforming process. The dissipation of lubricant in the high-temperature SPIF is a common phenomenon that results in significant adhesion wear. In this analysis, a Nickel alloy ball-roller tool has been designed and integrated into a high-frequency induction heat-assisted SPIF system. By increasing and maintaining a localised temperature of 700°C, the performance of different lubricants has been studied, and a novel method of lubricant application was proposed to improve the surface quality and remain geometric accuracy.

4.2. Materials and methods

4.2.1. Materials

All workpieces in this analysis were standard hot-rolling Ti-6Al-4V alloy sheets with a size of 150mm x 150mm and a thickness of 0.8mm with same chemical composition as **Table 3-1**.

The lubricants used in this analysis can be classified into three lubricants. Lubricant 1, provided by CRC Ltd, is a standard graphite grease that consists of graphite particles and MoS_2 paste. According to the supplier information, the lubricant can be serviced between -30 °C and 650 °C. lubricant 2 is a mixture of lubricant 1 and machine lubricant oil provided by Ambersil Ltd, which has a protective agent based on rust inhibitors and surfactants enabling it to reduce friction and wear on the workpiece surface. According to the supplier information, the lubricant oil can service up to 300 °C. Lubricant 3 has used lubricant 2 as the main component on the

workpiece surface with an external liquid lubricant from the water-cooling channel. The liquid lubricant is a mixture of coolant with MoS_2 powder. The coolant is provided by AZURE Ltd, which contains anti-corrosion additives to reduce friction and rust. The MoS_2 powder is 98.5% pure with an average of 1.5 μm particle size provided by OKS Spezialschmierstoffe GmbH Ltd. To mix MoS_2 powder with the coolant, DISPERMAT shear dissolver was used. According to the previous study by Hussain et al. [88] on the investigation of lubricant effects on SPIF, a high weight (20%) of MoS_2 powder has been used in water and alcohol to make liquid lubricant and spray to increase the endurance of lubricant. The lubricant indicated better endurance, however, the adherence on surface was pronounced. The other study by Azevedo et al. [91] has commented that high condensation can be observed in the dispersion of lubricant powder in water which affects the performance of the mixture lubricant. Diabb et al. [89] has proposed that the small size powder has better solubility than other liquid agents. The shear dissolver can provide a high shear force to dissolve the MoS_2 powder into the coolant by laminate orientation without the phenomenon of condensation. The details of each lubricant are illustrated in **Table 4-1.**

Table 4-1. Details of lubricants

Lubricant	Content	Mix method	State
1	Graphite grease	Non	Paste
2	Dispersion of lubricant 1 (20%) in machine oil	600 rpm of 30 mins	Paste
3	lubricant 2 on surface with external lubricant from water channel (2% MoS_2 powder in water coolant)	600 rpm of 60 mins	Paste and Liquid

4.2.2. Tool and SPIF system design

To deform high strength metal sheets like Ti-6Al-4V, a high forming force is required for the process. Wear and friction tracks are a common phenomenon usually present on the formed workpiece and forming tool [164-166]. The tool design is same as illustrated in **Figure 3-1**. To improve working of lubricant in this process, a water container with a tube was connected to the water-in valve to allow a water flow pass through the channel and smooth the ball-roller. At the meantime, another tube connected the water-out valve to a water tank to pump out the remaining water in the channel. The water tube was 5 mm diameter and connected to a pump with power of 300 rpm throughout the whole process.

4.2.3. Experimental parameters

The following equipment, tool design and parameters are same as explained in chapter 3:

- The tool design is same as illustrated in **Figure 3-1**.
- The final shape is same as illustrated in **Figure 3-3**.
- The tool path is same as illustrated in **Figure 3-3** with following modified parameters as shown in **Table 5-1**.

Table 4-2. Experimental parameters

EXPERIMENTAL PARAMETERS	TARGET TEMPERATURE (700 ℃)
Feed rate (mm/min)	1000
Step size	1.0
Power (kW)	5.5
Frequency (kHz)	700

4.3. Results and discussion

4.3.1. Temperature distribution and forming force

The temperature distribution for experiments with lubricants 1, 2 and 3 are illustrated in **Figure 4-1**. It can be seen that the temperature distributions for lubricants 1 and 2 are very close, the temperature rose rapidly for around 30 s to a relatively steady-state stage and then increased gradually, but marginally, until the end of the process. The temperature at the end of the experiment (final 100 s) was around 20 °C higher than the target temperature (700 °C). As the forming area was getting smaller, according to the SPIF process, the temperature was more concentrated thus resulting in a re-heating behaviour that increased the temperature. For the lubricant 3 experiment, it took around 60 s to increase the temperature to the steady-state stage and it maintained that level almost constantly until the end of the process. It was evident that the water-cooling system was sufficient to balance the temperature increase throughout the process. It should be noted that the measured temperature distributions were smoothed using Savitzky-Golay smoothing filter [167] to reduce the noise.

The forming force profiles from the experiments with lubricants 1, 2 and 3 are illustrated in **Figure 4-2**. Lubricants 1 and 2 have relatively similar profiles, whilst lubricant 3 differs. This is mainly attributed to the effects of water cooling throughout the process. As the sustainable localised coolant support from the forming tool, the hot strain-hardening work on the workpiece surface is reduced which results in a higher forming force, especially at the initiation stage. By comparing the results with the previous study by Honarpisheh et al. [168], on electric heating SPIF, and another by Al-Obaidi et al. [26], on induction heating assisted SPIF of Ti-6Al-4V sheet, it could be found that the forming force at the initiation stage is unstable, as the dynamic recrystallisation (DRX) at this stage is insufficient to form isotropic microstructure to maintain a constant forming force. This is the same reason for the forming force growth in this chapter. Due to the sustainable support of coolant, the temperature distribution on the surface of the lubricant 3 experiment is maintained better than lubricants 1 and 2 thus resulting in a relatively graduate growth of forming force. Please note that forming profiles are smoothed by Golay smoothing filters to reduce the noise frequency.

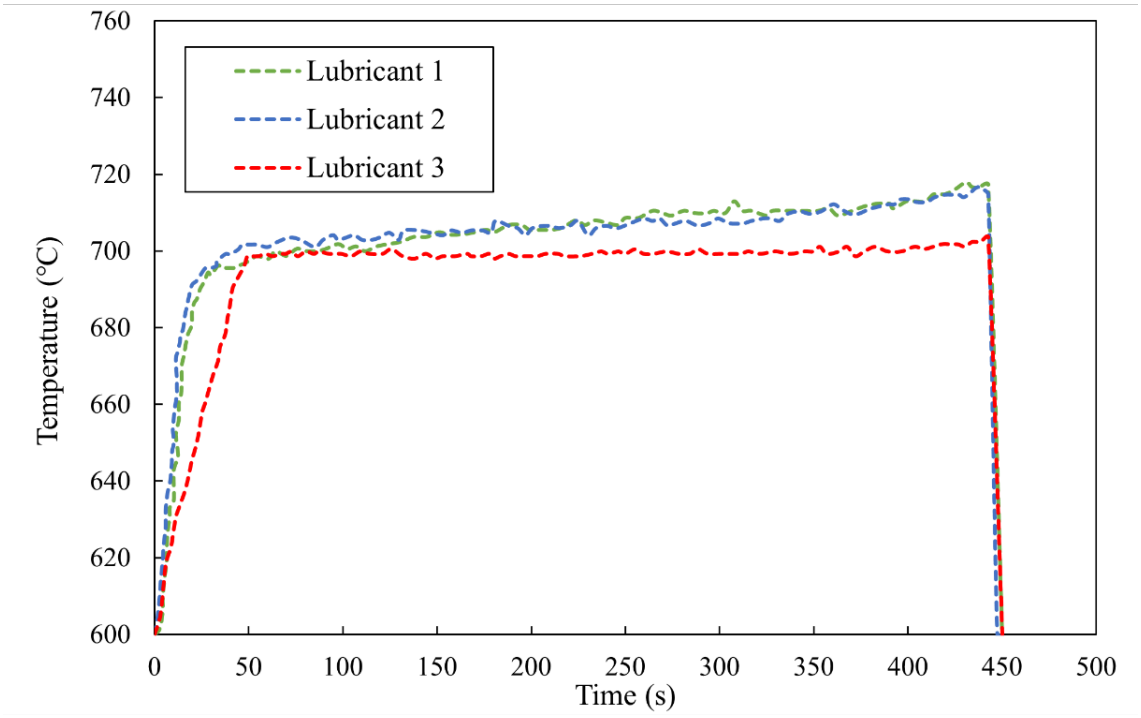

Figure 4-1. Measured temperature history for SPIF for lubricant 1, 2 and 3 experiments.

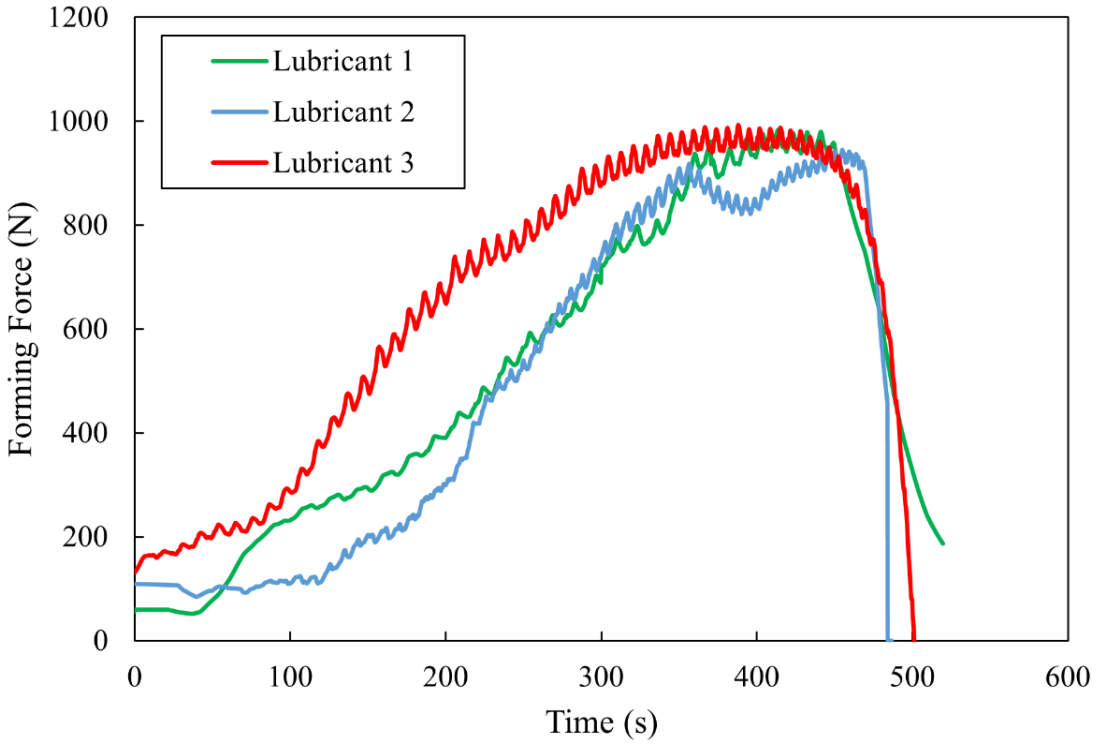

Figure 4-2. The experimental forming force profiles for lubricant 1, 2 and 3 Forming.

4.3.2. Surface roughness

For each formed workpiece (using lubricants 1, 2 and 3), three sections (5mm^2) were removed from the upper, centre and lower regions to determine surface roughness. All measurements were taken using the Alicona Infinite Focus optical 3D surface measurement system with a 50 nm minimum vertical resolution and 0.03 μm minimum measurable roughness and 2% error. The cut samples and optical microscope measured data for lubricants 1, 2 and 3experiments are illustrated in **Figure 4-3**, **Figure 4-4** and **Figure 4-5**.

It can be observed from **Figure 4-3**(a) that lubricant 1 produced the worst surface quality as wear micro-cracks (light areas) and observable cracks with peels of surface (dark areas) appeared on the workpiece surface. From the upper to lower region (**Figure 4-3**(b-d)), the lubricant dissipated according to the process. However, since the heating temperature was

higher than that recommended for the lubricant, the rapid dissipation resulted in a layer of contamination that adhered to the forming tool and workpiece surface, which increased the friction force that caused adhesive and abrasive wear. Similar results were observed in a study by Najafabady and Ghaei [162], on high-temperature SPIF of Ti-6Al-4V sheets, providing additional evidence that insufficient support from the lubricant is a common challenge in the high-temperature SPIF process. As the process progressed from the upper to lower region, the increase in temperature and dissipation of lubricant lead to severe wear tracks that formed surface cracks incrementally, resulting in unfavourable surface quality.

For lubricant 2, the result is displayed in **Figure 4-4**(a), it can be seen that the surface quality has been improved significantly than lubricant 1. There are no observable surface cracks in the upper region as shown in **Figure 4-4**(b), and the centre and lower regions in **Figure 4-4**(c-d) also reveal better surface quality. The lubricant oil from lubricant 2 has indicated a strong reason to retain the presence of lubricant 1 in high-temperature SPIF work. Although lubricant 2 was not functional throughout the whole process, the lubricant still exhibited enhanced performance over lubricant 1.

The best surface quality was achieved with lubricant 3, as shown in **Figure 4-5**(a). It can be observed that the wear tracks increased from the upper region to the centre region as shown in **Figure 4-5**(b-c). A slight track of micro-cracks has been observed in the lower region as illustrated in **Figure 4-5**(d). These results provide evidence that the sustainable coolant lubricant support from the water-cooling system is sufficient to reduce friction on the workpiece. Referring back to **Figure 4-1**, it appears that the coolant lubricant also functioned to balance temperature within a steady range, enabling lubricant 3 to remain effective throughout the whole high-temperature SPIF process. The surface quality of lubricant 3 is observable better than lubricants 1 and 2, and the results are comparable with the study by Ao et al. [60], on electric heat-assisted SPIF of Ti-6Al-4V sheets which has indicated significant

current-carrying wear, and another study by Ambrogio et al. [147], on induction heat-assisted SPIF of Ti-6Al-4V sheets where severe adhesive wear remained.

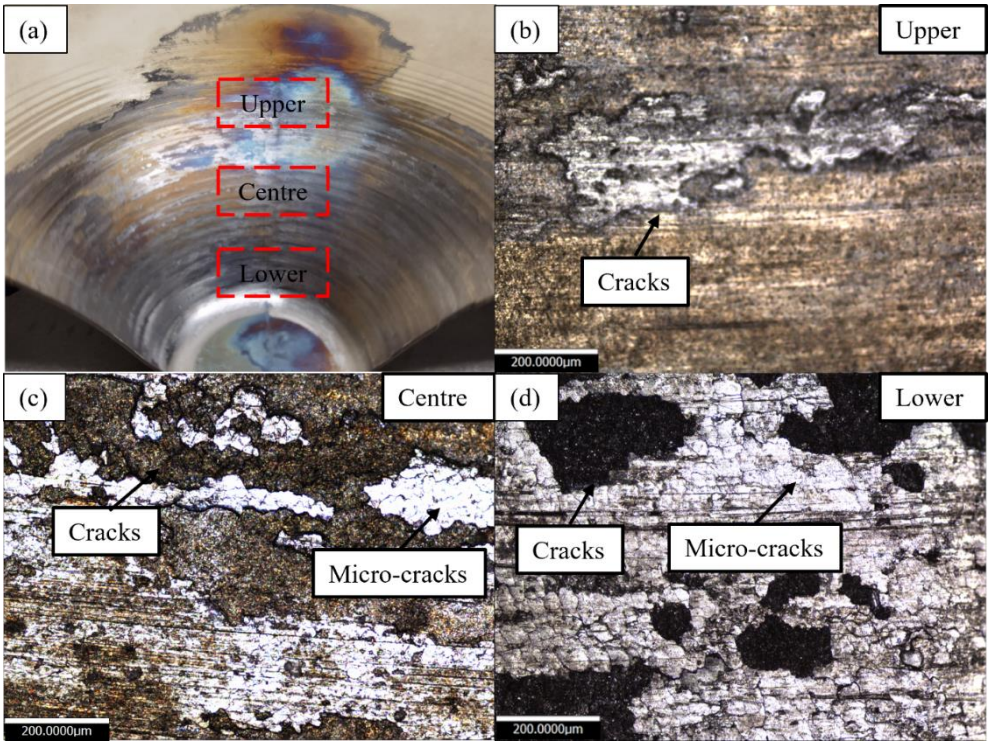

Figure 4-3. OM observation for lubricant 1: (a) locations of sample collection; (b) upper region sample; (c) centre region sample; (d) lower region sample.

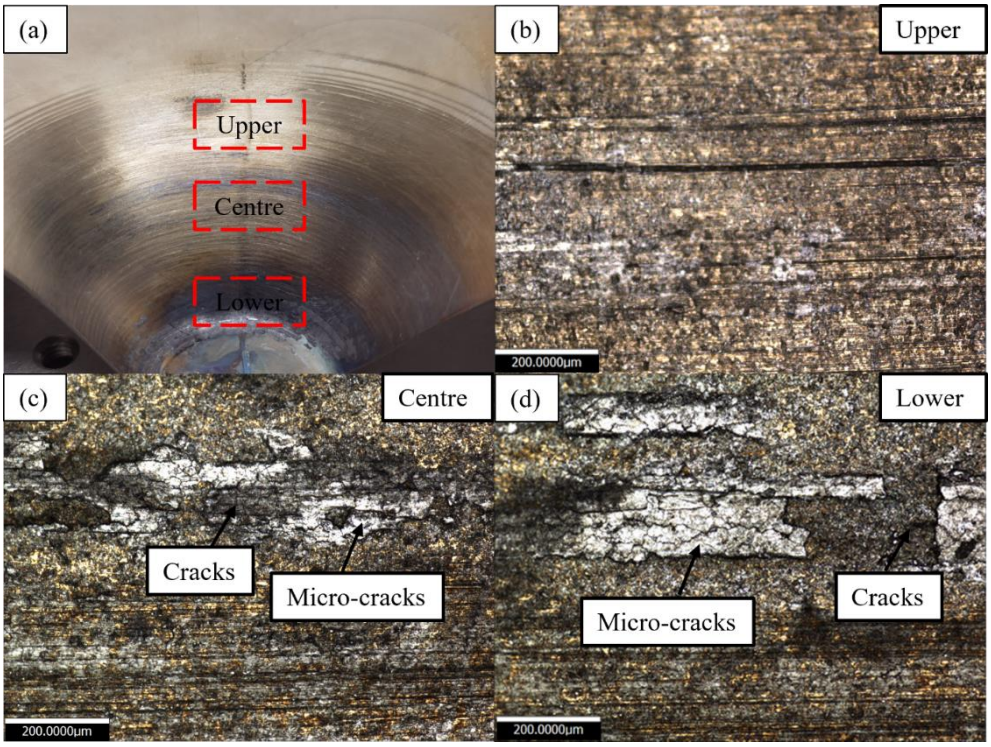

Figure 4-4. OM observation for lubricant 2: (a) locations of sample collection; (b) upper region sample; (c) centre region sample; (d) lower region sample.

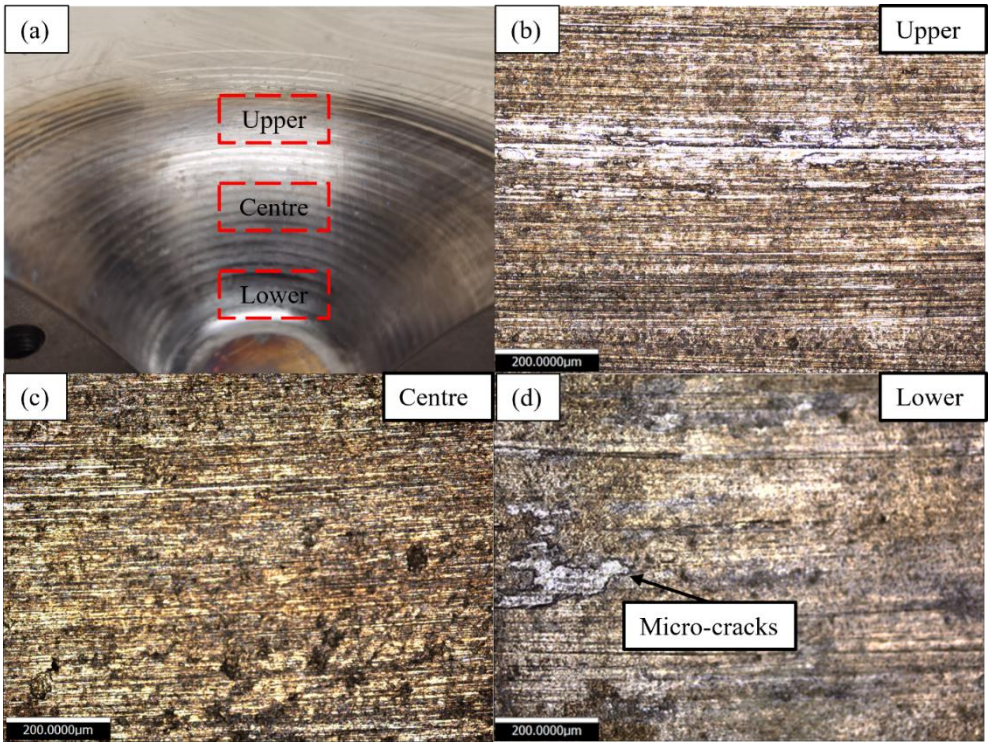

Figure 4-5. OM observation for lubricant 3: (a) locations of sample collection; (b) upper region sample; (c) centre region sample; (d) lower region sample.

The 3D surface topography roughness measurements of lubricants 1, 2 and 3 (upper, centre and lower) samples are presented in **Figure 4-6** to

Figure 4-8. The readings of average area surface roughness (S_a) are shown in **Figure 4-9**. The detail roughness values of root-mean-square height (S_q), maximum peak height (S_p), maximum valley depth (S_v), maximum height (S_z) of each lubricant of lubricant are listed in **Table 4-3**.

In **Figure 4-6**(b-c), it can be seen that lubricant 1 produced a high density of surface cracks in the centre and lower regions and these cracks expand a high difference between the workpiece outer surface layer and substrate. lubricant 2, **Figure 4-7**(b-c), reduced the effects significantly, and no observable surface cracks appeared when using lubricant 3,

Figure 4-8(b-c).

Figure 4-9 shows that the growth of surface roughness was the same for all three lubricants. The measurements of S_a increased incrementally through the process. The increase in S_a with lubricant 2 is less pronounced than for lubricant 1, and lubricant 3 results in the lowest growth trend. These results agree with the observations were seen in **Figure 4-3** to **Figure 4-5**.

By investigating the measured amplitude parameters of each sample in **Table 4-3**, it can be observed that the S_q is following the same trend as S_a. This provides evidence that friction is increased as the lubricant dissipates. It should be noticed that the S_z values (difference between S_q and S_v) upper regions of all three lubricants are in similar values, indicating the effective performance of the lubricants at upper regions. The S_z values for lubricant 1 centre and lower regions are incredible high, providing clear evidence that surface cracks destroyed the workpiece surface and left a valley between the outer layer and substrate. lubricant 2 generated slightly less damage, with significantly improved results than lubricant 1 and lubricant 3 has revealed the best performance in reducing surface damage. Please note that all presented data were filtered by the Gaussian filter for inclined planar surfaces to reduce the noise.

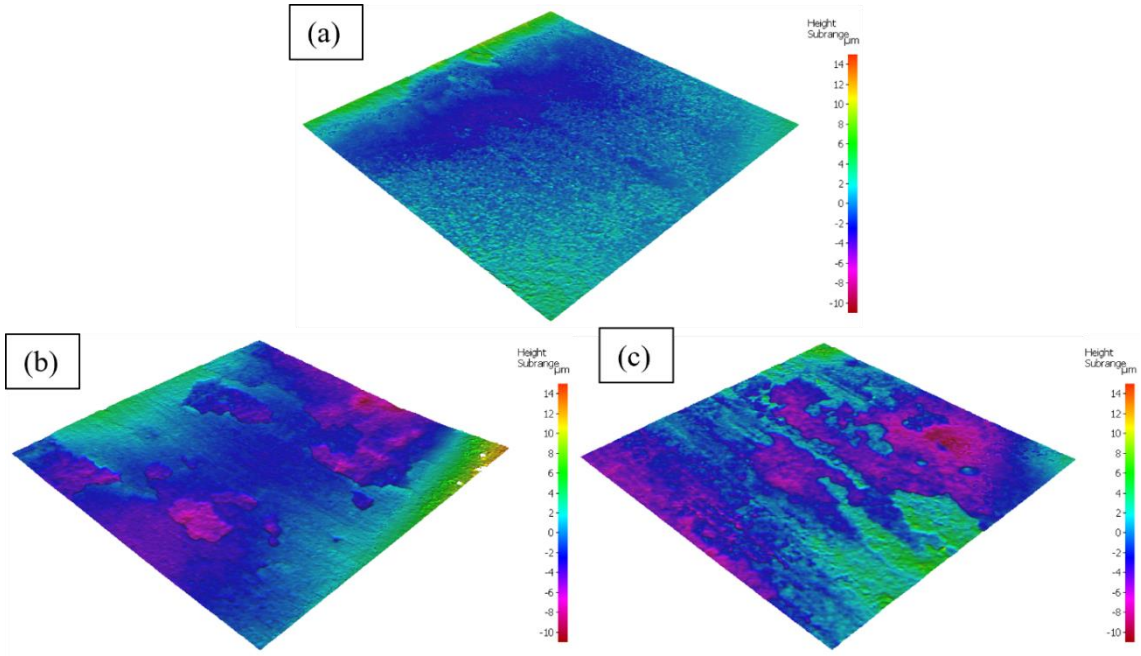

Figure 4-6. 3D surface topography surface roughness measurements for lubricant 1: (a) upper region; (b) centre region; (c) lower region.

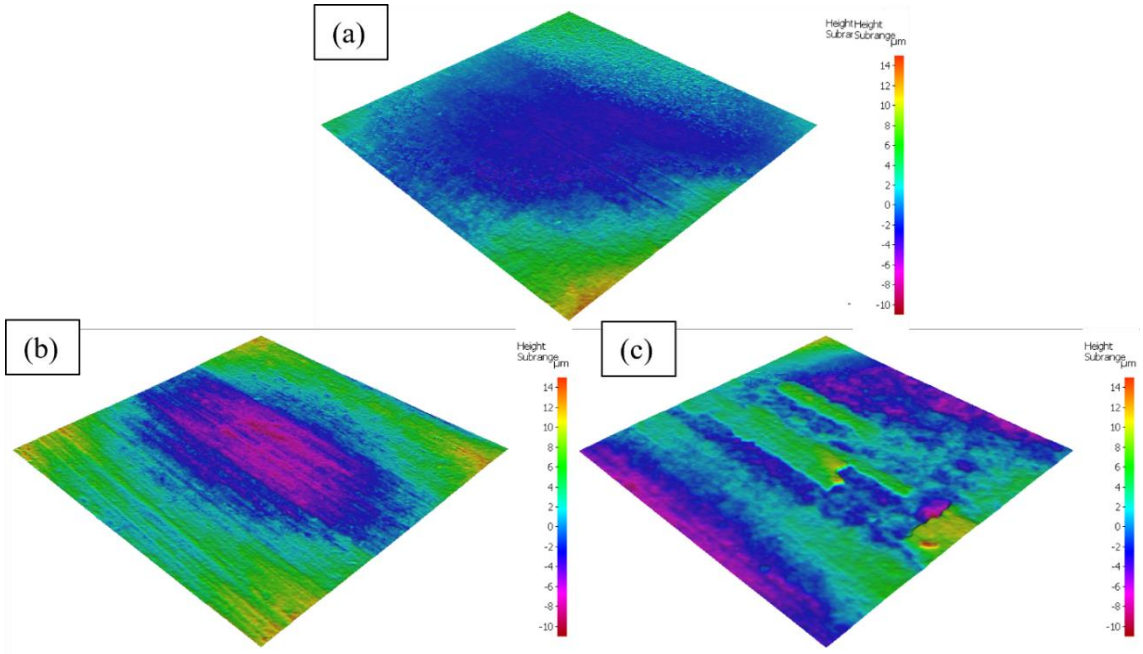

Figure 4-7. 3D surface topography surface roughness measurements for lubricant 2: (a) upper region; (b) centre region; (c) lower region.

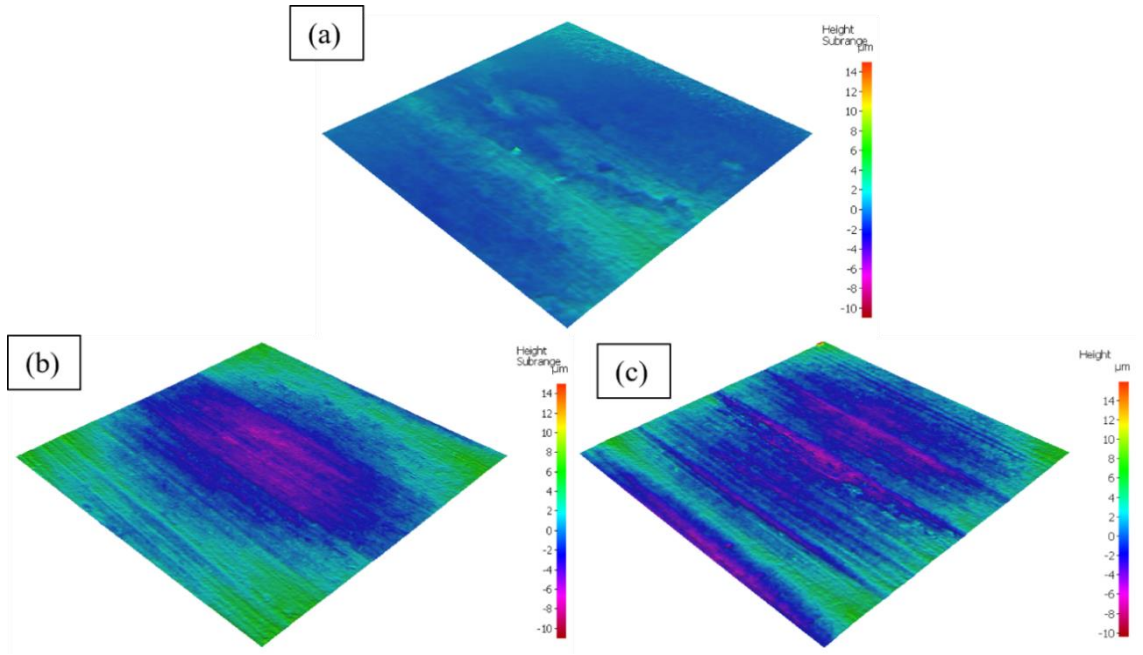

Figure 4-8. 3D surface topography surface roughness measurements for lubricant 3: (a) upper region; (b) centre region; (c) lower region.

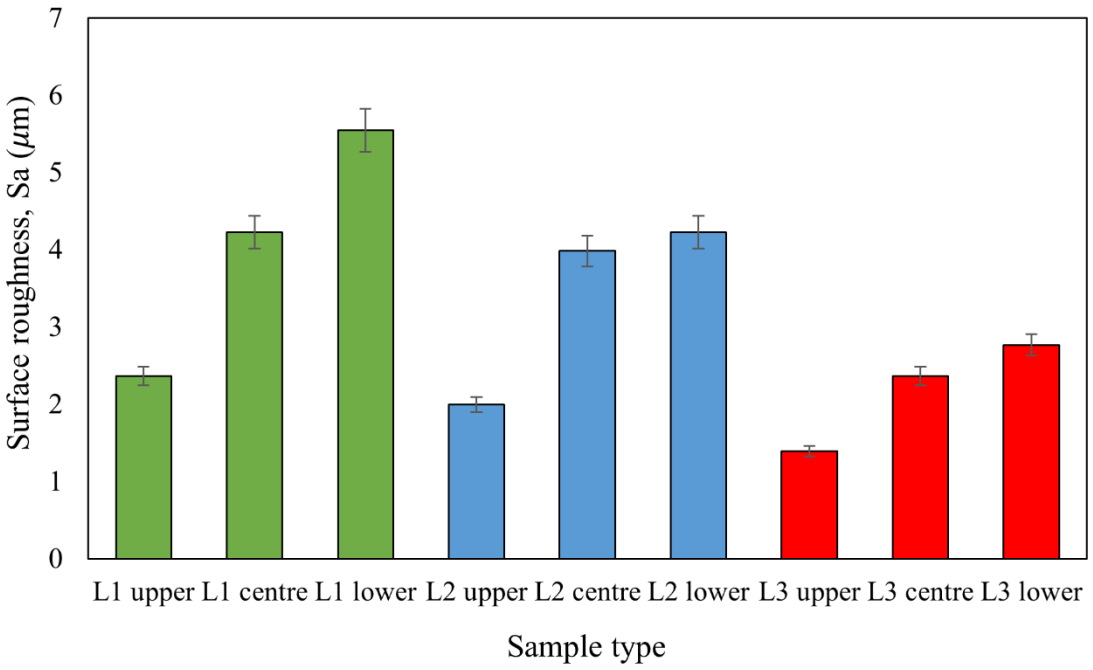

Figure 4-9. Average surface roughness measurements (Sa) for lubricants 1, 2 and 3 (upper, centre, lower).

Table 4-3. Measured amplitude parameters of each lubricant sample

	S_q (µm)	S_p (µm)	S_v (µm)	S_z (µm)
lubricant 1 upper region	1.012	5.221	3.827	9.048
lubricant 1 centre region	2.116	6.098	5.751	11.849
lubricant 1 lower region	2.261	6.985	6.913	13.898
lubricant 2 upper region	0.806	5.005	1.509	6.514
lubricant 2 centre region	1.381	6.135	5.593	11.728
lubricant 2 lower region	1.913	6.774	5.622	12.436

lubricant 3 upper region	0.504	2.155	1.334	3.444
lubricant 3 centre region	1.051	2.744	3.636	6.380
lubricant 3 lower region	2.247	4.185	4.913	9.231

4.3.3. Geometric profile

Geometric accuracy is a significant factor that reveals the overall performance and quality characteristics of products made by the SPIF process. The FARO Edge-scan 8-axis laser 3D scanning arm has been used in this study to measure the 3D geometric accuracy of the deformed parts. The resolution of this system is 40 μm, with an error of ± 0.2 μm. Geomagic was then used to process the cloud of points and obtain a highly accurate measurement of the final profile and thickness distribution.

The geometric profile of lubricants 1, 2 and 3 are shown in **Figure 4-10**. The experimentally measured profiles were obtained using FARO 3D scanning on the clamped workpiece to reduce the spring-back effects from unclamping and cooling. As illustrated in **Figure 4-10**, there was no significant difference between the three lubricants. By dividing the profiles into three stages, it can be seen that all three lubricants were practically identical at stage 1 (upper region). lubricant 3 then started to diverge slightly at stage 2 (centre region), before all three lubricants became diverse from each other at stage 3. The reasoning can be explained by the temperature and forming force profiles in **Figure 4-1** and **Figure 4-2**. For the experiments of lubricants 1 and 2, the temperature support for the upper regions was insufficient to dissipate the full volume of the lubricant on the surface. As the process progressed to the centre and lower regions, the dissipation of lubricant was more pronounced, thus increasing the surface roughness accordingly. The forming force distributions also indicated that the growth of lubricant 3 is more stable than lubricants 1 and 2 from the upper to centre region which revealed that the

water-cooling lubricant has support to cool down the tool and the corresponding workpiece surface and balanced the temperature at the lower region. Therefore, lubricant 3 revealed a superior geometric profile due to its relatively stable temperature and forming force distributions which provided better control of the geometric accuracy.

It was observed that the successful application of rapid localised heating enhanced the deformation process. Hence, it can be concluded that induction heat-assisted SPIF can deform Ti–6Al–4V sheets with high geometric accuracy by increasing the DRX in the material microstructure. This is a typical phenomenon that occurs in high-temperature SPIF as the thermomechanical behaviour may induce high residual stress and stress relaxation in the material, which can result in spring-back and pillow effects. Similar observations were also reported in a previous study by Ortiz et al. [140], on the geometric accuracy of the high-temperature SPIF process.

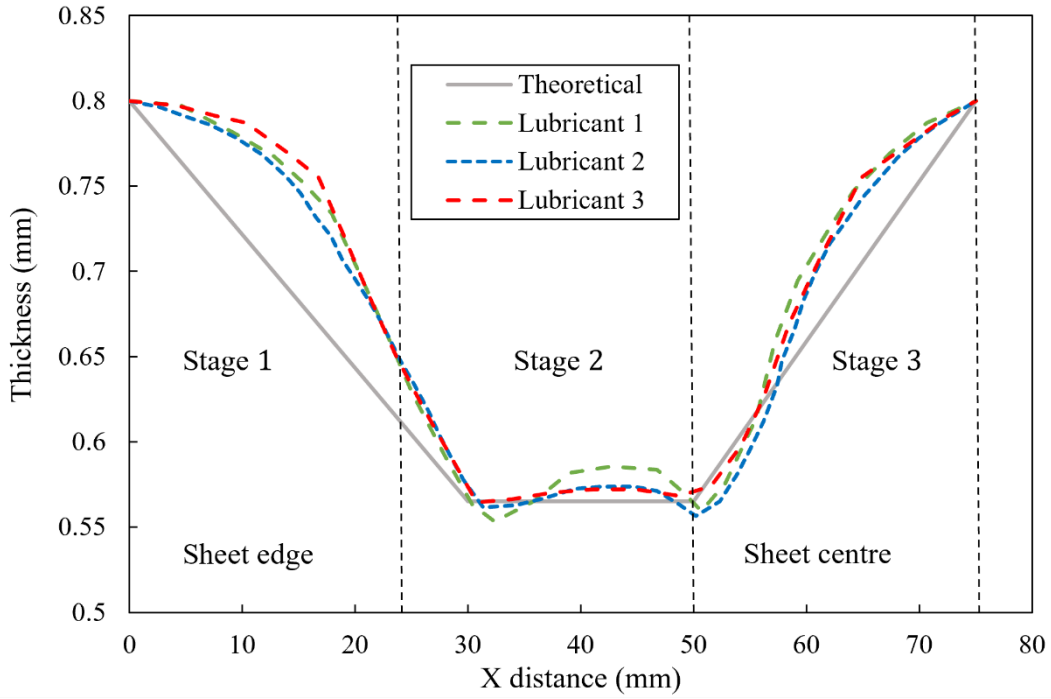

Figure 4-10. Geometric profile for lubricant 1, 2 and 3 experiments.

4.3.4. Thickness profile

For each lubricant, the thickness profiles, measured from the sheet edge to its centre were determined, as illustrated in **Figure 4-11**. The sheet thickness was obtained using the FARO 3D scanner for two paths, with one path on the upper surface of the deformed workpiece and the other one on the lower surface. The X, Y and Z coordinates were collected accordingly, and the data obtained using Equation 1, the theoretical thickness profile can be obtained from the sine law as shown in Equation 2. Cao et al. [141] studied the incremental sheet forming (ISF) process and reported that the sine law is efficient to predict the thickness distribution of deformed parts.

The sheet thickness distribution has been expressed in chapter 3, **Eq. (3-7)** and the theoretical thickness distribution was expressed in chapter 3, **Eq. (3-8).** This equation was proposed in a previous study by Hussain and Gao [32], to estimate the thickness distribution in SPIF. Lu et al. [143] also applied the same principle to predict the theoretical thickness of double-side ISF. Another study by Tolipov et al. [144], on multi-point forming, again verified the equation's efficiency in estimating the thickness distribution in sheet metal forming.

As illustrated in **Figure 4-11**, it can be seen that the sheet thinning is proportional to the cone depth. The sine law predicted sheet thinning of 0.565mm for a 45^{o} wall angle. By dividing the profile into 3 stages, it is observed that all three lubricants had diverse growth at stage 1 before converging into stage 2. However, the stage 2 progressed diversity was detected again at the thinnest thickness area, before convergence at stage 3. Similar to the geometric profile, such phenomenon can be attributed to the temperature and forming force profile, as shown in **Figure 4-1** and **Figure 4-2**, respectively, but with opposite results since the lubricant effects are not sensitive at the early stages. At stage 1, insufficient temperature and an unstable forming force resulted in differing initial profiles for the three lubricants. Once the temperature and forming force reach a steady-state between stages 1 and 2, good correspondence was achieved by all

three lubricants. The lubricant dissipation effects were shown to be most pronounced at the thinnest thickness area in stage 2. Here the temperature and forming profile were relatively stable, but the unstable friction force from lubricant 1 was the main reason that caused the change in its profile. Once the critical point is passed at Stage 3, all three lubricants tended to converge as the DRX for all experiments is fairly initiated. Studies by Ao et al. [60] and Vahdani et al. [61] also reported similar findings for the high-temperature SPIF process of Ti-6Al-4V sheets.

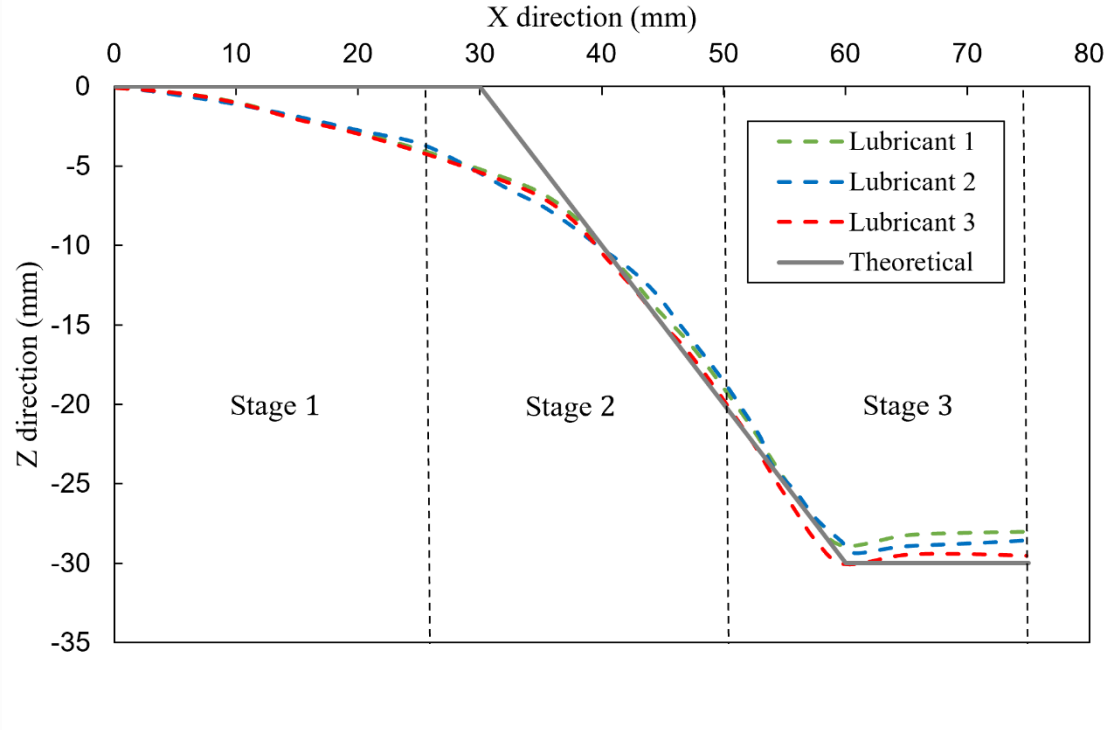

Figure 4-11. Thickness profile for lubricant 1, 2 and 3 lubricant experiments.

4.3.5. SEM

A tabletop Hitachi TM3030 SEM was used to analyse the microstructure of the as-received and deformed samples. The SEM and EDX images of the investigation area were taken at magnifications of 600x to 2000x with an accelerating voltage of 15 kV. The SEM samples were divided into two groups, surface samples and cross-section samples. The surface samples group:

The as-received samples and deformation samples (upper, centre and lower) of each lubricant were cleaned with 70% alcohol and then ultrasonically cleaned with 100 W and 40 kHz for 20 mins to remove any contamination from the samples. During the SEM investigation, the area with major surface cracks and contamination was the focus of EDX zone mapping. The cross-section samples group: the cross-section of the as-received sample and deformation samples (upper, centre and lower) for each lubricant were mounted, chemically and mechanically polished with 0.04 μm Colloidal Silica (OP-S) suspension and etching using Kroll's reagent (2 ml HF, 10 ml HCl, 88 ml H2O) to investigate the microstructural evolution throughout the workpiece.

4.3.6. SEM investigation on surface samples

As shown in **Figure 4-12**, the black area is the remaining contamination that was impossible to remove from the surface by cleaning. It can be seen that the contamination and surface cracks became more pronounced from the upper to lower region. At the centre region, there was clear growth of micro-cracks that stretch the deformation surface and contaminants were generally located at the boundaries of the micro-cracks. As the growth of micro-cracks increased in the lower region, a large area of the remaining contamination was observed. By cross-referencing the surface roughness measurements in **Figure 4-6**, it could be concluded that the increase in surface roughness is due to the growth of the microstructural cracks and residual contamination. The phenomenon is pronounced for lubricant 1 as apparent cracks and contamination are observed on the centre and lower region scanning area. Lubricant 2 (**Figure 4-13**) indicated a better deformation surface as the phenomenon of micro-cracks was reduced by comparing with lubricant 1 (**Figure 4-12**). The upper region could be deemed as clean as there was no detectable ‘black area’ and the micro-cracks at the centre region were reduced significantly. In the lower region, due to dissipation of the lubricant, contamination was detected in different areas rather

than one single area. This is clear evidence that lubricant 2 has shown a better surface quality. For lubricant 3, shown in **Figure 4-14**, no detectable micro-cracks were observed in the upper region and the growth of micro-cracks at the centre and lower region was significantly reduced, which produced the best surface quality among the three lubricants.

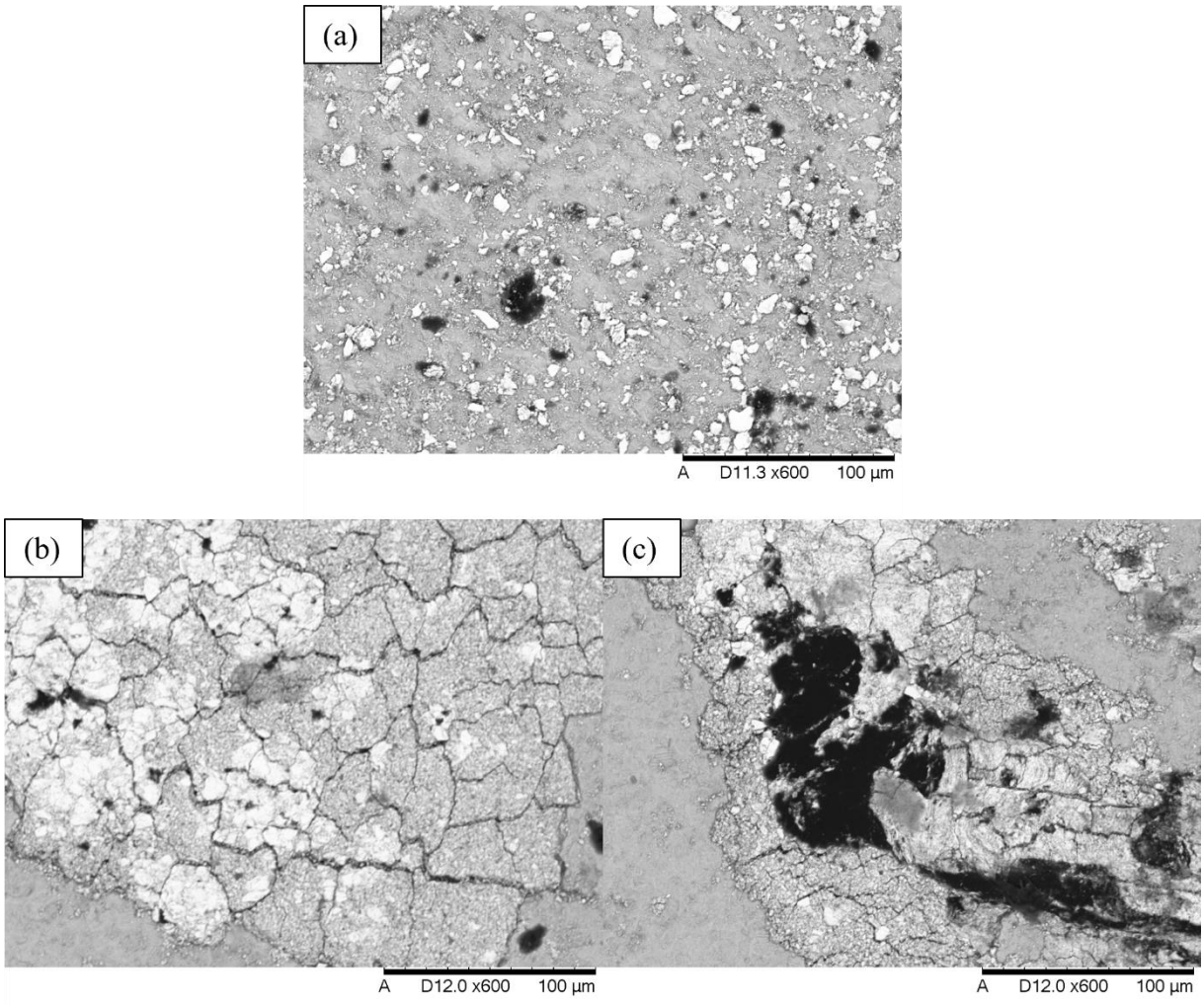

Figure 4-12. SEM images of the deformation surface for lubricant 1: (a) upper region; (b) centre region; (c) lower region.

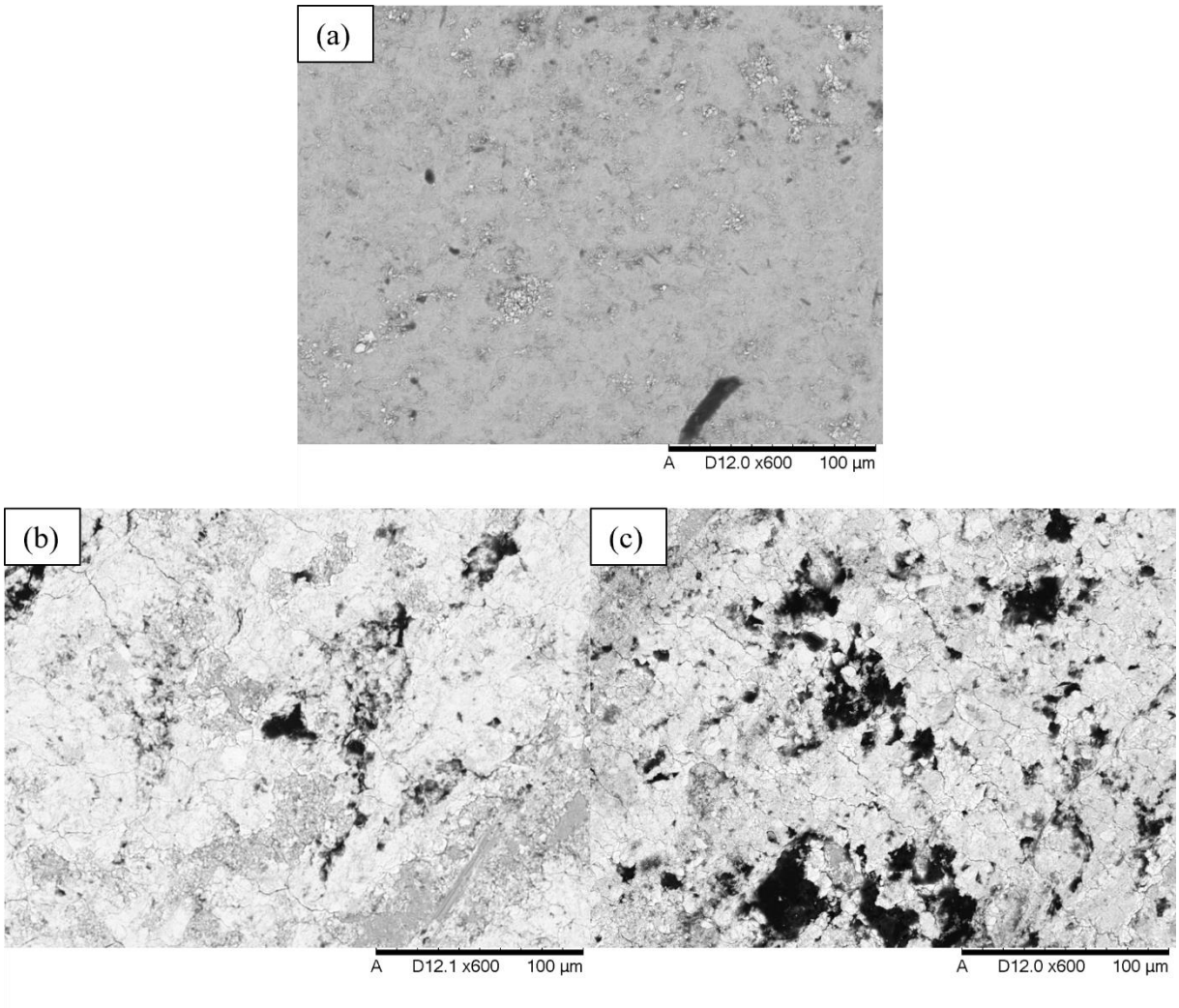

Figure 4-13. SEM images of the deformation surface for lubricant 2: (a) upper region; (b) centre region; (c) lower region.

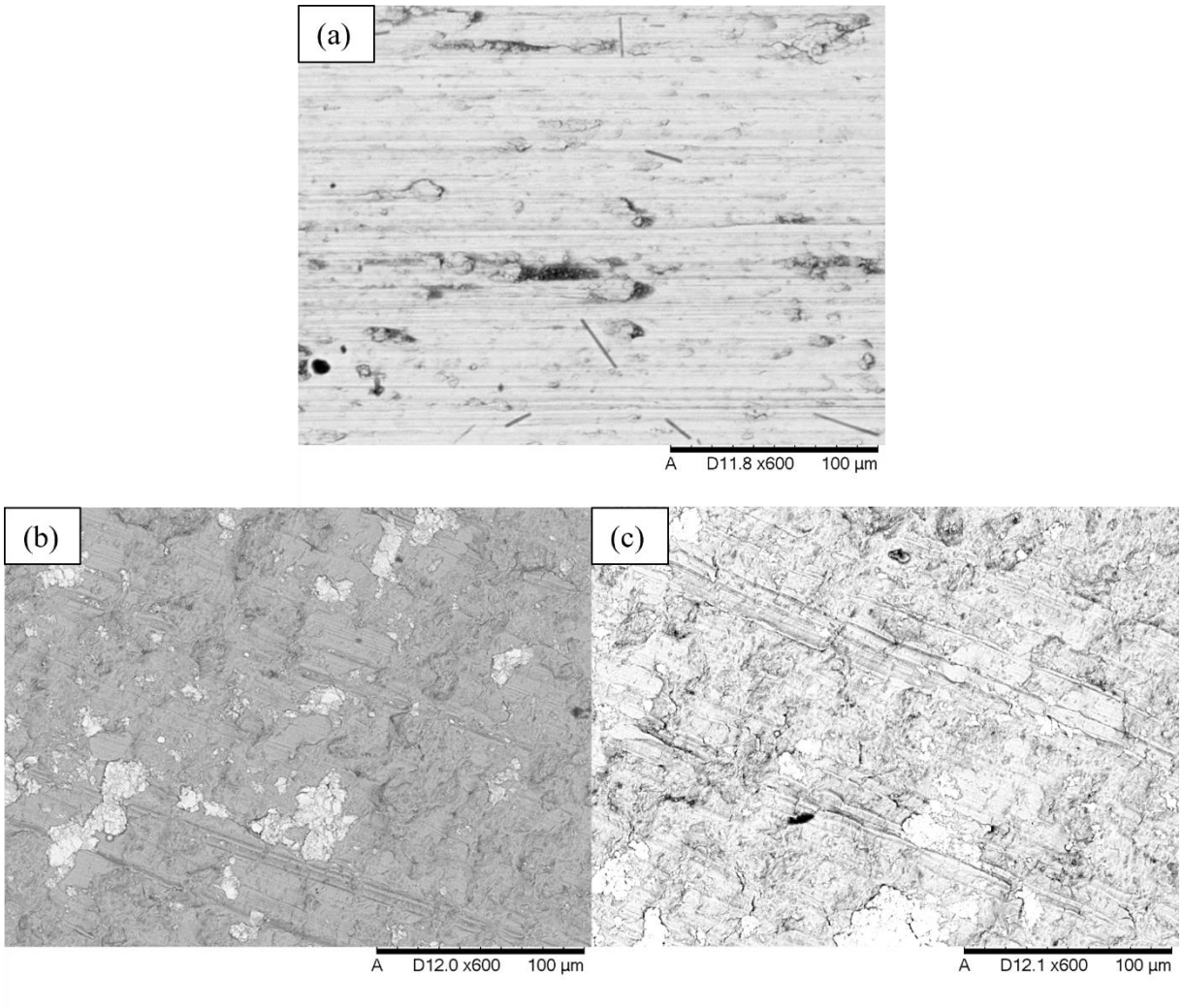

Figure 4-14. SEM images of deformation surface lubricant 3: (a) upper region; (b) centre region; (c) lower region.

4.3.7. EDX zone mapping

To investigate the content of the elements of the sample surfaces, EDX analysis was applied to the same scanning area as the SEM investigation. Note that the red colour is the Molybdenum (Mo) element, the green colour is the Carbon (C) element and the blue colour is the Titanium (Ti) element.

It can be seen from **Figure 4-15** that in the upper region of the lubricant 1 sample there were detectable levels of the elements Mo and C, which are the main components of the lubricant contamination [169]. The growth of the contamination was more apparent at the centre and

lower region, where the area with micro-cracks has been covered by these elements. This is clear evidence that the contaminations are caused by the dissipation of lubricants due to the temperature during the process. The loss of lubricating function led to micro-cracks developing on the deformation surface and the contaminants have adhered to the boundaries of the micro-carks thus resulting in great growth of contamination according to the process. The use of lubricant 2, shown in **Figure 4-16**, illustrates a comparably low content of contamination in the upper region indicating there was good functioning of the lubricant at the starting stage. However, in the centre and lower regions, contaminants still adhered to the surface due to the dissipation of lubricant. The volume of contamination is significantly reduced for lubricant 3, as shown in **Figure 4-17**. It can be seen that the detectable content of contamination was very low in the upper region and the growth of contamination was very limited in comparison with lubricants 1 and 2. A previous study by Careri et al. [170], on the investigation of tool wear in IN718 heat treatments, revealed similar results, and the study concluded that high temperature was the main reason for adhesive wear between the workpiece surface and the tool, and the force from the deformation speed enhanced the adhesive wear, resulting in abrasive wear. Other studies [171, 172], on the deformation and sheet forming of titanium alloys, were in agreement that high deformation force and temperature result in the formation of micro-cracks that encourage contaminants from the lubricant to adhere and accumulate at the boundaries of the micro-cracks. A study by Wang et al. [173] on the materials removal process also indicated that water cooling has balanced the thermal expansion of the tool in a toolpath with rapid rotating movement. This is evidence that the water-cooling lubricant from the water channel has sustainable support to reduce the thermal effects on the ball-roller tool tip, and enhance the rotating movement in the hot SPIF process.

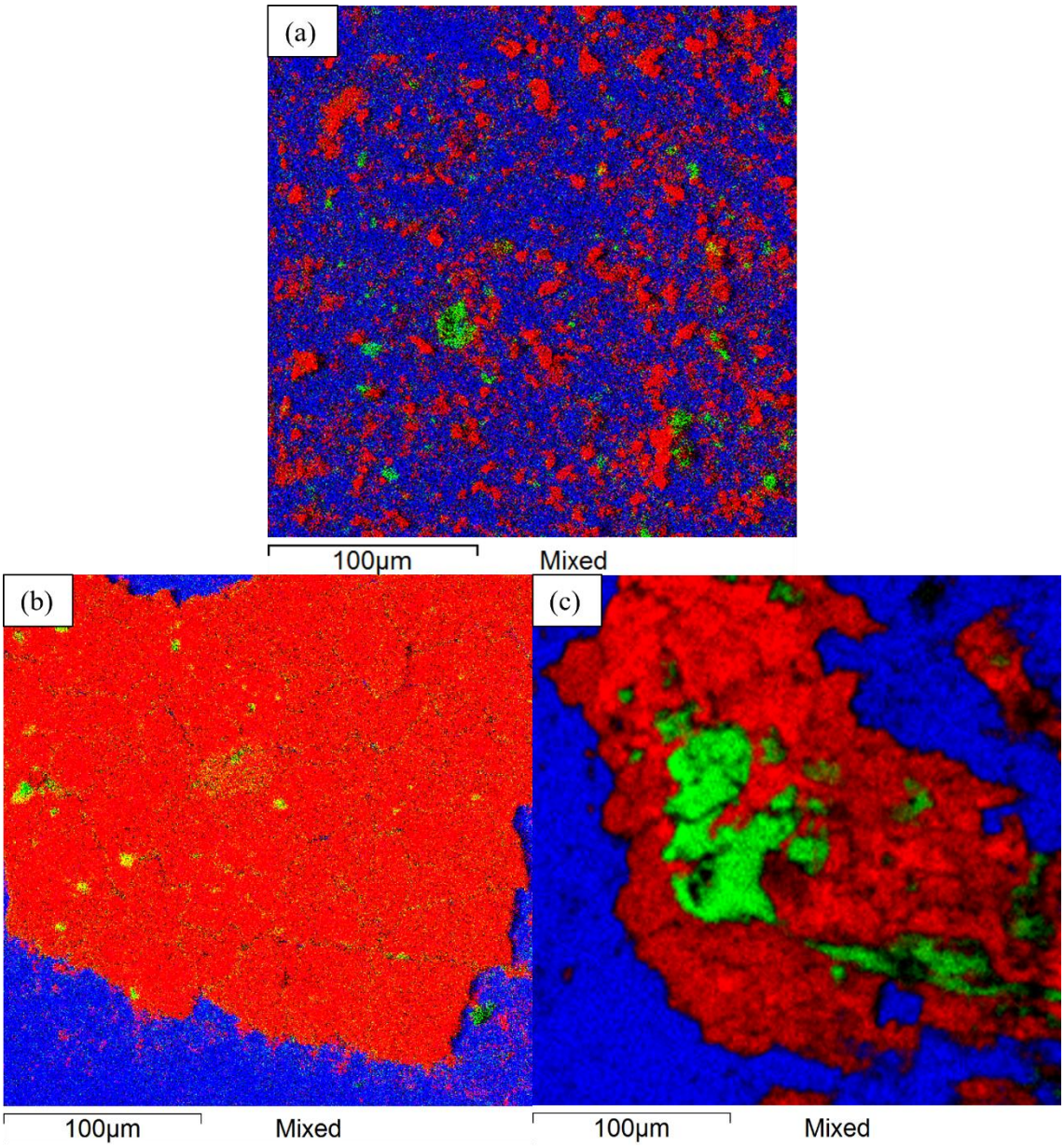

Figure 4-15. EDX zone mapping of the lubricant 1 adherence on the surface: (a) upper region; (b) centre region; (c) lower region.

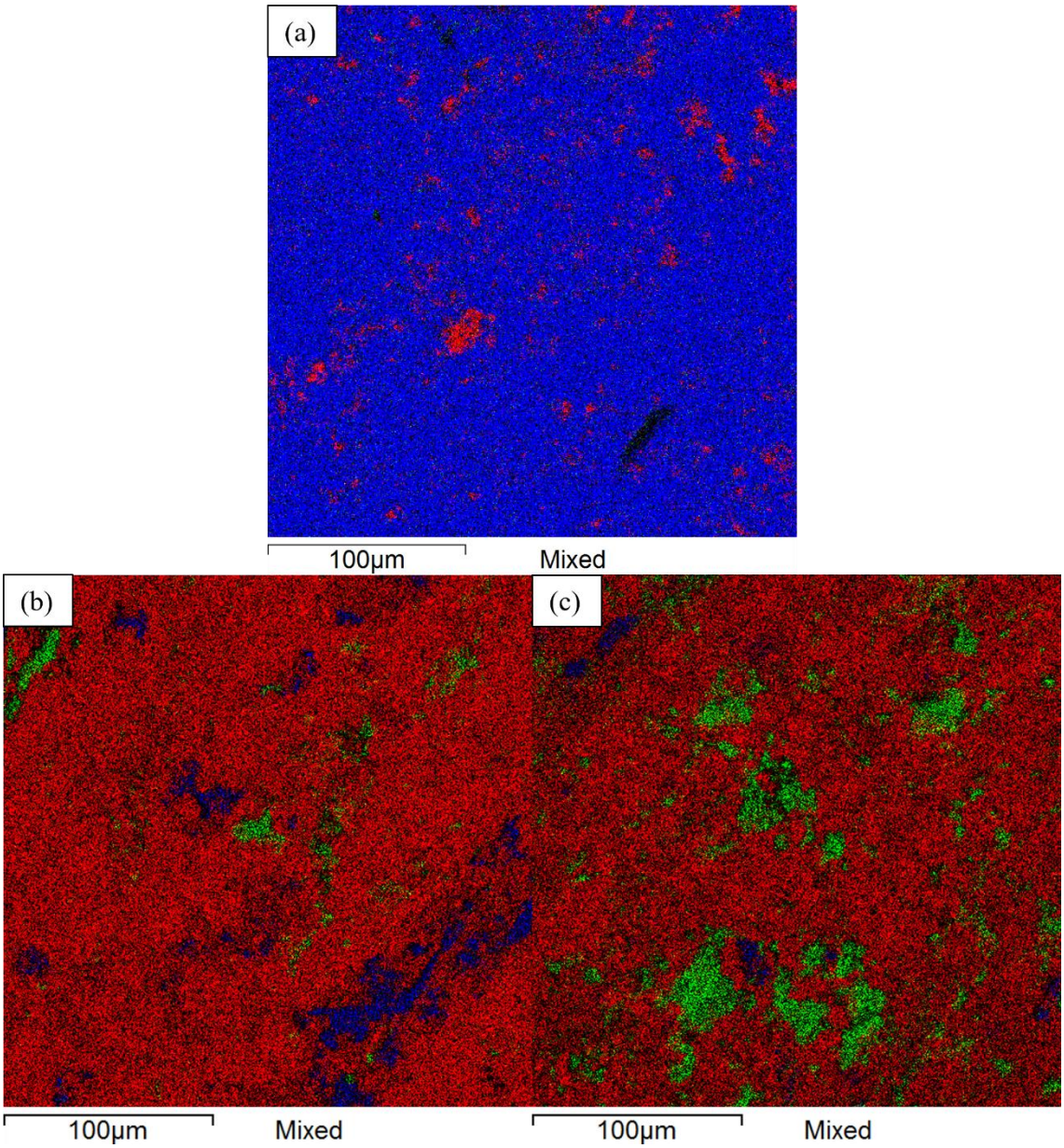

Figure 4-16. EDX zone mapping of the lubricant 2 adherence on the surface: (a) upper region; (b) centre region; (c) lower region.

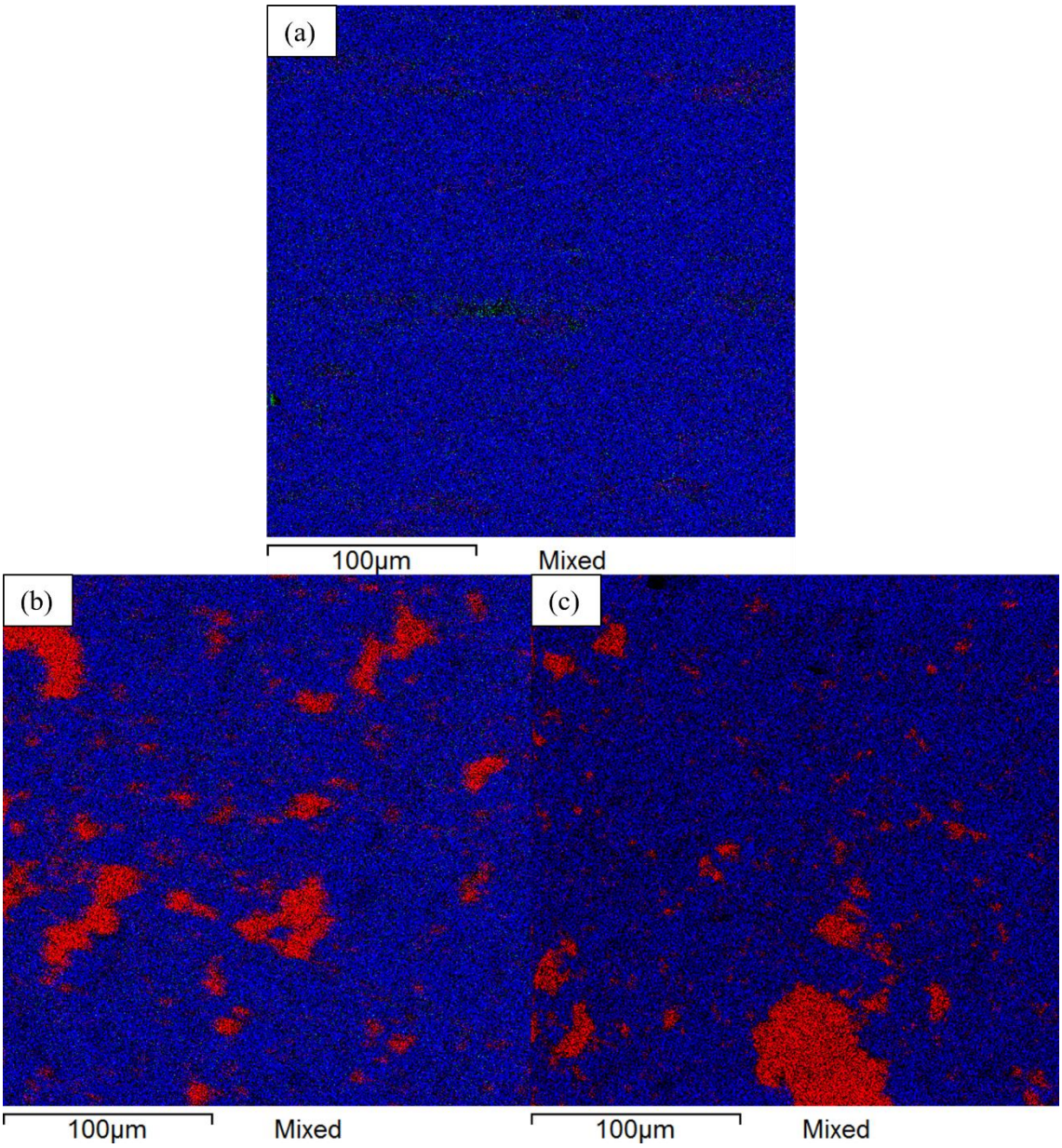

Figure 4-17. EDX zone mapping of the lubricant adherence on the surface: (a) upper region; (b) centre region; (c) lower region.

4.3.8. SEM investigation on cross-section samples

To investigate the microstructural evolution through the thickness of the material the lower region samples regarding to each applied lubricant were compared with the as-received sample. As observed in **Figure 4-18**(a), the as-received sample indicated a microstructure composed of the high content of primary α phase with random equiaxed grain shape and an estimated α grain

size from 5 - 10 μm. The detectable intergranular β phase grains are distributed at the boundaries of the α phase. At the lower region samples of all lubricants in **Figure 4-18**(b-d) revealed a noticeable growth of finer α grains detected and the grain size was significantly reduced. There was no significant difference in the microstructures between lubricants 1 and 2, providing evidence that the temperature profile is relatively the same for these two lubricants which initiated close DRX behaviour. Lubricant 3 indicated a microstructure with relatively coarse intergranular β grains which revealed the effects of the water-cooling lubricant system that enhances the cooling rate of the surface.

Ambrogio et al. [4] and Honarpisheh et al. [133] have investigated the hot SPIF process of Ti–6Al–4V sheets and commented that a phenomenon of slight oxidising on the deforming surface which was caused by the heating temperature above 700 °C. By comparing with microstructural evolution between the images in **Figure 4-18**(b-d), it could be seen that there was no observance of the oxide layer and α-case on the top surface, which means the temperature has been controlled well without exceeding to form alpha-case at the deformation direction. In addition, there is no observed reaction between the surface and the lubricant to form an oxide layer. By investigating **Figure 4-18**(d), it can be seen that the cooling from the tool resulted a relatively coarse intergranular β grains than the observations for lubricants 1 (**Figure 4-18**(b)) and 2 (**Figure 4-18**(c)) which indicated a microstructure with slight initiation to form martensite feature due to the rapid cooling at these areas. Such phenomenon reduced the temperature increase at the ending stage and produced a relatively balanced temperature distribution. The observed DRX behaviour in **Figure 4-18**(b-d) was attributed to the temperature raising rate from the SPIF process, lubricants 1 and 2 have slightly higher raising rates and lubricant 3 has relatively stable temperature distribution, thus the DRX behaviour was pronounced at lubricant 1 and 2 to produce finer α grains and the nucleation of DRX has been reduced for lubricant 3.

Since **Figure 4-18**(b) (lubricant 1) and **Figure 4-18**(c) (lubricant 2) produced a close

microstructure, thus, the comparison of cross-sectional thickness is focus on lubricants 1 and 3 as shown in **Figure 4-19**(a, b). It can be noticed that lubricant 1 has revealed finer grains in the thickness section and lubricant 3 has overall coarse grains with a slight phenomenon of secondary α_{II} Lamellae which indicated the rapid cooling is still sufficient at the thickness section. The results are in agreement with a study by Qu et al. [148] and Oberwinkler et al. [174], on the microstructure and oxidation behaviours of titanium alloy at low temperatures. Another by Ding and Guo [175] on the investigation of hot deformation of Ti–6Al–4V alloy concluded that the heat-treatment of Ti–6Al–4V alloys above 700 °C was sufficient for DRX initiation in producing finer grains and enhancing the ductility and formability for deformation. Therefore, the sustainable water-cooling lubricant support from lubricant 3 was sufficient to produce constant temperature support from the beginning to the centre region and balanced the temperature at the lower region with reduced DRX behaviour. The system improved the surface quality, geometric accuracy and thickness profile at an even growth of DRXed grains in microstructural evolution when compare with lubricants 1 and 2.

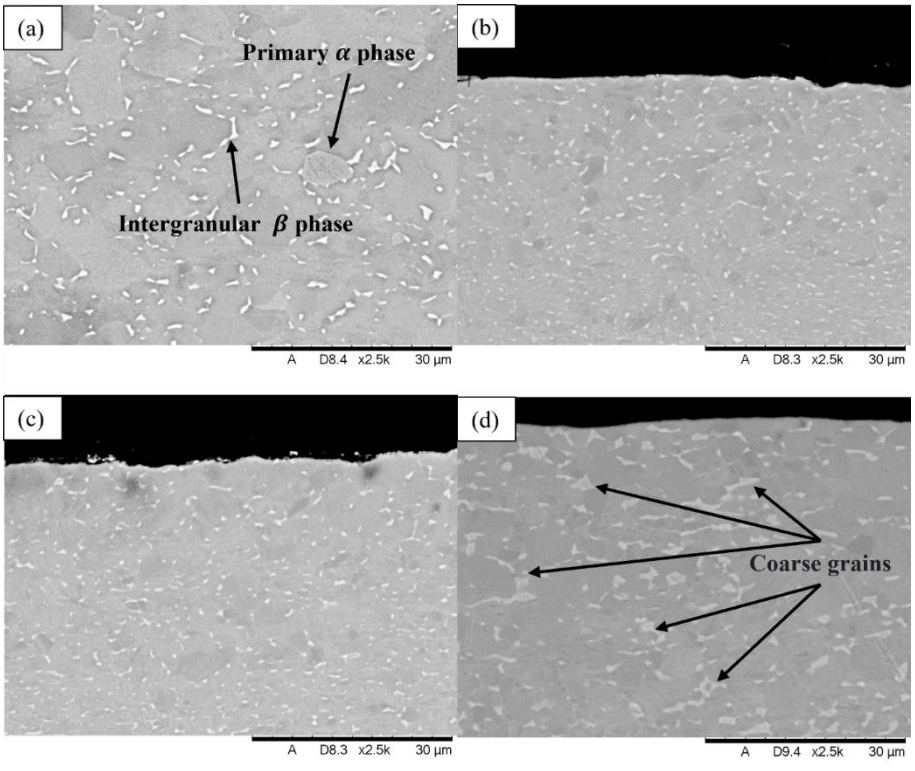

Figure 4-18. SEM images of the top surfaces of cross-section: (a) as-received; (b) lubricant 1; (c) lubricant 2; (d) lubricant 3.

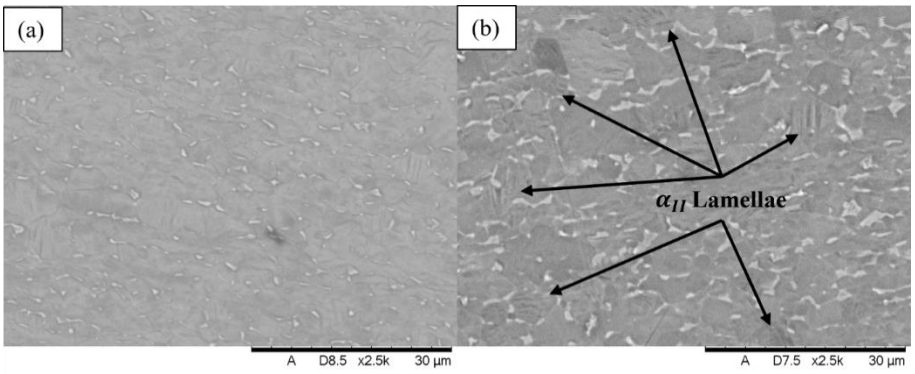

Figure 4-19. SEM images of the thickness of cross-section: (a) lubricant 1; (b) lubricant 3.

4.3.9. Micro-hardness

A Wilson® hardness tester was used in this project to provide highly accurate hardness results of the as-received and deformed samples. The measurements follow the GB/T 4340.1-2009 HV 0.1 metal hardness testing standard with a testing load of 100 gm. The machine reading error is 0.5%.

The micro-hardness measurements were determined by making indents on the surfaces of each deformation and cross-sectional sample. The orientation of the indents was in a step-down arrangement, covering measurements from the upper sample edge to the lower edge. A total of 9 indents were applied to each sample. To illustrate the most significant effects of the samples, only the lower samples were tested.

In **Figure 4-20**(a), it can be seen that for all three lubricants the micro-hardness profile of the deformation surfaces followed a similar flat trendline. lubricants 1 and 2 had very close results whereas lubricant 3 had higher readings. This is supportive evidence that the water-cooling system is sufficient to reduce the temperature on the ball-roller and further lead to a reduction in the contacting area. The temperature reduction during the hot SPIF process caused a slight

quenching effect which increased the strain hardening work thus indicating higher reading measurements. Dai et al. [153] and Abbas et al. [176] have investigated the heat treatment and hardness of Ti–6Al–4V alloy and commented that the quenching has a strong effect on increasing the hardness due to the rate of quenching. Julien et al. [177] and Wang et al. [178] also commented that the quenching enhances a rapid lamellar coarsening in the microstructural evolution which increased the dislocations during the plastic deformation and enhances stress relaxation. Even though the water-cooling lubricant system is insufficient to provide a rapid cooling on the deformation surface, the slight decrease of temperature on the contacting area between the ball-roller and workpiece still presented relatively higher hardness measurements. Reviewing the micro-hardness profiles for the cross-section samples in **Figure 4-20**(b), it can be seen that the use of lubricants 1 and 2 resulted in a low-high-low distribution profile, whilst lubricant 3 exhibits a high-low profile. Such behaviour can be attributed to the working mechanism of induction heating. In the system, the magnetic field penetrates the workpiece generating a rapid alternating eddy current at the centre of the material, which is then spreading to the outer regions. Thus, due to the mechanism of induction heating and movement of the tool, the highest thermomechanical strain will occur in the centre region in the lubricant 1 and 2 experiments. However, for the lubricant 3 experiment, the water cooling on the workpiece applied a strong strain hardening on the workpiece surface and diffused in the thickness. Such a phenomenon enhanced the hardness readings of the lubricant 3 on the deformation surface and top surface of the workpiece. By passing through the centre region, the readings have been reduced and tend to get close to lubricant 1 and 2 experiments.

Overall, it can be noticed that the readings on the deformation surfaces were slightly higher than for the cross-section surfaces. A previous study by Dai et al. [153], on microstructure and hardness of Ti–6Al–4V sheet surface under heat-treatment work, reported that the average hardness readings on the deformation surfaces are higher than on the substrate region, due to

the surface finishing process that induces thermal-strain. Such behaviour may result in limited oxidation that enhances the α-stabilising of Ti-6Al-4V, thus increasing surface hardness. It was observed that the deformation process in this analysis applied a strong strain hardening force on the workpiece, which resulted in higher micro-hardness readings.

A previous study by Najafabady and Ghaei [154], on the investigation of effects on the hardness of Ti-6Al-4V alloy by heat incremental forming, reported that strain hardening was pronounced above 600 °C, and was effective in increasing the micro-hardness. Another study by Sabat et al. [155], on the texture and microstructure evolution of Ti-6Al-4V alloys, revealed that the strain hardening and grain deformation induced higher micro-hardness readings at 600 °C. However, the temperature was insufficient to generate the full DRX process, resulting in the creation of a deforming microstructure, demonstrated by the presence of a strong deformation texture. Using a higher temperature of 700 °C accelerated the dislocation mobility and resulted in full DRX, which manifested in grain refinement, as shown in the measurements readings.

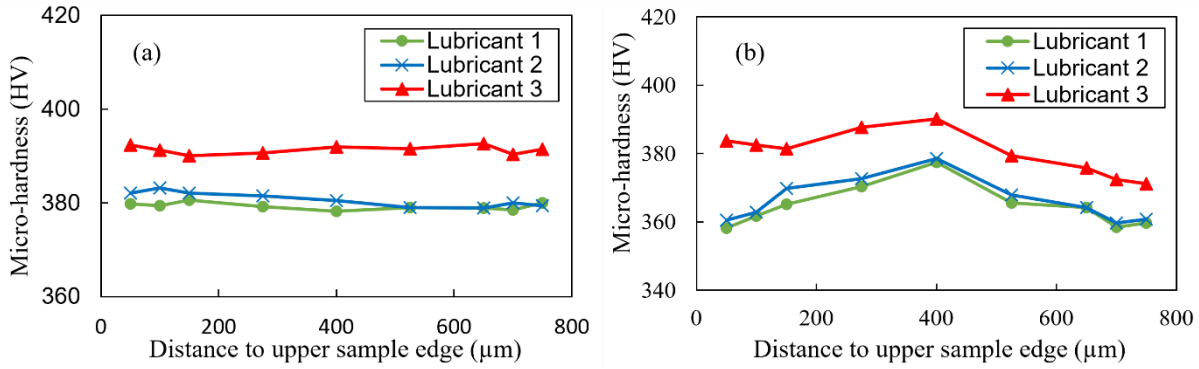

Figure 4-20. Micro-hardness profile for (a) deformation surfaces of lubricant 1, 2 and 3 experiments; (b) cross-sections of lubricant 1, 2and 3 experiments.

4.4. Conclusion

- The lubricant grease (lubricant 1) was not sufficient to support the whole induction heat-assisted SPIF process as it dissipated rapidly halfway through the working process.

Significant adhesive and abrasive wear were detected and huge areas of surface cracks appeared on the workpiece.

- The mixture of lubricant grease with lubricant oil (lubricant 2) produced better surface quality and the resistance to dissipation is much longer than the lubricant 1.
- The best performance was achieved by applying the water-cooling system in lubricant 3. The water-cooling lubricant was efficient to reduce the temperature on the ball-roller and the corresponding contact area on the surface and produced a better surface quality.
- The stable temperature distribution in lubricant 3 has produced a stable forming force behaviour which induced better geometric and the thickness profile.
- The microstructural evolution indicated that lubricant 3 has revealed coarse β grains with regional α_{II} grains which indicated a slight quenching effect that increasing the strain work hardening.
- The micro-hardness measurements on deformation surfaces for all lubricants are in flat distribution and higher than the cross-section values which indicated a slight increase from the adherence of lubricant. Lubricant 3 indicated the highest values where the rapid cooling rate enhancing the hardness on the deformation surface.
- The micro-hardness measurements on cross-section surfaces for lubricant 1 and 2 indicated low-high-low profiles due to the centre mass heating from induction. Lubricant 3 indicated high-low profile which indicated a diffusion from the cooling work that improved the micro-hardness on the deformation and top surface. The readings were reduced and getting closer to lubricant 1 and 2.

Acknowledgement

This work was funded by the Department of Mechanical Engineering, University of Birmingham.

5. Crystal plasticity model of induction heating assisted incremental sheet forming with recrystallisation simulation in cellular automata

Weining Li [a], Sheng Li [a], Sheng Li [a], Xuexiong Li [b], Dongsheng Xu [b], Yinghui Shao[c], Moataz M Attallah [d], Khamis Essa [a].

[a] *Mechanical Engineering, University of Birmingham, Edgbaston, Birmingham, B15 2TT, UK*

[b] *Institute of Metal Research, Chinese Academy of Science, Shenyang, China, 110016*

[c] *School of Computer Science, China University of Geosciences, Wuhan 430079, China*

[d] *School of Metallurgy and Materials, University of Birmingham, Edgbaston, Birmingham, B15 2TT, UK*

This research was accepted as a full-length research article in *International Journal of Advanced Manufacturing Technology*

Credit authorship contribution statement

Weining Li: Conceptualization, Investigation, Methodology, Validation, Software, Formal analysis, Writing - original draft.

Sheng Li: Writing - review & editing, EBSD booking, Microstructure part recommendation.

Xuexiong Li: Writing - review & editing, CPFEM modelling, Computing unit provider.

Dongsheng Xu: Writing - review & editing, Computing unit provider.

Yinghui Shao: Writing - review & editing, CA modelling.

Moataz M Attallah: review & editing, Resources of lab equipment, Supervision.

Khamis Essa: Writing - review & editing, Resources of lab equipment, Supervision, Project administration.

Research contributions:

This chapter aims to complete the objective 5 which covers the following insights:

- A new method to link the experiments and multi-scale modelling includes CPFEM, RVE and CA models to study the plastic deformation and microstructural evolution of heat-assisted SPIF system.
- Experimental and numerical studies of the recrystallisation, grain refinement, dislocation density and crystallographic texture of heat-assisted SPIF with dynamic strain rate and temperature.
- The relationship between the experimental parameters (strain, strain rate, temperature) and microstructural behaviours (recrystallisation, grain size, dislocation density, crystallographic texture, grain boundary angles) are studied.

Abstract

During heat-assisted incremental sheet forming (SPIF) process on high-strength alloys, thermal and straining induce pronounced springback and risk of crack which are attributed to the unstable microstructural evolution in the sheet metals. To relate the thermomechanical behaviour with microstructural evolution for Ti-6Al-4V sheet, multi-scale models based on crystal plasticity finite element model (CPFEM), representative elementary volume (RVE) and cellular automaton (CA) were established in this chapter. An experimental-scale CPFEM was built in advance to provide macro grain level strain, strain rate and temperature outputs data which were then used in representative elementary volume (RVE) and cellular automaton (CA) as inputs to simulate the microstructural evolution throughout the SPIF process. The output results including the pole figures, dynamic recrystallisation (DRX) maps and statistics results of the alpha (α) phase of the Ti-6Al-4V (α-Ti) alloy from stage to stage throughout the 700℃ SPIF. The obtained statistics results of dislocation density, grain orientation angles, and grain size were verified with the electron backscatter diffraction (EBSD). The CA analysis revealed the DRX growth and discovered that the incremental increase of the strain rate has significant effects to the dislocation density that produced a proportional relationship to the DRX percentage. The results revealed that the strain rate has strong domination in affecting the slip of grains orientation which overcomes the effect of temperature increase in this SPIF process. Further, it was found that the large amount of DRXed grains were generated at the grains boundaries that reduced the mean grain size and increased the DRX percentage which produced an inversely proportional relationship to the dislocation density. The thermomechanical behaviour on the SPIF workpiece was increased incrementally that is insufficient for DRX initiation at the upper region and the behaviour was enhanced at the centre and lower region which can be corresponded to the microstructural evolution throughout the process.

Keywords: incremental sheet forming; crystal plasticity; cellular automata; grain size;

5.1. Introduction

Ti–6Al–4V alloy is a high strength material that is widely applied in the aerospace and medical sectors. Ma et al. [179] have studied the crystal plasticity of titanium alloys and commented that the deformation of such material is usually performed at a high temperature to avoid the formation of strong deformed textures, which may result in an anisotropic mechanical behaviour due to the slip changes in the hexagonal closest packed (HCP) structure of α-Ti. Zhan et al. [180] have investigated the DRX of incremental sheet forming of Aluminium alloy sheets under room temperature, the results indicate that the DRX is raised during the process and refine the grains along the toolpath which enhance higher strength and better plasticity of the material. For heat-assisted SPIF processes, the current challenges have remained on the shortage of studies on the thermomechanical behaviour and the relevant microstructural evolution throughout the process from stage to stage. Therefore, it is essential to study the relationship between thermomechanical behaviour and its effects on microstructural evolution and establish a numerical model to complete the loop in this scientific field.

Yang et al. [181] found that the initiation of DRX and microstructural evolution of Ti–6Al–4V are usually observed when the thermomechanical behaviour is above 700 ℃. A pronounced α-phase DRX can be detected, and the process influences the mechanical properties significantly. In recent years, CA models are generally studied to simulate the DRX process of alloys. For instance, Ding and Guo [175] investigated the microstructural evolution of a Ti–6Al–4V titanium alloy during β-phase processing by using CA models, the simulated results successfully represented the microstructural evolution under experimental conditions. However, the stress-strain relevant parameters were obtained from experimental observed results, which induced calculation errors on grain growth kinetics and dislocation density calculations in CA models. The results led further impact on the accuracy of DRXed calculation. In order to reveal

precision grain level behaviour of hot compression of Ti–6Al–4V alloy, Chuan et al. [113] and Said et al. [182] have investigated a novel approach involving combining CPFEM method to provide crystal orientation and grain level strain distribution as CA model input, the simulated results revealed accurate grain growth and re-grain size through comparing with experimental data, the calculated recrystallisation kinetics and flow stress successfully predicted the regime of the material microstructure evolution. Chen et al. [183] has proposed multiscale modelling to simulate discontinuous dynamic recrystallization during hot works by coupling multilevel cellular automaton which also proves that the novelty of study on multiscale modelling of hot deformation metal forming processes.

In this chapter, the DRX of α-phase Ti–6Al–4V alloy during hot SPIF will be simulated by combining CA and CPFEM. An experimental-scale finite element method (FEM) model was established by implementing the VUMAT subroutine in ABAQUS to simulate the SPIF experimental process. The grain level strain distribution will be obtained from the elements, each localise element presents one grain. The received strain distribution will be used as an input to implement an EBSD based RVE to obtain the crystallographic texture. Further, the CPFEM grain level strain outputs can be used as inputs to simulate the microstructural evolution during the heat assisted SPIF process. To validate the CA model, the simulation results including grain size, dislocation density and DRX fraction were compared with experimental results. Finally, this chapter aims to study the relationship between the grain level parameters and the thermomechanical behaviours from experiments.

5.2. Materials and Methods

5.2.1. Materials

All workpieces in this chapter are standard Ti-6Al-4V alloy sheets with dimensions of 150 mm × 150 mm × 0.8 mm with same chemical composition as stated in **Table 3-1**.

5.2.2. Experimental parameters

For hot sheet forming process of Ti-6Al-4V, the common temperature has been used is around 400 - 500 ℃ which is sufficient for plastic deformation behaviour [145, 184]. However, the obtained results did not reveal high geometric accuracy as the forming temperature is insufficient to produce enough DRX level to reduce the forming force. The titanium α-phase HCP crystal plasticity model has been established in the previous study by Amouzou et al. [185] which has validated that a pronounced phenomenon of DRX was achieved at hot deformation of 700 ℃. The studies [65, 186] have investigated the microstructure of Ti-6Al-4V under 700 ℃ induction heating assisted SPIF, which indicated a pronounced DRX level at 700 ℃. Thus, this study aims to develop the localised crystallographic texture and DRX behaviour of Ti-6Al-4V thin sheets under 700 ℃ SPIF process. The feasible model will be able for users to apply in other metal forming process with modification of materials properties. As the processing temperature is lower than the β-phase transition (980 ℃), only the α-phase HCP structure is considered for the crystallographic sliding to simplify the calculations. As the hot SPIF process combines thermomechanical deformation and dynamic straining behaviour which contributes to the complexity of the microstructural level simulation. Sun et al. [187] have investigated the shear banding in titanium under deformation and dynamic compression which commented that the shear banding behaviour is pronounced at slip in basal and prism planes where the other planes can be neglected. Zhang et al. [189] Zhang et al. [189] have investigated the deformation and shear bands in the texture of α-phase HCP, The study commented that three families of the slip system: basal $< a >$, prismatic $< a >$, pyramidal $< c + a >$ are recommended to focus as main slip systems for deformation under phase transition temperature. By applying same families of the slip system, 3 basal, 3 prismatic, and 6 pyramidal were considered in this chapter.

The following equipment, tool design and parameters are same as explained in chapter 3:

- The tool design is same as illustrated in **Figure 3-1**.
- The final shape is same as illustrated in **Figure 3-3**.
- The tool path is same as illustrated in **Figure 3-3** with following modified parameters as shown in **Table 5-1**.

Table 5-1. Machine setting and experimental parameters

PARAMETERS	VALUES
Tool feed rate (mm/min)	2000
Step size (mm)	0.5
Temperature (℃)	700

5.2.3. CPFEM of experimental scale SPIF

For a thin sheet material in this study, the Voronoi tessellation method is not efficient as the Voronoi cells at the thin edge are unable to be fully demonstrated for an experimental scale. Thus, FEM was established to present experimental scale CPFEM simulation. Each element in the CPFEM can be used to collect grain level strain variables for a specific area, and the elements at the edge can be accumulated to present the crystal plasticity behaviour through thickness. The accumulative strain variable output will be used as input variables in an RVE model to simulate the results in detail. In the experimental scale CPFEM, coupled temperature-displacement implicit regime is selected. The tool is defined as a rigid body and assigned a

temperature boundary condition of 700 ℃ and the temperature is transformed to the workpiece by contact. Since the heat transfer is synchronised with the tool movement and the heating area is the same as the tool tip. Therefore, contact behaviour is the best way to simulate heat transfer. The friction coefficient was set as 0.1. The four sides of the workpiece are constraint (Displacement to x, y, z = 0) as shown in **Figure 5-1**(a). The orientation of elements is displayed in **Figure 5-1**(b), a total of 90000 elements (x-axis: 150 elements, y-axis: 150 elements, z-axis: 4 elements) have been applied to the workpiece. The equivalent plastic strain of the deformed SPIF simulation is illustrated in **Figure 5-1**(c).

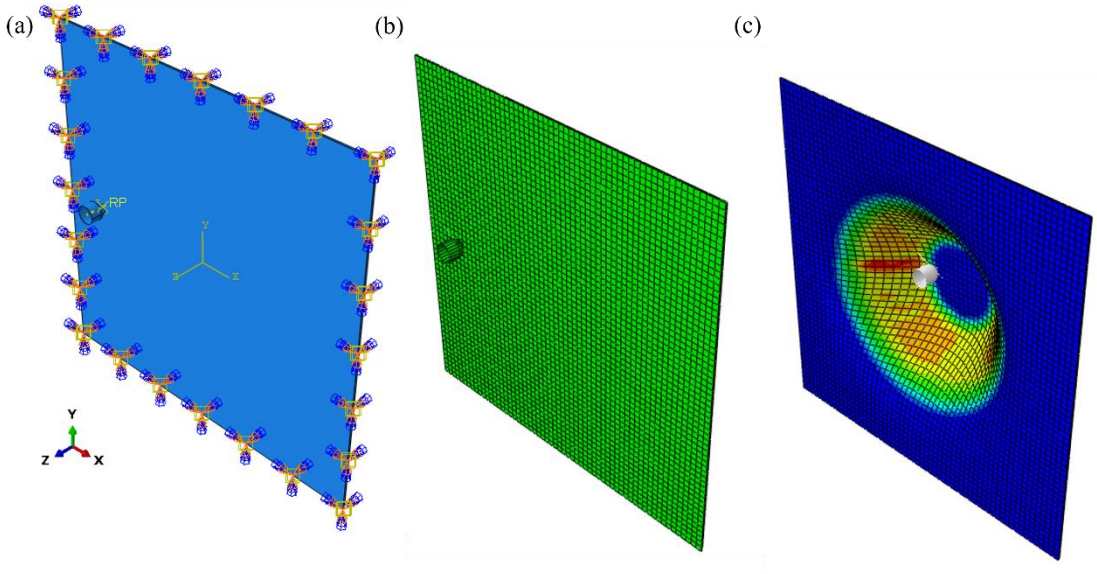

Figure 5-1. CPFEM of heat-assisted SPIF (a) boundary conditions, (b) finite element mesh (c) equivalent plastic strain from deformed SPIF simulation.

The elastic constants in **Table 5-2** were obtained from the study Chatterjee et al. [190] on experimental tensile and CPFEM simulation of Ti-6Al-4V where the conditions are met with this chapter. The slip systems parameters in **Table 5-3** were obtained from Thomas et al. [191] on hot deformation and CPFEM analysis of Ti-6Al-4V under similar experimental temperature and strain conditions as this chapter, the results are shown in **Table 5-2** and **Table 5-3**.

Table 5-2. Elastic constants (GPa) for the α phase of Ti-6Al-4V

C_{11}	C_{12}	C_{13}	C_{14}
170.0	98.0	86.0	42.5

Table 5-3. The parameters for slip systems in the α-Ti grains

slip system	m	$g_0^{\alpha}(\mathrm{MPa})$	$\dot{\tilde{\gamma}}(\mathrm{s}^{-1})$	$h_0(MPa)$	r	$\tilde{\gamma}(\mathrm{MPa})$	n	$K^{\alpha}\left(\mathrm{MPa}\sqrt{\mu\mathrm{m}}\right)$
Basal ⟨a⟩	0.02	284.00	0.0023	100.0	0.1	450.0	0.01	164.5
Prism. ⟨a⟩	0.02	282.24	0.0023	100.0	0.1	550.0	0.01	164.5
Pyr. ⟨c+a⟩	0.02	623.30	395.00	100.0	0.1	1650.0	0.01	164.5

5.2.4. Representative Volume Elements (RVE)

The CPFEM of SPIF was used to provide the grain level mechanical behaviours approximately. To simulate the detailed microstructural development, the RVE model was established using the mechanical output from the CPFEM of SPIF.

The structure of RVE was generated by incorporating the EBSD output as input data into the DREAM.3D and extruding the result as an ABAQUS input file. This software was used to

reconstruct the EBSD output and make segments and mesh the features of the dataset. The details of the software can be found in the documentation of DREAM.3D which is induced by the previous study Groeber and Jackson [104] on 3D materials microstructure modelling. As shown in **Figure 5-2**(a), a sub-grain part from the EBSD data of the as-received sample was used to create the RVE model. This part is 100% α-phase with strong HCP texture and contains 356 grains, the orientation of these grains is then used as input data in DREAM.3D to create an RVE structure, presented in **Figure 5-2**(b). The created RVE from DREAM.3D was saved as an ABAQUS input file to create a FEM for analysis as illustrated in **Figure 5-2**(c). The FEM is 23 µm × 23 µm × 23 µm with 12167 elements.

The same material properties and mechanical behaviours from the CPFEM of SPIF were used in this RVE model to simulate the detailed microstructural development.

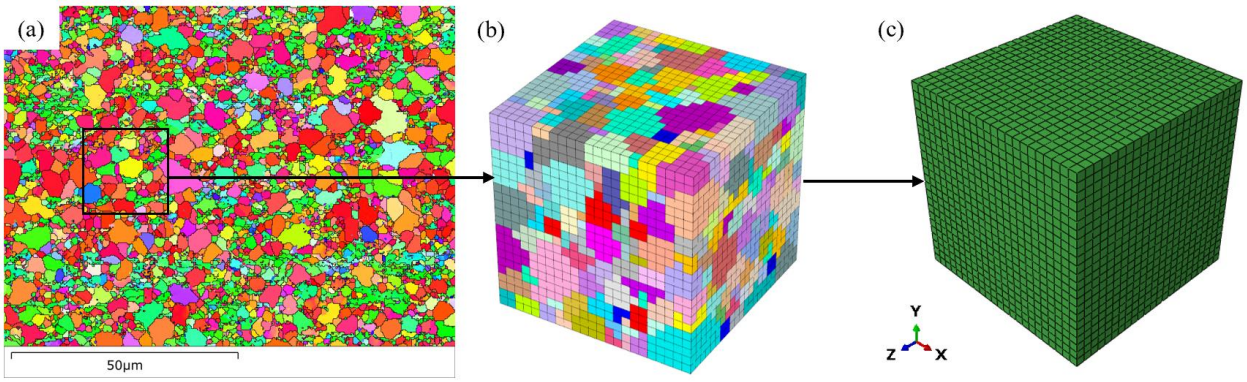

Figure 5-2. The process of generation of RVE (a) EBSD IPF (Inverse Pole Figure) map of the as-received sample, (b) RVE created by DREAM.3D, (c) ABAQUS model.

5.2.5. Single-crystal constitutive model

Single-crystal constitutive can be defined as a mesoscale approach which explicitly models discrete grains and slip systems and accounts for the anisotropy of single-crystal properties and crystallographic texture. The model has been applied in recent studies [102, 103] on SPIF

process which successfully simulated the crystal plasticity behaviour throughout the thin thickness. This model is more predictive and robust than macroscopic plasticity to simulate the evolution of crystallographic texture and models both anisotropic elasticity and plasticity. The main objective kinematics of the single-crystal plasticity constitutive model is finalised on the dislocation mechanism which has been investigated by Zhuang et al. [192]. The foundations of constitutive laws can be traced to the works by Hill and Rice [193] on the investigation of the constitutive laws of elastic-plastic crystals at arbitrary strain. Peirce et al. [194] has improved the constitutive laws and applied Kröner-Lee decomposition which is induced by calculation of deformation of gradient tensor F of a single crystal from Kröner-Lee decomposition Kröner [195] on the study of elastic-plastic behaviour of crystals. To simplify the constitutive calculations of single-crystal deformation, two independent atomic mechanisms are assumed: (1) general elastic lattice distortion (2) plastic deformation with no effect on lattice geometry. Under isothermal conditions, the intermediate configured lattice orientation in the can be assumed as the same as the initial state. The deformation of single-crystal [193] is dominated by dislocation glide, under deformation gradient tensor F and its derivatives as expressed as:

$$F = F^e \cdot F^P \tag{5-1a}$$

$$detF^p = 1 \tag{5-2b}$$

$$J = detF = detF^e \tag{5-2c}$$

Where F^P is the plastic deformation gradient, which denotes the crystalline slip plane plastic shear deformation, and where the non-plastic component, F^e is a non-plastic component, denotes the lattice elastic stretch and rotation. J denotes the ratio of the deformed to the undeformed volume. By assuming no change in volume during plastic deformation, the macroscopic velocity gradient L can be expressed as:

$$L = \dot{F} \cdot F^{-1} = L^e + L^p \tag{5-3a}$$

$$L^e = \dot{F}^e \cdot F^{e-1} \tag{5-3b}$$

$$L^p = F^e \cdot \dot{F}^p \cdot F^{p-1} \cdot F^{e-1} \tag{5-3c}$$

Where L^e is the velocity gradient for the elastic part of the crystal, L^p is velocity gradient for the plastic part. $\dot{\gamma}^\alpha$ denotes the α slip system shear rate. Asaro and Rice [196] on analysis of strain behaviour in single crystals have defined the plastic deformation for the crystal slip system using shear rate as:

$$\dot{F}^p \cdot F^{p-1} = \sum_{\alpha=1}^{n} \dot{\gamma}^\alpha s^\alpha \otimes m^\alpha \tag{5-4}$$

Where s^α is the unit vector for slip direction and m^α is the unit vector for slip plane for α^{th} slip system. During single-crystal deformation, the lattice would be rotated and stretched. The normal vector $\tilde{s}^\alpha$ and $\tilde{m}^\alpha$ to the α^{th} slip system has been expressed by Nanson's formula as displayed in **Eq. (5-5a)** and **(5-5b)**.

$$\tilde{s}^\alpha = F^e \cdot s^\alpha \tag{5-5a}$$

$$\tilde{m}^{(\alpha)} = detF^e \cdot m^{(\alpha)} \cdot F^{e-1} \tag{5-5b}$$

By approximating the elastic deformation is $detF^e = 1$ which is made in Eq. (5-2b). Eq. (5-5a) and (5-5b) can be transformed as:

$$\tilde{s}^{(\alpha)} = F^e \cdot s^{(\alpha)} \tag{5-6a}$$

$$\tilde{m}^{(\alpha)} = m^{(\alpha)} \cdot F^{e-1} \tag{5-6b}$$

Further, **Eq. (5-6a)** and **(5-6b)** can be rewritten as:

$$\tilde{s}^{(\alpha)} = L^e \cdot \tilde{s}^{(\alpha)} \tag{5-7a}$$

$$\tilde{m}^{(\alpha)} = -\tilde{m}^{(\alpha)} \cdot L^e \tag{5-7b}$$

By combining the **Eq. (5-5)**, **(5-6)**, **(5-7)**, the final equation of plastic velocity gradient tensor L^P can be expressed as shown in **Eq. (5-8)**.

$$L^P = \sum_{\alpha} \dot{\gamma} S_0^{\alpha}, \qquad S_0^{\alpha} \equiv m_0^{\alpha} \otimes n_0^{\alpha} \tag{5-8}$$

Where m_0^{α} denotes the vectors of slip direction and n_0^{α} denotes the vectors the slip plane normal in the slip systems with a variable of 0. α^{th} denotes the sequence of slip system, S_0^{α} is the slip resistance in unit of Schmid tensor. The elastic strain can be expressed as:

$$E^* = \frac{1}{2[(F^*)^T F^* - I]} \tag{5-9}$$

Where E^* is the elastic strain, I denotes the 2nd order tensor of identity. The grain level stress

of elastic constitutive laws can be expressed as:

$$T^* = CE^* \tag{5-10}$$

Where T^* in **Eq. (5-10)** denotes the crystalline Cauchy stress, C is a fourth-order elasticity tensor. The stress measure and the elastic work conjugate to the elastic strain can be expressed as:

$$T^* = (detF^*)F^{*-1}TF^{*-T} \tag{5-11}$$

Where T is the grain level symmetrical Cauchy stress tensor and the resolved shear stress is given by:

$$\tau^\alpha = T^* : S_0^\alpha \tag{5-12}$$

To investigate the grain level deformation, the movement of each grain is considered as rigid rotation and orientation evolution. The shear strain rate and the shear stress must be integrated into the slip system, the equation of the deformation can be expressed as:

$$F^* = R^* U^* \tag{5-13}$$

Where F^* denotes the non-plastic deformation gradient, R^* is the lattice rigid rotation, U^* is the stretch tensor, the following equation expressed the orientation of grains:

$$Q = R^* Q (R^*)^T \tag{5-14}$$

Where Q denotes the grain orientation formed rotation tensor in terms of Euler angles. The following equation has expressed the strain rate using power-law flow rule:

$$\dot{\gamma}^\alpha = \dot{\gamma}_0 \left(\frac{\tau^\alpha}{s^\alpha}\right)^{\frac{1}{\chi}} \operatorname{sgn}(\tau^\alpha) \tag{5-15}$$

Where $\dot{\gamma}^\alpha$ and $\dot{\gamma}_0$ denote the shear rate and reference shear rate for α^{th} slip system, χ denotes the coefficient of material rate sensitivity, τ^α denotes the α slip system acting resolved shear stress, s^α denotes the dislocation acted deformation resistance. The equations are given by:

$$s^\alpha = s_0 + \frac{1}{2}\mu b\sqrt{\rho^\alpha} \tag{5-16a}$$

With

$$s_0 = \frac{1}{N}\left(u_1 \exp\left(-\frac{T}{T_0}\right) + \frac{u_2}{\sqrt{d}}\right) \tag{15b}$$

Where μ denotes the shear modulus, b represents the Burger's vector, Eq. (5-16b) was proposed by Kocks and Mecking [197] on the study of work hardening, where s_0 is the slip resistance that is dependent on initial grain size, ρ^{α} denotes the density of dislocation for α^{th} slip system. N represents the number of slip systems in total and the term $u_1 \exp\left(-\frac{T}{T_0}\right)$ represents the slip resistance that is dependent on the temperature, where u_1 is a constant for fitting, T and T_0 represent the working temperature and the reference temperature. $\frac{u_2}{\sqrt{d}}$ represents the slip resistance that dependents on the size effect. u_2 denotes the coefficient of Hall–Petch, d represents the average grain size. To simplify the calculations, the initial slip resistance of each slip system was assumed as the same which has been proposed by Hémery et al. [198] on the investigation of the slip behaviours with the degree of micro-texture in Ti–6Al–4V. The development of dislocation density is governed by the annihilation and multiplication of dislocation movements. Mishra and Ma [199] on the analysis of dislocation evolution has induced K–M model to express the multiplication term:

$$d\dot{\rho}^{+} = k_1\sqrt{\rho}\dot{\varepsilon} \tag{5-17}$$

Where $d\dot{\rho}^{+}$ denotes the density of dislocation in the increasing order, k_1 represents the work hardening constant, ρ represents the density of dislocation, $\dot{\varepsilon}$ denotes the strain rate. To describe the term of dislocation annihilation, the following equation has been proposed:

$$d\dot{\rho}^{-} = -k_2\rho\varepsilon \tag{5-18}$$

Where $d\dot{\rho}^{-}$ denotes the dislocation density in decreasing order, k_2 can be defined as a function which depends on the working strain rate and temperature. k_2 can be expressed as follows:

$$k_2 = k_{20}\left[\dot{\varepsilon}\exp\left(\frac{Q_{act}}{RT}\right)\right]^{\frac{1}{\omega}} \tag{5-19}$$

Both k_{20} and ω are constants for fitting, Q_{act} denotes the deformation formed activation energy, R represents the gas constant.

5.2.6. CA model

cellular automaton is a discrete model of computation studied in automata theory to provide analysis for homogeneous structures and iterative arrays [200]. As the crystal plasticity behaviour is calculated by CPFEM, the output from the CPFEM is then used as input in the CA model to predict the DRX process. To address the recrystallisation nucleation and subsequent growth, two assumptions are proposed:

(1) The dislocation density of primary grains are uniform and identical. DRX occurs as the value reaches the critical level. Each DRXed grain is depending on continued deformation with variation for each grain and the mechanism is fully applied to the changes in dislocation density.

(2) The occurrence of DRX nucleation on the grain boundaries is applied for all primary and DRXed grain boundaries.

The modelling nucleation rate has been proposed by Peczak [201] on the study of deformation temperature on dynamic recrystallization which can be described as:

$$\dot{n}(T) = \dot{n}(T_{\mathrm{m}}) \exp\left[-\frac{Q_{\mathrm{act}}}{RT_{\mathrm{m}}}\left(\frac{T_{\mathrm{m}}}{T} - 1\right)\right] \tag{5-20}$$

Where $\dot{n}(T)$ denotes the nucleation rate, $\dot{n}(T_{\mathrm{m}})$ represents the nucleation rate at melting temperature T_{m}, Q_{act} denotes the activation energy. The previous study by Derby and Ashby [202] on DRX analysis has proposed that the nucleation rate can be assumed as linearly proportional to the strain rate function $\dot{n} = C\dot{\varepsilon}^{m}$. According to the study by Peczak and Luton [203] on the investigation of nucleation models of DRX, m can be assumed as 0.9. Another study by Peczak [201] proposed that the nucleation rate for DRX can be induced by the temperature and strain rate as follows:

$$\dot{n}(\dot{\varepsilon}, T) = C\dot{\varepsilon}^{m} \exp\left(-\frac{Q_{\mathrm{act}}}{RT}\right) \tag{5-21}$$

Where C is a constant which can be determined from the nucleation rate $\dot{n}(\ \mathrm{s}^{-1}\ \mathrm{m}^{-3})$ at a specific DRX level, the exponent m can be assumed as 1 to demonstrate the full plastic flow during DRX which is suggested by the study Ding and Guo [204] on DRX simulation. The DRX fraction can be expressed as:

$$\eta = \dot{n}\frac{\varepsilon}{\dot{\varepsilon}} \cdot \frac{4}{3}\pi r_{\mathrm{d}}^{3} \tag{5-22}$$

Where η denotes the DRX fraction, ε represents the true strain, $\dot{\varepsilon}$ denotes the strain rate, r_{d} is the mean radius of DRXed grain. Derby [205] has studied the steady state grain size under DRX

has proposed that the Eq. (5-22) can be relevant to flow stress as follows:

$$\frac{\sigma_{\mathrm{s}}}{\mu}\left(\frac{2r_{\mathrm{d}}}{b}\right)^{n} = K \tag{5-23}$$

Where σ_{s} denotes the steady-state flow stress, μ represents the shear modulus, b is Burger's vector and the exponent n can be considered as $\frac{2}{3}$ and K is a constant (range from 1 to 10) for titanium alloys. In this chapter, the nucleation of α-DRX occurs as a critical level of dislocation density or strain is initiated, the equation is given by:

$$\rho_c = \left(\frac{20\lambda\dot{\varepsilon}}{3b^5 l M \mu^2}\right)^{\frac{1}{3}} \tag{5-24}$$

Where ρ_c denotes the dislocation density at the critical level, λ represents the grain boundary energy, l denotes the average free path for dislocation, and M denotes the mobility at the grain boundary. The nucleation rate can be expressed as:

$$\dot{n} = C_1 \dot{\varepsilon}^{\varphi} \exp\left(-\frac{Q_{act}}{RT}\right) \tag{5-25}$$

Where $\dot{n}$ is the nucleation rate, C_1 and φ are constants. The deformation of neighbouring grains is initiated by the stored energy and it is governed by the recrystallisation nucleation which can be expressed as:

$$Q_{\text{deform}} = \frac{1}{2}\rho_{GND}\mu b^2\psi \tag{5-26}$$

Where Q_{deform} is the stored energy under deformation, ψ denotes the material molar volume, ρ_{GND} represents the geometrically necessary dislocations (GND). According to the previous study Hallberg and Ristinmaa [206] has investigated the influence of dislocation density in a reaction-diffusion system, the DRXed grain can be assumed as spherical and the driving force is given by:

$$P = \frac{dE_i}{dr_i} = \frac{dE_i^{vol} + dE_i^{sur}}{dr_i} \tag{5-27}$$

Where P denotes the driving force, dE_i^{vol} represents the evolution in the volume energy, dE_i^{sur} is the evolution in the energy of grain boundary. The above equation can be re-arranged as:

$$dE_i^{vol} = 4\pi r^2(\rho_m - \rho_r)\mu b^2 \tag{5-28}$$

Where ρ_m is the matrix grain of dislocation densities, ρ_r is the matrix grain of DRXed grains. The retarding force can be expressed as:

$$dE_i^{sur} = -8\pi r\lambda dr \tag{5-29}$$

Where dE_i^{sur} is the retarding force, r is the grain radius, Varshni [207] has defined the shear modulus under material temperature as **Eq. (5-30)**:

$$\mu = 49.02 - \frac{5.821}{\exp\left(\frac{181}{T}\right) - 1}\,\text{GPa} \tag{5-30}$$

Where μ denotes the shear modulus. By applying the Read–Shockley equation, the grain boundary energy is given by:

$$\lambda = \begin{cases} \lambda_m & \theta \geqslant 15^\circ \\ \lambda_m \frac{\theta}{\theta_m}\left(1 - \ln\frac{\theta}{\theta_m}\right) & \theta < 15^\circ \end{cases} \tag{5-31}$$

Where λ denotes the grain boundary energy, λ_m corresponds to the boundary energy above 15°and it is given by:

$$\lambda_m = \frac{\mu b \theta_m}{4\pi(1-v)} \tag{5-32}$$

Where θ_m denotes critical misorientation angle at 15°, v represents the Poisson ratio. The driving pressure can be calculated as:

$$p = \frac{P}{4\pi r^2} \tag{5-33}$$

Where p is the driving pressure, r is the radius of DRXed grains, the DRX growth is produced by the grain boundaries migration and the migration rate can be expressed with the grain boundary mobility M as:

$$M = \frac{b\delta D_{0b}}{K_B \theta} \exp\left(-\frac{Q_{diffu}}{R\theta}\right) \tag{5-34}$$

Where δ denotes the characteristic grain boundary thickness, D_{0b} represents the coefficient of diffusion at ideal 0 K, Q_{diffu} denotes the activation energy for self-diffusion activation energy and the migration rate is given by:

$$v = Mp \tag{5-35}$$

Where v is the migration rate that interacts with the isothermal macroscopic flow stress σ and the average dislocation density σ which can be expressed as:

$$\sigma = 0.5\mu b\sqrt{\bar{\rho}} \tag{5-36}$$

Where σ is the isothermal macroscopic flow stress under hot deformation, $\bar{\rho}$ denotes the

average dislocation density. By assuming the $\bar{\rho}$ is equivalent to the mean value of all the grains, the equation can be re-arranged as:

$$\bar{\rho} = \frac{1}{V_{\text{total}}} \sum_{i=1}^{N} \rho_i V_i \tag{5-37}$$

Where ρ_i denotes the dislocation density, V_i represents the volume at i^{th} grain and V_{total} is the volume in total.

5.2.7. CA model and CPFEM model combination

In this chapter, the 2D CA model was produced by MATLAB using Moore's neighbouring rule with periodic boundary conditions. The inputs are extracted from the CPFEM outputs to maintain the grain level variables. The CA is presented in 500 × 500 cells with each cell simulating 2 μm. By referring the study by Chen et al. [208] on the mesoscale simulation of the high-temperature DRX of steel, the process of CA and CPFEM consists of the following stages:

(1) Generation of experimental scale CPFEM to obtain state variables of crystal orientation and grain level strain, strain rate and temperature distribution.

(2) Select a section from EBSD to get grains orientation, use DREAM.3D to build an ABAQUS RVE model and apply the state variables from CPFEM.

(3) Use the output crystal orientation to generate a pole figure to compare with EBSD results.

(4) The CA model is established by applying state variables from CEPFEM as input.

(5) By using the K–M equation, the dislocation density for the grains is calculated.

(6) The nucleation of DRX occurs when the the misorientation angle exceeds 15° in-between neighbouring cells.

A flowchart of the procedures of CPFEM and CA combination is shown in **Figure 5-3**. The grain level strain and strain rate will be calculated from CPFEM and used as input in CA modelling to calculate the cell dislocation.

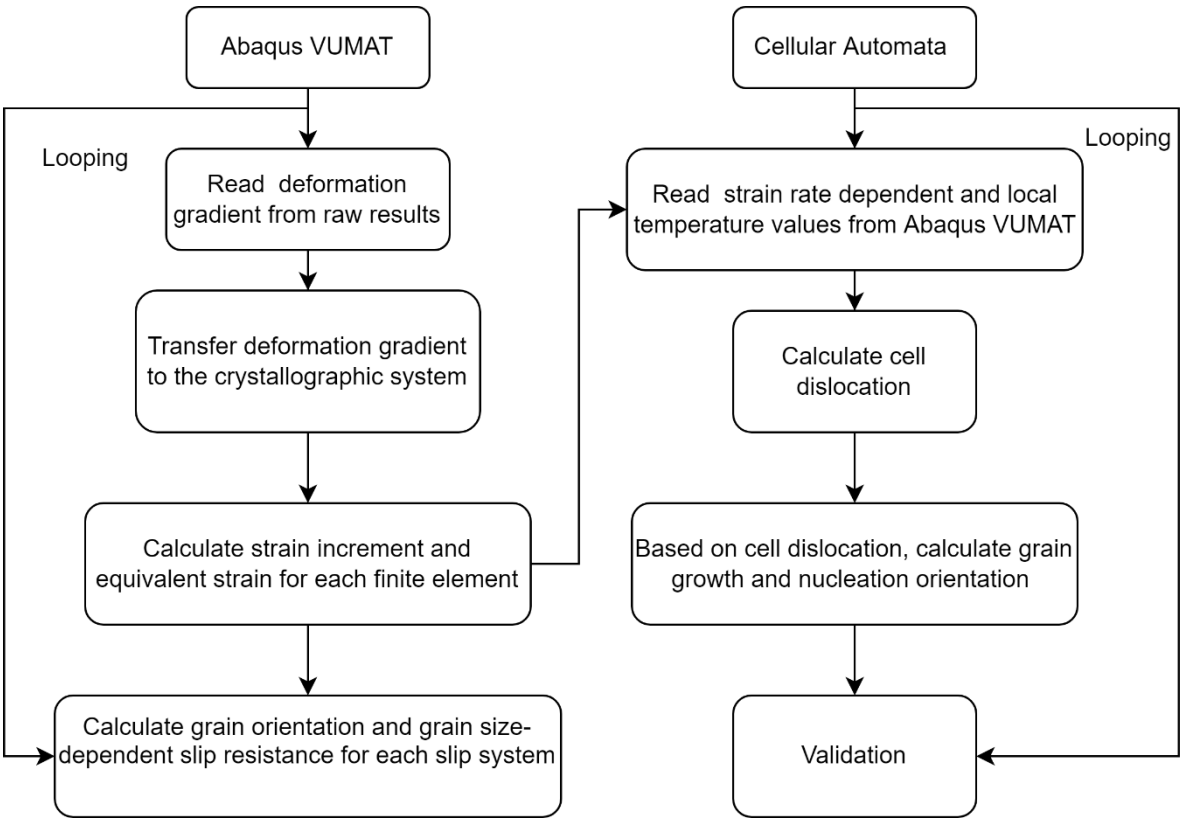

Figure 5-3. The flowchart of the combination of CPFEM (Abaqus VUMAT) and CA modelling.

By obtaining the Q_{act} values from the study by Li et al. [65] on the same experiments with similar conditions and another study by Xu et al. [122] on the investigation of hot deformation machining of Ti-6Al-4V, the relevant parameters are presented in **Table 5-4**.

Table 5-4. Materials parameters for CPFEM and CA model

$b(\mathrm{m}^{-1})$	$\delta \mathrm{D}_{0b}\left(\frac{\mathrm{m}^3}{\mathrm{s}}\right)$	$Q_{\mathrm{diffu}}\left(\frac{\mathrm{kJ}}{\mathrm{mol}}\right)$	$Q_{\mathrm{act}}\left(\frac{\mathrm{kJ}}{\mathrm{mol}}\right)$	$\dot{\gamma}_0(\mathrm{s}^{-1})$	$k_1(\mathrm{m}^{-1})$	k_{20}
2.95×10^{-10}	7.5×10^{-17}	153×10^3	321.43	0.7	5.0×10^7	200

5.3. Results and discussion

5.3.1. CPFEM

As illustrated in **Figure 5-4**(a), 3 specimens were cut off from the sample, and the transverse surface was used for EBSD investigation as **Figure 5-4**(c). The corresponded elements on the CPFEM thickness side were used for data collection as illustrated in **Figure 5-4**(b). The node with 4 x 4 elements surrounding it was selected to calculate the strain distribution along with the thickness. Where a typical element is presented in **Figure 5-4**(d).

The CPFEM outputs based on calculations from section 5.2.5 of temperature, plastic strain (ε_{zz}) and strain rate distribution data for **Figure 5-4**(b) are illustrated in **Figure 5-5**. Please note that these data were average data of the 4 x 4 elements, and the strain rate data were filtered by the Savitzky-Golay method which is induced by study Press and Teukolsky [167] on the study of high-frequency noise reduction in physical signals.

It can be noticed that a critical point (temperature, strain, strain rate) is reached while the tool

passes through the selected node. As shown in **Figure 5-5**(a), the temperature distribution for the upper node is different from the centre and the lower node, since the temperature is rising at the experiment initiation stage, while the tool is passing through the centre and lower node, the temperature is slightly increased and the area at the end is fully heated. The temperature distributions result in differences in plastic strain (ε_{zz}) distributions. It can be seen in **Figure 5-5**(b), that the lower temperature distribution results in lower strain distribution at the upper node, and the strain is increased as the strain rate is increased. It is noticed in **Figure 5-5**(c), the strain rate value reaches the peak value of 0.6, 07 and 0.8 s^{-1} for the upper, centre and lower region while the tool passes through the unique node. Therefore, this is evidence that the strain rate is increased slightly for each increment and the equivalent strain is increased accordingly. Nixon et al. [209] has investigated the experimental and constitutive modelling of α-titanium and proposed that the strain of the workpiece is sensitive to the displacement rate of indenter. In this work, the increment increase of strain rate has induced a strong strain hardening effects on the workpiece. Due to the temperature supply from the induction heater, an initiation of DRX is achieved and the process is following the movement of forming tool from upper to the lower region.

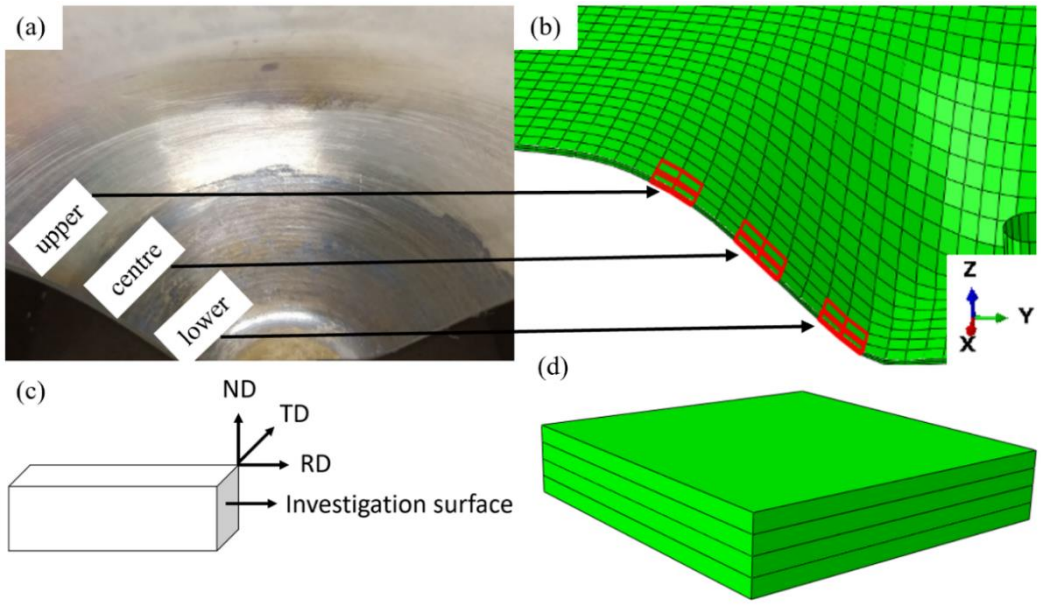

Figure 5-4. Represented specimen and model for (a) 3 cut-off investigation specimens from the experimental sample, (b) the correlated elements (upper, centre, lower) on the CPFEM model, (c) EBSD investigation symmetry and scan surface, (d) isotropic view of a typical element.

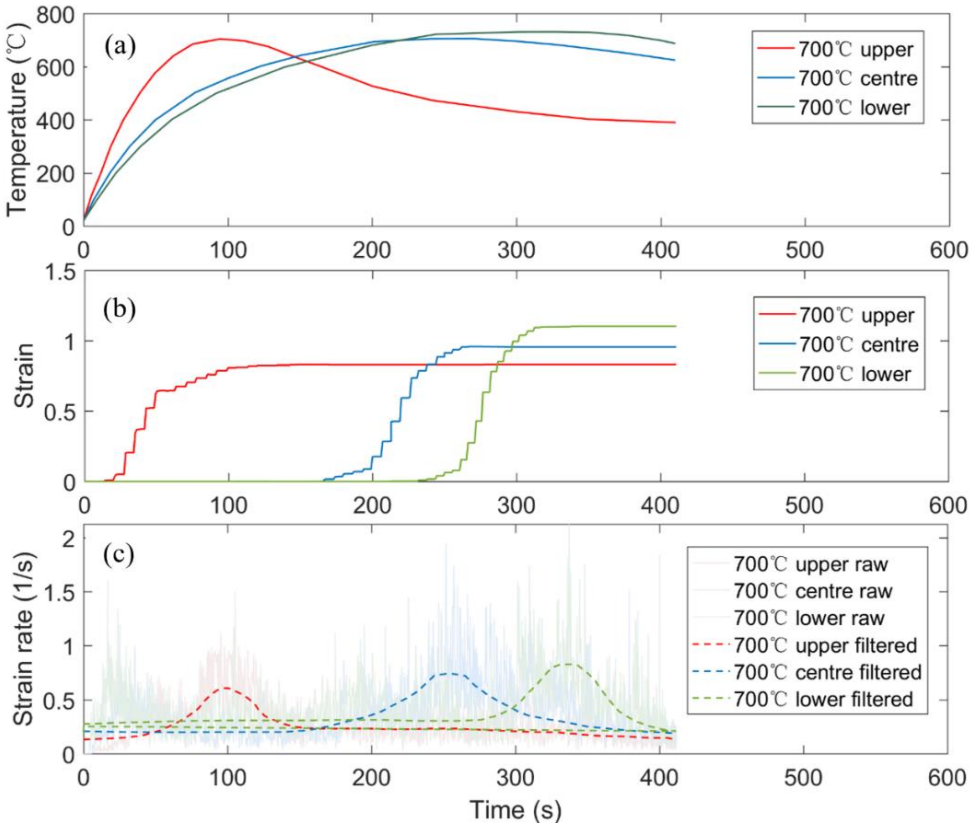

Figure 5-5. Grain level parameters (a) temperature, (b) plastic strain (ε_{zz}), (c) strain rate.

5.3.2. RVE and pole figures

The mesh of RVE is illustrated in **Figure 5-6**(a). As stated in section 5.2.4, the RVE has 356 grains using 8-node thermally coupled brick, trilinear displacement and temperature (C3D8T). A total of 12167 elements were generated on the RVE model. The boundary conditions are illustrated in **Figure 5-6**(b), the bottom surface is constrained with displacement $U_x = U_y = U_z = 0$. A time-dependent temperature and strain rate (**Figure 5-5**) were applied on the top surface of the RVE model. the grains orientation will be obtained from the simulation of RVE to form pole figures to compare with experimental pole figure results using MATLAB toolbox MTEX which is produced by Niessen et al. [149] on the investigation of grain reconstruction and microstructure evolution of metals.

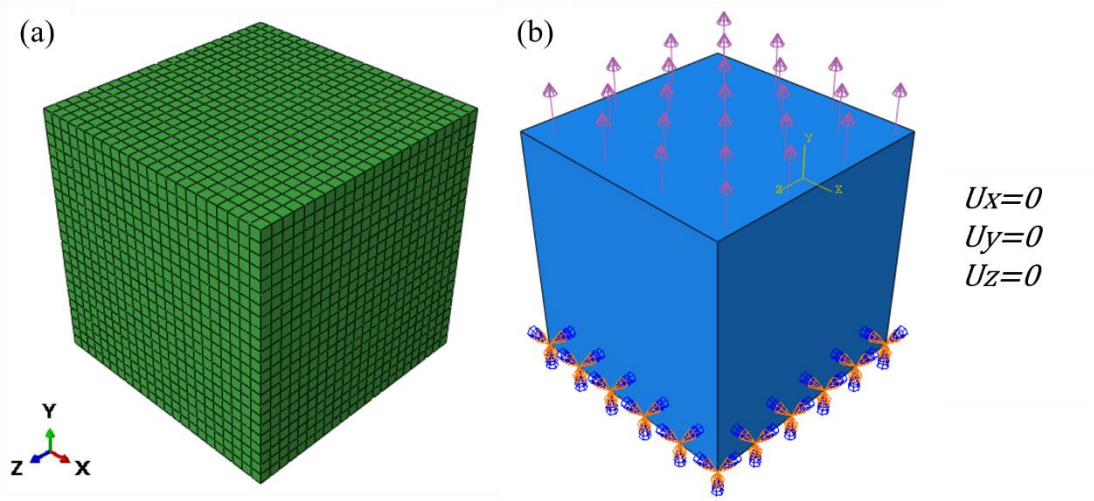

Figure 5-6. The simulation of RVE (a) mesh of RVE, (b) boundary conditions of RVE.

To validate the RVE and CA results, EBSD has been done on the transverse (thickness) direction of as-received, 700℃ upper, centre, lower samples and pole figures were obtained from EBSD investigation to compare with pole figure results from MTEX. The EBSD machine used was TESCAN MIRA3 FEG-SEM and the data were analysed by AZtecCrystal. The

following parameters were applied to EBSD characterisation, step size: 0.2 μm, pixel binning mode: 2 × 2, accelerating voltage: 30 kV, electron beam current: 5 nA. The crystal coordinate system (CCS) and sample coordinate system (SCS) are in the following relationship, where normal direction (ND) = [0001] sample, rolling direction (RD) = $[10\bar{1}0]$ sample, transverse direction (TD) = $[11\bar{2}0]$ sample. To investigate the in-depth evolution in microstructure, the TD surface was selected for the EBSD investigation.

In this chapter, the basal $\{0001\}$ and prismatic $\{10\bar{1}0\}$ slip systems are the main objective to study, the common slip direction for these two systems is $\langle 11\bar{2}0\rangle$ which is parallel to basal poles. The pole figures of the as-received sample are shown in **Figure 5-7**. The texture of the as-received sample illustrates a strong hot-rolled HCP basal feature which is more preferentially distributed along the TD direction and formed a fairly equiaxed basal/transverse texture.

As the experiment progressed to the 700 ℃ upper region, it can be noticed in **Figure 5-8** that the basal pole texture is gradually transformed from basal/transverse to the concentrated c-axis (parallel to the normal direction), and a prismatic slip $\{1010\}$ is approximately formed. Since the DRX is time-consuming and sensitive to the changes in temperature and strain rate, the prismatic slip texture at this stage is not substantial. However, it is still noticed that the nucleation of DRX towards the centre of basal oriented grain boundary, which indicates the rotation of grains angle leads to a pronounced increase of misorientation angles inside the basal pole to form a strong texture.

As the experiment processed to the 700 ℃ centre region in **Figure 5-9**, the basal pole exhibits an expansion towards the rolling direction (RD) and a high-intensity prismatic pole is observed. This indicates that the growth of DRXed grains is formed at the initial basal pole grain boundary. The temperature at this stage is more steady-state and sufficient than the upper region which enhances the DRX process and suppresses the twinning thus resulting in an efficient basal slip

and promoting a prismatic pole. The previous study by Warchomicka et al. [210] has investigated the high temperature deformation behaviour in Ti–5Al–5Mo–5V–3Cr–1Zr and revealed that the dynamic strain-induced boundary migration (D-SIBM) is an important factor in DRX to form the deformation texture. As the temperature is sufficient, the nucleation of DRXed grains is usually formed at the grain boundaries with the D-SIBM due to the change of stored energies and dislocation densities between basal and prismatic orientated grains. Li and Yang [211] have studied the D-SIBM on hot compressed Ti-5Al-5Mo-5V-1Cr-1Fe Alloy and proposed that the grains in the prismatic pole have greater Taylor factor than the basal pole, which led to higher stored energy in the hot compression that initiated a driving force for D-SIBM from basal to prismatic oriented grains. This is good evidence that D-SIBM is combined with DRX at this stage to dominate the microstructure evolution.

For the 700 ℃ lower region in **Figure 5-10**, the grains at the basal pole towards the RD axis form relatively higher intensity at the edge. The prismatic pole remains with a relatively lower intensity but clear texture which shows that more sufficient DRX is achieved at this stage. The deformed grains are diffused from basal to prismatic pole. It can be observed that the strain and temperature from experiments exhibit a high impact on the crystal slip systems.

For the RVE produced pole figures shown in part (b) from **Figure 5-7** to **Figure 5-10**, it can be seen that the as-received samples have shown a great match, and the accuracy has incrementally reduced from the upper to lower region. This is mainly attributed to the lack of grains calculated in the RVE modelling, the calculation error in transporting data from the CPFEM to RVE and the error from the mechanism of the hot SPIF process. The number of grains counted in RVE is only 356 grains obtained from the EBSD as-received sample, this number is sufficient for RVE to present a close pole figure, however, the inaccuracy will be increased in the calculation of the complex deformation system. It can be seen from **Figure 5-8**(b) and **Figure 5-9**(b), the

pole figures are still matched in an acceptable way which means the RVE is still able to predict the grains orientation at a relatively low DRX level, and the increase of temperature and strain rate at the lower region may cause further unpredictable DRXed grains. Furthermore, the twinning is suppressed in this study to reduce the complexity in transporting data between each system, thus it results in a relatively different pole figure in **Figure 5-10**(b). It is still noticeable that the grains orientation in **Figure 5-10**(b) has shown a tendency of grains slip of HCP crystal in hot deformation process which can be assumed as accurate if a stable deformation and temperature distribution can be applied during the experiment. The tendency of grains slip and orientation of titanium HCP grains under stable deformation can be viewed in the study by Hama et al. [212] on the work-hardening and twinning behaviours of titanium sheet, where similar pole figures were obtained that represents the high critical resolved shear stress in the hot deformation of titanium sheet. Zhang et al. [213] on grain refinement of Ti–6Al–4V in hot deformation has presented similar results and commented that the grains orientation has resulted from a grain refinement that implied significant improvement in the micro-hardness and tensile properties of the alloy.

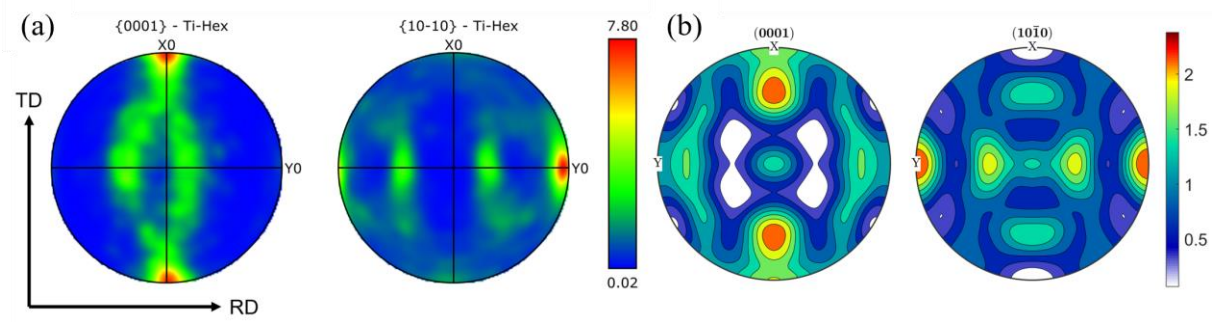

Figure 5-7. Pole figures of as-received sample (a) experimental, (b) RVE.

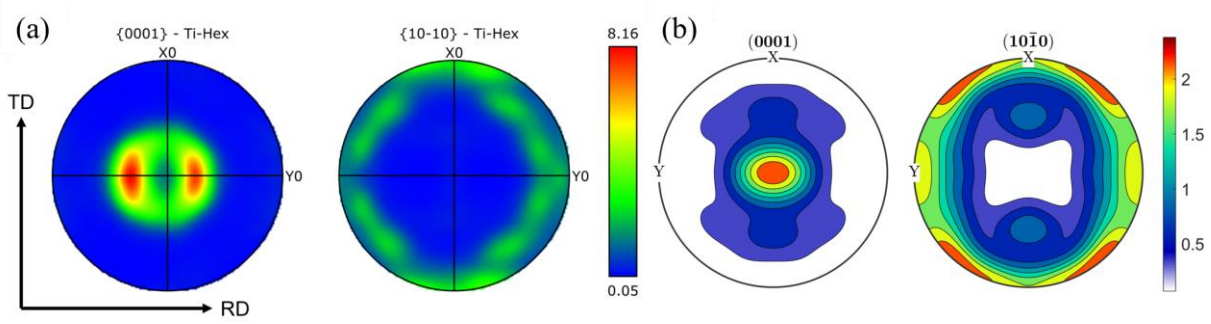

Figure 5-8. Pole figures of 700 ℃ upper sample (a) experimental, (b) RVE.

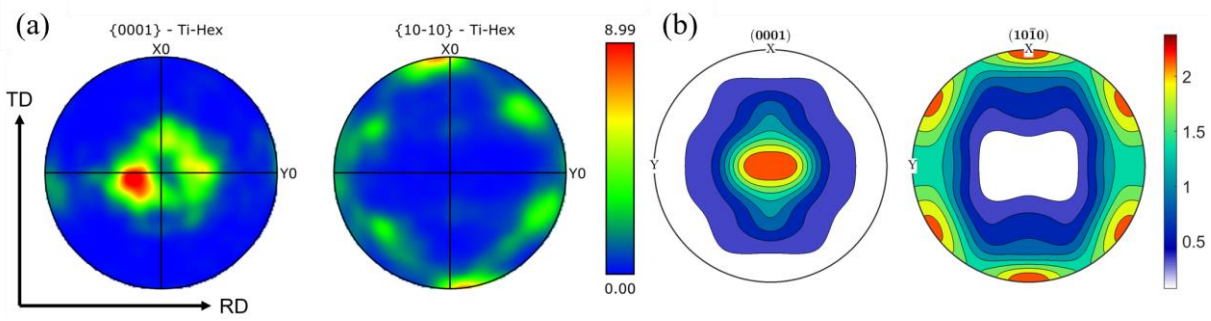

Figure 5-9. Pole figures of 700 ℃ centre sample (a) experimental, (b) RVE.

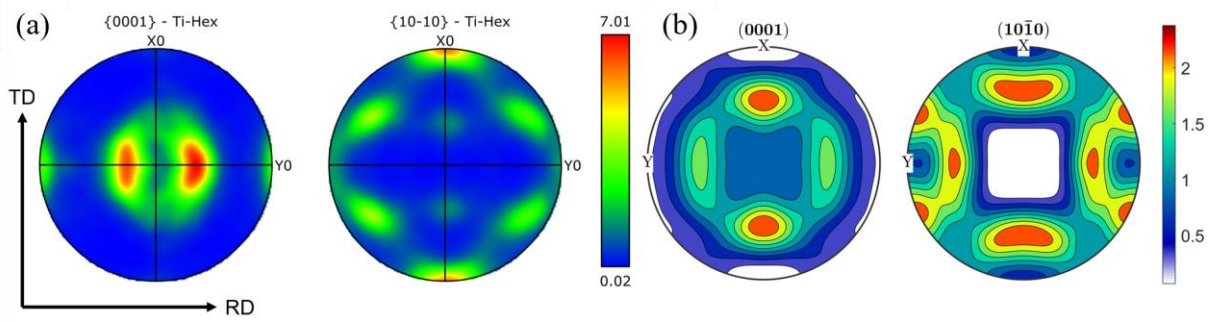

Figure 5-10. Pole figures of 700 ℃ lower sample (a) experimental, (b) RVE.

5.3.3. CA and EBSD

The EBSD IPF maps for 700 ℃ upper, centre and lower stage are shown in **Figure 5-11**. It is noted from **Figure 5-11**(a) that the as-received sample consists of numbers of initial recrystallised grains which illustrates a typical hot-rolled Ti-6Al-4V feature. As the experiment

moved to the 700 ℃ upper region, the DRX is initiated which tends to decrease the true stress. The initiation of DRX is more pronounced at the 700 ℃ centre region until the grains are recrystallised to coarser grains with a size around 1 μm. The nucleation is increased incrementally that limits the DRXed grain sizes and reduce the grain size. the detailed information of grain size can be found in **Table 5-5**.

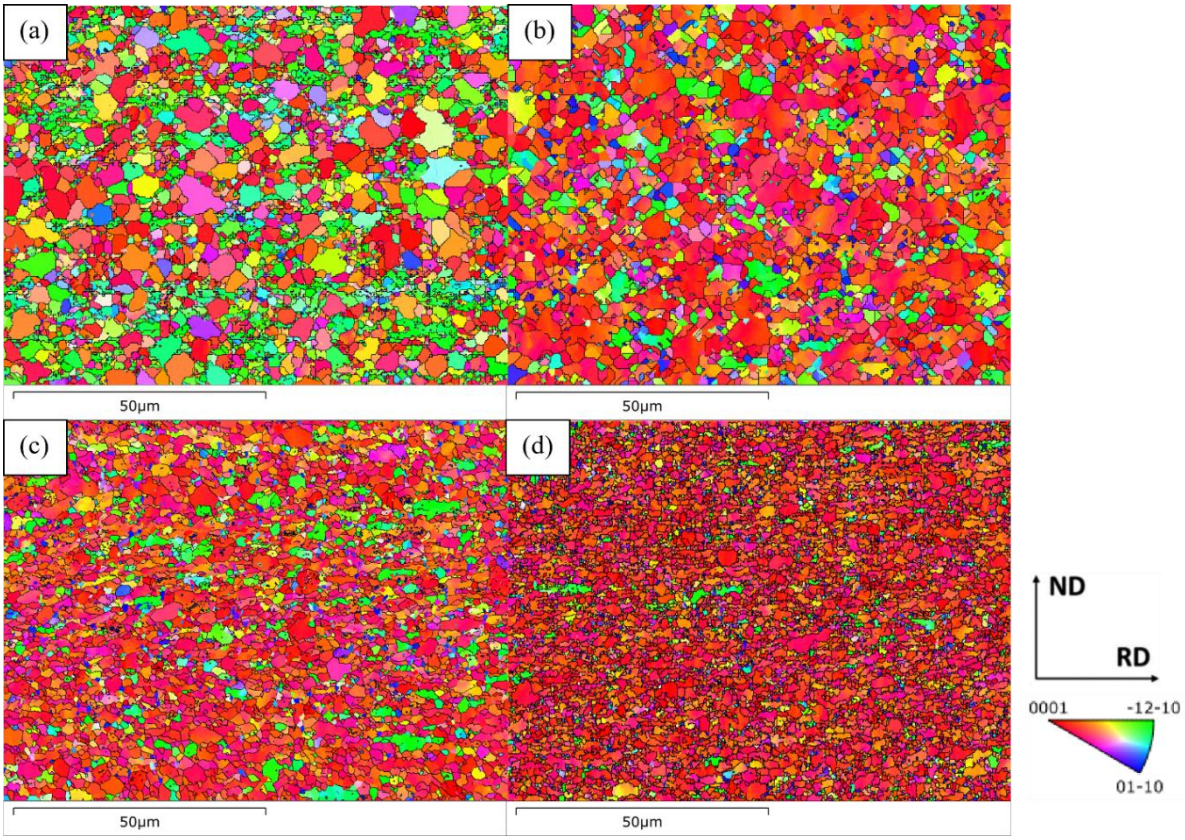

Figure 5-11. EBSD IPF maps of (a) as-received, (b) 700 ℃ upper, (c) 700 ℃ centre, (d) 700 ℃ lower.

The recrystallised percentage of the as-received and experimental samples are shown in **Figure 5-12**. It can be noted that the recrystallised fraction is increasing according to the experimental process, from 19.7% for the as-received sample and process to 71% for the lower sample. The simulated CA microstructure is shown in **Figure 5-14**. It is worth noting that a noticeable agreement has been achieved between the CA simulation and the EBSD results. By

investigating the CA simulated results, it can be seen that the nucleation of DRXed grains is more pronounced at grain boundaries, which indicates an increase of grains angle due to thermomechanical strain change throughout the process as shown in **Figure 5-13**. The previous study by Shrivastava and Tandon [116] on microstructure analysis of SPIF commented that SPIF has strong work hardening behaviour that transfers the low-angle grains (< 15°) to high-angle grains (> 15°).

Please note, to simulate a microstructure close to the close-experimental as-received sample, the initial CA is first applied with a strain rate of 0.01 s^{-1} and a temperature of 700 ℃ to reach a recrystallisation level of 20%. The parameters follow the study by Paghandeh et al. [214] on investigations of microstructural evolution of Ti-6Al-4V alloy. This formed map is then set as the initial microstructure, the experimental parameters will be applied on this map to simulate the evolution.

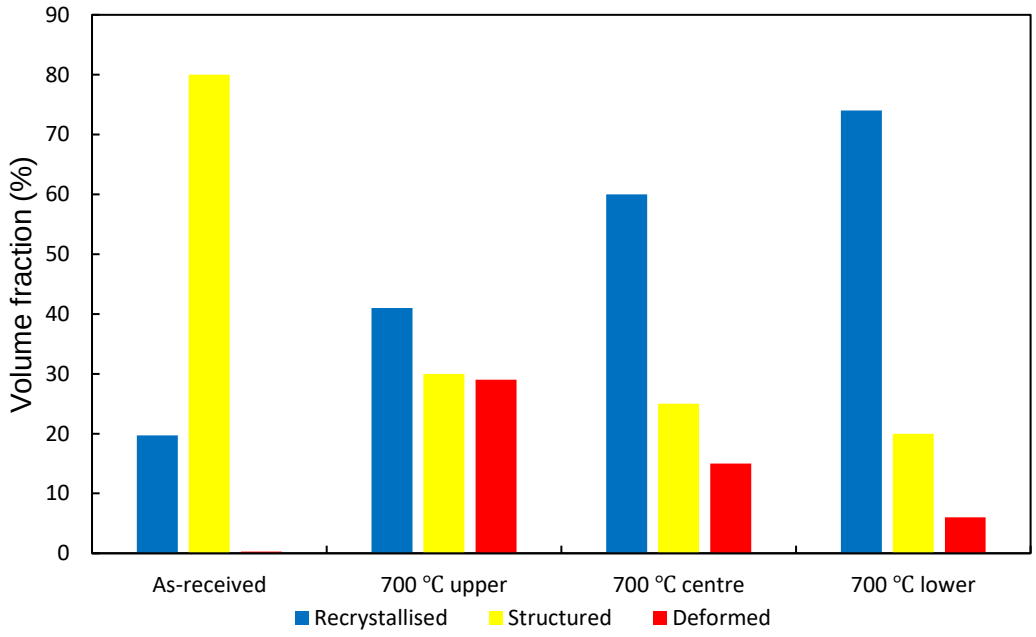

Figure 5-12. Recrystallised level of as-received, 700 ℃ upper, 700 ℃ centre, 700 ℃ lower.

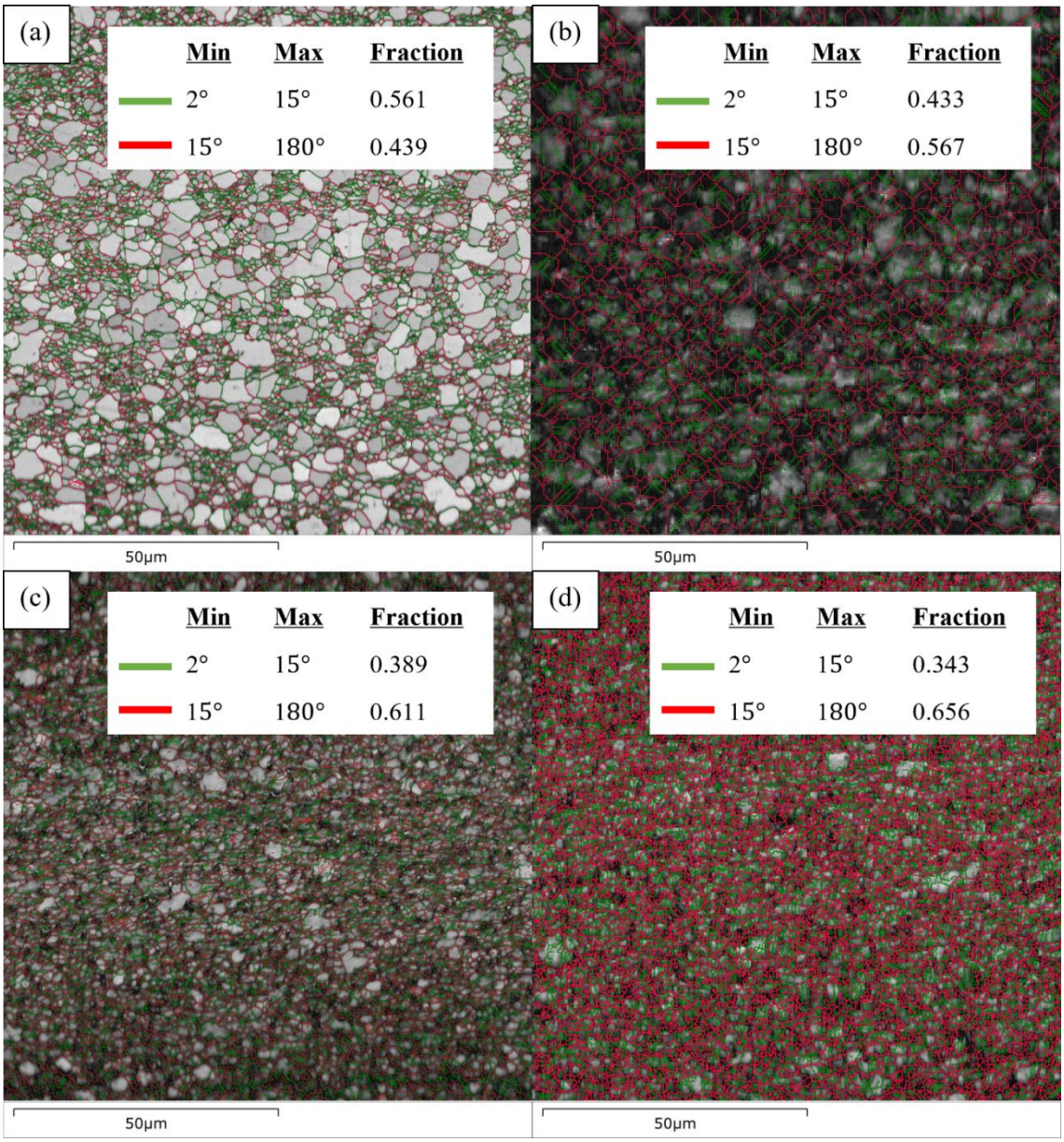

Figure 5-13. EBSD band contrast-based grain boundary distribution maps (a) as-received, (b) 700 ℃ upper, (c) 700 ℃ centre, (d) 700 ℃ lower.

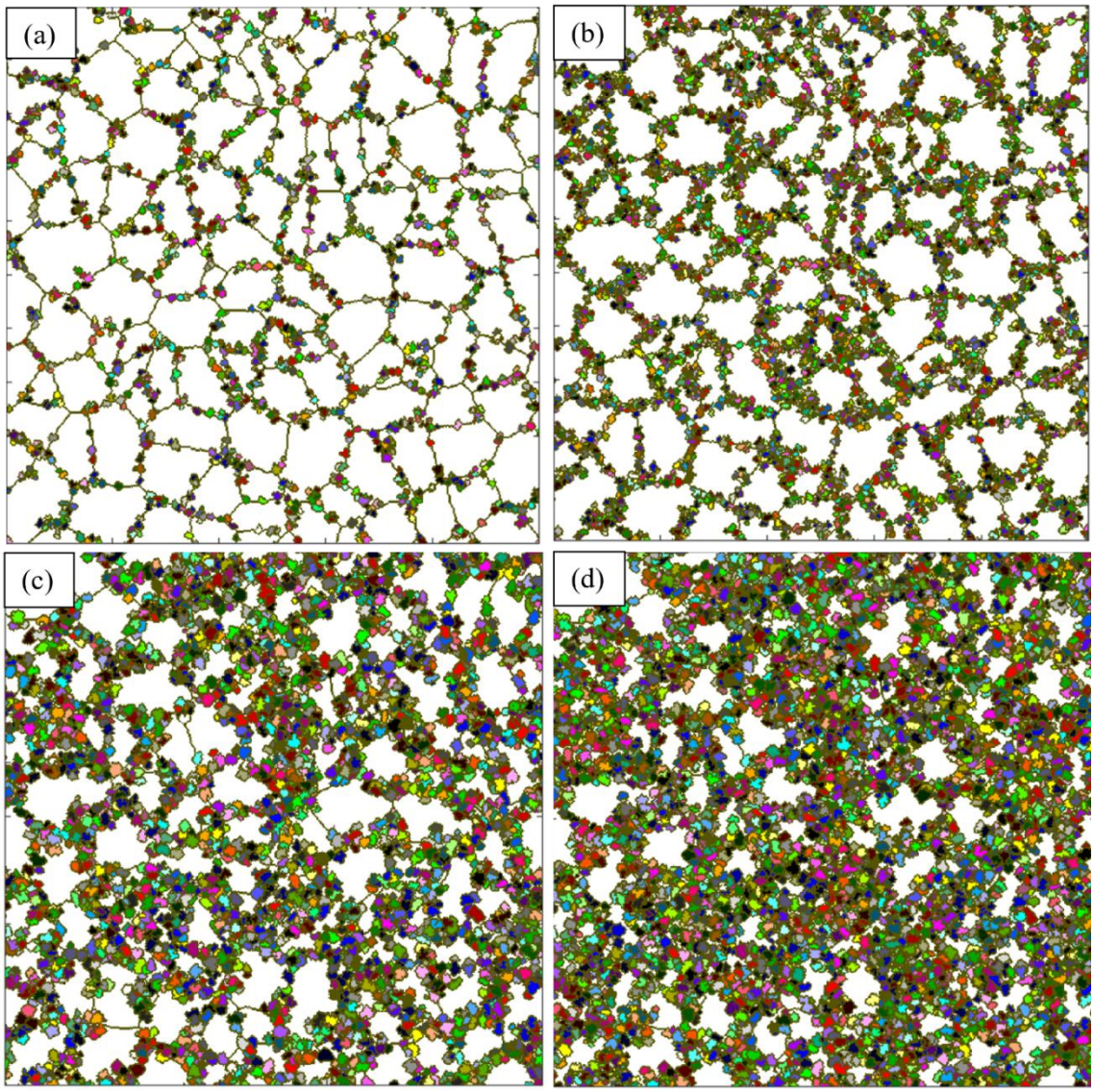

Figure 5-14. CA simulated microstructure under dynamic strain rate and temperature (a) as-received, (b) 700 ℃ upper, (c) 700 ℃ centre, (d) 700 ℃ lower.

By integrating the CPFEM grain orientation from upper, centre and lower node into the CA model to calculate the DRX fraction, the obtained simulating results are compared with the corresponding EBSD obtained results as shown in **Figure 5-15**. As illustrated, the increase of DRX percentage is linear with the strain distribution. As the forming tool passes through the node (upper, centre, lower) of the investigation, a critical value of temperature and strain is achieved and induced peak DRX percentage. It can be noticed the increasing trend tends to reduce and maintain a steady-state level once the peak DRX percentage has passed and the

results are agreed with the EBSD measured recrystallisation. It can be revealed that the temperature increases from upper to lower node induces an increased trend of strain distribution according to these nodes. The reason can be correlated to the relatively constant strain rate, the temperature implies significant effects on the strain distribution. From the upper to lower stage, a 30 ℃ temperature variation is detected during the process, and it affects the increase of strain. At the upper stage, the induced temperature is not stable thus resulting in lower strain distribution which leads to the lowest DRX level. The temperature is at a steady-state at the centre stage and the highest temperature (730 ℃) is obtained at the lower stage. The DRX is increasing accordingly to the temperature-induced strain. This proves that a small temperature variation may result in changes in strain distribution that significantly affects the DRX performance. By comparing with the EBSD examined recrystallised fraction, it can be observed that the EBSD values are slightly higher than the DRX results from CA. This is attributed to the calculation method in CA simulation that the continuous DRX only count the evolution of low angle ($< 15°$) boundary grains to high angle ($> 15°$) grains. This may cause an error with the recrystallisation calculation in the AZtecCrystal software, that the DRX percentage includes the geometric DRX, continuous DRX and discontinuous DRX. Regardless of the limited difference, both results still match well.

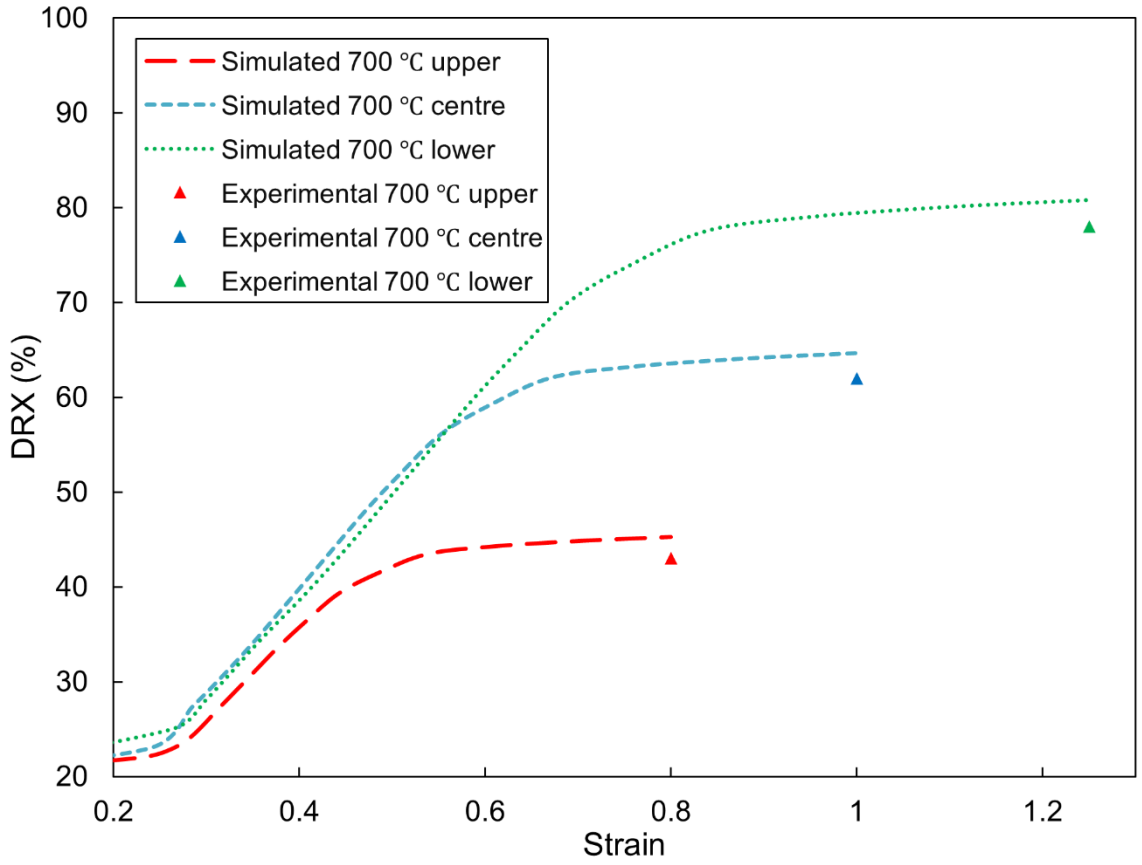

Figure 5-15. Comparison of DRX fraction between experimental and CA simulated results.

The CA simulated dislocation density results for the upper, centre and lower regions are shown in **Figure 5-16**. It is noted that the evolution of dislocation density is proportional to the DRX fraction, where the thermomechanical behaviours (strain rate and temperature) indicate significant effects in dislocation density development. The critical level of dislocation density also follows the zone of forming tool passing through the node area, and a steady-state region is reached once the critical level is passed.

It could be noted that the growth of dislocation density at the 700 ℃ upper stage is more rapid than the centre and lower stage, however, the peak point value is relatively low. The rapid increase of the growth can be attributed to the increase of strain rate at the centre and lower stage. As illustrated in **Figure 5-5**, the peak value of strain rate for upper stage is around 0.6 s^{-1}, and the value is increased to 0.7 s^{-1} at the centre stage and 0.8 s^{-1} at the lower stage. According

to the previous study by Ding and Guo [204] on the hot deformation DRX analysis, the critical dislocation density can be reached more readily at a lower strain rate as it results in the initiation of DRX at a relatively small strain that leads to a rapid increase of DRX percentage. At a higher strain rate, the increase of critical strain and DRX percentage is more graduate thus reducing the rapid growth of dislocation density such as the phenomenon in this chapter.

Another study by Ding and Guo [175] on the experimental and simulation of microstructure evolution of Ti–6Al–4V alloy, suggested that strain rate and temperature have a significant effect on the dislocation density as the critical value is increased with strain rate but decreased with temperature. In this chapter, it could be seen that the strain rate dominates the growth of dislocation density over the temperature, as the incremental increase of strain rate provides a noticeable increase in dislocation density even at the temperature at the centre and lower stage. Zhu et al. [215] on GND analysis in shear localisation of pure titanium commented that the work hardening is primarily contributed by active $< a >$ slips that results in higher $< a >$ type dislocation density. Another study Sangid et al. [216] on the energetics of residual dislocations suggested that the local stress concentration in dislocations may generate residual dislocations on the energy barriers thus resulting in higher dislocation density. The low-angle to high-angle transmission in this work is a role that increases the residual dislocations. Further, a study by Guo et al. [217] on the investigation of effects of stacking-fault energy (SFE) of α-Ti stated that change of slip mechanism could occur as temperature increases and addition of Al elements. According to the study by Williams et al. [218] on the investigation of single-crystals Ti-Al alloys, the titanium alloys with an Al concentration of 5–6 wt.% have shown identical critical resolved shear stress (CRSS) during temperature from 400 – 1000 K. At this temperature range, the cross-slip is not pronounced and may results in dislocation entanglements in the alloy. Britton et al. [219] has commented that such a phenomenon may reduce the values of CRSS and increase the basal and prism slip. Thus, it can be assumed that the incremental induced

deformation results in a slip in basal and prism planes (stated in section 5.3.2) increases the dislocation density and results in substantial creep through the TD direction.

For a thermomechanical deformation with dynamic straining behaviour such as the experiments in this chapter, Hama et al. [220] have commented that the prismatic $< a >$ type slip is more favoured for shear banding behaviour and in-plane anisotropy in work hardening. Thus, by using $< a >$ type mode and Burger's vector of 0.5 in EBSD calculation of GND, The GND distribution maps and statistics results are displayed in **Figure 5-17** and **Figure 5-18**. It can be clearly seen that the 700 ℃ upper stage indicates an area of relatively low dislocation density ($6.0 \times 10^{14}/m^2$) and it is increased to higher dislocation density at centre ($6.6 \times 10^{14}/m^2$) and lower stage ($6.9 \times 10^{14}/m^2$). It is worth noticing that the GND results have a good agreement with the CA simulated results.

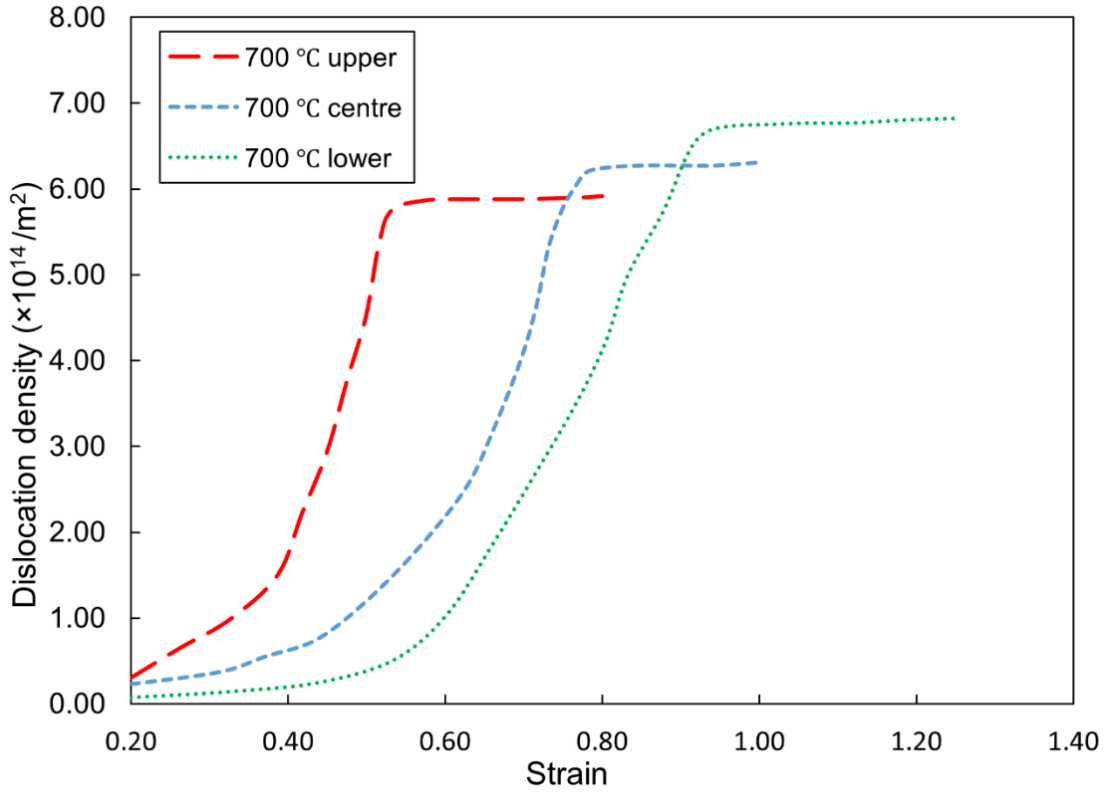

Figure 5-16. Dislocation density from CA simulated results.

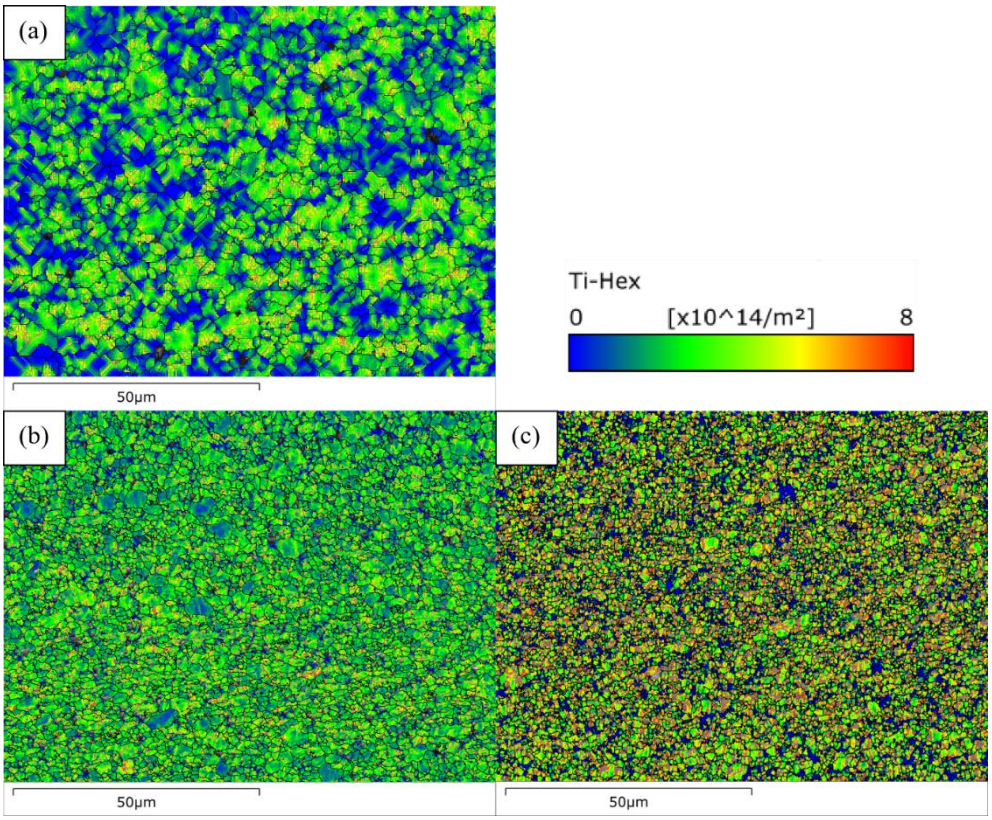

Figure 5-17. EBSD band contrast-based GND maps. (a) 700 ℃ upper, (b) 700 ℃ centre, (c) 700 ℃ lower.

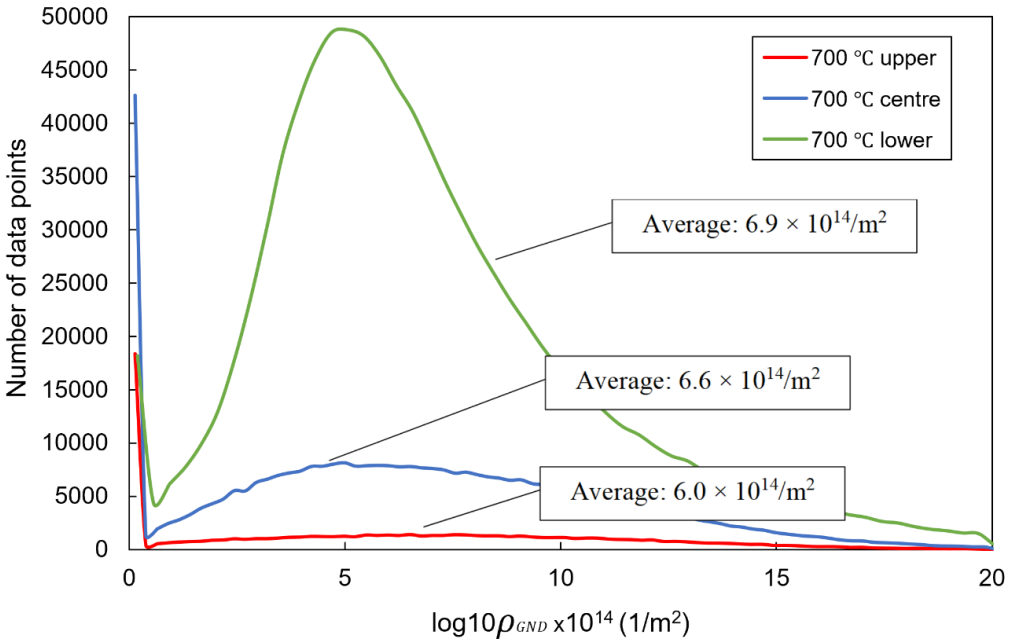

Figure 5-18. Statistics plots of GND results.

The comparation of experimental mean grain size and CA simulated grain size regarding upper, centre and lower region are shown in **Figure 5-19**. It can be seen that the reduction of CA simulated grain size after the incremental straining work has a good agreement with the experimental results with a relative error less than 5% which is a good validation of the model. By comparing with **Figure 5-15**, it can be noted that the mean grain size has been significantly refined with the incremental increase of strain and DRX percentage. For each stage, (upper, centre, lower) of the process, the incremental increase of temperature enhances the DRX initiation and results in a stress release in-between the subgrain which accelerates the mobility of the grain boundaries misorientation. Zherebtsov et al. [221] has investigated the microstructure and mechanical behaviour of Ti–6Al–4V between 450 - 700 ℃ with dynamic strain rate, the study reported that the hot deformation behaviour above 550 ℃ indicates an ultrafine α and β subgrains which is attributed to the enhancement of diffusion from the dynamic microstructural coarsening.

By referring to the EBSD measured data in **Table 5-5**, it is noticed that the low angle ($< 15°$) grains evolute to high angle ($> 15°$) grains according to the experiment process. By comparing with the grain size adding in the experimental grain size data (obtained from EBSD), it can be seen that the experimental grain size is following the evolution of CA. Due to the small grain size measured from EBSD, the results from CA cannot provide a perfect match, however, the evolution between the CA and experimental results still agree. The previous study by Orozco-Caballero et al. [150] has represented the similar behaviour and commented that the grains slip in α-Ti which usually occurs while the temperature is above 650 ℃, with a constant strain rate. In this chapter, the thermomechanical behaviour at 700 ℃ upper is unable to accelerate the grains slip and dislocation for a full DRX, thus the result of 700 ℃ upper is much lower than the centre and lower results. As the experiment is processed to the centre and lower region, enhanced DRX is achieved that makes the results closer to each other.

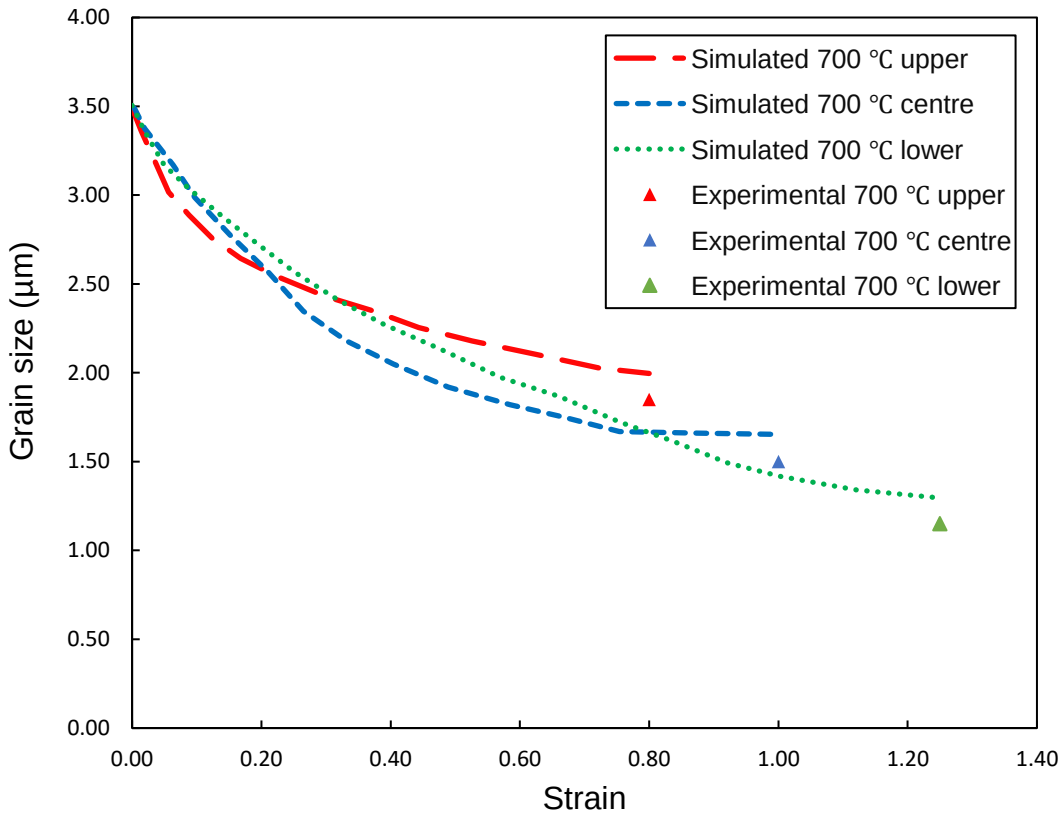

Figure 5-19. Comparison of simulated and experimental mean grain sizes as a function of deformation strain.

The fraction of grain size for each experimental parameter is illustrated in **Figure 5-20**. With assistance from **Table 5-5**, it is noted that the grain size is in a descending trend according to the experimental conditions. As the experiment initiates, the grain size is reduced to around 1 to 1.5 µm, there is no significant difference between 700 ℃ upper to 700 ℃ lower sample. However, the maximum and minimum grain size distinguish the results. The maximum grain size of the upper sample is 10.4 µm to 6.3 µm, and the minimum grain size is reduced from 0.71 µm to 0.2 µm. The β-phase content and the sharp increase of grains angle from low to high also indicate that the thermomechanical behaviour from the SPIF is dynamic at upper region and it is getting more steady and centre and lower region which balance the DRX process.

Wang et al. [222] has investigated the hot deformation and the microstruture evolution of Ti-

6Al-4V alloy. The study has detected a phenomenon that indicates a transformation of stable grains slip to active slip modes during 650 ℃ deformation. Thus, it can be evident that the sustainable support temperature of 700 ℃ in this work is sufficient to initiate the DRX process. With an increment increase of strain rate from the upper to lower region, the straining behaviour is also enhanced thus leads to development in dislocation density.

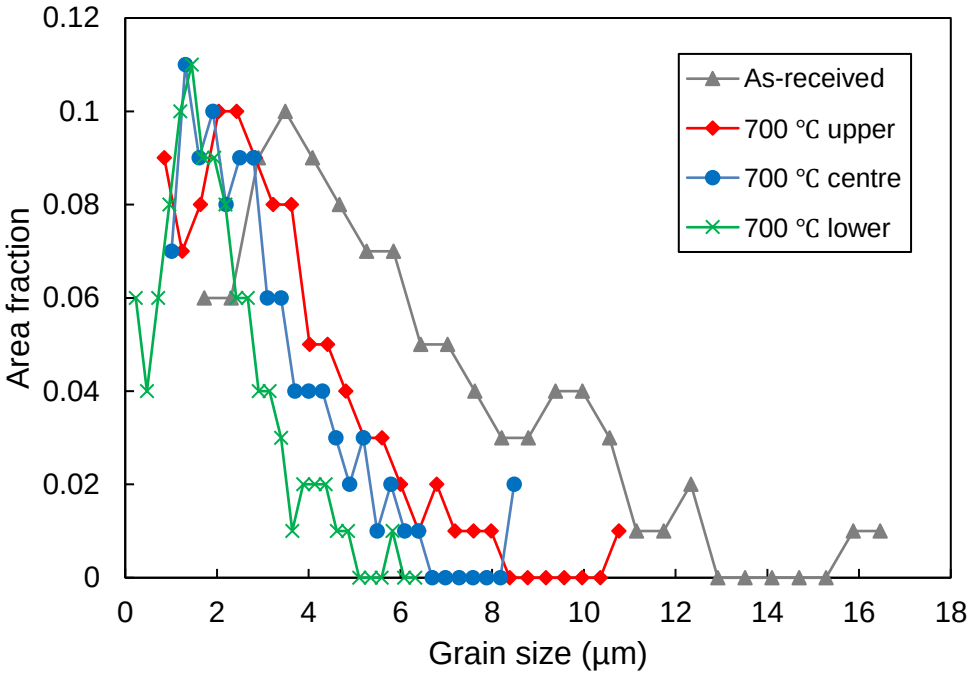

Figure 5-20. The area fraction of grain size for different experimental parameters.

Table 5-5. Grains data measured by EBSD

Average grain size (µm)	Max grain size (µm)	Min grain size (µm)	Ti-Hex (%)	Ti-Cubic (%)	Grain boundaries ≤ 15° (%)	Grain boundaries ≥ 15° (%)

As received	2.80	15.90	1.1	98.8	1.2	56.1	43.9
700℃ upper	1.53	10.40	0.71	98	2	43.3	56.7
700 ℃ centre	1.20	8.18	0.5	97.6	2.4	38.9	61.1
700 ℃ lower	1.04	6.30	0.2	94.6	5.4	34.4	65.6

5.4. Conclusion

- The grain level strain, strain rate and temperature distribution from the element-to-grain CPFEM is verified as useful to be used as input to establish the RVE model.
- The pole figures obtained from the RVE reveal good agreement with EBSD results and the changes of the pole figures at each stage indicates the microstructural evolution for the heat-assisted SPIF process.
- The recrystallisation percentage is proportional to the incremental stage of the process and the relationship is actively linked to the evolution of dislocation density. The temperature and strain rate distribution are key factors that dominate the distribution of dislocation density.
- For an incremental increase of strain rate and temperature, the dislocation density is increased accordingly which indicates that the strain rate shows higher domination in controlling the dislocation density which overcomes the reduction of dislocation density

from the temperature increase. Further, it can be found that the dislocation entanglements and residual dislocations are secondary factors that increase the basal and prism slip which results in an increase in dislocation density.

- The grain size evolution is inversely proportional to the recrystallisation percentage and dislocation density where the slip of grains is increased with the increase of misorientation angles from a low angle ($< 15°$) grains to a high angle ($> 15°$) grains homogenously. Such behaviour results in a reduction in grain size.
- The critical point of the DRX percentage, dislocation density and grain size corresponds to the contacting zone of forming tool passing through the node area. Once the peak value is reached, a steady-state region will be achieved.

This study proposed a combination of CPFEM, RVE and CA modelling of heat-assisted SPIF work of Ti-6Al-4V sheets to provide the plasticity behaviour and microstructural evolution of the sheet materials under thermomechanical deformation. This study is only available for single crystal constitutive law based on HCP crystal structure. Therefore, there is no measurement of phase transition and twin grain calculation. The current modelling can be improved in future to apply polycrystalline inputs to simulate the plasticity behaviour above phase transition.

Acknowledgement

This work was funded by the Department of Mechanical Engineering, University of Birmingham.

6. Application of machine learning on tool path optimisation and cooling lubricant control in induction heating-assisted single point incremental sheet forming of Ti-6Al-4V sheets

Weining Li [a], Chang Shu [a], Ali Hassan [b], Moataz M Attallah [c], Khamis Essa [a].

[a] *Mechanical Engineering, University of Birmingham, Edgbaston, Birmingham, B15 2TT, UK*

[b] *School of computing, Engineering and Digital Technologies, Teesside University, Middlesbrough, TS1 3BX, UK*

[c] *School of Metallurgy and Materials, University of Birmingham, Edgbaston, Birmingham, B15 2TT, UK*

This research was accepted as a full-length research article in *International Journal of Advanced Manufacturing Technology*

Credit authorship contribution statement

Weining Li: Conceptualization, Investigation, Methodology, Validation, Software, Formal analysis, Writing - original draft.

Chang Shu: Investigation on machine learning work.

Ali Hassan: Cutting for workpieces.

Moataz M Attallah: review & editing, Resources of lab equipment, Supervision.

Khamis Essa: Writing - review & editing, Resources of lab equipment, Supervision, Project administration.

Research contributions:

This chapter aims to complete the objective 6 which covers the following insights:

- Induction heating system to provide rapid and localised heating at 950, 980 and 1040 ℃ to deform Ti-6Al-4V sheet metals above beta-transus temperature.
- A controllable ball-roller to reduce the friction and thermal expansion, and further dominate the microstructure evolution during the elevated temperature deformation.
- ANN (radial basis function network) to study the tool path plan, temperature and forming force from groups of experiments and output a machine learning optimised tool path to compensate the thermal expansion of the sheet metal during the process.

Abstract

Induction heating-assisted single point incremental sheet forming was established for Ti-6Al-4V thin sheets at closed and above beta-transus temperature (980 ℃). In order to eliminate geometric inaccuracy and adherence of lubricant on the surface caused by elevated temperature, a cooling lubricant system was designed for the forming tool to decrease the thermal expansion and friction. A radial basis function (RBF) based tool path optimisation was developed to study the measured geometric accuracy, temperature and forming force. By adjusting cooling lubricant control and integrating the RBF framework, the first optimised tool path was used to collect the results and to validate with the finite element (FE) model and theoretical geometric profiles. The output data were further studied by RBF and generate a second optimised tool path. The measured geometric coordinates revealed that the error percentage has been reduced to less than 5%. Further, the microstructure evolution analysed by scanning electron microscopy (SEM) indicated noticeable oxidation and alpha-layer for temperature around 1040 ℃ and the phenomenon was removed at temperature closed to 950 ℃. The surface roughness and energy dispersive X-ray analysis (EDX) revealed the optimised tool path significantly improved the surface quality. The cooling lubricant system indicated optimal performance with RBF optimised tool path to support constant temperature and reduce friction and lubricant adherence on the surface.

Keywords: high temperature incremental sheet forming of Ti-6Al-4V; machine learning network; tool design; geometric accuracy; surface roughness; microstructural analysis.

6.1. Introduction

The process of single point incremental sheet forming (SPIF) has been developed over a number of decades for the deformation of sheet materials using flexible methods for complicated prototypes. High geometric accuracy and surface quality have been achieved with respect to low-strength metal alloys. For instance, Dabwan et al. [223] has applied SPIF on AA1050-H14 aluminium alloy at room temperature which revealed excellent geometric accuracy and surface quality. However, the study commented that the step transition region indicated highly deformed region which increased the geometric inaccuracy and waviness error. Shrivastava and Tandon [116] has investigated the microstructure of AA1050 under room temperature SPIF and proposed that the grain refinement during the process increased the straining behaviour thus induced springback. Ambrogio et al. [224] has investigated SPIF on AZ31 magnesium alloy which revealed high performance in increase of formability and geometric accuracy, however, the risk of fracture was increased in forming of complex shapes. Trzepiecinski et al. [225] have investigated room temperature SPIF on EN-2024-T3 and EN AW-7075-T6 aluminium alloys sheets. The results revealed that the efficient application of lubricant and reduction of step size significantly improved the surface quality. Room temperature SPIF indicated that high geometric accuracy and surface quality can be achieved for low-temperature materials as the maintenance of modest forming force and efficient lubrication. However, heat sources must be integrated for high-strength materials to reduce the forming force such as steel or titanium.

Sakhtemanian et al. [48] have studied pure titanium alloy SPIF using ultrasonic vibration at temperatures of up to 250 °C in order to synthesise a high-quality product. However, pronounced friction wear can be observed on the formed surface with detectable springback behaviour. Cheng et al. [52] investigated the deformation behaviour and material flow during the SPIF process. The results commented that the dynamic effects from the ultrasonic vibration induced a noticeable reduction of the forming force and a significant increase of wear on

deforming surface. The similar study by Li et al. [163] found that the heating temperature for high-strength alloys should be maintained as constant to produce stable plastic deformation to the sheet materials. These limitations were overcome by integrating heat sources into the SPIF system in order to provide regional or localised heating to the workpiece, thus increasing ductility and assisting deformation. The electrical current system was integrated prior to carrying out the process on the Ti-6Al-4V sheets.

To further improve the geometric accuracy and surface quality, Li et al. [65] developed a high-frequency induction heating SPIF system which provided localised heating to deform Ti-6Al-4V sheets with a ball-roller tool, thus reducing friction at the tool-contact interface. The ball-roller tool design was proposed by Iseki and Naganawa [71] following tool path optimisation investigations. It was applied in relation to the electric heating SPIF of Ti-6Al-4V sheets by Liu et al. [29]. It was validated that this process led to the production of more optimal surface quality than conventional tools. Comparison with a common induction heater demonstrated that high-frequency induction heating could provide rapid eddy current transfer which was able to accelerate heat generation and to maintain a constant temperature. Ortiz et al. [145] observed that the microstructure evolution indicated a pronounced dynamic recrystallisation (DRX) at temperature of 700 ℃, which successfully increased the deforming behaviour and reduced the forming force. This geometric accuracy was superior to that attained at lower temperatures. However, the rise in temperature also increased lubricant dissipation; this lubrication anomaly impacted surface quality. In order to minimise this effect, a ball-roller tool was designed which reduced the contact area between the surface and the tool, thus efficiently enhancing surface quality.

Lubricant is another factor affecting the surface quality in heat-assisted SPIF. Formisano et al. [226] have investigated lubricant application and its effects on surface roughness during the SPIF process on titanium alloys, observing that sustainable support of low viscosity lubricant

is a key factor in enhancing lubricating functionality. Oleksik et al. [227] agreed the statement and suggested that localised heating is more efficient to maintain the endurance of lubricant.

It can be observed from previous research that the application of a heat source is an effective method by which to deform Ti-6Al-4V sheets during the SPIF process. The temperature support for electric current and laser heating SPIF is normally maintained between 400 °C and 600 °C; induction heating is able to provide a constant localised temperature of up to 700 °C. Owing to the incremental deformation from the tool motion, constant temperature is hard to maintain during the process. However, it is essential to improve temperature conditions during the heating-assisted SPIF process of Ti-6Al-4V sheets so as to improve their formability, wear, corrosion and temperature oxidation resistance further.

Zhang et al. [228] investigated the mechanisms underlying deformation and fracture for Ti-6Al-4V alloys under different heat treatments and noted that excellent hardening and deforming behaviour can be achieved at the beta-transus temperature (980 °C). Furter, Singh et al. [229] suggested that the increase of cooling rate may increase the hardening effects. This was principally ascribed to the maintenance of constant temperature and rapid cooling rate on surface which increased the volume of α'-martensite and grain refinement within the microstructure. This proved that the above beta-transus temperature SPIF on Ti-6Al-4V could achieve favourable effects in straining behaviour to enhance the formability. However, the temperature must be controlled as a constant support with a sustainable cooling rate during the process to prevent the thermal expansion of tool and sheet metals to affect the geometric and surface quality.

In recent years, machine learning has been integrated into the SPIF system in order to predict temperature and springback behaviours. Jiang et al. [37] investigated the temperature prediction for an electric current SPIF process using an artificial neural network (ANN) framework. The model was trained using the temperature outputs from the finite element model (FEM) and

validated with experimental data. The findings were useful for the prediction of parameters, such as temperature distribution and forming force, and facilitated estimation of microstructural evolution during the process. Wang et al. [35] developed an online adaptive shape predictive model for the purposes of predicting the forming geometry within each incremental step. The model was incorporated into a coupled constrained control algorithm so as to minimise geometric error and to optimise the potential step which could provide an accurate tool path to improve geometric accuracy.

It can be noticed from the above literature that the issues in the field of heat-assisted SPIF processing that yet need to be addressed. These include uneven temperature distribution, thermal expansion-induced springback, unpredictable DRX and phase transition-induced straining behaviours. These factors significantly affect the geometric accuracy, surface quality as well as structure integrity. The aim of this study was to develop an induction heating SPIF system in order to deform Ti-6Al-4V sheets at a temperature above and in the region of beta-transus, and to apply a machine learning method in order to optimise tool path generation. The initial training experiments were designed with identical experimental parameters. Following their completion, the obtained geometric coordinates, temperature and forming force data were input into the machine learning system to develop an optimised tool path. The cooling lubricant and optimal tool path were then applied in order to validate the optimal results. Forming force, geometric accuracy and surface roughness of the initial and machine learning optimisation samples were assessed using scanning electron microscopy (SEM) and electron backscatter diffraction in order to observe the mechanical behaviours and to document the relevant outputs, thus providing data on microstructural evolution.

6.2. Materials and set-up

6.2.1. Sheet metals and lubricants

The workpieces are Ti-6Al-4V alloy thin sheets, 150 mm x 150 mm in dimension, and with a thickness of 1 mm. The chemical composition is presented in **Table 6-1**. This material composites more content of vanadium which slightly decreased beta-tranus temperature.

Table 6-1. Chemical composition of Ti-6Al-4V (wt.%)

Ti	Al	V	O	C	N	H	Fe
Balanced	5.5	4.5	0.2	0.08	0.05	0.015	0.25

The cooling lubricant system in this study is same as explained in the previous chapter 4 with a number of adjustments to enhance lubrication performance. A layer of MoS_2 paste lubricant was applied generally to the workpiece. The lubricant type and lubricating method are same as is same as explained in the previous chapter 4. The tool was designed to facilitate provision of enduring tool lubrication as shown in **Figure 6-1**. The tool design will be explained in next section.

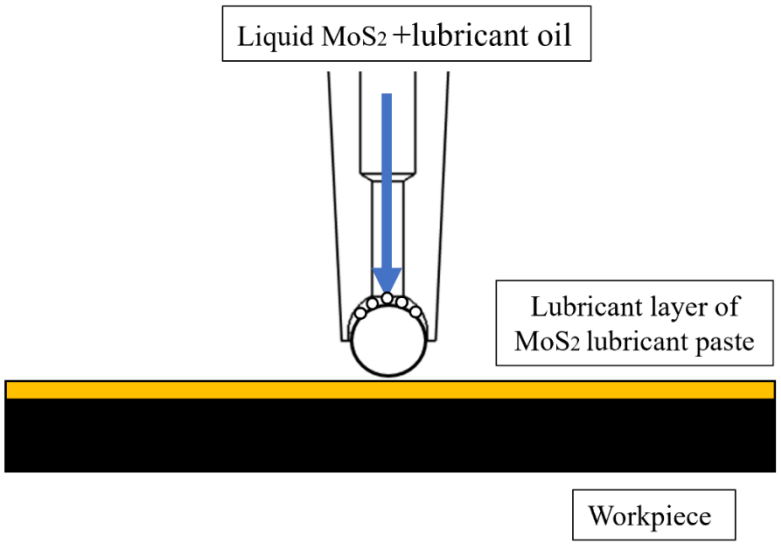

Figure 6-1. Schematic of the lubricating system.

6.2.2. Tool design

Tarín et al. [230] investigated alpha-beta transformation in Ti-6Al-4V alloys, and concluded that the beta-transus temperature was approximately 980 ℃ for 4 wt.% of vanadium. For the thin Ti-6Al-4V sheets used in this study, the beta-transus temperature could be estimated to be between 960 ℃ and 970 ℃. In a localised heating-assisted SPIF process, deformation is based on the synchronisation of the constant temperature supply and the tool's movement. Since the temperature was close to the beta-transus, a nickel ball-roller was selected for this study in order to improve the tool's operational temperature.

The tool design in this chapter made a modification on the ball-roller explained in chapter 4. The details are shown in **Figure 6-2**, the ball is modified to 5 mm in diameter and made of IN 625 nickel alloy, which has a service temperature of 980 ℃. The ball-roller is attached to the main tool body; lubricant balls are interposed between the ball-roller and the steel net of the cooling channel. The lubricant balls are also composed of IN 625 nickel alloy which has a diameter of 1 mm. The steel net, which has a grid length of 0.5 mm, keeps the lubricant balls in the lubricating slots. The purpose of the lubricant balls is to prevent any extrusion between the ball-roller and the slot wall. In the course of the process, potent thermal expansion may result in the strong adherence of the ball-roller to the tool wall and affect the rotation. Additionally, the lubricating balls can enhance liquid lubricant flow to the ball-roller.

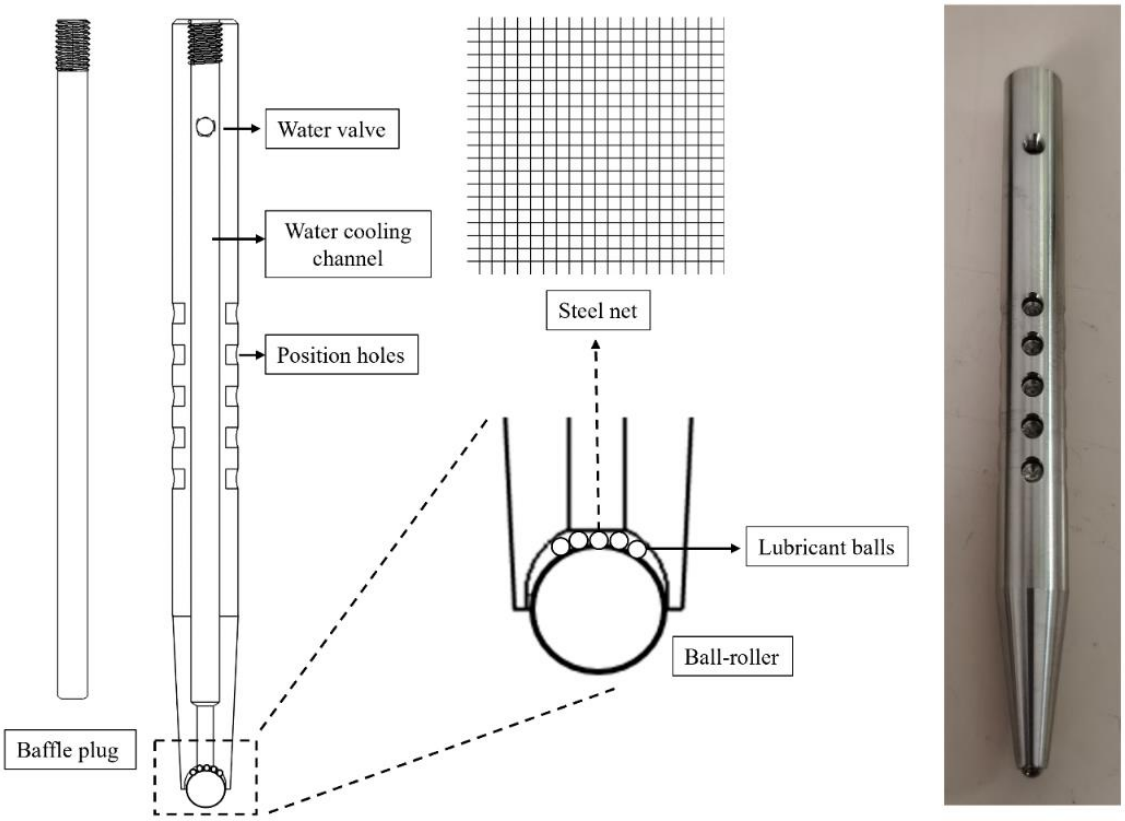

Figure 6-2. Tool design: left, scheme draft of the tool design; right, the produced tool.

6.2.3. Experimental set-up

The equipment used in this chapter is same as explained in the previous chapter 4. Certain modifications were made and illustrated in **Figure 6-3**.

A water tank was filled with 10 L liquid lubricant in order to provide an ongoing lubricating function to the tool. The flow rate could be controlled by a submersible pump, which operated within the range 1 L/h to 50 L/h; this was connected to the inlet cooling valve. Another water tank included a submersible pump with similar parameters which was connected to the cooling channel's outlet valve. During the experiment, the flow rate would be controlled according to the tool path's locations in order to provide sufficient liquid lubricant to reduce ball-roller tool thermal expansion and friction.

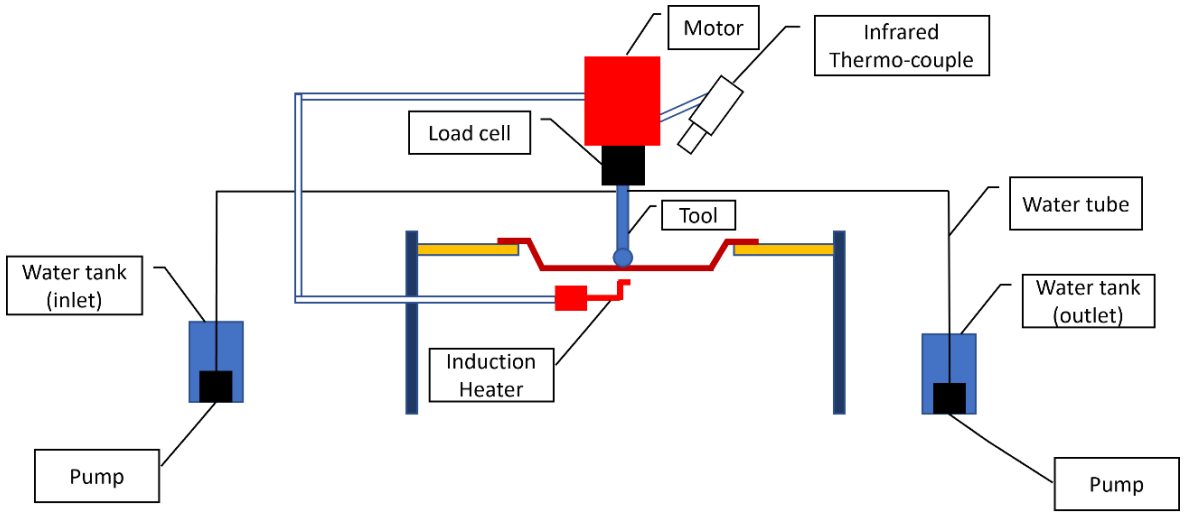

Figure 6-3. Induction heating SPIF system set-up.

6.2.4. Forming shape

The tool path design is same as described in the previous chapter 4. The final shape took the form of a truncated cone with a main diameter, height and wall angle of 100 mm, 30 mm and 45^{o}, respectively (**Figure 6-3**(a)). MATLAB was used to form the tool path and to generate a G-code coordinates output file for application by the computer numerical control (CNC) machine. The tool path points are illustrated in **Figure 6-3**(b). It can be observed that the step tool path maintained the peak percentage of position coordinates which results in more tool movements. Such behaviour may increase the temperature variance at these positions and influence the geometric accuracy of the forming shape. Thus, the RBF networks were used to optimise the step tool path for superior geometric accuracy.

It is important to note that a contour tool path was applied in this study; a clear mark of a step tool path would be evident within the forming shape thus potentiating the likelihood of geometric, temperature and forming force instabilities. These factors can be enhanced by RBF network optimisation; the tool path is applicable for a wide range of SPIF processes. A helical tool path has the potential to diminish such behaviours as there is no step tool path. However, Malhotra et al. [231] stated that the algorithm is only limited to the axisymmetric movements. Behera et al. [8] further commented that the forming shape of helical tool path is not fully

completed at the beginning and ending stage, and the output geometry is designed by wall angle not step size. Behera et al. [9] and Han et al. [232] suggested that a contour tool path provided a more complete forming shape as the step size can be defined in the CNC setting, whereas the helical tool path is only applicable to axisymmetric geometry and for the provision of high surface quality. The latter is complex to generate since the algorithm is specific for each forming shape and the process can only be controlled by the ramp angle in the CNC settings.

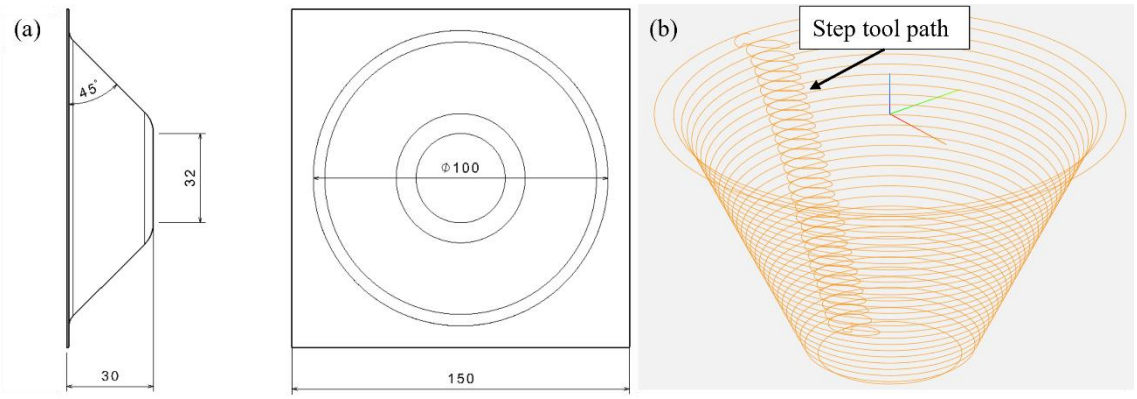

Figure 6-4. Designated forming shape: (a) dimensions; (b) tool path CNC forming points.

6.3. Methodology

6.3.1. Application of radial basis function networks and design of experiments

RBF network is an artificial neural network that uses radial basis functions as activation functions. The output of the network is a linear combination of radial basis functions of the inputs and neuron parameters which have been shown in heat-assisted SPIF studies [37, 233] to predict the temperature and tool path. As shown in **Figure 6-4**(b), it can be observed that the tool step path demonstrated the most position points. Owing to the rapid heating support from the high-frequency induction heater, the temperature variance for this particular path was higher than the rest of the tool path and thus increased the springback during the experiment. Thus, the coordinates associated with the corresponding temperature and forming force on this path could be collected for training by the machine learning algorithm.

In order to apply the RBF optimisation effectively, the experiments were designed in 3 phases, i.e. as initial, first RBF optimisation and second RBF optimisation sets, respectively. Each set consisted of 5 experiments with the same conditions. The machine learning studied the geometric coordinate output as the main data and related the behaviours to temperature and forming force in order to predict an optimised tool path and to improve geometric accuracy.

A RBF network was selected due to its universal approximation and rapid learning speed so that multiple factors could be evaluated and undergo analysis. RBF can be defined as a type of feedforward ANN network which has three layers (**Figure 6-5**). The input layer consists of input data, such as geometric coordinates, temperature and forming force, on the corresponding tool path points. The hidden layer comprises a series of RBF non-linear activation units which facilitate study of the input layer. The final output is in the form of workout activation implemented in Gaussian functions. As illustrated in **Figure 6-5**, the example analysis data set includes inputs from $x_1$to x_n, together with hidden layer RBF calculating units from $w_1$to w_n and an output from y_1 to y_n. A RBF training model has numerous nodes in the hidden layer; the training is terminated when the calculation error meets the requirement of the desired volume or when a training iteration has been completed.

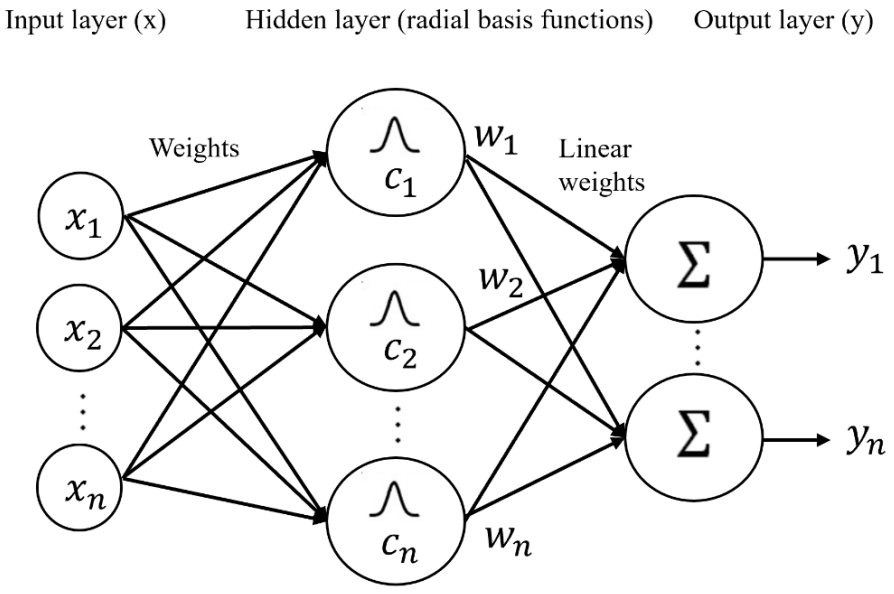

Figure 6-5. Example of RBF network.

The output of the *i*th radial basis activation function, ϕ_i, in the hidden layer of the network can be calculated using **Eq. (6-1)** based on the Euclidean distance between the input pattern, x, and the centre, i, where $\|\cdot\|$ denotes the Euclidean distance between x and c_i, and c_j and σ_j are the centre and width of the hidden neuron, j, respectively.

$$\phi_i(x) = \exp\left(-\frac{\|x - c_i\|^2}{2\sigma_j^2}\right) \tag{6-1}$$

The output of the node, k, of the output layer of the network can then be calculated utilising **Eq. (6-2)**:

$$y_k = \sum_{j=1}^{n} \omega_{jk}\phi_j(x) \tag{6-2}$$

The majority of classical approaches deployed in the literature for training RBFs are performed in two stages. In the first stage, the centres and widths are determined using, for example, an unsupervised clustering algorithm, whilst in the second stage, the connection weights between the hidden and output layers are determined in such a way that the error criterion, e.g. the root mean squared error (RMSE), is minimised throughout the data set.

6.3.2. Accuracy analysis

Since the input in this study was based on the tool step path, the variant could be defined by the X and Z coordinates; the Y coordinates could be neglected. Thus, the model could be simplified to a 2-dimensional (2D) RBF paradigm which significantly reduced the calculation time in the RBF network. In this study, 130 tool path geometric coordinates with respect temperature and forming force data were considered as neurons in the RBF study. The output layer is 1 (tool path coordinates) and 3 input layers (tool path coordinates, temperature, forming force). A total of 12,000 input-output pairs were generated to respond the inputs. Please refer to the support

document for the detailed calculation and explanation.

Fiorentino et al. [234] commented that the network training can be defined as a feedback loop which facilitates the study of the process parameters and Dittrich et al. [84] further classified machine learning of tool path generation in CNC processes which proposed that the model was contrasted against the experimental data; where five statistical parameters were compared, including the RMSE, the squared multiple correlation coefficient (R^2), the bias or distortion (β), the Wilmott index (I_w) proposed by Wilmott [235] to measure the prediction error for RMSE, and the error function (ε) proposed by Haller et al. [236] to measure the standard normal cumulative probability.

$$RMSE = \left[\sum_{i=1}^{N} \frac{\left(\frac{X_{c_i} - X_{m_i}}{X_{m_i}}\right)^2}{N}\right]^{1/2} \tag{6-3}$$

$$R^2 = \frac{\left(\sum_{i=1}^{N} \left(X_{m_i} - \bar{X}_m\right)\left(X_{c_i} - \bar{X}_c\right)\right)^2}{\sum_{i=1}^{N} \left(X_{m_i} - \bar{X}_m\right)^2 \sum_{i=1}^{N} \left(X_{c_i} - \bar{X}_c\right)^2} \tag{6-4}$$

$$\beta = \frac{\sum_{i=1}^{N} \left(\frac{X_{c_i}}{X_{m_i}}\right)}{N} \tag{6-5}$$

$$I_w = 1 - \frac{\sum_{i=1}^{N} \left(X_{c_i} - \bar{X}_{m_i}\right)^2}{\sum_{i=1}^{N} \left(\left|X_{c_i} - \bar{X}_m\right| + \left|X_{m_i} - \bar{X}_m\right|\right)^2} \tag{6-6}$$

$$\varepsilon = \left[\frac{\sum_{i=1}^{N} \left(X_{c_i} - \bar{X}_{m_i}\right)^2}{\sum_{i=1}^{N} X_{m_i}^2}\right]^{1/2} \tag{6-7}$$

In the above equations, N represents the number of data in each group, and X_c and X_m indicate predicted and measured experimental data, e.g. geometric coordinates, temperature and forming

force, respectively. The training was terminated when the values of R^2 and I_w were equivalent or lower than 1.0, and ε was reduced to 2%, a strategy which revealed enhanced agreement with the results. The learning basis was recommended by Sharif Ahmadian [237], who investigated the use of RBF networks in numerical modelling; these were validated to give a precise output for 2D accuracy analysis.

6.3.3. Particle swarm algorithm

In this study, the platform, TensorFlow [238] was applied in order to run the RBF network training. The input layer of the RBF network consisted of the points on the step tool path, together with the corresponding data points including geometric coordinates, temperature and forming force from the experimental measurements. The output layer is the optimised tool which was predicted on the corresponding input layers.

To converge the training from RBF network, a simplified optimisation should be used to accelerate the convergence of the algorithm. Particle swarm algorithm (PSO) is best method to apply multi-level inputs, Han et al. [232] has investigated different ANN networks to predict the springback of SPIF and proposed that the PSO can be integrated to the RBF network to study the random parameters. The PSO aims to search the potential solution (particle) in space. Each particle has independent space and velocity, the values on the direction and space can be determined by the optimisation function. Please see the attached supporting document for the step-by-step PSO integration.

The results of machine learning geometric accuracy results are selected to validate the RBF model as illustrated in **Figure 6-6**. It can be noticed that the test and training are consistent and converged after 1,500 epochs. The prediction accuracy is shown in **Table 6-2**. The results proved that the RBF model achieved excellent determination with low root mean squared error (R^2) and distortion (β).

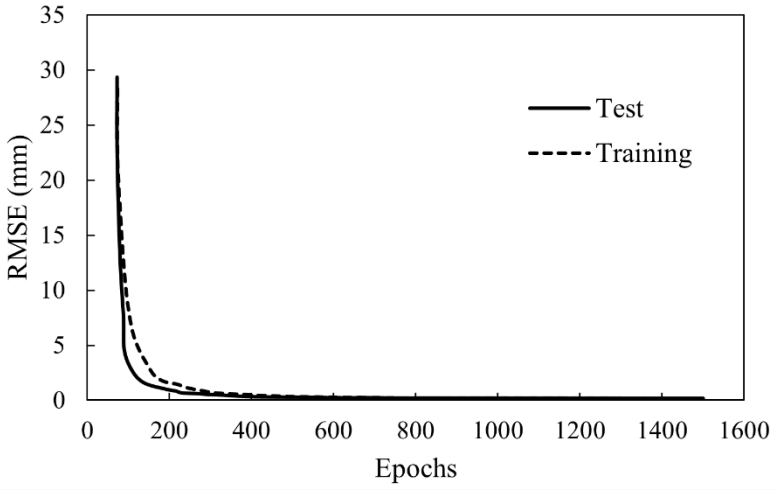

Figure 6-6. RBF learning curves. (RMSE values are in log scale)

Table 6-2. Prediction accuracy of machine learning.

Parameters	**RMSE (mm)**	**R^2 (%)**	**β (%)**
Training	0.62	95.4	1.95
Test	0.65	95.4	2.06

6.3.4. Experimental procedure and parameters

The experimental categories were described in Section 6.3.1. Since cooling is an external support to reduce the thermal effect on the tool, there was therefore no application of cooling lubricant in the initial experiment. For the first and second optimisations, cooling lubricant was assisted using modified cooling flow rate (**Table 6-3**). The experimental process is illustrated in **Figure 6-7**. The first 5 experiments utilised the same process parameters without any RBF tool path optimisation; geometric coordinates, temperature and forming force data were collected after each experiment. The RBF framework then worked on the obtained data in order to compute the optimal tool path and run the cycle again for more data. It is important to note

that the first RBF optimised tool path was based on initial group of experiments and second RBF optimised tool path was based on the first optimised group of experiments.

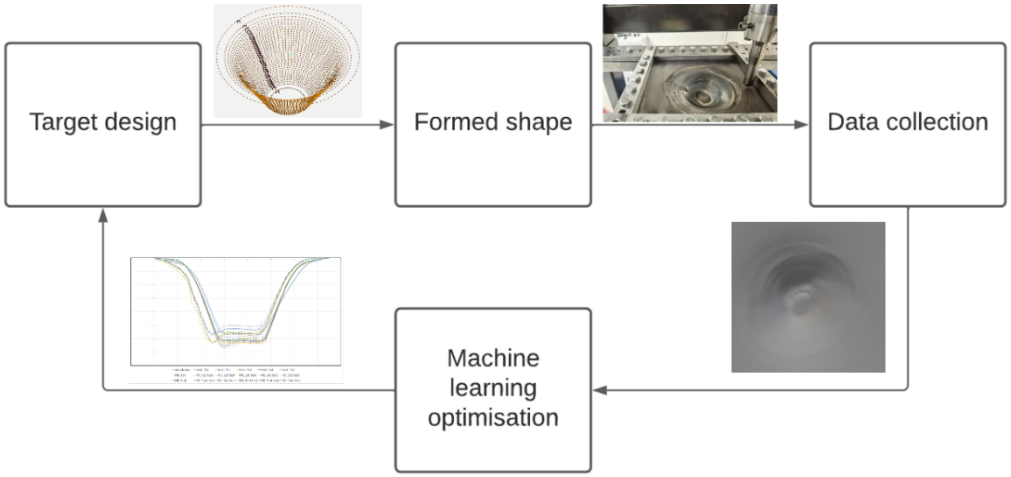

Figure 6-7. Working scheme of the machine learning-based networks.

Table 6-3. Experimental parameters.

Parameters	**Initial**	**First RBF**	**Second RBF**
Target temperature (℃)	950	950	950
Feed rate (mm/min)	500	500	500
Step size (mm)	1.0	1.0	1.0
Power (kW)	6.0	6.0	6.0
Frequency (kHz)	900	900	900
Cooling flow rate (L/h)	No	4 (step tool path)	8 (step tool path)
		2 (the remaining tool path)	2 (the remaining tool path)

6.3.5. Finite element model

ABAQUS/Explicit was used in order to establish an ideal model which has a constant temperature distribution to validate geometric accuracy, temperature and forming force from the initial and optimisation experiments. The simulation results will be compared with experiments to validate the improvements of RBF network tool path optimisation. By following the parameters from Li et al. [65] on the investigation of induction heating SPIF for Ti-6Al-4V sheets at temperatures of 600 ℃ and 700 ℃. The tool in the simulation was considered to be an analytical rigid body, 5 mm in diameter. The dimensions of the workpiece comprised 150, 150 and 4 elements in x-, y- and z- directions, respectively. A total of 90,000 coupled temperature and displacement (C3D8T) elements were assigned to the workpiece. The interaction was set as surface-to-surface contact of tangential behaviour with a friction value of 0.1. This value was used in the previous study by Gatea et al. [131] in numerical modelling to study the fracture and damage behaviour based on Coulomb's friction law calculation which theoretically matched with the analytical model and experiments. And the value has been further validated by Gatea et al. [123] to study the forming parameters in SPIF process.

Since the beta-transus temperature is typically hard to utilise and to maintain in experiments, Oberwinkler et al. [174] proposed that 950 ℃ could be easier for the heating source to maintain which improved the agreement between experiments and simulations. Wang et al. [178] has validated the source and obtained better matched results. Thus, the temperature boundary condition was modified to 950 ℃ and then kept constant in order to reduce any effects from temperature variance. A BlueBEAR high performance computing system was employed in order to perform the simulation; the computing node included 36 Ice Lake Intel® Xeon® cores with 3.9 GHz per core and 120 GB memory.

In order to simulate the process accurately, stress and strain parameters were collected through

the uniaxial tensile test. The specimens were elongated up to the fracture. The test specimen geometry, with dimensions in alignment with ASTM E8 standards, are shown in **Figure 6-8**(a); **Figure 6-8**(b) depicts the obtained stress-strain curves. The mechanical and thermal properties were tested accordingly and represented in **Table 6-4** and **Table 6-5**, respectively.

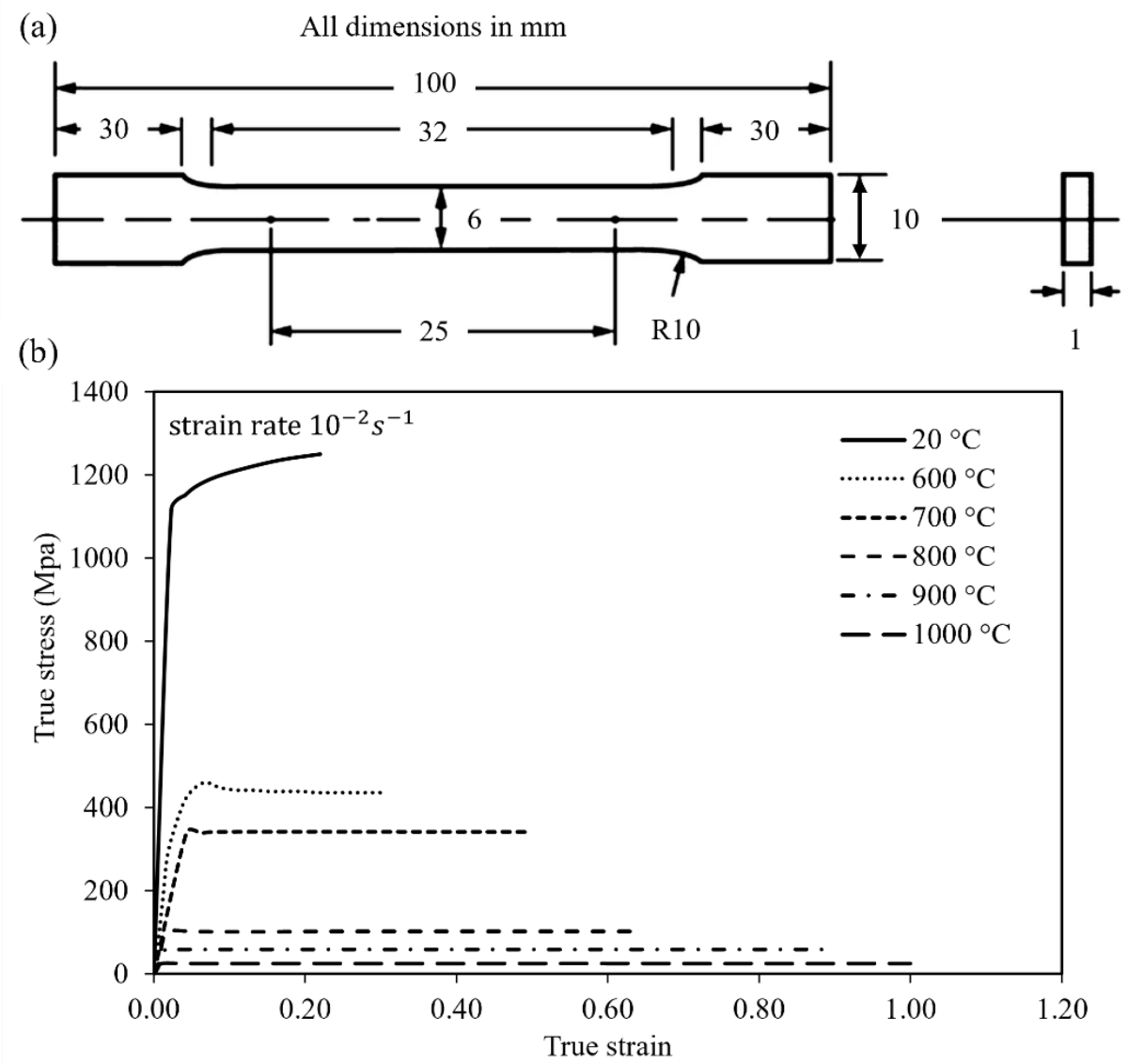

Figure 6-8. Mechanical tensile test of Ti-6Al-4V alloy: (a) dimensions of the dog bone workpiece; (b) true stress-strain curves.

Table 6-4. Mechanical properties of Ti-6Al-4V.

Temperature (℃)	**Young's Modulus (GPA)**	**Poisson's Ratio**	**Density (kg/m^3)**
20	113	0.34	4420
600	65.57	0.38	4336
700	50.08	0.38	4324
800	32.92	0.39	4309
900	24.07	0.42	4294
1000	14.85	0.43	4282

Table 6-5. Thermal properties of Ti-6Al-4V.

Temperature (℃)	**Conductivity (w/m℃)**	**Expansion**	**Heat Capacity (J/kg℃)**
20	7	8.90×10^{-6}	546
600	14.2	1.02×10^{-5}	673
700	15.5	1.04×10^{-5}	694
800	17.8	1.05×10^{-5}	714
900	20.2	1.08×10^{-5}	734
1000	22.7	1.11×10^{-5}	753

6.4. Results and discussion

6.4.1. Geometric accuracy

The geometric profile of the formed shapes was measured using the FARO 3-dimensional (3D) scanning arm. All geometric coordinates were measured from the workpiece deforming surface centre path according to the step transition tool path. To reduce the unclamped springback from the workpiece, the sample edges was clamped prior to any geometric profile scanning. The CAD and simulation geometric profiles were used in the figures for experimental result validation. Each RBF optimised tool path was trained geometric coordinates, temperature and forming force distribution on the step transition tool path to compensate the thermal expansion from the workpiece and predict the correction for the displacement between theoretical and experimental profiles.

Figure 6-9(a, c, e) demonstrates the observable springback behaviour which occurred in the superior and inferior areas. The agreement between the experimental and simulation results was enhanced by the application of the first and second RBF optimisations and adjustment of cooling lubricant (**Figure 6-9**(b, d, f)).

This provided critical evidence that the predicted RBF tool path had a compensation effect on springback behaviour. The process ending stage at the lower area, revealed that the processing temperature above beta-transus (980 ℃) induced unpredictable springback and pronounced adherence of lubricant. By applying RBF optimised tool path and cooling lubricant, the temperature had been reduced and the variance was dominated. The RBF optimised tool path thus compensated the deviation from the thermal expansion to reduce the springback. Further, the cooling lubricant system adjustment had noticeable effects on reducing the tool movement tracks as shown in **Figure 6-14**(f). The continuous and sustainable support enabled the tool to undergo sufficient lubrication thus reducing lubricant adherence to the workpiece. The detailed

error percentage were presented in **Table 6-6**. It can be observed that the initial set of experiments deserved the peak error percentage and the values were decreased by each RBF networks optimisations. By introducing first and second RBF optimisation, the average error percentage was reduced to 5.32% and 3.38% which showed a significant improvement in geometric accuracy. Please note that the error measurements from the experiments were averaged from the set experiments and compared with the simulation result.

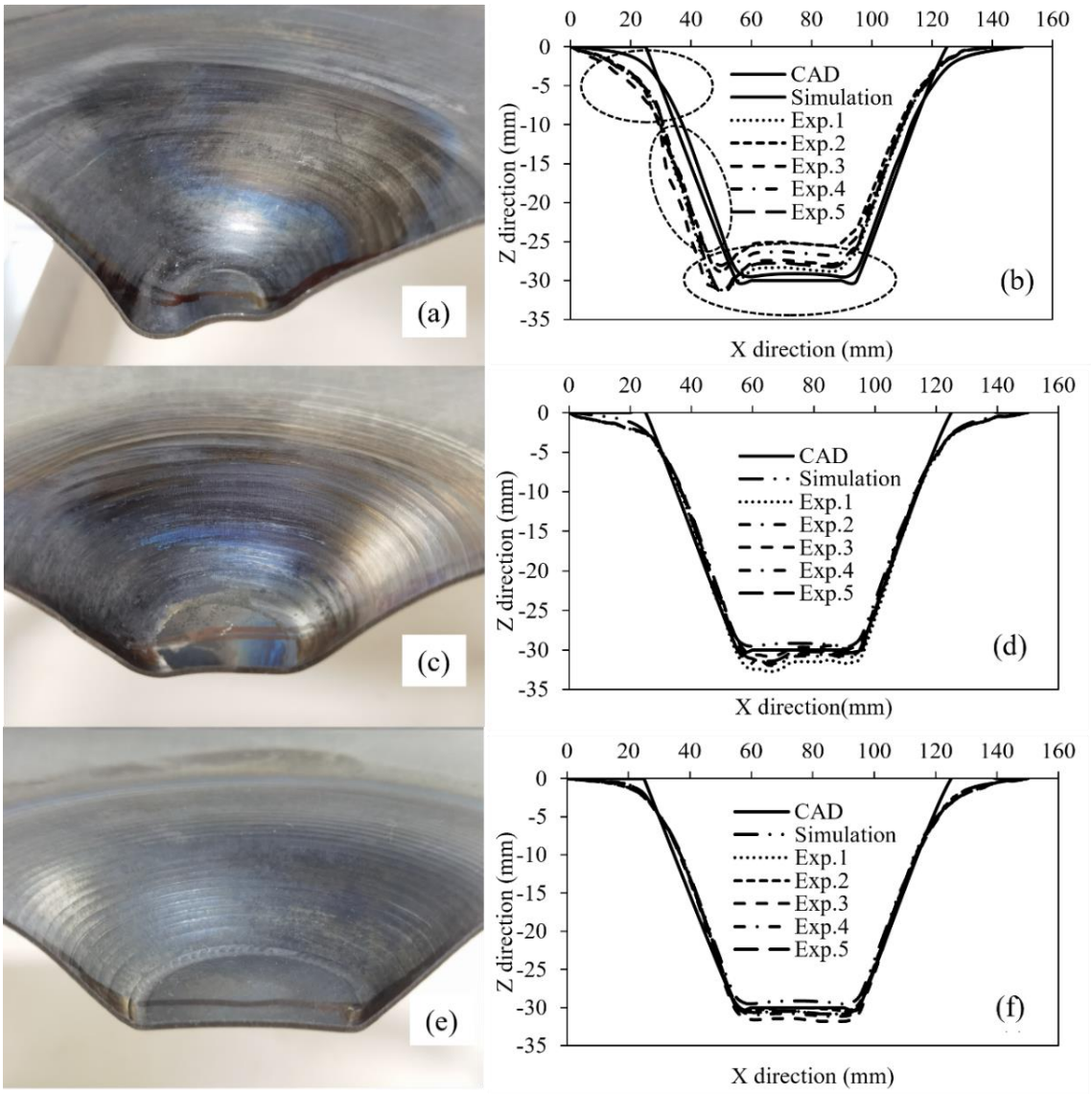

Figure 6-9. Observation of the formed shapes: (a) initial formed shape, (b) first RBF, (c) second RBF; measured geometric accuracy: (d) initial, (e) first RBF, (f) second RBF.

Table 6-6. Error percentage of geometric accuracy between experiment groups

	Maximum error (%)	Minimum error (%)	Average error (%)
Initial	26.13	1.53	12.11
First RBF	8.21	0.79	5.82
Second RBF	4.33	0.19	3.38

6.4.2. Forming temperature

The experimental temperature profiles were measured using the infrared thermo-couple on the deforming surface, which corresponded to the contact area under the tool. The double-dotted line in **Figure 6-10** distinguishes the tool path from the truncated cone; the parameters in the region are virtual in order to connect the measured values.

It can be seen that the simulation temperature profile had a stable distribution with a small variation within the range 3 ℃ to 8 ℃. This could be presumed to be solid evidence of geometric accuracy. In the initial experiments, the temperature distribution at the step path appeared higher. There was a rapid increase in temperature; the temperature distribution at the common tool path demonstrated a relatively steady increase. It could be considered that the temperature control was insufficient for the step tool path relative to the common tool path due to its increased duration. Throughout, the temperature variance for the initial experiments was 120 ℃ (920 ℃ - 1040 ℃). Following the first and second RBF network optimisations, this parameter was reduced to 70 ℃ (910 ℃ - 980 ℃) and 45 ℃ (905 ℃ - 950 ℃), respectively. Thus, the introduction of the RBF network optimisations and cooling temperature control diminished the temperature variance to a constant level closer to the ideal simulation results.

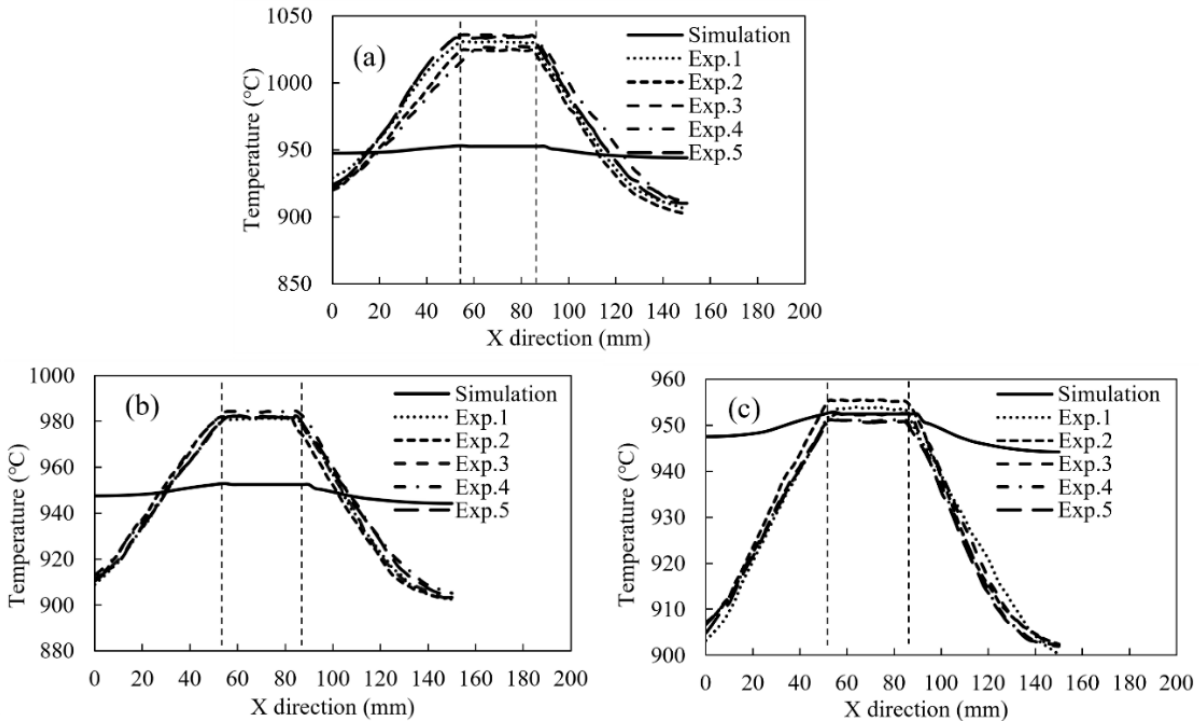

Figure 6-10. Temperature measurements according to the step transition tool path: (a) initial, (b) first RBF optimisation, (c) second RBF optimisation.

6.4.3. Forming force

The forming forces presented in this study were measured according to the step tool path. The experimental results were compared with the simulation in order to validate the performance of the RBF network optimisations. Similarly to the forming temperature data, **Figure 6-11** illustrates the forming force according to the tool path along the step line. The double-dotted line distinguishes the tool path and the truncated cone; the values in the region are virtual in order to connect the measured parameters.

A pronounced variance can be observed between the simulation and experimental results (**Figure 6-11**(a)). The former became steady from the starting stage, i.e. 15 mm from the X direction, whilst the experimental data demonstrated an unstable increase. This could be accounted for as, according to the step tool path, the variance from the temperature distributions exerted a strong effect, impacting the forming force applied. The unstable temperature and forming force distributions resulted in notable deflections in geometric accuracy.

When compared with the initial experimental data set, the experimental results following application of the first RBF network optimisation (**Figure 6-11**(b)) were concentrated together and fitted the simulation result. After the second RBF network optimisation, improved fitting between experimental and simulation results was evidenced (**Figure 6-11**(c)). This indicated that the temperature distribution according to this path was steady and able to provide superior geometric accuracy. Overall, the results from the experiment were lower than from the simulation as the temperature in the former was higher than in the latter. This increased workpiece material ductility, thus reducing the forming force distribution.

In summary, it can be observed that the forming force in the experiments revealed unstable distributions when compared with the temperature profiles. This effect could be attributed to the high temperature used in this study, which was greater than the beta-transus of Ti-6Al-4V. The strong DRX and beta transition have potent effects, affecting the material microstructure and therefore inducing unstable forming forces and increasing geometric inaccuracy. These observations matched the mechanical behaviour reported by Jha et al. [239], who documented the high-temperature deformation behaviour of a Ti-6Al-4V alloy. The RBF network optimisation, incorporating a cooling lubricant system, enhanced the steady performance of the temperature distribution which resulted in a stable forming force distribution according to the step tool path and thus, improved geometric accuracy.

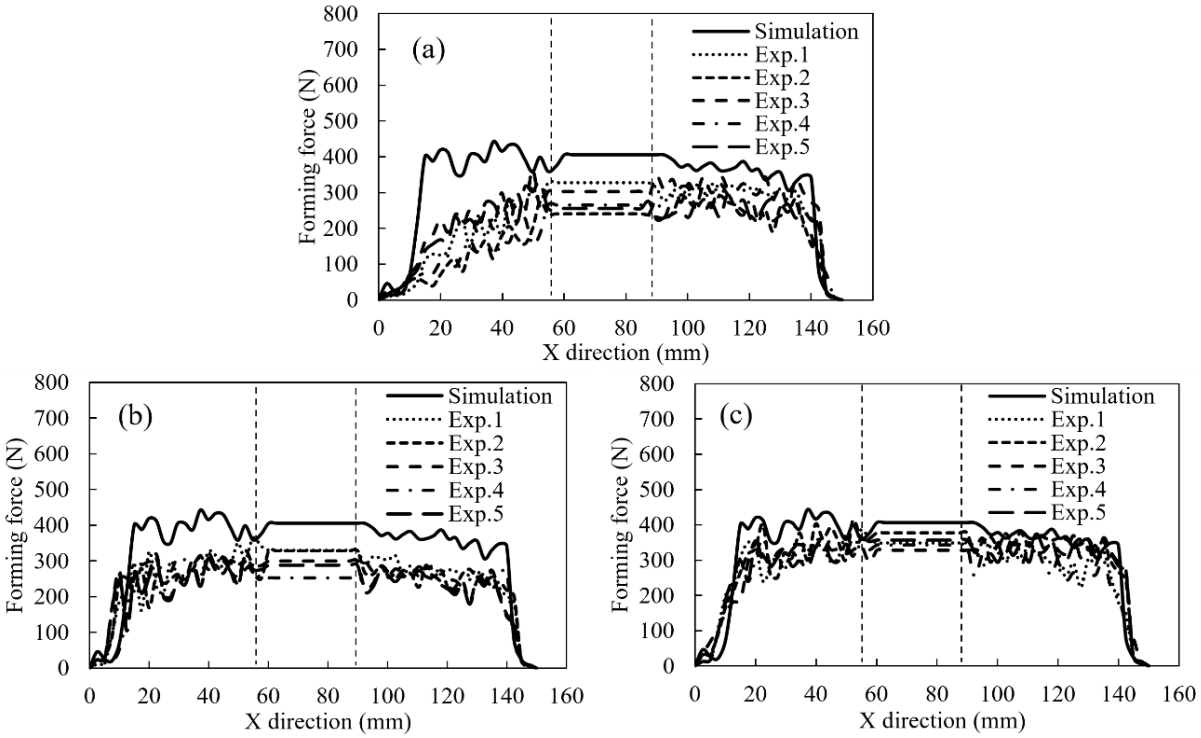

Figure 6-11. Forming force according to the step tool path: (a) initial, (b) first RBF optimisation, (c) second RBF optimisation.

6.4.4. Scanning electron microscopy (SEM) and energy dispersive X-ray analysis (EDX)

Hitachi TM3030 SEM/EDX system was used to evaluate the surface quality on deforming surface and the diffusion of compound layer, microstructure evolution on thickness section. All samples (initial, first and second RBF) were prepared from the lower part of formed shapes. The first EDX analysis was applied to the samples' deforming surfaces by first cleaned using 70% alcohol, followed by ultrasonic cleaning at 30 kHz for 30 mins in order to remove any remaining contamination. Further SEM and EDX were applied to the thickness section by chemical polished with 0.04 μm Colloidal Silica (OP-S) suspension and etched using Kroll's reagent (2 mL HF, 10 mL HCl, 88 mL H2O).

As shown in **Figure 6-12**(a), the initial experiment illustrated a pronounced area of large micro-cracks, sizeable valleys and a notable amount of remaining lubricant adherence. Such phenomena resulted in a reaction between the material and lubricant elements which led to the

formation of a compound mixture layer (**Figure 6-12**(d)). The pronounced alpha-case and interlamellar β grains indicated a beta-transus. The formation of the compound layer and the alpha-case induced the geometric inaccuracy described in Section 6.4.1. The microstructure matched the findings of de Castro et al. [240] who assessed 1050 ℃ heat treatment on Ti-6Al-4V alloy for 30 min with heating and cooling rates of 20 °C/min and 6 °C/min, respectively. Where a Widmanstätten-type structure was obtained with a basket-weave microstructure. The alpha-case with basket-weave microstructure proved that the temperature has exceeded the beta-transus with a slow cooling rate. The study proposed that the annealing of Ti-6Al-4V above beta-transus increased the DRX process significantly and induced notable thermal expansion during the process. Therefore, the microstructure formed in this study increased the micro-cracks due to the strong thermal expansion and resulted in deeper diffusion of compound layer and alpha-case.

By applying the first RBF optimisation and cooling lubricant, the incidence of micro-cracks was reduced and the cracks per se became smaller (**Figure 6-12**(b)). Additionally, the compound layer was decreased (**Figure 6-12**(e)). Lamella α grains with nucleation of β grains were detected to initiate a slight α' martensite microstructure. The phenomenon can be attributed to the enhanced cooling rate from the cooling lubricant. Zhang et al. [241] have evaluated the oxidation behaviour of Ti–6Al–4V during varied hot deformation processes, proposed that the activation energy at beta-transus temperature will exceed the formation and growth of critical nucleus grain boundaries and react with interfacial energy for nucleation of new phases and alpha-case formation. Seth et al. [242] agreed with statement and suggested that alpha-case is more pronounced at beta-transus temperature heat treatment with rapid cooling rate, and the structure exhibits brittle failure due to the numerous cracks in the alpha-case. In this study, it can be proven that the cooling lubricant only removed the compound layer and the reduced temperature decelerated the formation of β grains and alpha-case.

After the second RBF network optimisation (**Figure 6-12**(c)), only small micro-cracks were observed owing to the reduced temperature and cooling lubricant. The obtained phenomenon indicated a complete removal of compound layer as shown in **Figure 6-12**(f). A bimodal microstructure which composed of primary α grains and transformed β grains has been illustrated. According to Chong et al. [243] on the investigation of deformation mechanism and properties of Ti-6Al-4V alloy, the bimodal microstructure bearing balanced volume of α-β grains and refined grain size which enhancing the straining behaviour. The microstructure will enhance the straining during the SPIF process where no alpha-case to increase the risk for brittle fracture and less compound layer to affect the surface quality.

The EDX maps in **Figure 6-12**(g-i) indicated the removal of compound layer corresponding to initial, first and second optimisation experiment maps. It can be noticed that the compound layer has been removed according to the reduction of temperature and increased rate of cooling-lubricant. The results indicated a good cooperation between cooling lubricant system and RBF optimised tool path. The temperature initiation and friction at the contact area had been reduced after each RBF optimisation, which results in formation of bimodal microstructure that enhanced grain-boundary straining and promoted better surface quality with reduction of micro-cracks and diffusion of lubricant compound layer.

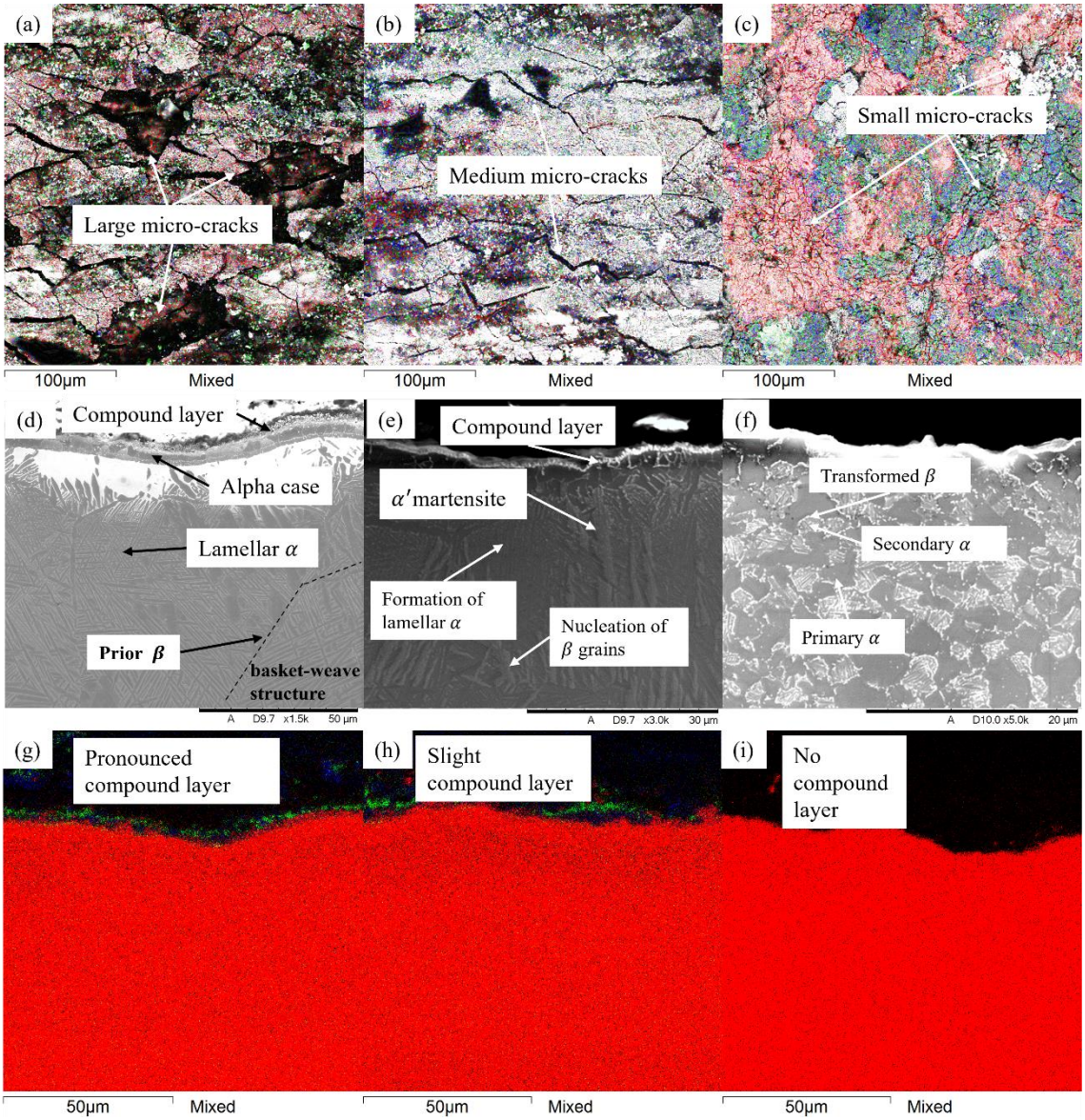

Figure 6-12. EDX and SEM maps: EDX and micro-cracks on deforming surface: (a) initial, (b) first RBF, (c) second RBF; SEM maps on cross-section top surfaces: (d) initial, (e) first RBF, (f) second RBF; EDX maps on cross-section top surfaces: (g) initial, (h) first RBF, (i) second RBF; (Element map: titanium, red; molybdenum, green; oxygen, blue).

6.4.5. Surface roughness

The deforming surfaces from the SEM samples have been characterised using the Alicona Infinite Focus optical surface measurement system in order to obtain surface roughness measurements. The imaging capture area was 2.5 mm × 2.5 mm for all samples. A Gaussian

filter was used so as to reduce the noise on inclined planar surfaces.

The surface roughness measurements were maximal following the initial experiment (**Figure 6-13** (a)), results which could relate to the peak dissipation of lubricant seen at this stage. This phenomenon resolved following the first optimisation (**Figure 6-13**(b)). Following the second RBF optimisation (**Figure 6-13**(c)), a reduction in surface roughness peak value was achieved which implies that the dissipation of lubricant had decreased. This offered strong evidence that the temperature variance was controlled during the second RBF optimisation; the consequently reduced temperature and forming force resulted in a slow dissipation of lubricant.

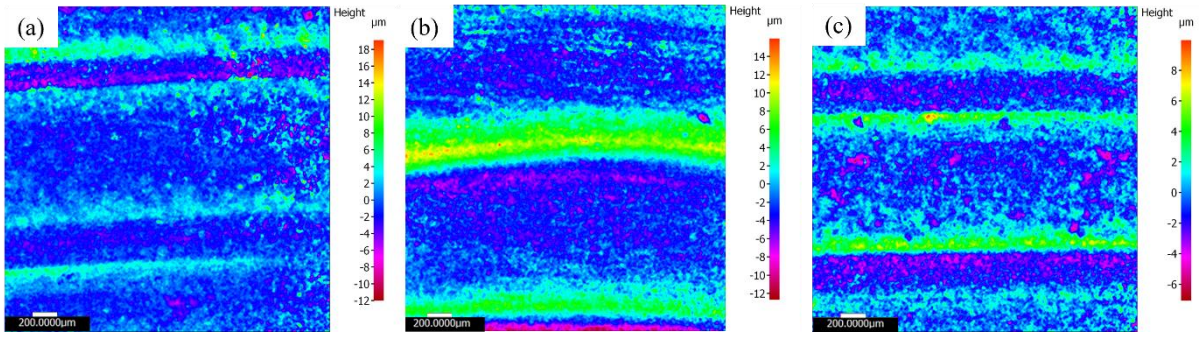

Figure 6-13. Measurements of surface roughness: (a) initial, (b) first RBF optimisation, (c) second RBF optimisation.

The measurements of average surface roughness (S_a) for the samples are illustrated in **Figure 6-14**. The first RBF optimisation revealed a decrease from the initial experiments to the second RBF network optimisation, which indicated that the unstable temperature and forming force resulted in an uneven surface. With the dissipation of the lubricant, the surface roughness was higher than in the second RBF network optimisation.

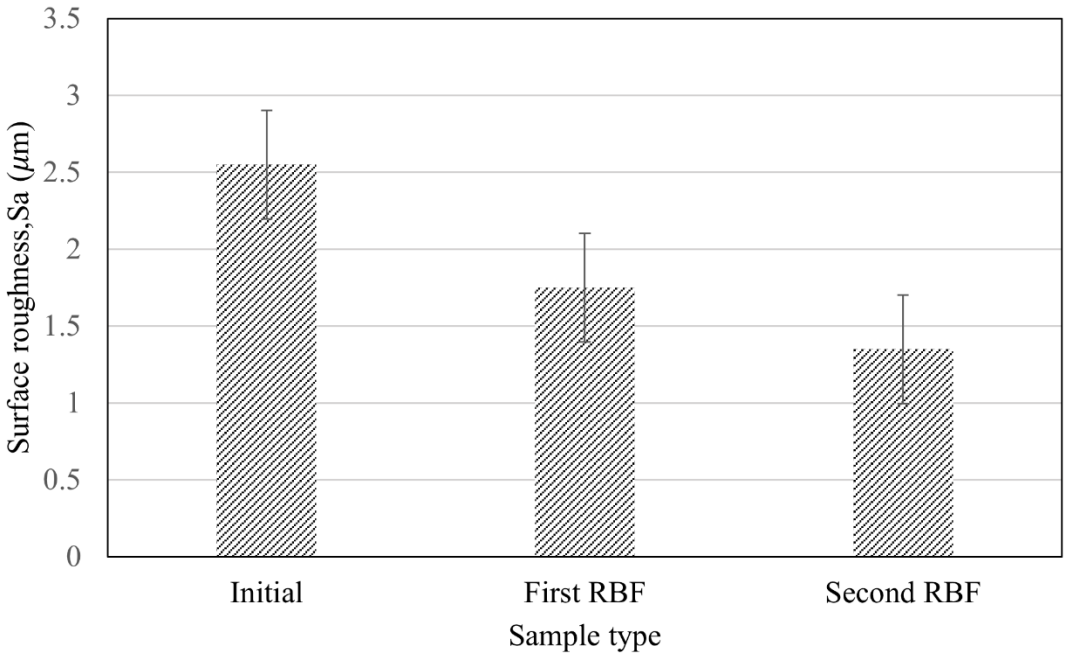

Figure 6-14. Average surface roughness for the selected area.

6.5. Conclusion

- RBF network is a useful machine learning method to study the experimental parameters (geometric coordinates, temperature, forming force) based on abundant training groups. The results shown that the RBF optimised tool path can be gradually improved depends on two sets (each set 5 experiments) of training experiments and reduced the springback to 5% and below.
- The ball-roller tool integration with cooling lubricant formed a functional way to reduce the thermal expansion on the tool. The sustainable support of liquid lubricant significantly improved the function of the lubricant and promoting geometric accuracy and surface quality.
- The FEM analysis indicated ideal profiles (geometric, temperature, forming force) to compare with the measured results to indicate the improvements. It can be noticed that each RBF tool path optimisation with cooling lubricant induced a reduction in

temperature which approached to the simulation and improved the geometric accuracy to the CAD profile.

- The non-cooling lubricant experiments indicated rapid temperature increase at ending stage over the set temperature which accelerated the lamellar microstructure growth to form basket-weave structure. Such growth increased the springback with further enhancement of compound layer diffusion and alpha-case which increased the surface roughness.
- The cooling lubricant indicated a pronounced temperature reduction which slow down the rapid growth of lamellar microstructure. The active lubricating service removed the formation of compound layer and balanced the temperature increase which improved the surface quality and enhanced the geometric accuracy.

Acknowledgement

This work was funded by the Department of Mechanical Engineering, University of Birmingham.

7. Conclusion and future research

Conclusion

This PhD research developed an induction-heating assisted SPIF to provide rapid and precise heating to Ti–6Al–4V sheets. The research comprised the experimental analysis of geometric accuracy, thickness distribution and surface quality under different temperatures and parameters. To reduce the observable springback, uneven thickness distribution and lubricant adherence, flexible ball-roller tool design integrated with lubricant system and machine learning tool path optimisation was designed. The experiments obtained mechanical properties including the forming force, straining behaviour, geometric coordinates and thickness were correlated with microstructural evolution in the DRX process, grain size development, grains orientation, crystalline texture and phase transition. This research investigated the combination of experimental scale FEM and CPFEM with grain level RVE and CA to predict the mechanical and microstructural behaviours; different parameters including step size, feed rate and temperatures were investigated to reveal the different mechanical and microstructural properties numerically. Further, this research first time investigated the heating temperature to above Ti–6Al–4V beta-transus (980 ℃) and using RBF network tool path optimisation with cooling lubricant to control the temperature and dominate the microstructural evolution to enhance the geometric accuracy. The main research contributions can be highlighted as:

Chapter 1 & 2:

Objective 1 on the study of background of ISF processes and objective 2 on the literature review in current technology.

- Comparison of current ISF processes and the advantages and limitations of SPIF process.

- The current heating methods in SPIF provides sufficient temperature to the high-strength alloy sheets and increase the ductility to improve the formability. However, the endurance and time of heat-transfer are not satisfied to complete the full SPIF process. The future improvements should be done to achieve localised heating in accordance with the tool and produce stable heating throughout the whole process.

- The ball-roller tools indicate better surface quality than conventional tools. However, the friction at the tool-surface contact area is increased due to dissipation of lubricant during heat-assisted SPIF process. The tools can be further improved to integrate with water-cooling system to reduce the thermo-expansion on the tool and enhance the endurance of lubricant.

- The lubricants used in current heat-assisted SPIF unable to meet the requirement to reduce the friction and wear tracks due to the rapid dissipation. The aspect can be improved by design of high-temperature lubricants and cooperating with tool design to allow a cooling water or liquid lubricant to enhance the surface quality on the workpiece.

- The geometric error on tool path for heat-assisted SPIF process is significantly greater than room temperature SPIF. Artificial intelligence can be integrated to optimise the tool path for better geometric accuracy.

- Numerical modelling is sufficient to provide macroscopic simulation for heat-assisted SPIF process. The further improvements can be done on the combination with CPFEM, RVE and CA modelling to link the macroscopic parameters to mesoscopic and microscopic structures to reveal the microstructural evolution and process the results to correlate with mechanical behaviours.

Chapter 3:

Objective 3 on the correlation between the mechanical and microstructural properties for induction heating assisted SPIF of Ti-6Al-4V at relatively low temperatures.

- Establish of an induction heating SPIF system to provide localised and rapid heating to deform workpieces.

- Experimental and numerical investigation on mechanical properties (straining, strain rate) and correlate with microstructure properties (grain refinement and micro-hardness) using Z-parameter calculations.

Chapter 4:

Objective 4 on the tool design and lubricant improvements to extend the endurance of lubricant and resistance to dissipation.

- A cooling lubricant system has been designed to integrate into the ball-roller forming tool to provide an efficient and sufficient liquid lubricant (MoS_2) to reduce the thermal expansion on the tool and the wear tracks on the tool-workpiece contact area. The lubricant dissipation and the adherence of lubricant were significantly reduced.

Chapter 5:

Objective 5 on microstructural numerical modelling to predict the evolution in crystal structure and correlate the outputs with the process parameters.

- A multi-scale modelling in combining of CPFEM, RVE and CA models to simulate the crystal plastic deformation and microstructural evolution with link with process parameters and mechanical properties from the heat-assisted SPIF process.

Chapter 6:

Objective 6 on developing of artificial neural network to optimise the tool path to improve the geometric accuracy.

- ANN (radial basis function network) was used in this chapter to correlate with controllable water-cooling integrated ball-roller tool to optimise the tool path plan and dominate the microstructural evolution.

Future improvements

The future improvements in heat-assisted SPIF can be classified into the following aspects: formability, geometric accuracy, thickness distribution and surface quality. All these aspects are relevant to the heating method, tool design, tool path optimisation, lubricant and analysis in microstructural evolution. Further, the accuracy of numerical analysis and cost reduction are accounting for external effects in the investigation, time consumption and cost production. All aspects and potential effects can be expressed as:

- The localised heating methods revealed more precise heating to the tool-surface contact area. Induction heating indicated better surface quality to remove the electric sparks and burns-off cracks on the deforming surface than electric heating and laser heating. However, the formability is limited due to the controlled movement of the heating coil and forming tool. Robotic arms can be integrated into the system to allow flexible movement of heating coil for complex forming shapes. This comprises the compensation of the tool path to accomplish the corrections of robotic movements and an analytical model to ensure the heater provides constant and rapid heating.

- Ball-roller tools indicated more efficient service in reducing friction at the tool-surface contact area; the integration of water channel enables the cooling and lubricating function to reduce the thermal expansion of the tool and balance the temperature on

deforming surface. Future improvements can be achieved by designing more freedom of axis-rotation to allow flexible tool-surface contact to increase the wall angles and formability. An analytical model can be established to analyse the cooling rate and its effects on the localised contact tool-surface area.

- During the heat-assisted SPIF for high strength materials, pronounced springback and pillow effects are common issues to affect the geometric accuracy. The effects are mainly attributed to the thermal and straining behaviour of the process. ANN network revealed excellent performance in analysing the effects from process parameters to produce an optimised tool path to reduce the springback. However, the temperature and straining induced DRX, DRV and further phase transition which increased the thermal expansion and impacted the forming tool to give unpredictable geometric errors. The material behaviours can be studied using machine learning techniques and imply the output data with parameter effects to produce an optimised tool path.

- Lubricants and coatings are commonly not efficient for high-temperature SPIF process which leads to dissipation of lubricant resulting in adherence, adhesion and abrasive wear on the deforming surface. Ball-roller tool and cooling lubricant indicated high performance to reduce such effects. Further improvements can be achieved by developing an advanced structure to allow adjustment for multi-lubricants and flow rate; paste lubricant can be mixed with liquid oil under chemical reactions such as plasma treatment to enhance the molecular activation for better lubricating service.

- The current FE modelling has shown excellent results agreed with the experiments which are able to present complex tool-surface contact and friction behaviour. However, the computational time is usually more than 40 h. To reduce the time consumption, time scaling must be controlled and mesh refinement should be applied to the deforming

region. Further, the crystal plasticity behaviour and grain size evolution can be approached by combining the CPFEM, RVE and CA as a single FE model. To simulate twin-phase materials and predict twin-grains behaviours, the polycrystalline model can be improved in calculations of grain boundary to improve the modelling. In addition, the analytical model of the heat source should be integrated into the modelling system to improve the accuracy of crystal plasticity behaviour.

- The microstructure analysis is essential for heat-assisted SPIF. The current analysis is limited to the microstructure map at the regional deforming surface after experiment. It can be improved by applying microscopic investigation on specific area to the crystal plasticity, texture, misorientation grain boundary angles and grain size data to correlate with mechanical properties from experiments. Further, the output data (stress, strain, grain orientation and grain size) from microstructure can be integrated into the numerical modelling to improve the accuracy.

References

1. Zhu, H., H. Ou, A. Popov, *Incremental sheet forming of thermoplastics: a review.* The International Journal of Advanced Manufacturing Technology, 2020. **111**(1-2): p. 565-587. DOI: 10.1007/s00170-020-06056-5.
2. Honarpisheh, M., M. Keimasi, I. Alinaghian, *Numerical and experimental study on incremental forming process of Al/Cu bimetals: Influence of process parameters on the forming force, dimensional accuracy and thickness variations*. Vol. 13. 2018. 35-51.
3. Al-Ghamdi, K.A., G. Hussain, *Threshold tool-radius condition maximizing the formability in SPIF considering a variety of materials: Experimental and FE investigations.* International Journal of Machine Tools and Manufacture, 2015. **88**: p. 82-94. DOI: 10.1016/j.ijmachtools.2014.09.005.
4. Ambrogio, G., F. Gagliardi, A. Chamanfar, W.Z. Misiolek, L.J.T.I.J.o.A.M.T. Filice, *Induction heating and cryogenic cooling in single point incremental forming of Ti-6Al-4V: process setup and evolution of microstructure and mechanical properties.* 2017. **91**(1): p. 803-812. DOI: 10.1007/s00170-016-9794-7.
5. Formisano, A., M. Durante, L. Boccarusso, A.J.T.I.J.o.A.M.T. Astarita, *The influence of thermal oxidation and tool-sheet contact conditions on the formability and the surface quality of incrementally formed grade 1 titanium thin sheets.* 2017. **93**(9): p. 3723-3732. DOI: 10.1007/s00170-017-0805-0.
6. Fan, G., F. Sun, X. Meng, L. Gao, G. Tong, *Electric hot incremental forming of Ti-6Al-4V titanium sheet.* The International Journal of Advanced Manufacturing Technology, 2009. **49**(9-12): p. 941-947. DOI: 10.1007/s00170-009-2472-2.
7. Göttmann, A., J. Diettrich, G. Bergweiler, M. Bambach, G. Hirt, P. Loosen, R.

Poprawe, *Laser-assisted asymmetric incremental sheet forming of titanium sheet metal parts.* Production Engineering, 2011. **5**(3): p. 263-271. DOI: 10.1007/s11740-011-0299-9.

8. Behera, A.K., R.A. de Sousa, G. Ingarao, V. Oleksik, *Single point incremental forming: An assessment of the progress and technology trends from 2005 to 2015*. Journal of Manufacturing Processes, 2017. **27**: p. 37-62. DOI: 10.1016/j.jmapro.2017.03.014.
9. Behera, A.K., B. Lu, H. Ou, *Characterization of shape and dimensional accuracy of incrementally formed titanium sheet parts with intermediate curvatures between two feature types.* The International Journal of Advanced Manufacturing Technology, 2015. **83**(5-8): p. 1099-1111. DOI: 10.1007/s00170-015-7649-2.
10. Möllensiep, D., P. Kulessa, L. Thyssen, B. Kuhlenkötter, *Regression-based compensation of part inaccuracies in incremental sheet forming at elevated temperatures.* The International Journal of Advanced Manufacturing Technology, 2020. **109**(7-8): p. 1917-1928. DOI: 10.1007/s00170-020-05625-y.
11. Prakash Singh, R., S. Kumar Gupta, P. Kumar Singh, S. Kumar, *Robot assisted incremental sheet forming of Al6061 under static pressure: Preliminary study of thickness distribution within the deformation region.* Materials Today: Proceedings, 2021. **47**: p. 2737-2741. DOI: 10.1016/j.matpr.2021.03.056.
12. Lublasser, E., J. Braumann, D. Goldbach, S. Brell-Çokcan. *Robotic Forming : rapidly Generating 3D Forms and Structures through Incremental Forming*. 2016.
13. Bagudanch, I., M. Sabater, M.L. Garcia-Romeu, *Single Point versus Two Point Incremental Forming of thermoplastic materials.* Advances in Materials and Processing Technologies, 2016. **3**(1): p. 135-144. DOI: 10.1080/2374068x.2016.1250245.

14. Mostafanezhad, H., H.G. Menghari, S. Esmaeili, E.M. Shirkharkolaee, *Optimization of two-point incremental forming process of AA1050 through response surface methodology.* Measurement, 2018. **127**: p. 21-28. DOI: 10.1016/j.measurement.2018.04.042.

15. Attanasio, A., E. Ceretti, C. Giardini, L. Mazzoni, *Asymmetric two points incremental forming: Improving surface quality and geometric accuracy by tool path optimization.* Journal of Materials Processing Technology, 2008. **197**(1-3): p. 59-67. DOI: 10.1016/j.jmatprotec.2007.05.053.

16. Ham, M., J. Jeswiet, *Single Point Incremental Forming and the Forming Criteria for AA3003.* CIRP Annals, 2006. **55**(1): p. 241-244. DOI: https://doi.org/10.1016/S0007-8506(07)60407-7.

17. Strano, M., *Technological Representation of Forming Limits for Negative Incremental Forming of Thin Aluminum Sheets.* Journal of Manufacturing Processes, 2005. **7**(2): p. 122-129. DOI: 10.1016/s1526-6125(05)70089-x.

18. Davarpanah, M.A., A. Mirkouei, X. Yu, R. Malhotra, S. Pilla, *Effects of incremental depth and tool rotation on failure modes and microstructural properties in Single Point Incremental Forming of polymers.* Journal of Materials Processing Technology, 2015. **222**: p. 287-300. DOI: https://doi.org/10.1016/j.jmatprotec.2015.03.014.

19. Silva, M.B., L.M. Alves, P.A.F. Martins, *Single point incremental forming of PVC: Experimental findings and theoretical interpretation.* European Journal of Mechanics - A/Solids, 2010. **29**(4): p. 557-566. DOI: 10.1016/j.euromechsol.2010.03.008.

20. Franzen, V., L. Kwiatkowski, P.A.F. Martins, A.E. Tekkaya, *Single point incremental forming of PVC.* Journal of Materials Processing Technology, 2009. **209**(1): p. 462-469. DOI: 10.1016/j.jmatprotec.2008.02.013.

21. Martins, P.A.F., L. Kwiatkowski, V. Franzen, A.E. Tekkaya, M. Kleiner, *Single point*

incremental forming of polymers. CIRP Annals, 2009. **58**(1): p. 229-232. DOI: 10.1016/j.cirp.2009.03.095.

22. Jeswiet, J., F. Micari, G. Hirt, A. Bramley, J. Duflou, J. Allwood, *Asymmetric Single Point Incremental Forming of Sheet Metal.* CIRP Annals, 2005. **54**(2): p. 88-114. DOI: 10.1016/s0007-8506(07)60021-3.

23. Panjwani, D., S. Priyadarshi, P.K. Jain, M.K. Samal, J.J. Roy, D. Roy, P. Tandon, *A novel approach based on flexible supports for forming non-axisymmetric parts in SPISF*. The International Journal of Advanced Manufacturing Technology, 2017. **92**(5-8): p. 2463-2477. DOI: 10.1007/s00170-017-0223-3.

24. Sousa, R., *Incremental Sheet Forming Technologies*, in *Reference Module in Materials Science and Materials Engineering*. 2016, Elsevier.

25. Lu, B., Z. Li, H. Long, F. Chen, J. Chen, H. Ou, *Microstructure refinement by tool rotation-induced vibration in incremental sheet forming.* Procedia Engineering, 2017. **207**: p. 795-800. DOI: https://doi.org/10.1016/j.proeng.2017.10.831.

26. Al-Obaidi, A., V. Kräusel, D. Landgrebe, *Hot single-point incremental forming assisted by induction heating.* The International Journal of Advanced Manufacturing Technology, 2016. **82**(5): p. 1163-1171. DOI: 10.1007/s00170-015-7439-x.

27. Göttmann, A., D. Bailly, G. Bergweiler, M. Bambach, J. Stollenwerk, G. Hirt, P. Loosen, *A novel approach for temperature control in ISF supported by laser and resistance heating.* The International Journal of Advanced Manufacturing Technology, 2012. **67**(9-12): p. 2195-2205. DOI: 10.1007/s00170-012-4640-z.

28. Odenberger, E.L., M. Oldenburg, P. Thilderkvist, T. Stoehr, J. Lechler, M. Merklein, *Tool development based on modelling and simulation of hot sheet metal forming of Ti–6Al–4V titanium alloy.* Journal of Materials Processing Technology, 2011. **211**(8): p. 1324-1335. DOI: 10.1016/j.jmatprotec.2011.03.001.

29. Liu, R., B. Lu, D. Xu, J. Chen, F. Chen, H. Ou, H. Long, *Development of novel tools for electricity-assisted incremental sheet forming of titanium alloy.* The International Journal of Advanced Manufacturing Technology, 2016. **85**(5): p. 1137-1144. DOI: 10.1007/s00170-015-8011-4.

30. Rauch, M., J.-Y. Hascoet, J.-C. Hamann, Y. Plenel, *Tool path programming optimization for incremental sheet forming applications.* Computer-Aided Design, 2009. **41**(12): p. 877-885. DOI: 10.1016/j.cad.2009.06.006.

31. Asgar, J., R. Lingam, V. Reddy. *Tool path influence on electric pulse aided deformation during incremental sheet metal forming*. in *AIP Conference Proceedings*. 2013. AIP.

32. Hussain, G., L. Gao, *A novel method to test the thinning limits of sheet metals in negative incremental forming.* International Journal of Machine Tools and Manufacture, 2007. **47**(3-4): p. 419-435. DOI: 10.1016/j.ijmachtools.2006.06.015.

33. Ortiz, M., M. Penalva, E. Iriondo, L.N. López de Lacalle, *Accuracy and Surface Quality Improvements in the Manufacturing of Ti-6Al-4V Parts Using Hot Single Point Incremental Forming.* Metals, 2019. **9**(6): p. 697.

34. Liu, S., Y. Xia, Y. Liu, Z. Shi, H. Yu, Z. Li, J. Lin, *Tool path planning of consecutive free-form sheet metal stamping with deep learning.* Journal of Materials Processing Technology, 2022. **303**: p. 117530. DOI: 10.1016/j.jmatprotec.2022.117530.

35. Wang, C., A. He, K.J. Weegink, S. Liu, P.A. Meehan, *3D surface representation and trajectory optimization with a learning-based adaptive model predictive controller in incremental forming.* Journal of Manufacturing Processes, 2020. **58**: p. 796-810. DOI: 10.1016/j.jmapro.2020.08.062.

36. Najm, S.M., I. Paniti, *Artificial neural network for modeling and investigating the effects of forming tool characteristics on the accuracy and formability of thin*

aluminum alloy blanks when using SPIF. The International Journal of Advanced Manufacturing Technology, 2021. **114**(9-10): p. 2591-2615. DOI: 10.1007/s00170-021-06712-4.

37. Jiang, Z., K.F. Ehmann, J. Cao, *Prediction of forming temperature in electrically-assisted double-sided incremental forming using a neural network.* Journal of Materials Processing Technology, 2022. **302**: p. 117486. DOI: 10.1016/j.jmatprotec.2021.117486.

38. Giuseppina, A., C. Claudio, F. Luigino, G. Francesco, *Theoretical model for temperature prediction in Incremental Sheet Forming – Experimental validation.* International Journal of Mechanical Sciences, 2016. **108-109**: p. 39-48. DOI: 10.1016/j.ijmecsci.2016.01.030.

39. Liu, Z., *Friction stir incremental forming of AA7075-O sheets: investigation on process feasibility.* Procedia Engineering, 2017. **207**: p. 783-788. DOI: 10.1016/j.proeng.2017.10.829.

40. Grün, P.A., E.H. Uheida, L. Lachmann, D. Dimitrov, G.A. Oosthuizen, *Formability of titanium alloy sheets by friction stir incremental forming.* The International Journal of Advanced Manufacturing Technology, 2018. **99**(5-8): p. 1993-2003. DOI: 10.1007/s00170-018-2541-5.

41. Ambrogio, G., F. Gagliardi, *Temperature variation during high speed incremental forming on different lightweight alloys.* The International Journal of Advanced Manufacturing Technology, 2014. **76**(9-12): p. 1819-1825. DOI: 10.1007/s00170-014-6398-y.

42. Jimma, T., Y. Kasuga, N. Iwaki, O. Miyazawa, E. Mori, K. Ito, H. Hatano, *An application of ultrasonic vibration to the deep drawing process.* Journal of Materials Processing Technology, 1998. **80-81**: p. 406-412. DOI: 10.1016/s0924-

0136(98)00195-2.

43. Murakawa, M., M. Jin, *The utility of radially and ultrasonically vibrated dies in the wire drawing process.* Journal of Materials Processing Technology, 2001. **113**(1-3): p. 81-86. DOI: 10.1016/s0924-0136(01)00635-5.

44. Baghlani, V., P. Mehbudi, J. Akbari, M. Sohrabi, *Ultrasonic Assisted Deep Drilling of Inconel 738LC Superalloy.* Procedia CIRP, 2013. **6**: p. 571-576. DOI: 10.1016/j.procir.2013.03.096.

45. Shen, X.-H., J. Zhang, D.X. Xing, Y. Zhao, *A study of surface roughness variation in ultrasonic vibration-assisted milling.* The International Journal of Advanced Manufacturing Technology, 2011. **58**(5-8): p. 553-561. DOI: 10.1007/s00170-011-3399-y.

46. Mousavi, S.A.A.A., H. Feizi, R. Madoliat, *Investigations on the effects of ultrasonic vibrations in the extrusion process.* Journal of Materials Processing Technology, 2007. **187-188**: p. 657-661. DOI: 10.1016/j.jmatprotec.2006.11.168.

47. Bagudanch, I., M.L. Garcia-Romeu, G. Centeno, A. Elías-Zúñiga, J. Ciurana, *Forming force and temperature effects on single point incremental forming of polyvinylchloride.* Journal of Materials Processing Technology, 2015. **219**: p. 221-229. DOI: 10.1016/j.jmatprotec.2014.12.004.

48. Sakhtemanian, M.R., M. Honarpisheh, S. Amini, *A novel material modeling technique in the single-point incremental forming assisted by the ultrasonic vibration of low carbon steel/commercially pure titanium bimetal sheet.* The International Journal of Advanced Manufacturing Technology, 2019. **102**(1-4): p. 473-486. DOI: 10.1007/s00170-018-3148-6.

49. Cheng, R., N. Wiley, M. Short, X. Liu, A. Taub, *Applying ultrasonic vibration during single-point and two-point incremental sheet forming.* Procedia Manufacturing, 2019.

34: p. 186-192. DOI: 10.1016/j.promfg.2019.06.137.

50. Bai, L., Y. Li, M. Yang, Y. Lin, Q. Yuan, R. Zhao, *Modeling and Analysis of Single Point Incremental Forming Force with Static Pressure Support and Ultrasonic Vibration.* Materials (Basel), 2019. **12**(12). DOI: 10.3390/ma12121899.

51. Sun, Y., Z. Lu, C. Li, R. Wang, W. Zhai, *Study on the Springback Effect and Surface Property for Ultrasonic-Assisted Incremental Sheet Forming of Aluminum Alloy.* Symmetry, 2021. **13**(7). DOI: 10.3390/sym13071217.

52. Cheng, Z., Y. Li, J. Li, F. Li, P.A. Meehan, *Ultrasonic assisted incremental sheet forming: Constitutive modeling and deformation analysis.* Journal of Materials Processing Technology, 2022. **299**: p. 117365. DOI: 10.1016/j.jmatprotec.2021.117365.

53. Fan, G., L. Gao, G. Hussain, Z. Wu, *Electric hot incremental forming: A novel technique.* International Journal of Machine Tools and Manufacture, 2008. **48**(15): p. 1688-1692. DOI: https://doi.org/10.1016/j.ijmachtools.2008.07.010.

54. Li, Z., S. Lu, T. Zhang, C. Zhang, Z. Mao, *Electric assistance hot incremental sheet forming: an integral heating design.* The International Journal of Advanced Manufacturing Technology, 2018. **96**(9-12): p. 3209-3215. DOI: 10.1007/s00170-018-1792-5.

55. Magnus, C.S., *Joule heating of the forming zone in incremental sheet metal forming: Part 1.* The International Journal of Advanced Manufacturing Technology, 2016. **91**(1-4): p. 1309-1319. DOI: 10.1007/s00170-016-9786-7.

56. Min, J., P. Seim, D. Störkle, L. Thyssen, B. Kuhlenkötter, *Thermal modeling in electricity assisted incremental sheet forming.* International Journal of Material Forming, 2016. **10**(5): p. 729-739. DOI: 10.1007/s12289-016-1315-6.

57. Meier, H., C. Magnus, *Incremental Sheet Metal Forming with Direct Resistance*

Heating Using Two Moving Tools. Vol. 554-557. 2013. 1362-1367.

58. Vahdani, M., M.J. Mirnia, H. Gorji, M. Bakhshi-Jooybari, *Experimental Investigation of Formability and Surface Finish into Resistance Single-Point Incremental Forming of Ti–6Al–4V Titanium Alloy Using Taguchi Design.* Transactions of the Indian Institute of Metals, 2019. **72**(4): p. 1031-1041. DOI: 10.1007/s12666-019-01577-4.

59. Vahdani, M., M.J. Mirnia, H. Gorji, M. Bakhshi-Jooybari, *Experimental Investigation of Formability and Surface Finish into Resistance Single-Point Incremental Forming of T‰ 6Al 4V Titanium Alloy Using Taguchi Design.* Transactions of the Indian Institute of Metals, 2019. **72**: p. 1031-1041.

60. Ao, D., J. Gao, X. Chu, S. Lin, J. Lin, *Formability and deformation mechanism of Ti-6Al-4V sheet under electropulsing assisted incremental forming.* International Journal of Solids and Structures, 2020. **202**: p. 357-367. DOI: 10.1016/j.ijsolstr.2020.06.028.

61. Vahdani, M., M.J. Mirnia, M. Bakhshi-Jooybari, H. Gorji, *Electric hot incremental sheet forming of Ti-6Al-4V titanium, AA6061 aluminum, and DC01 steel sheets.* The International Journal of Advanced Manufacturing Technology, 2019. **103**(1-4): p. 1199-1209. DOI: 10.1007/s00170-019-03624-2.

62. Duflou, J.R., B. Callebaut, J. Verbert, H. De Baerdemaeker, *Laser Assisted Incremental Forming: Formability and Accuracy Improvement.* CIRP Annals, 2007. **56**(1): p. 273-276. DOI: 10.1016/j.cirp.2007.05.063.

63. Lehtinen, P., T. Väisänen, M. Salmi, *The Effect of Local Heating by Laser Irradiation for Aluminum, Deep Drawing Steel and Copper Sheets in Incremental Sheet Forming.* Physics Procedia, 2015. **78**: p. 312-319. DOI: 10.1016/j.phpro.2015.11.045.

64. Al-Obaidi, A., V. Kräusel, D. Landgrebe, *Induction Heating Validation of Dieless Single-Point Incremental Forming of AHSS.* 2017. **1**(1): p. 5.

65. Li, W., M.M. Attallah, K. Essa, *Experimental and numerical investigations on the*

process quality and microstructure during induction heating assisted incremental forming of Ti-6Al-4V sheet. Journal of Materials Processing Technology, 2022. **299**: p. 117323. DOI: 10.1016/j.jmatprotec.2021.117323.

66. Li, W., K. Essa, S. Li, *A novel tool to enhance the lubricant efficiency on induction heat-assisted incremental sheet forming of Ti-6Al-4 V sheets.* The International Journal of Advanced Manufacturing Technology, 2022. DOI: 10.1007/s00170-022-09284-z.
67. Al-Obaidi, A., V. Kräusel, D. Landgrebe, *Hot single-point incremental forming assisted by induction heating.* The International Journal of Advanced Manufacturing Technology, 2015. **82**(5-8): p. 1163-1171. DOI: 10.1007/s00170-015-7439-x.
68. Kumar, A., V. Gulati, P. Kumar, V. Singh, B. Kumar, H. Singh, *Parametric effects on formability of AA2024-O aluminum alloy sheets in single point incremental forming.* Journal of Materials Research and Technology, 2019. **8**(1): p. 1461-1469. DOI: 10.1016/j.jmrt.2018.11.001.
69. Jeswiet, J., D. Adams, M. Doolan, T. McAnulty, P. Gupta, *Single point and asymmetric incremental forming.* Advances in Manufacturing, 2015. **3**(4): p. 253-262. DOI: 10.1007/s40436-015-0126-1.
70. Iseki, H., *An approximate deformation analysis and FEM analysis for the incremental bulging of sheet metal using a spherical roller.* Journal of Materials Processing Technology, 2001. **111**(1-3): p. 150-154. DOI: 10.1016/s0924-0136(01)00500-3.
71. Iseki, H., T. Naganawa, *Vertical wall surface forming of rectangular shell using multistage incremental forming with spherical and cylindrical rollers.* Journal of Materials Processing Technology, 2002. **130-131**: p. 675-679. DOI: 10.1016/s0924-0136(02)00735-5.
72. Kilani, L., T. Mabrouki, M. Ayadi, H. Chermiti, S. Belhadi, *Effects of rolling ball tool parameters on roughness, sheet thinning, and forming force generated during SPIF*

process. The International Journal of Advanced Manufacturing Technology, 2020. **106**(9-10): p. 4123-4142. DOI: 10.1007/s00170-019-04918-1.

73. Lu, B., Y. Fang, D.K. Xu, J. Chen, H. Ou, N.H. Moser, J. Cao, *Mechanism investigation of friction-related effects in single point incremental forming using a developed oblique roller-ball tool.* International Journal of Machine Tools and Manufacture, 2014. **85**: p. 14-29. DOI: 10.1016/j.ijmachtools.2014.04.007.

74. Naranjo, J.A., V. Miguel, J. Coello, M.C. Manjabacas, A. Martinez-Martinez, E. Garcia-Martinez, *Tribological Characterization of the Heat-Assisted Single Point Incremental Forming Process Applied to the Ti6Al4V Alloy with the Definition of an Adhesion Parameter for the Tool Surface.* Materials (Basel), 2021. **14**(24): p. 7641. DOI: 10.3390/ma14247641.

75. Suresh, K., A. Khan, S.P. Regalla, *Tool Path Definition for Numerical Simulation of Single Point Incremental Forming.* Procedia Engineering, 2013. **64**: p. 536-545. DOI: 10.1016/j.proeng.2013.09.128.

76. Reddy, N.V., R. Lingam, J. Cao, *Incremental Metal Forming Processes in Manufacturing*, in *Handbook of Manufacturing Engineering and Technology*. 2015. p. 411-452.

77. Skjoedt, M., M.H. Hancock, N. Bay, *Creating Helical Tool Paths for Single Point Incremental Forming.* Key Engineering Materials, 2007. **344**: p. 583-590. DOI: 10.4028/www.scientific.net/KEM.344.583.

78. Azaouzi, M., N. Lebaal, *Tool path optimization for single point incremental sheet forming using response surface method.* Simulation Modelling Practice and Theory, 2012. **24**: p. 49-58. DOI: 10.1016/j.simpat.2012.01.008.

79. Behera, A.K., J. Verbert, B. Lauwers, J.R. Duflou, *Tool path compensation strategies for single point incremental sheet forming using multivariate adaptive regression*

splines. Computer-Aided Design, 2013. **45**(3): p. 575-590. DOI: 10.1016/j.cad.2012.10.045.

80. Praveen, K., R. Lingam, N. Venkata Reddy, *Tool path design system to enhance accuracy during double sided incremental forming: An analytical model to predict compensations for small/large components.* Journal of Manufacturing Processes, 2020. **58**: p. 510-523. DOI: 10.1016/j.jmapro.2020.08.014.

81. Fu, Z., J. Mo, F. Han, P. Gong, *Tool path correction algorithm for single-point incremental forming of sheet metal.* The International Journal of Advanced Manufacturing Technology, 2012. **64**(9-12): p. 1239-1248. DOI: 10.1007/s00170-012-4082-7.

82. Behera, A.K., B. Lauwers, J.R. Duflou, *Tool path generation framework for accurate manufacture of complex 3D sheet metal parts using single point incremental forming.* Computers in Industry, 2014. **65**(4): p. 563-584. DOI: 10.1016/j.compind.2014.01.002.

83. Nasulea, D., G. Oancea, *Integrating a New Software Tool Used for Tool Path Generation in the Numerical Simulation of Incremental Forming Processes.* Strojniški vestnik - Journal of Mechanical Engineering, 2018. **64**(10): p. 643-651. DOI: 10.5545/sv-jme.2018.5475.

84. Dittrich, M.-A., F. Uhlich, B. Denkena, *Self-optimizing tool path generation for 5-axis machining processes.* CIRP Journal of Manufacturing Science and Technology, 2019. **24**: p. 49-54. DOI: 10.1016/j.cirpj.2018.11.005.

85. Akrichi, S., A. Abbassi, S. Abid, N. Ben yahia, *Roundness and positioning deviation prediction in single point incremental forming using deep learning approaches.* Advances in Mechanical Engineering, 2019. **11**(7): p. 1687814019864465. DOI: 10.1177/1687814019864465.

86. Bautista-Monsalve, F., F. García-Sevilla, V. Miguel, J. Naranjo, M.C. Manjabacas, *A Novel Machine-Learning-Based Procedure to Determine the Surface Finish Quality of Titanium Alloy Parts Obtained by Heat Assisted Single Point Incremental Forming.* Metals, 2021. **11**(8): p. 1287. DOI: 10.3390/met11081287.

87. Sornsuwit, N., S. Sittisakuljaroen, *The Effect of Lubricants and Material Properties in Surface Roughness and Formability for Single Point Incremental Forming Process.* Advanced Materials Research, 2014. **979**: p. 359-362. DOI: 10.4028/www.scientific.net/AMR.979.359.

88. Hussain, G., L. Gao, N. Hayat, Z. Cui, Y.C. Pang, N.U. Dar, *Tool and lubrication for negative incremental forming of a commercially pure titanium sheet.* Journal of Materials Processing Technology, 2008. **203**(1-3): p. 193-201. DOI: 10.1016/j.jmatprotec.2007.10.043.

89. Diabb, J., C.A. Rodríguez, N. Mamidi, J.A. Sandoval, J. Taha-Tijerina, O. Martínez-Romero, A. Elías-Zúñiga, *Study of lubrication and wear in single point incremental sheet forming (SPIF) process using vegetable oil nanolubricants.* Wear, 2017. **376-377**: p. 777-785. DOI: 10.1016/j.wear.2017.01.045.

90. Hussain, G., K.A. Al-Ghamdi, *PEO coating as lubrication means for SPIF of titanium sheet: characteristics and performance.* Materials Research Innovations, 2014. **18**(sup2): p. S2-727-S2-733. DOI: 10.1179/1432891714z.000000000504.

91. Azevedo, N.G., J.S. Farias, R.P. Bastos, P. Teixeira, J.P. Davim, R.J. Alves de Sousa, *Lubrication aspects during Single Point Incremental Forming for steel and aluminum materials.* International Journal of Precision Engineering and Manufacturing, 2015. **16**(3): p. 589-595. DOI: 10.1007/s12541-015-0079-0.

92. Li, Z., S. He, Y. Zhang, Z. Gao, Z. An, S. Lu, *A novel current-carrying lubrication in electric hot incremental forming of Ti–6Al–4V titanium sheet.* Journal of the Brazilian

Society of Mechanical Sciences and Engineering, 2022. **44**(5): p. 216. DOI: 10.1007/s40430-022-03485-z.

93. Silva, M.B., P.A.F. Martins, *Incremental Sheet Forming*, in *Comprehensive Materials Processing*, S. Hashmi, et al., Editors. 2014, Elsevier: Oxford. p. 7-26.

94. Durgun, I., E. Tamer, İ. Özdemir, B. Baranoğlu, A. Sakin, O. Music, *Simulation for Incremental Sheet Forming Process: a Comparison of Implicit and Explicit Finite Element Analysis with Experimental Data*. 2013.

95. Gupta, P., J. Jeswiet, *Parameters for the FEA simulations of single point incremental forming.* Production & Manufacturing Research, 2019. **7**(1): p. 161-177. DOI: 10.1080/21693277.2019.1608330.

96. Essa, K., P. Hartley, *An assessment of various process strategies for improving precision in single point incremental forming.* International Journal of Material Forming, 2010. **4**(4): p. 401-412. DOI: 10.1007/s12289-010-1004-9.

97. Essa, K.E.A., *Finite element prediction of deformation mechanics in incremental forming processes*. 2011.

98. Essa, K., P. Hartley, *Numerical simulation of single and dual pass conventional spinning processes.* International Journal of Material Forming, 2009. **2**(4): p. 271-281. DOI: 10.1007/s12289-009-0602-x.

99. Desalegn, D., P.J. Ramulu, D. Hailu, S.S. Kumaran, P. Velmurugan, D. Venkateswarlu, *Formability Analyses on Single Point Incremental Sheet Forming Process on Aluminum 1050.* Materials Science Forum, 2019. **969**: p. 703-708. DOI: 10.4028/www.scientific.net/MSF.969.703.

100. Lora, F.A., U. Boff, C.C. Yurgel, L.F. Folle, L. Schaeffer, *Validation of the Computer Simulation Process Applied to the Incremental Forming Process for the Evaluation of Strain Paths.* Key Engineering Materials, 2013. **554-557**: p. 2453-2461. DOI:

10.4028/www.scientific.net/KEM.554-557.2453.

101. Ambrogio, G., L. Filice, L. Fratini, G. Ingarao, L. Manco, *Measuring of Geometrical Precision of Some parts Obtained by Asymmetric Incremental Forming Process After Trimming.* AIP Conference Proceedings, 2007. **908**(1): p. 431-436. DOI: 10.1063/1.2740849.

102. Esmaeilpour, R., H. Kim, T. Park, F. Pourboghrat, Z. Xu, B. Mohammed, F. Abu-Farha, *Calibration of Barlat Yld2004-18P yield function using CPFEM and 3D RVE for the simulation of single point incremental forming (SPIF) of 7075-O aluminum sheet.* International Journal of Mechanical Sciences, 2018. **145**: p. 24-41. DOI: 10.1016/j.ijmecsci.2018.05.015.

103. Esmaeilpour, R., H. Kim, A. Asgharzadeh, S.A. Nazari Tiji, F. Pourboghrat, M. Banu, A. Bansal, A. Taub, *Experimental validation of the simulation of single-point incremental forming of AA7075 sheet with Yld2004-18P yield function calibrated with crystal plasticity model.* The International Journal of Advanced Manufacturing Technology, 2021. **113**(7-8): p. 2031-2047. DOI: 10.1007/s00170-021-06706-2.

104. Groeber, M.A., M.A. Jackson, *DREAM.3D: A Digital Representation Environment for the Analysis of Microstructure in 3D.* Integrating Materials and Manufacturing Innovation, 2014. **3**(1): p. 56-72. DOI: 10.1186/2193-9772-3-5.

105. Han, F., M. Diehl, F. Roters, D. Raabe, *Using spectral-based representative volume element crystal plasticity simulations to predict yield surface evolution during large scale forming simulations.* Journal of Materials Processing Technology, 2020. **277**: p. 116449. DOI: 10.1016/j.jmatprotec.2019.116449.

106. Hansen, L.T., D.T. Fullwood, E.R. Homer, R.H. Wagoner, H. Lim, J.D. Carroll, G. Zhou, H.J. Bong, *An investigation of geometrically necessary dislocations and back stress in large grained tantalum via EBSD and CPFEM.* Materials Science and

Engineering: A, 2020. **772**: p. 138704. DOI: 10.1016/j.msea.2019.138704.

107. Li, W., L. Wang, B. Zhou, C. Liu, X. Zeng, *Grain-scale deformation in a Mg−0.8 wt% Y alloy using crystal plasticity finite element method.* Journal of Materials Science & Technology, 2019. **35**(10): p. 2200-2206. DOI: 10.1016/j.jmst.2019.04.030.

108. Raabe, D., F. Roters, *DAMASK – Duesseldorf Advanced Material Simulation Kit for multi-physics phenomena.* Computational Materials Science, 2019. **158**: p. 420-478.

109. Ruiz Sarrazola, D.A., D. Pino Muñoz, M. Bernacki, *A new numerical framework for the full field modeling of dynamic recrystallization in a CPFEM context.* Computational Materials Science, 2020. **179**: p. 109645. DOI: 10.1016/j.commatsci.2020.109645.

110. Zhang, J., X. Li, D. Xu, C. Teng, H. Wang, L. Yang, H. Ju, H. Xu, Z. Meng, Y. Ma, Y. Wang, R. Yang, *Phase field simulation of the stress-induced α microstructure in Ti–6Al–4 V alloy and its CPFEM properties evaluation.* Journal of Materials Science & Technology, 2021. **90**: p. 168-182. DOI: 10.1016/j.jmst.2020.12.085.

111. Sedighiani, K., M. Diehl, K. Traka, F. Roters, J. Sietsma, D. Raabe, *An efficient and robust approach to determine material parameters of crystal plasticity constitutive laws from macro-scale stress–strain curves.* International Journal of Plasticity, 2020. **134**: p. 102779. DOI: 10.1016/j.ijplas.2020.102779.

112. Quey, R., P.R. Dawson, F. Barbe, *Large-scale 3D random polycrystals for the finite element method: Generation, meshing and remeshing.* Computer Methods in Applied Mechanics and Engineering, 2011. **200**(17-20): p. 1729-1745. DOI: 10.1016/j.cma.2011.01.002.

113. Chuan, W., Y. He, L.H. Wei, *Modeling of discontinuous dynamic recrystallization of a near-α titanium alloy IMI834 during isothermal hot compression by combining a*

cellular automaton model with a crystal plasticity finite element method. Computational Materials Science, 2013. **79**: p. 944-959. DOI: 10.1016/j.commatsci.2013.08.004.

114. Li, W., K. Essa, M.M. Attallah, S. Li, X. Li, D. Xu, *Crystal plasticity model of induction heating assisted incremental sheet forming with recrystallisation simulation in cellular automata.* The International Journal of Advanced Manufacturing Technology, under review.

115. Niessen, F., T. Nyyssonen, A.A. Gazder, R. Hielscher, *Parent grain reconstruction from partially or fully transformed microstructures in MTEX.* J Appl Crystallogr, 2022. **55**(Pt 1): p. 180-194. DOI: 10.1107/S1600576721011560.

116. Shrivastava, P., P. Tandon, *Microstructure and texture based analysis of forming behavior and deformation mechanism of AA1050 sheet during Single Point Incremental Forming.* Journal of Materials Processing Technology, 2019. **266**: p. 292-310. DOI: 10.1016/j.jmatprotec.2018.11.012.

117. Zhang, H., X. Chu, S. Lin, H. Bai, J. Sun, *Temperature Influence on Formability and Microstructure of AZ31B during Electric Hot Temperature-Controlled Incremental Forming.* Materials (Basel), 2021. **14**(4): p. 810. DOI: 10.3390/ma14040810.

118. Zhang, S., G.H. Tang, J.D. Shen, Z. Li, X.K. Jiang, *Influence of forming temperature on microstructure and fracture morphology of magnesium alloy during warm incremental sheet forming.* Suxing Gongcheng Xuebao/Journal of Plasticity Engineering, 2021. **28**(3): p. 84-91. DOI: 10.3969/j.issn.1007-2012.2021.03.011.

119. Duflou, J.R., A.M. Habraken, J. Cao, R. Malhotra, M. Bambach, D. Adams, H. Vanhove, A. Mohammadi, J. Jeswiet, *Single point incremental forming: state-of-the-art and prospects.* International Journal of Material Forming, 2018. **11**(6): p. 743-773. DOI: 10.1007/s12289-017-1387-y.

120. Xu, D.K., B. Lu, T.T. Cao, H. Zhang, J. Chen, H. Long, J. Cao, *Enhancement of process capabilities in electrically-assisted double sided incremental forming.* Materials and Design, 2016. **92**: p. 268-280. DOI: 10.1016/j.matdes.2015.12.009.

121. Johnson, G.R., W.H. Cook. *A CONSTITUTIVE MODEL AND DATA FOR METALS SUBJECTED TO LARGE STRAINS, HIGH STRAIN RATES AND HIGH TEMPERATURES*. 2018.

122. Xu, X., J. Zhang, J. Outeiro, B. Xu, W. Zhao, *Multiscale simulation of grain refinement induced by dynamic recrystallization of Ti6Al4V alloy during high speed machining.* Journal of Materials Processing Technology, 2020. **286**: p. 116834. DOI: 10.1016/j.jmatprotec.2020.116834.

123. Gatea, S., B. Lu, J. Chen, H. Ou, G. McCartney, *Investigation of the effect of forming parameters in incremental sheet forming using a micromechanics based damage model.* International Journal of Material Forming, 2019. **12**(4): p. 553-574. DOI: 10.1007/s12289-018-1434-3.

124. Nemat-Nasser, S., W.-G. Guo, V.F. Nesterenko, S.S. Indrakanti, Y.-B. Gu, *Dynamic response of conventional and hot isostatically pressed Ti–6Al–4V alloys: experiments and modeling.* Mechanics of Materials, 2001. **33**(8): p. 425-439. DOI: 10.1016/s0167-6636(01)00063-1.

125. Kotkunde, N., A.D. Deole, A.K. Gupta, S.K. Singh, *Comparative study of constitutive modeling for Ti–6Al–4V alloy at low strain rates and elevated temperatures.* Materials & Design, 2014. **55**: p. 999-1005. DOI: 10.1016/j.matdes.2013.10.089.

126. Lee, W.-S., C.-F. Lin, *High-temperature deformation behaviour of Ti6Al4V alloy evaluated by high strain-rate compression tests.* Journal of Materials Processing Technology, 1998. **75**(1-3): p. 127-136. DOI: 10.1016/s0924-0136(97)00302-6.

127. Wang, F., J. Zhao, N. Zhu, Z. Li, *A comparative study on Johnson–Cook constitutive*

modeling for Ti–6Al–4V alloy using automated ball indentation (ABI) technique. Journal of Alloys and Compounds, 2015. **633**: p. 220-228. DOI: 10.1016/j.jallcom.2015.01.284.

128. Xia, Y.-f., W. Jiang, Q. Cheng, L. Jiang, L. Jin, *Hot deformation behavior of Ti—6Al—4V—0.1Ru alloy during isothermal compression.* Transactions of Nonferrous Metals Society of China, 2020. **30**(1): p. 134-146. DOI: 10.1016/s1003-6326(19)65186-1.

129. Essa, K., P. Hartley, *Numerical simulation of single and dual pass conventional spinning processes.* International Journal of Material Forming, 2009. **2**(4): p. 271. DOI: 10.1007/s12289-009-0602-x.

130. Huang, L., H. Yang, M. Zhan, L.-j. Hu, *Numerical simulation of influence of material parameters on splitting spinning of aluminum alloy.* Transactions of Nonferrous Metals Society of China, 2008. **18**(3): p. 674-681. DOI: 10.1016/s1003-6326(08)60117-x.

131. Gatea, S., H. Ou, B. Lu, G. McCartney, *Modelling of ductile fracture in single point incremental forming using a modified GTN model.* Engineering Fracture Mechanics, 2017. **186**: p. 59-79. DOI: 10.1016/j.engfracmech.2017.09.021.

132. Honarpisheh, M., M.J. Abdolhoseini, S. Amini, *Experimental and numerical investigation of the hot incremental forming of Ti-6Al-4V sheet using electrical current.* International Journal of Advanced Manufacturing Technology, 2016. **83**(9-12): p. 2027-2037. DOI: 10.1007/s00170-015-7717-7.

133. Honarpisheh, M., M.J. Abdolhoseini, S.J.T.I.J.o.A.M.T. Amini, *Experimental and numerical investigation of the hot incremental forming of Ti-6Al-4V sheet using electrical current.* 2016. **83**(9): p. 2027-2037. DOI: 10.1007/s00170-015-7717-7.

134. Essa, K., P. Hartley, *An assessment of various process strategies for improving*

precision in single point incremental forming. International Journal of Material Forming, 2011. **4**(4): p. 401-412. DOI: 10.1007/s12289-010-1004-9.

135. Moser, N., D. Pritchet, H. Ren, K.F. Ehmann, J. Cao, *An efficient and general finite element model for double-sided incremental forming.* Journal of Manufacturing Science and Engineering, Transactions of the ASME, 2016. **138**(9). DOI: 10.1115/1.4033483.

136. Bantounas, I., D. Dye, T.C. Lindley, *The effect of grain orientation on fracture morphology during high-cycle fatigue of Ti–6Al–4V.* Acta Materialia, 2009. **57**(12): p. 3584-3595. DOI: 10.1016/j.actamat.2009.04.018.

137. Guan, D., W.M. Rainforth, J. Gao, L. Ma, B. Wynne, *Individual effect of recrystallisation nucleation sites on texture weakening in a magnesium alloy: Part 2-shear bands.* Acta Materialia, 2018. **145**: p. 399-412. DOI: 10.1016/j.actamat.2017.12.019.

138. Hussain, G., L. Gao, N. Hayat, Z. Cui, Y.C. Pang, N.U. Dar, *Tool and lubrication for negative incremental forming of a commercially pure titanium sheet.* Journal of Materials Processing Technology, 2008. **203**(1): p. 193-201. DOI: https://doi.org/10.1016/j.jmatprotec.2007.10.043.

139. Fan, G., F. Sun, X. Meng, L. Gao, G. Tong, *Electric hot incremental forming of Ti-6Al-4V titanium sheet.* The International Journal of Advanced Manufacturing Technology, 2010. **49**(9): p. 941-947. DOI: 10.1007/s00170-009-2472-2.

140. Ortiz, M., M. Penalva, E. Iriondo, L. Lacalle, *Accuracy and Surface Quality Improvements in the Manufacturing of Ti-6Al-4V Parts Using Hot Single Point Incremental Forming.* Metals - Open Access Metallurgy Journal, 2019. **9**: p. 697. DOI: 10.3390/met9060697.

141. Cao, T., B. Lu, D. Xu, H. Zhang, J. Chen, H. Long, J. Cao, *An efficient method for*

thickness prediction in multi-pass incremental sheet forming. International Journal of Advanced Manufacturing Technology, 2015. **77**(1-4): p. 469-483. DOI: 10.1007/s00170-014-6489-9.

142. Hussain, G., L. Gao, *A novel method to test the thinning limits of sheet metals in negative incremental forming.* International Journal of Machine Tools and Manufacture, 2007. **47**(3): p. 419-435. DOI: https://doi.org/10.1016/j.ijmachtools.2006.06.015.

143. Lu, B., Y. Fang, D.K. Xu, J. Chen, S. Ai, H. Long, H. Ou, J. Cao, *Investigation of material deformation mechanism in double side incremental sheet forming.* International Journal of Machine Tools and Manufacture, 2015. **93**: p. 37-48. DOI: 10.1016/j.ijmachtools.2015.03.007.

144. Tolipov, A., A. Elghawail, M. Abosaf, D. Pham, H. Hassanin, K. Essa, *Multipoint forming using mesh-type elastic cushion: modelling and experimentation.* The International Journal of Advanced Manufacturing Technology, 2019. **103**(5-8): p. 2079-2090. DOI: 10.1007/s00170-019-03635-z.

145. Ortiz, M., M. Penalva, E. Iriondo, L.N. López de Lacalle, *Investigation of Thermal-Related Effects in Hot SPIF of Ti–6Al–4V Alloy*. International Journal of Precision Engineering and Manufacturing-Green Technology, 2019. **7**(2): p. 299-317. DOI: 10.1007/s40684-019-00038-z.

146. Satko, D.P., J.B. Shaffer, J.S. Tiley, S.L. Semiatin, A.L. Pilchak, S.R. Kalidindi, Y. Kosaka, M.G. Glavicic, A.A. Salem, *Effect of microstructure on oxygen rich layer evolution and its impact on fatigue life during high-temperature application of α/β titanium.* Acta Materialia, 2016. **107**: p. 377-389. DOI: 10.1016/j.actamat.2016.01.058.

147. Ambrogio, G., L. Filice, F. Gagliardi, *Formability of lightweight alloys by hot*

incremental sheet forming. Materials & Design, 2012. **34**: p. 501-508. DOI: 10.1016/j.matdes.2011.08.024.

148. Qu, S.J., S.Q. Tang, A.H. Feng, C. Feng, J. Shen, D.L. Chen, *Microstructural evolution and high-temperature oxidation mechanisms of a titanium aluminide based alloy.* Acta Materialia, 2018. **148**: p. 300-310. DOI: 10.1016/j.actamat.2018.02.013.

149. Niessen, F., T. Nyyssönen, A.A. Gazder, R. Hielscher, *Parent grain reconstruction from partially or fully transformed microstructures in MTEX.* arXiv preprint arXiv:2104.14603, 2021.

150. Orozco-Caballero, A., F. Li, D. Esqué-de los Ojos, M.D. Atkinson, J. Quinta da Fonseca, *On the ductility of alpha titanium: The effect of temperature and deformation mode.* Acta Materialia, 2018. **149**: p. 1-10. DOI: 10.1016/j.actamat.2018.02.022.

151. Zherebtsov, S.V., E.A. Kudryavtsev, G.A. Salishchev, B.B. Straumal, S.L. Semiatin, *Microstructure evolution and mechanical behavior of ultrafine Ti6Al4V during low-temperature superplastic deformation.* Acta Materialia, 2016. **121**: p. 152-163. DOI: https://doi.org/10.1016/j.actamat.2016.09.003.

152. Wang, C., D. Yu, Z. Niu, W. Zhou, G. Chen, Z. Li, X. Fu, *The role of pyramidal <c + a> dislocations in the grain refinement mechanism in Ti-6Al-4V alloy processed by severe plastic deformation.* Acta Materialia, 2020. DOI: https://doi.org/10.1016/j.actamat.2020.08.076.

153. Dai, J., T. Wang, L. Chai, X. Hu, L. Zhang, N. Guo, *Characterization and correlation of microstructure and hardness of Ti–6Al–4V sheet surface-treated by pulsed laser.* Journal of Alloys and Compounds, 2020. **826**: p. 154243. DOI: 10.1016/j.jallcom.2020.154243.

154. Najafabady, S.A., A. Ghaei, *An experimental study on dimensional accuracy, surface quality, and hardness of Ti-6Al-4 V titanium alloy sheet in hot incremental forming.*

The International Journal of Advanced Manufacturing Technology, 2016. **87**(9): p. 3579-3588. DOI: 10.1007/s00170-016-8712-3.

155. Sabat, R.K., M.V.S.S.D.S. Surya Pavan, D.S. Aakash, M. Kumar, S.K. Sahoo, *Mechanism of texture and microstructure evolution during warm rolling of Ti–6Al–4V alloy.* Philosophical Magazine, 2018. **98**(28): p. 2562-2581. DOI: 10.1080/14786435.2018.1493237.

156. Smith, J., W.K. Liu, J. Cao, *A general anisotropic yield criterion for pressure-dependent materials.* International Journal of Plasticity, 2015. **75**: p. 2-21. DOI: 10.1016/j.ijplas.2015.08.009.

157. Tabei, A., F.H. Abed, G.Z. Voyiadjis, H. Garmestani, *Constitutive modeling of Ti-6Al-4V at a wide range of temperatures and strain rates.* European Journal of Mechanics - A/Solids, 2017. **63**: p. 128-135. DOI: 10.1016/j.euromechsol.2017.01.005.

158. Weiss, I., S.L. Semiatin, *Thermomechanical processing of alpha titanium alloys—an overview.* Materials Science and Engineering: A, 1999. **263**(2): p. 243-256. DOI: 10.1016/s0921-5093(98)01155-1.

159. Xiao, J., D.S. Li, X.Q. Li, T.S. Deng, *Constitutive modeling and microstructure change of Ti–6Al–4V during the hot tensile deformation.* Journal of Alloys and Compounds, 2012. **541**: p. 346-352. DOI: 10.1016/j.jallcom.2012.07.048.

160. Ammouri, A.H., G. Kridli, G. Ayoub, R.F. Hamade, *Relating grain size to the Zener–Hollomon parameter for twin-roll-cast AZ31B alloy refined by friction stir processing.* Journal of Materials Processing Technology, 2015. **222**: p. 301-306. DOI: 10.1016/j.jmatprotec.2015.02.037.

161. Valoppi, B., A.J. Sánchez Egea, Z. Zhang, H.A. González Rojas, A. Ghiotti, S. Bruschi, J. Cao, *A hybrid mixed double-sided incremental forming method for forming Ti6Al4V alloy.* CIRP Annals - Manufacturing Technology, 2016. **65**(1): p. 309-312.

DOI: 10.1016/j.cirp.2016.04.135.

162. Najafabady, S.A., A. Ghaei, *An experimental study on dimensional accuracy, surface quality, and hardness of Ti-6Al-4 V titanium alloy sheet in hot incremental forming.* The International Journal of Advanced Manufacturing Technology, 2016. **87**(9-12): p. 3579-3588. DOI: 10.1007/s00170-016-8712-3.

163. Li, Y., W. Zhai, Z. Wang, X. Li, L. Sun, J. Li, G. Zhao, *Investigation on the material flow and deformation behavior during ultrasonic-assisted incremental forming of straight grooves.* Journal of Materials Research and Technology, 2020. **9**(1): p. 433-454.

164. Song, X., J. Zhang, W. Zhai, M. Taureza, S. Castagne, A. Danno, *Numerical and experimental investigation on the deformation mechanism of micro single point incremental forming process.* Journal of Manufacturing Processes, 2018. **36**: p. 248-254. DOI: 10.1016/j.jmapro.2018.10.035.

165. Yoganjaneyulu, G., C. Sathiya Narayanan, R. Narayanasamy, *Investigation on the fracture behavior of titanium grade 2 sheets by using the single point incremental forming process.* Journal of Manufacturing Processes, 2018. **35**: p. 197-204. DOI: 10.1016/j.jmapro.2018.07.024.

166. Bong, H.J., D.H. Yoo, D. Kim, Y.-N. Kwon, J. Lee, *Correlative Study on Plastic Response and Formability of Ti-6Al-4V Sheets under Hot Forming Conditions.* Journal of Manufacturing Processes, 2020. **58**: p. 775-786. DOI: 10.1016/j.jmapro.2020.08.053.

167. Press, W.H., S.A. Teukolsky, *Savitzky-Golay Smoothing Filters.* Computers in Physics, 1990. **4**(6): p. 669-672. DOI: 10.1063/1.4822961.

168. Honarpisheh, M., M.J. Abdolhoseini, S. Amini, *Experimental and numerical investigation of the hot incremental forming of Ti-6Al-4V sheet using electrical*

current. The International Journal of Advanced Manufacturing Technology, 2015. **83**(9-12): p. 2027-2037. DOI: 10.1007/s00170-015-7717-7.

169. Wang, H.-d., *Graphite Solid Lubrication Materials*, in *Encyclopedia of Tribology*, Q.J. Wang and Y.-W. Chung, Editors. 2013, Springer US: Boston, MA. p. 1550-1555.

170. Careri, F., D. Umbrello, K. Essa, M.M. Attallah, S. Imbrogno, *The effect of the heat treatments on the tool wear of hybrid Additive Manufacturing of IN718.* Wear, 2021. **470-471**: p. 203617. DOI: 10.1016/j.wear.2021.203617.

171. Gatea, S., B. Lu, J. Chen, H. Ou, G. McCartney, *Investigation of the effect of forming parameters in incremental sheet forming using a micromechanics based damage model.* International Journal of Material Forming, 2018. **12**(4): p. 553-574. DOI: 10.1007/s12289-018-1434-3.

172. Bai, M., R. Namus, Y. Xu, D. Guan, M.W. Rainforth, B.J. Inkson, *In-situ Ti-6Al-4V/TiC composites synthesized by reactive spark plasma sintering: processing, microstructure, and dry sliding wear behaviour.* Wear, 2019. **432-433**: p. 202944. DOI: 10.1016/j.wear.2019.202944.

173. Wang, S., Q. Zhang, Q. Zhao, B. Guo, *Surface generation and materials removal mechanism in ultra-precision grinding of biconical optics based on slow tool servo with diamond grinding wheels.* Journal of Manufacturing Processes, 2021. **72**: p. 1-14. DOI: 10.1016/j.jmapro.2021.10.010.

174. Oberwinkler, B., M. Riedler, W. Eichlseder, *Importance of local microstructure for damage tolerant light weight design of Ti–6Al–4V forgings.* International Journal of Fatigue, 2010. **32**(5): p. 808-814. DOI: 10.1016/j.ijfatigue.2009.06.021.

175. Ding, R., Z.X. Guo, *Microstructural evolution of a Ti–6Al–4V alloy during β-phase processing: experimental and simulative investigations.* Materials Science and Engineering: A, 2004. **365**(1-2): p. 172-179. DOI: 10.1016/j.msea.2003.09.024.

176. Abbas, A., A. Seif, I. El-Mahallawi, W. Khalifa. *Microstructure and Hardness of Subzero Quenched and Heat Treated Ti-6Al-4V Alloy*. 2017. Cham: Springer International Publishing.

177. Julien, R., V. Velay, V. Vidal, Y. Dahan, R. Forestier, F. Rézaï-Aria, *Characterization and modeling of forged Ti-6Al-4V Titanium alloy with microstructural considerations during quenching process.* International Journal of Mechanical Sciences, 2018. **142-143**: p. 456-467. DOI: 10.1016/j.ijmecsci.2018.05.023.

178. Wang, L.Y., Y.X. Wu, W.W. Sun, Y. Bréchet, L. Brassart, A. Arlazarov, C.R. Hutchinson, *Strain hardening behaviour of as-quenched and tempered martensite.* Acta Materialia, 2020. **199**: p. 613-632. DOI: https://doi.org/10.1016/j.actamat.2020.08.067.

179. Ma, R., A.L. Pilchak, S.L. Semiatin, T.J. Truster, *Modeling the evolution of microtextured regions during α/β processing using the crystal plasticity finite element method.* International Journal of Plasticity, 2018. **107**: p. 189-206. DOI: 10.1016/j.ijplas.2018.04.004.

180. Zhan, X., X. Liu, M. Yang, M. Li, X. Li, J. Chen, *Dynamic recrystallization and solute precipitation during friction stir assisted incremental forming of AA2024 sheet.* Materials Characterization, 2021. **174**: p. 111046. DOI: 10.1016/j.matchar.2021.111046.

181. Yang, J., J. Wu, Q. Zhang, R. Han, K. Wang, *Investigation of flow behavior and microstructure of Ti–6Al–4V with annealing treatment during superplastic forming.* Materials Science and Engineering: A, 2020. **797**: p. 140046. DOI: 10.1016/j.msea.2020.140046.

182. Said, L.B., J. Mars, M. Wali, F. Dammak, *Numerical prediction of the ductile damage in single point incremental forming process.* International Journal of Mechanical

Sciences, 2017. **131-132**: p. 546-558. DOI: 10.1016/j.ijmecsci.2017.08.026.

183. Chen, F., H. Zhu, W. Chen, H. Ou, Z. Cui, *Multiscale modeling of discontinuous dynamic recrystallization during hot working by coupling multilevel cellular automaton and finite element method.* International Journal of Plasticity, 2021. **145**: p. 103064. DOI: 10.1016/j.ijplas.2021.103064.

184. Palaniappan, K., M. Sundararaman, H. Murthy, R. Jeyaraam, B.C. Rao, *Influence of workpiece texture and strain hardening on chip formation during machining of Ti–6Al–4V alloy.* International Journal of Machine Tools and Manufacture, 2022. **173**: p. 103849. DOI: 10.1016/j.ijmachtools.2021.103849.

185. Amouzou, K.E.K., T. Richeton, A. Roth, M.A. Lebyodkin, T.A. Lebedkina, *Micromechanical modeling of hardening mechanisms in commercially pure α-titanium in tensile condition.* International Journal of Plasticity, 2016. **80**: p. 222-240. DOI: 10.1016/j.ijplas.2015.09.008.

186. Francesco, G., A. Giuseppina, F. Luigino, *Incremental Forming with Local Induction Heating on Materials with Magnetic and Non-magnetic Properties.* Procedia Engineering, 2017. **183**: p. 143-148. DOI: 10.1016/j.proeng.2017.04.037.

187. Sun, J.L., P.W. Trimby, F.K. Yan, X.Z. Liao, N.R. Tao, J.T. Wang, *Shear banding in commercial pure titanium deformed by dynamic compression.* Acta Materialia, 2014. **79**: p. 47-58. DOI: 10.1016/j.actamat.2014.07.011.

188. Li, H., X. Sun, H. Yang, *A three-dimensional cellular automata-crystal plasticity finite element model for predicting the multiscale interaction among heterogeneous deformation, DRX microstructural evolution and mechanical responses in titanium alloys.* International Journal of Plasticity, 2016. **87**: p. 154-180. DOI: 10.1016/j.ijplas.2016.09.008.

189. Zhang, Z., D.E. Eakins, F.P.E. Dunne, *On the formation of adiabatic shear bands in*

textured HCP polycrystals. International Journal of Plasticity, 2016. **79**: p. 196-216. DOI: 10.1016/j.ijplas.2015.12.004.

190. Chatterjee, K., M.P. Echlin, M. Kasemer, P.G. Callahan, T.M. Pollock, P. Dawson, *Prediction of tensile stiffness and strength of Ti-6Al-4V using instantiated volume elements and crystal plasticity.* Acta Materialia, 2018. **157**: p. 21-32. DOI: 10.1016/j.actamat.2018.07.011.

191. Thomas, J., M. Groeber, S. Ghosh, *Image-based crystal plasticity FE framework for microstructure dependent properties of Ti–6Al–4V alloys.* Materials Science and Engineering: A, 2012. **553**: p. 164-175. DOI: 10.1016/j.msea.2012.06.006.

192. Zhuang, Z., Z. Liu, Y. Cui, *Dislocation-Based Single-Crystal Plasticity Model*, in *Dislocation Mechanism-Based Crystal Plasticity*, Z. Zhuang, Z. Liu, and Y. Cui, Editors. 2019, Academic Press. p. 91-119.

193. Hill, R., J.R. Rice, *Constitutive analysis of elastic-plastic crystals at arbitrary strain.* Journal of the Mechanics and Physics of Solids, 1972. **20**(6): p. 401-413. DOI: 10.1016/0022-5096(72)90017-8.

194. Peirce, D., R.J. Asaro, A. Needleman, *Material rate dependence and localized deformation in crystalline solids.* Acta Metallurgica, 1983. **31**(12): p. 1951-1976. DOI: 10.1016/0001-6160(83)90014-7.

195. Kröner, E., *Allgemeine kontinuumstheorie der versetzungen und eigenspannungen.* Archive for Rational Mechanics and Analysis, 1960. **4**(4): p. 273-334.

196. Asaro, R.J., J.R. Rice, *Strain localization in ductile single crystals.* Journal of the Mechanics and Physics of Solids, 1977. **25**(5): p. 309-338. DOI: https://doi.org/10.1016/0022-5096(77)90001-1.

197. Kocks, U.F., H. Mecking, *Physics and phenomenology of strain hardening: the FCC case.* Progress in Materials Science, 2003. **48**(3): p. 171-273. DOI: 10.1016/s0079-

6425(02)00003-8.

198. Hémery, S., A. Naït-Ali, M. Guéguen, J. Wendorf, A.T. Polonsky, M.P. Echlin, J.C. Stinville, T.M. Pollock, P. Villechaise, *A 3D analysis of the onset of slip activity in relation to the degree of micro-texture in Ti–6Al–4V.* Acta Materialia, 2019. **181**: p. 36-48. DOI: 10.1016/j.actamat.2019.09.028.

199. Mishra, R.S., Z. Ma, *Friction stir welding and processing.* Materials science and engineering: R: reports, 2005. **50**(1-2): p. 1-78.

200. Wolfram, S., *Statistical mechanics of cellular automata.* Reviews of Modern Physics, 1983. **55**(3): p. 601-644. DOI: 10.1103/RevModPhys.55.601.

201. Peczak, P., *A Monte Carlo study of influence of deformation temperature on dynamic recrystallization.* Acta Metallurgica et Materialia, 1995. **43**(3): p. 1279-1291. DOI: 10.1016/0956-7151(94)00280-u.

202. Derby, B., M.F. Ashby, *On dynamic recrystallisation.* Scripta Metallurgica, 1987. **21**(6): p. 879-884. DOI: 10.1016/0036-9748(87)90341-3.

203. Peczak, P., M.J. Luton, *The effect of nucleation models on dynamic recrystallization I. Homogeneous stored energy distribution.* Philosophical Magazine B, 2006. **68**(1): p. 115-144. DOI: 10.1080/13642819308215285.

204. Ding, R., Z.X. Guo, *Coupled quantitative simulation of microstructural evolution and plastic flow during dynamic recrystallization.* Acta Materialia, 2001. **49**(16): p. 3163-3175. DOI: 10.1016/s1359-6454(01)00233-6.

205. Derby, B., *Dynamic recrystallisation: The steady state grain size.* Scripta Metallurgica et Materialia, 1992. **27**(11): p. 1581-1585. DOI: 10.1016/0956-716x(92)90148-8.

206. Hallberg, H., M. Ristinmaa, *Microstructure evolution influenced by dislocation density gradients modeled in a reaction–diffusion system.* Computational Materials Science, 2013. **67**: p. 373-383. DOI: https://doi.org/10.1016/j.commatsci.2012.09.016.

207. Varshni, Y.P., *Temperature Dependence of the Elastic Constants.* Physical Review B, 1970. **2**(10): p. 3952-3958. DOI: 10.1103/PhysRevB.2.3952.

208. Chen, F., Z. Cui, J. Liu, W. Chen, S. Chen, *Mesoscale simulation of the high-temperature austenitizing and dynamic recrystallization by coupling a cellular automaton with a topology deformation technique.* Materials Science and Engineering: A, 2010. **527**(21-22): p. 5539-5549. DOI: 10.1016/j.msea.2010.05.021.

209. Nixon, M.E., O. Cazacu, R.A. Lebensohn, *Anisotropic response of high-purity α-titanium: Experimental characterization and constitutive modeling.* International Journal of Plasticity, 2010. **26**(4): p. 516-532. DOI: 10.1016/j.ijplas.2009.08.007.

210. Warchomicka, F., C. Poletti, M. Stockinger, *Study of the hot deformation behaviour in Ti–5Al–5Mo–5V–3Cr–1Zr.* Materials Science and Engineering: A, 2011. **528**(28): p. 8277-8285. DOI: 10.1016/j.msea.2011.07.068.

211. Li, K., P. Yang, *The Formation of Strong {100} Texture by Dynamic Strain-Induced Boundary Migration in Hot Compressed Ti-5Al-5Mo-5V-1Cr-1Fe Alloy.* Metals, 2017. **7**(10): p. 412.

212. Hama, T., H. Nagao, A. Kobuki, H. Fujimoto, H. Takuda, *Work-hardening and twinning behaviors in a commercially pure titanium sheet under various loading paths.* Materials Science and Engineering: A, 2015. **620**: p. 390-398. DOI: 10.1016/j.msea.2014.10.024.

213. Zhang, Z.X., S.J. Qu, A.H. Feng, J. Shen, *Achieving grain refinement and enhanced mechanical properties in Ti–6Al–4V alloy produced by multidirectional isothermal forging.* Materials Science and Engineering: A, 2017. **692**: p. 127-138. DOI: 10.1016/j.msea.2017.03.024.

214. Paghandeh, M., A. Zarei-Hanzaki, H.R. Abedi, Y. Vahidshad, *The enhanced warm temperature ductility of Ti-6Al-4V alloy through strain induced martensite reversion*

and recrystallization. Materials Letters, 2021. **302**: p. 130405. DOI: 10.1016/j.matlet.2021.130405.

215. Zhu, C., V. Livescu, T. Harrington, O. Dippo, G.T. Gray, K.S. Vecchio, *Investigation of the shear response and geometrically necessary dislocation densities in shear localization in high-purity titanium.* International Journal of Plasticity, 2017. **92**: p. 148-163. DOI: 10.1016/j.ijplas.2017.03.009.

216. Sangid, M.D., T. Ezaz, H. Sehitoglu, *Energetics of residual dislocations associated with slip–twin and slip–GBs interactions.* Materials Science and Engineering: A, 2012. **542**: p. 21-30. DOI: 10.1016/j.msea.2012.02.023.

217. Guo, Z., A.P. Miodownik, N. Saunders, J.P. Schillé, *Influence of stacking-fault energy on high temperature creep of alpha titanium alloys.* Scripta Materialia, 2006. **54**(12): p. 2175-2178. DOI: 10.1016/j.scriptamat.2006.02.036.

218. Williams, J.C., R.G. Baggerly, N.E. Paton, *Deformation behavior of HCP Ti-Al alloy single crystals.* Metallurgical and Materials Transactions A, 2002. **33**(3): p. 837-850. DOI: 10.1007/s11661-002-0153-y.

219. Britton, T.B., F.P.E. Dunne, A.J. Wilkinson, *On the mechanistic basis of deformation at the microscale in hexagonal close-packed metals.* Proceedings of the Royal Society A: Mathematical, Physical and Engineering Sciences, 2015. **471**(2178): p. 20140881. DOI: 10.1098/rspa.2014.0881.

220. Hama, T., A. Kobuki, H. Takuda, *Crystal-plasticity finite-element analysis of anisotropic deformation behavior in a commercially pure titanium Grade 1 sheet.* International Journal of Plasticity, 2017. **91**: p. 77-108. DOI: 10.1016/j.ijplas.2016.12.005.

221. Zherebtsov, S.V., E.A. Kudryavtsev, G.A. Salishchev, B.B. Straumal, S.L. Semiatin, *Microstructure evolution and mechanical behavior of ultrafine Ti 6Al 4V during low-*

temperature superplastic deformation. Acta Materialia, 2016. **121**: p. 152-163. DOI: 10.1016/j.actamat.2016.09.003.

222. Wang, C., D. Yu, Z. Niu, W. Zhou, G. Chen, Z. Li, X. Fu, *The role of pyramidal 〈 + 〉 dislocations in the grain refinement mechanism in Ti-6Al-4V alloy processed by severe plastic deformation.* Acta Materialia, 2020. **200**: p. 101-115. DOI: 10.1016/j.actamat.2020.08.076.

223. Dabwan, A., A.E. Ragab, M.A. Saleh, S. Anwar, A.M. Ghaleb, A.U. Rehman, *Study of the Effect of Process Parameters on Surface Profile Accuracy in Single-Point Incremental Sheet Forming of AA1050-H14 Aluminum Alloy.* Advances in Materials Science and Engineering, 2020. **2020**: p. 1-14. DOI: 10.1155/2020/7265941.

224. Ambrogio, G., L. Filice, G.L. Manco, *Warm incremental forming of magnesium alloy AZ31*. CIRP Annals, 2008. **57**(1): p. 257-260. DOI: 10.1016/j.cirp.2008.03.066.

225. Trzepiecinski, T., A. Kubit, A. Dzierwa, B. Krasowski, W. Jurczak, *Surface Finish Analysis in Single Point Incremental Sheet Forming of Rib-Stiffened 2024-T3 and 7075-T6 Alclad Aluminium Alloy Panels.* Materials (Basel), 2021. **14**(7): p. 1640. DOI: 10.3390/ma14071640.

226. Formisano, A., M. Durante, L. Boccarusso, A. Astarita, *The influence of thermal oxidation and tool-sheet contact conditions on the formability and the surface quality of incrementally formed grade 1 titanium thin sheets.* The International Journal of Advanced Manufacturing Technology, 2017. **93**(9-12): p. 3723-3732. DOI: 10.1007/s00170-017-0805-0.

227. Oleksik, V., T. Trzepiecinski, M. Szpunar, L. Chodola, D. Ficek, I. Szczesny, *Single-Point Incremental Forming of Titanium and Titanium Alloy Sheets.* Materials (Basel), 2021. **14**(21): p. 6372. DOI: 10.3390/ma14216372.

228. Zhang, Z., R. Wu, J. Hou, T. Wang, *Characterization of Microstructure and*

Mechanical Properties of Ti-6Al-4V Alloy after Cyclic Heat Treatment. Materials Science, 2021. **27**(1): p. 27-31. DOI: 10.5755/j02.ms.23023.

229. Singh, A.K., A. Kumar, K. Narasimhan, R. Singh, *Understanding the deformation and fracture mechanisms in backward flow-forming process of Ti-6Al-4V alloy via a shear modified continuous damage model.* Journal of Materials Processing Technology, 2021. **292**: p. 117060. DOI: https://doi.org/10.1016/j.jmatprotec.2021.117060.

230. Tarín, P., A. Gualo, A.G. Simón, N.M. Piris, J.M. Badía, *Study of Alpha-Beta Transformation in Ti-6Al-4V-ELI. Mechanical and Microstructural Characteristics.* Materials Science Forum, 2010. **638-642**: p. 712-717. DOI: 10.4028/www.scientific.net/MSF.638-642.712.

231. Malhotra, R., N.V. Reddy, J. Cao, *Automatic 3D Spiral Toolpath Generation for Single Point Incremental Forming.* Journal of Manufacturing Science and Engineering, 2010. **132**(6). DOI: 10.1115/1.4002544.

232. Han, F., J.-h. Mo, H.-w. Qi, R.-f. Long, X.-h. Cui, Z.-w. Li, *Springback prediction for incremental sheet forming based on FEM-PSONN technology.* Transactions of Nonferrous Metals Society of China, 2013. **23**(4): p. 1061-1071. DOI: 10.1016/s1003-6326(13)62567-4.

233. Yong, W., H. Zhang, H. Fu, Y. Zhu, J. He, J. Xie, *Improving prediction accuracy of high-performance materials via modified machine learning strategy.* Computational Materials Science, 2022. **204**: p. 111181. DOI: 10.1016/j.commatsci.2021.111181.

234. Fiorentino, A., C. Giardini, E. Ceretti, *Application of artificial cognitive system to incremental sheet forming machine tools for part precision improvement.* Precision Engineering, 2015. **39**: p. 167-172. DOI: 10.1016/j.precisioneng.2014.08.005.

235. Wilmott, C., *1., 1981. On the validation of models.* Phys. Georgr, 1981: p. 2,184-194.

236. Haller, M.C., R.A. Dalrymple, I.A. Svendsen, *Experimental study of nearshore*

dynamics on a barred beach with rip channels. Journal of geophysical research: oceans, 2002. **107**(C6): p. 14-1-14-21.

237. Sharif Ahmadian, A., *Numerical Modeling and Simulation*, in *Numerical Models for Submerged Breakwaters*, A. Sharif Ahmadian, Editor. 2016, Butterworth-Heinemann: Boston. p. 109-126.

238. Abadi, M., A. Agarwal, P. Barham, E. Brevdo, Z. Chen, C. Citro, G.S. Corrado, A. Davis, J. Dean, M. Devin, *Tensorflow: Large-scale machine learning on heterogeneous distributed systems.* arXiv preprint arXiv:1603.04467, 2016.

239. Jha, J.S., S.P. Toppo, R. Singh, A. Tewari, S.K. Mishra, *Deformation behavior of Ti-6Al-4V microstructures under uniaxial loading: Equiaxed Vs. transformed-β microstructures.* Materials Characterization, 2021. **171**: p. 110780. DOI: 10.1016/j.matchar.2020.110780.

240. de Castro, M.C.B., A.A. Couto, G.F.C. Almeida, M. Massi, N.B. de Lima, A. da Silva Sobrinho, M. Castagnet, G.L. Xavier, R.R. Oliveira, *The Effect of Plasma Nitriding on the Fatigue Behavior of the Ti-6Al-4V Alloy.* Materials (Basel), 2019. **12**(3). DOI: 10.3390/ma12030520.

241. Zhang, K., J. Mei, N. Wain, X. Wu, *Effect of Hot-Isostatic-Pressing Parameters on the Microstructure and Properties of Powder Ti-6Al-4V Hot-Isostatically-Pressed Samples.* Metallurgical and Materials Transactions A, 2010. **41**(4): p. 1033-1045. DOI: 10.1007/s11661-009-0149-y.

242. Seth, P., J.S. Jha, A. Alankar, S.K. Mishra, *Alpha-case Formation in Ti–6Al–4V in a Different Oxidizing Environment and Its Effect on Tensile and Fatigue Crack Growth Behavior.* Oxidation of Metals, 2021. **97**(1-2): p. 77-95. DOI: 10.1007/s11085-021-10079-y.

243. Chong, Y., T. Bhattacharjee, Y. Tian, A. Shibata, N. Tsuji, *Deformation mechanism of*

bimodal microstructure in Ti-6Al-4V alloy: The effects of intercritical annealing temperature and constituent hardness. Journal of Materials Science & Technology, 2021. **71**: p. 138-151. DOI: 10.1016/j.jmst.2020.08.057.

Appendix

Support document for research 3: Crystal plasticity model of induction heating assisted incremental sheet forming with recrystallisation simulation in cellular automata

MATLAB codes

Parameters:

```
%% Please note that all units in this code are SI units: m

T=1373;    % Deformation temperature, unit: K

StrainRate=0.1;   % strain rate

Strain=10;          % strain

L0=4e-6;   % The actual size of each cell, unit: m

%%

R=8.31;           %Gas constant, R=8.314J/mol/K

k=1.3806505e-23;     %

PoissonRatio=0.33;           % Poisson Ratio v=0.3-0.4

eps=1e-10;     % Customize an infinitesimal

OriginalDislocation=1e+10;     % Original Dislocation 1e+10=======

DRXOriginalDislocation=1e-10;      % DRX Original Dislocation 1e-10======
```

```
Burgers=2.86e-10 ;    % Burgers vector

ShearModulus=8.2e+10 ;  % Shear Modulus

lanmda=1;   %

Qgb=425000;     %grain boundary activation energy J/mol

Qact=446000;       % activation energy J/mol

DeltaDob=2.0e-4;

HardRate=8.179e+9;    % Hardening Rate

StressMax=120e+06;   % Maximum stress



Garmam=ShearModulus*Burgers/48/(1-PoissonRatio);

L=10*ShearModulus*Burgers/StressMax;

Tao=0.5*ShearModulus*(Burgers^2);

M=Burgers*DeltaDob/k/T*exp(-Qgb/(R*T));

k1=2*HardRate/0.5/ShearModulus/Burgers;

k2=2*HardRate/StressMax;

CriticalDislocation=power(20*Garmam*StrainRate/(3*Burgers*L*Tao^2*M),1/3);    %
Critical Dislocation

kGB=1.2;    %  Adjustment coefficient ==============================
```

```
Deltat=k2^2/(k1^2)/M/Tao*L0/kGB;     % Iteration step time

DeltaStrain=StrainRate*Deltat;     % Iterative dependent variable

Nstep=round(Strain/DeltaStrain);    % Iteration

Delta_t=Strain/Delta_Strain

DislocationMax=(k1/k2)^2;     % Maximum dislocation

Pnuc=0.75e+26*StrainRate*exp(-Qact/(R*T))*Deltat*L0^2;

M=0.7*M*1e1;
```

Initiate microstructure

```
clc;

close all;

% close all open windows

currentFolder = pwd;

addpath('./SourceFunction/');

addpath('./FunctionsMexWIN/');



nx=input(' Please enter the cell space size Nx:');

ny=input(' Please enter the cell space size Ny:');

numnucl=input(' Please enter the number of nucleation points:');
```

```
myseed=input(' Please enter random number seed:');

nstep=input(' Please enter the number of CA steps for grain homogenization growth:');



rng(myseed,'twister');

% set random number seed

ori=zeros(nx,ny);

% cell array initialization

ori(randperm(nx * ny,numnucl))=randperm(1000,numnucl);

% Randomly generate “numnucl” nucleation points in a cell array, the orientation value
distribution range of the nucleation points 1-180



ori2=zeros(size(ori));

ori4=ori2;

ori6=ori2;

ori8=ori2;

ori1=ori2;

ori3=ori2;

ori7=ori2;
```

```
ori9=ori2;
% The current cell array neighbors are pre-allocated to speed up computation
while any(~ori(:))
  % Nucleation Points Fill Cell Array
  [ori2,ori4,ori6,ori8]=neibo4_mex(ori);
  % call the neio function to generate the 4 neighbors of the current cell array
  ori=growth_mex(ori,ori2,ori4,ori6,ori8);
  % Call Mex file -- speed up operation
end


str=input(' Whether to introduce second phase particles:\n','s');
if str=='y'
    number_phase=input(' Please enter the number of second phase particles:');
    radius=input(' Please enter the second phase particle size:');
    ori=addphase(ori,radius,number_phase);
end


for i=1:nstep
```

```
    % The initial grains grow uniformly
[ori1,ori2,ori3,ori4,ori6,ori7,ori8,ori9]=neibo8_mex(ori);
    % call the neio function to generate the 8 neighbors of the current cell array
        ori=coarse_mex(ori,ori1,ori2,ori3,ori4,ori6,ori7,ori8,ori9);
    % Call the Mex file to complete the grain growth according to the grain boundary energy
reduction trend-speed up the operation
end


if str=='y'
    ori_gb=addgb_phase_mex(ori);
else
    ori_gb=addgb_mex(ori);
end


save ori ori;
save ori_gb ori_gb;
```

DRX

```
close all
```

```
clear all

clc

rng(randi(1000),'twister');

currentFolder = pwd;

addpath('./SourceFunction/');

addpath('./FunctionsMexWIN/');

load ori ori;

Parameters;

% Load the initial tissue cell matrix

[nx,ny]=size(ori);

originrow=nx;

origincol=ny;



[~,GB]=addgb_mex(ori);

% Array of grain boundaries, 1 for grain boundaries and 0 for grains

D=ones(nx,ny)*DRXOriginalDislocation;

% Dislocation density array

State=zeros(nx,ny);
```

```
% Cell crystal state array

C=ones(nx,ny)*181;

C(GB==1)=0;

% For display arrays, grain boundaries are 0, black; grains are 181, white

Grainnumber=zeros(nx,ny);

number=1;



drxdistance=zeros(nx,ny);

index=zeros(nx,ny);

locationnum=zeros(nx,ny);

AverageDislocation=zeros(Nstep,1);   % Dislocation Density Average

%======== state variables for all dies =====

% An array of preassignments for each grain area and an array of preassignments for each
grain diameter

RCA=struct('XunHuan1',struct('RAreaOfEachGrain',zeros(Nstep,1)),'XunHuan2',struct('RDia
meterOfEachGrain',zeros(Nstep,1)));

NumberOfAllGrains=zeros(Nstep,1);  % The total number of grains array is pre-assigned
after the recrystallization update once
```

```
AverageDiameterOfAllGrain=zeros(Nstep,1);  % The average grain size array is pre-assigned after the recrystallization update once


%========= State variables for recrystallized grains =========

DRXFraction=zeros(Nstep,1);    % Recrystallization percent array preassignment

NumberOfDRXGrain=zeros(Nstep,1);   % Recrystallized grain number array preassignment

AreaOfEachDRXGrain=zeros(nx,ny);

DiameterOfEachDRXGrain=zeros(nx,ny);

% Visualization of recrystallized tissue evolution

H=image(C);

set(H,'cdatamapping','scaled');

colormap colorcube

title('DRX CAS=0','Fontsize',14,'Fontname','Times New Roman');

set(gcf,'DoubleBuffer','on')

set(gcf,'color','w')

axis equal

axis([1 ny 1 nx])

% DRX evolution iteration
```

```
for i=1:Nstep
%     if mod(i,round(Nstep/4))==0
%
[ori,GB,C,D,State,Grainnumber,drxdistance,index,locationnum]=topo_mex(ori,GB,C,D,State,
Grainnumber,drxdistance,index,locationnum,originrow,origincol,i*DeltaStrain);
%     end


% The above three lines of code are topological deformation, which is disabled by default; if
you want to enable it, just remove the comment.
 % Dislocation Density Evolution Model
D=DislocationMatrix_mex(State,D,DislocationMax,DeltaStrain,k1,k2);


   % Recrystallization Nucleation Model
[ori,C,D,GB,State,Grainnumber,number]=Nucleation_mex(ori,C,D,GB,State,...
       Grainnumber,CriticalDislocation,DRXOriginalDislocation,Pnuc,number);
   % Calculate the size of each recrystallized grain, which is used to calculate the driving
force for the growth of the recrystallized grains
DRXFraction(i)=length(State(State>0))/nx/ny; % Percent recrystallization at different time
steps
       Threshold=0; % Set a threshold, can also be set to 0
```

% When the threshold value is set to 1, the individual nucleation points that only complete nucleation are ignored, and do not participate in the calculation of the average grain size as a single grain

% When the threshold is set to 0, the single nucleation point that only completes nucleation is used as a single grain to participate in the calculation of the average grain size

```
Table1= tabulate(Grainnumber(:));

Table1(Table1(:,2)<Threshold,:)=[];

NumberOfDRXGrain(i)=length(Table1)-1;



% Output the cell's color variable as an image

    H=image(C);

set(H,'cdatamapping','scaled');% Modify settings

    colormap colorcube

axis equal

axis([1 size(ori,2) 1 size(ori,1)])

% recrystallized grain growth

[ori,State,C,D,Grainnumber,drxdistance,index,locationnum]=DynamicRX_mex...

(ori,State,C,D,Grainnumber,drxdistance,index,locationnum,M,Tao,Deltat,L0);
```

```
    %% Dynamically recrystallized grain dislocation density grows again
D=DislocationDRX_mex(ori,D,DislocationMax,DeltaStrain,k1,k2);



    %% reset grain boundary
        [~,GB]=addgb_mex(ori);
    set(H,'CData',showgb_mex(C)); % Update the display of grayscale values
        ti=title([' DRX CAS=',num2str(i)]);
    set(gcf,'color','w')
    axis equal
    axis([1 size(ori,2) 1 size(ori,1)])
    pause(0.0005);



    % The total number of grains and the size of each grain after the recrystallization is updated
once.
    RLT = bwlabel(showgb_mex(C),4);
    RSTATS = regionprops(RLT,'Area');
    % The total number of grains after statistical recrystallization is updated once
```

```
    NumberOfAllGrains(i)=size(RSTATS(:,1),1);
    % Average grain diameter unit: m
        AverageDiameterOfAllGrain(i)=sqrt(nx * ny/NumberOfAllGrains(i) * L0^2 * 4/pi);
    for row=1:NumberOfAllGrains(i)
        % Area per die, unit:m^2
RCA.XunHuan1(i).RAreaOfEachGrain(row)=RSTATS(row).Area * L0^2; % The diameter
of each grain, unit: m
        RCA.XunHuan2(i).RDiameterOfEachGrain(row)=...
        sqrt(4 * RCA.XunHuan1(i).RAreaOfEachGrain(row)/pi);
    end
    % Record stress-strain data
        Stress(i+1)=0.5 * ShearModulus * Burgers * sqrt(sum(D(:))/...
        (size(ori,1) * size(ori,2))) * 1e-6; % unit: MPa
end


% The average grain area was obtained from the lattice area occupied by the recrystallized
grains
MeanAreaOfDRXGrain=DRXFraction * nx * ny * L0^2./NumberOfDRXGrain;
```

```
% From the average grain area of the recrystallized grains, find the average grain diameter,
unit: m

MeanDiameterOfDRXGrain=sqrt(MeanAreaOfDRXGrain * 4/pi);

% Average dislocation density

AverDislocation=[OriginalDislocation;AverageDislocation];

% dynamic recrystallization percentage

Fraction=[0;DRXFraction] * 100;

% Number of recrystallized grains

NumberOfDRXGrain;

% Average size of recrystallized grains

MeanDiameterOfDRXGrain;

% Average size of all grains

AverageDiameterOfAllGrain;

% save data

save data
```

Support document for research 4: Application of machine learning on tool path optimisation and cooling lubricant in induction heating-assisted single point incremental sheet forming of Ti-6Al-4V sheets

PSO algorithm integration to RBF network

Please note that the PSO algorithm was based on modification of the previous study by Han et al. [232]. By integrating this algorithm to RBF network, the particles in each iteration are updated by best fitness (P_i) obtained in previous and another best fitness in the full PSO trackable particles population. As the fitness value is global best, the value is named as (P_g). The PSO accelerates the velocity for each particle toward the P_i and P_g positions at each time. The position and velocity of particle ith updates can be expressed as:

$$V_i^{k+1} = wV_i^k + c_1 r_1 \left(p_i - X_i^k\right) + c_2 r_2 \left(p_g - X_i^k\right) \quad \text{(A-1)}$$

$$X_i^{k+1} = X_i^k + \lambda V_i^{k+1} \quad \text{(A-2)}$$

$$w = w_{\max} - \left((w_{\max} - w_{\min}) / \, k_{\max}\right) \times \text{ iter} \quad \text{(A-3)}$$

where X_i denotes the ith particle position. V_i denotes the ith particle velocity. P_i denotes the best fitness position of ith particle. w denotes the weight inertia. λ denotes the constriction factor which is integrated to w to dominate the limitation of velocity. c_1 and c_2 are constant variables in acceleration. r_1, r_2 are constant variables in the scope of $(0,1)$. w denotes the initial weighting coefficient. $w_{\max}$ and $w_{\min}$ are coefficients. $k_{\max}$ denotes the maximum value of

iterations. The calculation of PSO is terminated as the given maximum iteration or fitness values are met.

The integration flow process of PSO and RBF networks can be expressed as:

1. Set swarm initialisation size w, position and velocity of each particle as: thresholds for connection of RBF neural network θ_{ik}, θ_{kl}; the maximum iteration value $k_{\max}$, constant variables c_1, c_2; $w_{\max}, w_{\min}$ for initialization iteration $k = 1$.
2. The term $\{w_{ik}\}$ denotes the connection weights between the RBF network input and hidden layers. $\{w_{kl}\}$ denotes the connection weights between the RBF network hidden and the output layers. They can be expressed as: $x = \{w_{ik}, w_{kl}, \theta_{ik}, \theta_{kl}\}$.
3. Constraint the range of $\{w_{ik}\}$ and $\{w_{kl}\}$ as $[w'_{\min}, w'_{\max}]$ to initialise the swarm as: PSO $\{x_i(0), i = 1,2, \cdots, m\}$ based on m types of different neural network weights.
4. The fitness of particle x_i can be defined as:

$$f(X) = \frac{1}{1 + E(X)} \tag{A-4}$$

$$E = \frac{1}{2}\sum_{k}^{p}\sum_{j}^{m}\left[d_j(k) - y_j(k)\right]^2 \tag{A-5}$$

where $f(X)$ denotes the fitness value corresponding to x_i, $E(X)$ denotes the initiated error level after each RBF training by individual X. $d_j(k)$ denotes the weight update objective function output; m denotes the number of nodes for output layers.

5. The obtained fitness value $f\left(x_i^{(k)}\right)$ based on each particle will be compared with the value of individual extreme $f\left(p_i^{(k-1)}\right)$. Before imitation of each iteration, if the obtained fitness value is better fit the target than the individual extreme value, then update the individual extreme value $p_i^{(k)} = x_i^{(k-1)}$. Otherwise, repeat $p_i^{(k)} = p_i^{(k-1)}$.
6. For global extreme value updates. The values in $p_g^k = p_i^k$, $f\left(p_i^{(k)}\right) = \max\left\{f\left(p_1^{(k)}\right), \cdots, f\left(p_m^{(k)}\right)\right\}$ for all data points collection, and the values for all fitness values will be used as global extreme values.
7. Update the position x_i and velocity v_{i} of each particle in the **Eq. (A-1)**. To constraint the particles in the search space, V_i is limited as $-V_{\max} \leq V_i \leq V_{\max}$.
8. Each iteration evaluates the fitness value for new particle. The values of P_i and P_g will be determined by each iteration and update P_g of the swarm and P_i of each particle. The iteration and RBF network solution is terminated as the maximum iteration $k_{\max}$ is reached or the training error E is specified as lower the minimum, proceed to step 9. Otherwise, repeat step 4.
9. Exit the PSO algorithm and assign the values to the range of $\{w_{ik}\}$ and $\{w_{kl}\}$ in RBF network.

Machine learning parameters setting for this study

The number of hidden layers can be expressed as:

$$n = \sqrt{a + b} + c \tag{A-6}$$

where a denotes the number of output layers, b denotes the number of input layers, and c denotes a constant in range of 1 to 10. In order to reduce the computing time, c is considered as 8 and n is calculated as 10.

In the algorithm training, following parameters were used, initial and threshold values: $[-1,1]$, learning rate value, $\eta = 0.5$. Momentum factor, $\alpha = 0.6$; Initial population size, $m = 100$; RBF network structure: 3-10-1; inertia weight $\omega = 0.8$; the linear decrease in the number of iterations = 0.4; learning factor of $c_1 = c_2 = 2$; maximum speed $v_{\max} = 0.5$; maximum number of iterations $w_{\max} = 500$; Please note that the above parameters were obtained on less computing time for acceptable error percentage of 2%.

The values of learning rate and momentum factor were adjusted using following equations:

$$\Delta W_{ij} = -\eta \frac{\partial E}{\partial W_{ij}} \tag{A-7}$$

$$W_{ij}(k) = \eta \delta_j(k) y_i(k) + \alpha \Delta W_{ij}(k-1) \tag{A-8}$$

where ΔW_{ij} denotes the deviation of RBF network particle of weight and threshold. $(k-1)$ denotes the time.